UC Berkeley
UC Berkeley Electronic Theses and Dissertations

Title
Advanced Control of Atmospheric Pressure Plasma Jets for Medical Applications

Permalink
https://escholarship.org/uc/item/5cm5d1qt

Author
Gidon, Dogan

Publication Date
2019

Peer reviewed|Thesis/dissertation

Advanced Control of Atmospheric Pressure Plasma Jets for Medical Applications

by

Dogan Gidon

A dissertation submitted in partial satisfaction of the

requirements for the degree of

Doctor of Philosophy

in

Chemical Engineering

in the

Graduate Division

of the

University of California, Berkeley

Committee in charge:

Professor Ali Mesbah, Chair
Professor David B. Graves
Professor Jeffrey A. Reimer
Professor Anil Aswani

Spring 2019

Advanced Control of Atmospheric Pressure Plasma Jets for Medical Applications

Abstract

Advanced Control of Atmospheric Pressure Plasma Jets for Medical Applications

by

Dogan Gidon

Doctor of Philosophy in Chemical Engineering

University of California, Berkeley

Professor Ali Mesbah, Chair

Atmospheric Pressure Plasma Jets (APPJs) are versatile tools for materials processing and medical applications. A key objective for APPJ treatment is the delivery of cumulative and spatially distributed treatment effects, i.e., a plasma dose. However, variability in APPJ operation and their sensitivity to exogenous disturbances can compromise reliable treatment. Particularly, for medical applications, it is necessary to ensure that APPJ effects are delivered safely and repeatably. Feedback control strategies can be crucial in ensuring the APPJ effects are regulated and maintained below critical limits instantaneously and cumulatively.

The APPJ dynamics are nonlinear, multivariable and coupled across multiple timescales. Moreover, the dose delivery problem is spatially distributed. This presents a significant challenge for regulation of APPJ characteristics with basic control strategies based on proportional-integral type controllers. Optimization-based advanced control strategies, such as model predictive control, can systematically account for the APPJ dynamics and the complexities of the dose delivery problem. This work experimentally demonstrates the use of advanced control strategies for regulation of APPJ effects and dose delivery in the presence of common disturbances, including variations in substrate characteristics and changes in jet tip-to-substrate separation distance. In particular, the thermal effects of the APPJ on treated substrate and thermal dose delivery is investigated. An experimental setup of a kHz-excited APPJ in He is constructed to allow implementation of control algorithms. The key issues of modeling, problem formulation, and control synthesis are undertaken for the development of control strategies.

Development of control-oriented models of APPJs, which describe the dynamic response of controlled outputs to manipulated variables, are required for model-based control strategies. A lumped-parameter physics-based model is developed to describe dynamics of power dissipation in the APPJ and the consequent thermal effects on treated substrates. A fluid model of the transport phenomena in the APPJ in COMSOL informs the structure of the lumped-parameter model, which take the form of a set of differential-algebraic equations. The lumped-parameter model is found to adequately describe the experimentally observed APPJ dynamics despite its simplicity. Moreover, a linear data-driven modeling strategy is

shown to be a viable alternative in describing the aspects of APPJ operation that are difficult to model based on physics, albeit for a limited range of operating conditions.

Experimental investigation reveals that basic proportional-integral (PI) strategies tuned using internal model control rules allow rejection of a range of disturbances in a single-input-single-output setting. However, basic control strategies are found to be ineffective in simultaneous control of multiple APPJ effects and for dose delivery. In contrast, MPC strategies are shown to be capable of systematically addressing the multi-variable APPJ dynamics as well as the cumulative nature of the dose delivery problem. With MPC strategies simultaneous regulation of multiple APPJ effects as well as the delivery of a point-wise multi-component dose is made possible in the presence of disturbances. For spatially uniform dose delivery, a hierarchical control strategy is developed. Lower-level basic controllers are found to allow disturbance rejection in fast timescales. On the other hand, the MPC framework allows systematically addressing the different aspects of the dose delivery problem, including the total treatment time, spatially distributed APPJ effects, the multivariable system dynamics, and the translation trajectory of the APPJ over the treated substrate.

Results presented in this work indicate that advanced feedback control strategies are crucial in enabling reliable and reproducible operation of APPJs, particularly in medical applications where safety considerations are stringent and high performance operation is required. The effective regulation of APPJ characteristics can create opportunities for new APPJ applications and the study of APPJ effects by creating controlled environments. Emerging areas for future work include the application of data analytics and machine learning methods for real-time diagnostics, modeling, and control of the complex time-varying APPJ phenomena.

To my parents, my sister and Linoş

Contents

List of Figures

List of Tables

Acknowledgments

Taking on this project was an unexpected yet rewarding challenge. Being at UC Berkeley on this project for the past five years allowed me to work with some brilliant people who transformed the way I look at the world and how I approach challenging problems.

Firstly, I would like to thank my advisors for their continued support and patience as I navigated the challenges of marrying atmospheric plasma with advanced process control. I am lucky to take with me lessons in precision, rigor, and attention to detail from Ali Mesbah. Our detailed discussions with David Graves taught me how to critically approach complex problems, appreciating subtleties of the physics while keeping my eye on the goal. I am grateful for their guidance.

The members of Graves Lab provided technical on and psychological support indispensable for the completion of this work. I thank Carly Anderson, for her never-ending enthusiasm and for her lasting friendship; post-docs I-Wei Yang and Yao-Jhen Yang for giving me the confidence to take on experimental challenges and always being excited to discuss research; undergraduates Eileen Wu, Mahima Parashar and Eliot Foss from whom I learned as much as they did from me if not more. Special thanks to Brandon Curtis, for introducing me to the world of open-source hardware and software and laying the groundwork on which this project stands. More thanks to Xuekai Pei for sharing his expertise in building extraordinary devices, his willingness to discuss and collaborate.

This work would not have been possible without the expertise of fellow members of the Mesbah Lab in model predictive control. I thank Vinay Bavdekar for his patience and teaching me about basic concepts early in my studies; to Tor Heirung for sharing his experience and unique point of view. Special thanks to Joel Paulson for our collaboration, helping me implement complex control algorithms, and his continued interest in my research. More thanks to Angelo Bonzanini for his fresh perspective and his camaraderie.

My experience at UC Berkeley is by no means confined to research. In particular, I would like to acknowledge my cohort; I would not be able to survive the first year of grad school without their support. I thank Nicolas Grosso Giordano, Ari Fischer, Deep Shah, Julie Rorrer and Matt Witman who made my experience in Berkeley much more colorful and enjoyable. I would be amiss without further acknowledging my collaborations with friends; more thanks to Julie for involving me in her brilliant project "Color Me Ph.D." and to Matt for our unexpected collaboration which introduced me to the exciting world of reinforcement learning. I further want to thank CBE staff and in particular Carlet Altamirano for helping me navigate the administrative challenges of the program. Coming to Berkeley, having left my family across two continents and an ocean seemed an insurmountable challenge at the time. I want to especially acknowledge my first roommate William Lamb whose help made my transition much easier. More thanks to my partner Isabelle Cohen for making Berkeley my home – her unyielding support kept me going I tackled some of the most stressful aspects of my work. In Berkeley, I was able to do things I never thought I could. I can't wait to take on what is next.

Chapter 1

Introduction

Cold atmospheric pressure plasmas (CAPs) are uniquely capable of locally generating and delivering a verity of active agents including reactive chemical species, ions, electric fields, UV-visible photons, and thermal effects to heat and pressure sensitive targets. Atmospheric pressure plasma jets (APPJs), a popular class of CAPs, have promising applications in materials processing and medicine [1]–[3]. The generation of the active agents in APPJs rely on complex physical phenomena coupled across multiple timescales, maintained in thermal non-equilibrium [3], [4]. Therefore, APPJs can suffer from considerable variability in their operation: the inherent variability of plasma dynamics and the sensitivity of plasma characteristics to exogenous disturbances can hamper reliable APPJ operation. As a result, the key objective of safe, reproducible and effective delivery of a spatially varying cumulative effect (i.e., dose) on treated substrates can be compromised.

APPJs are particularly sensitive to environmental conditions and exogenous disturbances. Changes in ambient humidity [5], properties of the treated substrate [6], and variations in the distance between the device and the treated substrate [7] can drastically effect plasma properties. Moreover, treatment-relevant plasma characteristics such as gas and substrate temperatures, and delivered reactive species concentrations exhibit sharp spatial and temporal gradients [8] which can complicate regulation of the spatially distributed APPJ effects. The intrinsic variability associated with the inherently non-equilibrium processes that govern plasma generation compounds these issues. Significant variations and drifts in operation in APPJ characteristics are observed even in the absence of significant external perturbations [9]–[11]. Hence, it can be challenging to achieve consistency and reliability in the APPJ operation.

A common objective in APPJ treatment is the delivery of a spatially varying dose. However, the complexity of plasma-substrate interactions and the multi-variable nature of the plasma treatment makes it challenging to effectively quantify and measure a dose. Moreover, the typically small dimensions of APPJs often require their translation across treated substrates, introducing additional complexity to treatment. In the absence of effective dosimetry and online diagnostics, the common practice is to devise treatment protocols offline, largely based on user's experience [12], [13]. As a result, key aspects of the dose delivery, such

as choice of appropriate translation trajectories, ensuring repeatability of operation, and effective mitigation of exogenous disturbances are not systematically addressed.

Plasma medicine is a growing field driven by increasing evidence for the effectiveness of APPJ treatment in alternative and complementary therapies [3], [10], [12]. Promising results are reported with in applications such as reduction of head and neck cancer and accelerated healing of chronic wounds [13], [14]. Some APPJ devices such as KINPen (neoplas tools GmbH, Greifswald, Germany) [15] and SteriPlas (Adtec Plasma Technology, Adtec Europe, Hunslow, UK) [12], [16] have received approval for use in clinical trials. However, variabilities in APPJ operation and the issues in reliable dose delivery present particularly significant challenges in medical applications. The performance requirements are more stringent in the medical context and ensuring safety is of paramount importance. Moreover, a certain amount of variability in external conditions cannot be easily avoided in medical applications. Clinically, treatments are often administered in an uncontrolled environment. Additional sources of variability such as the complex responses of biological substrates and patient-to-patient variability can compromise the safety and repeatably of APPJ treatment.

The question of dose definition is also particularly challenging in plasma medicine. Ideally, a plasma dose would reflect some delivered cumulative effect relating to the end goal of treatment, in this case, the biological response. Where the delivered effect is singular, for example in radiotherapy [17], or hyperthermia [18], this task is relatively straightforward. In contrast, the coupled, multi-variable and highly variable nature of plasma treatment does not lend itself to such a clear definition [15]. Moreover, it is not clear to what extent, if at all, the different active agents generated in the plasma can be decoupled and manipulated independently. This has some direct practical consequences for the treatment. From a safety standpoint, it is necessary that each of the delivered agents is maintained below critical limits. For example, it is not acceptable to burn the patient in trying to deliver a higher concentration of reactive species. The combined effect of therapeutic agents might also result in synergy [19]. For example, the same concentration of delivered reactive species may result in a different biological effect under different electric fields due to electroporation effects [20], [21]. Compounded by the variability observed in operation, it is exceedingly challenging to define and standardize a "plasma dose", particularly for medical applications.

Feedback control strategies can significantly alleviate the challenges outlined above by reducing the variability in APPJ operation, enabling safe, reliable, and reproducible dose delivery. The basic idea behind feedback control is to monitor process outputs in real-time and to maintain them at desired levels by automatically adjusting the process inputs. Based on the discussion above, it is clear that feedback control can provide a range of benefits for plasma medicine applications including:

- safety,

- broadened and flexible operating range,

- reduced variability in treatment,

- systematic adjustment and trade-off between different plasma effects,

- spatially uniform delivery of dose metrics,

- creating a controlled environment for the systematic study of biochemical treatment mechanisms.

1.1   Objective

There are well-established process control practices in plasma fusion [22] and low-pressure plasma etch [23] applications. However, process control has not been implemented in APPJs for plasma medicine or for other applications. To allow implementation of effective real-time control schemes, first, some practical issues need to be resolved. Construction of an appropriate experimental setup, choice, and placement of sensors and actuators, and the development of hardware and software platforms for interfacing and running the control algorithms area some key practical considerations. Particularly, electrical interference from the plasma and the fast timescales of plasma processes impede the real-time diagnostics of APPJ. A goal of this work is to resolve these issues, where possible, using open source tools to increase accessibility of the developed solutions.

The main objective of this dissertation is to develop and apply advanced control strategies for high performance, safe, reliable, and reproducible operation of APPJs with medical applications in mind. That is, reducing the variability of APPJ operation in the face of disturbances and enabling regulation of a multi-component and spatially varying dose. The thermal effects of APPJs on treated substrates have a key significance from a safety standpoint, and spatially-resolved diagnostics of substrate temperature is straightforward. Hence, the regulation of substrate temperature and cumulative thermal effects of the APPJ on the substrate are considered as the main controlled variables. To a lesser extent, the regulation of electrical and optical characteristics of the APPJ are also considered. To achieve the broader objective of developing effective advanced control strategies for APPJs, the following key issues are addressed:

- *Control-oriented modeling:* This work focuses on model-based control approaches which enable using knowledge of system dynamics to inform the design of the control strategies. One key issue the present work investigates is physics-based and data-driven methods of modeling of APPJ devices with the express purpose of designing control strategies.

- *Control problem formulation:* Choice of controlled and actuated variables as well as determining control objectives relating to the medical applications are key aspects of control problem formulation. Some of the key questions addressed in the problem formulation include: What aspects of the process need to be controlled? To what extent can the available actuation influence the process dynamics? What are the typical disturbances and how well can they be rejected?

- *Choice and Evaluation of Model-Based Control Strategies:* Developing and evaluating the performance of control strategies, as well as determining the appropriate strategies for the relevant control problems is the main experimental focus of this work. Basic control strategies relying on proportional-integral (PI) controllers and advanced control strategies relying on model predictive control (MPC) are investigated in this work to address the control challenges of APPJs.

Next sections further elaborate on each of these issues.

1.1.1 Control-oriented Modeling

This work focuses on model-based control strategies so as to leverage the knowledge of the system dynamics for process controls. So-called control-oriented models, which are capable of predicting how measurable application-relevant quantities change over time in response to changing inputs, are developed for this purpose. For APPJs, the key modeling requirements include capturing the coupled multiple-input-multiple-output nature of the dynamics and quantification of the medically-relevant cumulative APPJ effects on treated substrates. Two main approaches, physics-based and data-driven modeling are investigated for obtaining control-oriented models.

Physics-based models can make explicit use of the knowledge of underlying physical phenomena and well-established physical laws to describe process dynamics. However, stemming from the complexity and disparity of timescales of plasma processes, development of physics-based modeling of APPJs can be exceedingly complex. Most typical models of APPJs in literature rely on the solution of coupled partial differential equations describing electrostatic, kinetic and transport phenomena [24], [25]. These high-dimensional models are computationally complex, making their use prohibitive for process control applications. Particularly for advanced control strategies, it is often necessary to solve the model several times over the timescale on which controller is implemented. Thus, it is necessary to focus on simpler model structures for control-oriented modeling. Reduced-order and lumped-parameter models can be instrumental in meeting this challenge. Such models are developed based on assumptions (e.g., spatial and temporal averaging of phenomena), allowing for some knowledge of physics to dictate qualitative model behavior, while relying on some lumped-parameters for quantitative accuracy. Particularly, the separation of timescales in discharge phenomena can guide lumped-parameter modeling strategies. The key challenges in developing physics-based lumped-parameter models are the selection of appropriate assumptions and, where necessary, empirical parametrizations to balance complexity and descriptive capability of the model. Moreover, the stiffness of model equations can present numerical challenges.

Data-driven models present an alternative for control-oriented modeling, based only on input-output data collected from the experimental setup. The key advantage to data-driven models is that they can describe the dynamics of variables which are difficult to describe based on simplified physics-based models. For example, total optical emissions from APPJs have contributions from several transition states related to the dissociated molecules. Devel-

oping a physics-based description of how all the photon-emitting transition processes relate to the manipulated inputs can be a daunting task. In contrast, a data-driven model can be obtained based only on the measurements of optical intensity and the manipulated variables. A key consideration in developing data-driven control-oriented models is the choice of model structure. While it is comparatively easy to fit and validate linear dynamic models, for example, based on subspace identification methods [26], it can be challenging to capture the nonlinear behavior with numerous potential model structures available. However, nonlinear behavior is prevalent in APPJs. Therefore, linear models can be effectively used over only a narrow operating region over which they are identified. This, in turn, can limit the performance of the control strategies developed relying on such models.

Another significant modeling consideration for effective control of APPJs is the quantification of the plasma dose. Dose modeling is intricately related to the end-goal of the APPJ treatment and therefore the problem formulation. The control-oriented model should incorporate a dose definition based on controllable and preferably measurable quantities relating to the interactions of the APPJ and the treated substrate. Although as of yet there are no agreed-upon definitions of plasma dose, dose metrics are likely described by integrating and possibly nonlinear functions of some plasma effects. For the purposes of this work, a tentative dose metric from hypothermia literature [27] is adopted.

1.1.2 Control Problem Formulation

Problem formulation involves translating the goals and practical considerations for the specific APPJ application to a well-defined problem for which a control strategy is designed to solve. Choice of controlled and actuated variables, determining control objectives, and identifying constraints relating to safety and implementation (e.g., available ranges for manipulated variables) are some of the key considerations in problem formulation. The two main objectives of operation are regulating the instantaneous effects of the APPJ on the substrate in the presence of variability (e.g., external disturbances), and the delivery of a desired spatially varying dose.

The regulation problem involves maintaining instantaneous discharge characteristics in the presence of setpoint changes and disturbances. Effective regulation is a key necessity to ensure repeatable and safe operation in the face of the sensitivity of APPJs to disturbances. The multi-variable nature of the APPJ dynamics lends itself to regulation problems where more than one APPJ effects need to be regulated simultaneously. In this case, the coupling between APPJ dynamics can become a significant challenge in determining what combination of setpoints are achievable. The problem formulation should then account for the trade-off between potentially competing objectives, emphasizing which aspects of operation has priority.

Unlike regulation problems which are based on instantaneous effects, dose delivery presents an "end-point" problem. In other words, the objective for dose delivery is defined in terms of the desired *final* value, or spatial distribution, of dose. Since the APPJs typically have small dimensions (few mm in diameter) and exhibit sharp spatial gradients in temperature and

species concentrations [8], it is often necessary to translate them across treated substrates for treatment of practical areas (few cm^2). With this in mind, the components of the dose delivery problem can be summarized as

- total treatment time,

- spatial distribution of dose,

- dynamics of the underlying variables,

- the treatment area,

- translation of the APPJ, and

- equipment and treatment constraints.

Note that these components are interdependent. For example, achievable combinations of reference dose distribution and the total treatment time rely on the underlying dynamics (e.g., temperature dynamics for thermal dose delivery), constraints, and the translation rate. Thus, it is necessary to holistically address the dose delivery problem where possible, taking into account all the components simultaneously. MPC strategies are particularly amenable to addressing this type of problems.

Note that although the regulation and dose delivery problems are distinct, they are inter-related as the delivered dose is defined in terms of the integrating functions of an underlying variable, i.e., an instantaneous effect. Indeed, when the spatial component of the dose delivery is neglected and a known rate of dose delivery is assumed, it is possible to convert the dose delivery problem into a regulation problem [28]. However, these assumptions represent only a very limited subset of practical dose delivery problems.

1.1.3   Model-based Control

The choice of the control strategies and architectures rely on the requirements described in the problem formulation. Basic PI and advanced MPC strategies are investigated in this work to address the challenges of controlling APPJs. Basic control strategies are widely used in countless industrial applications and have well-established properties [29], [30]. PI controllers are easy to design and implement, however, they cannot easily handle integrating processes such as dose delivery or multiple-input-multiple-output system dynamics. Thus, basic controllers are better suited to address single-input-single-output regulation problems.

Model predictive control strategies have shown exceptional success for advanced control of complex systems in a wide range of applications including robotics and path planning, aerospace, and automotive applications, energy systems, and chemical processes (e.g., [31]–[33]). In contrast to basic control strategies, MPC relies on solving a constrained optimization problem based on a system model in real-time, in order to compute the manipulated inputs [34], [35]. Thus, MPC can address some of the key challenges in the control of APPJs.

MPC is capable of systematically accounting for the nonlinear and multiple-inputs-multiple-output APPJ dynamics, integrating and spatially distributed nature of the dose delivery problems, and state and input constraints necessitated by the implementation and safety considerations. Thus MPC is investigated to address multi-variable regulation and spatially-varying dose delivery problems.

The main drawback of MPC strategies is their heavy reliance on dynamic models. The descriptiveness and computational complexity of the dynamic model used with MPC can have a significant impact on the control performance. Moreover, in order to ensure process stability, MPC strategies are often used together with basic control strategies [36]. MPC can act in a supervisory capacity, manipulating the setpoints of multiple lower-level basic controllers which can act on faster timescales. This allows leveraging the strength of the MPC strategies to coordinate more complex tasks, such as spatial dose delivery while retaining the advantage of the fast response time of basic control strategies for disturbance rejection.

1.2   Organization of the Thesis

The following chapters take upon the key issues discussed above, in order to demonstrate that advanced feedback control strategies can enable (i) effective regulation of multiple APPJ effects and (ii) point-wise and spatially uniform delivery of a nonlinear dose, in presence of disturbances (e.g., changes in substrate properties, variations in jet position, and changes jet-tip-to-substrate separation distance). Moreover, the automated and controlled experimental setups used for control allow the collection of large data sets across a broad range of operating conditions. This, in turn, enables the use of data analytics methods for the development of more complicated data-driven system models and diagnostic tools based on information-rich spectral signals.

The rest of this work is organized as follows. **Chapter 2** describes the key characteristics of CAP and APPJs, with a particular focus on the various sources of variability in their operation. **Chapter 3** describes the kHz-excited APPJ setup in helium used in control experiments including the issues in sensing and actuation. **Chapter 4** discusses the development of control-oriented models of APPJs using physics-based and data-driven approaches. These models are then used to design control strategies in the following chapters. **Chapter 5** demonstrates the use of basic control strategies for rejecting a range of disturbances common to APPJ operation in a single-input-single-output context. **Chapter 6** contrasts the PI control strategy to a simple linear MPC based on a data-driven model in regulating multiple APPJ effects in the presence of disturbances. **Chapter 7** demonstrates the use of a physics-based lumped-parameter model to develop a nonlinear MPC (NMPC) including point-wise dose metrics. Simulation and experimental studies show the effectiveness of the NMPC strategy for delivery of a multi-component plasma dose in the presence of disturbances. **Chapter 8** investigates the spatial dose delivery in 1D with APPJ translation with a multi-level control structure.**Chapter 9** extends these results to 2D, and demonstrates uniform dose delivery in presence of disturbances.**Chapter 10** shows few examples of the

data analytics methods enabled by the large data sets collected from automated experimental setups for diagnostics of CAPs. Finally, **Chapter 11** summarizes the conclusions of this work and outlines some open questions for possible future directions for research in control of CAP devices.

Chapter 2

Atmospheric Pressure Plasma Jets for Plasma Medicine

Plasma medicine promises a variety of novel applications which rely on cold atmospheric pressure plasma (CAP) sources to operating in local thermal non-equilibrium. CAPs induce therapeutic effects by locally generating and delivering reactive species, electric fields, UV-visible range photons, and thermal effects. Atmospheric pressure plasma jets (APPJs), a popular subclass of CAPs are preferred for their operational flexibility. However, CAPs and APPJs, in particular, suffer from variabilities in operation which can hamper safety and effectiveness of treatment. This chapter overviews the basics of plasma medicine, generation of CAPs, properties of APPJs and the sources of variabilities which motivate the need for feedback control.

2.1 Introduction

Plasma, the fourth state of matter, can be defined as a quasi-ionized (including fully ionized) gas which exhibits collective behavior [37]. Most of the visible matter in the universe is in the plasma state. Some neutrally-occurring and artificial plasmas are shown in Figure 2.1. Evidently, the plasma state can occur under a variety of conditions which can result in different properties and appearance. For example, high energy collisions in the nuclei of stars create a fully ionized plasma. The temperature in the solar core can be so high that nuclear fusion reactions occur, creating heavier elements from fusing atomic nuclei. Under these conditions, the light emitted from the plasma is a result of black body radiation. Charged particles at the edge of stars, in the so-called corona region, are hurled into the vacuum of space with the rotating motion of stars (e.g., solar wind). The low-pressure environment in space prevents the charged electrons and ions from recombining. Thus, low-density plasmas pervade the vacuum of space. As they are composed of charged particles, plasmas respond to electric and magnetic fields. One example of this phenomena is observed from Earth. The aurora (aurora borealis and aurora australis) are a result of space plasma responding
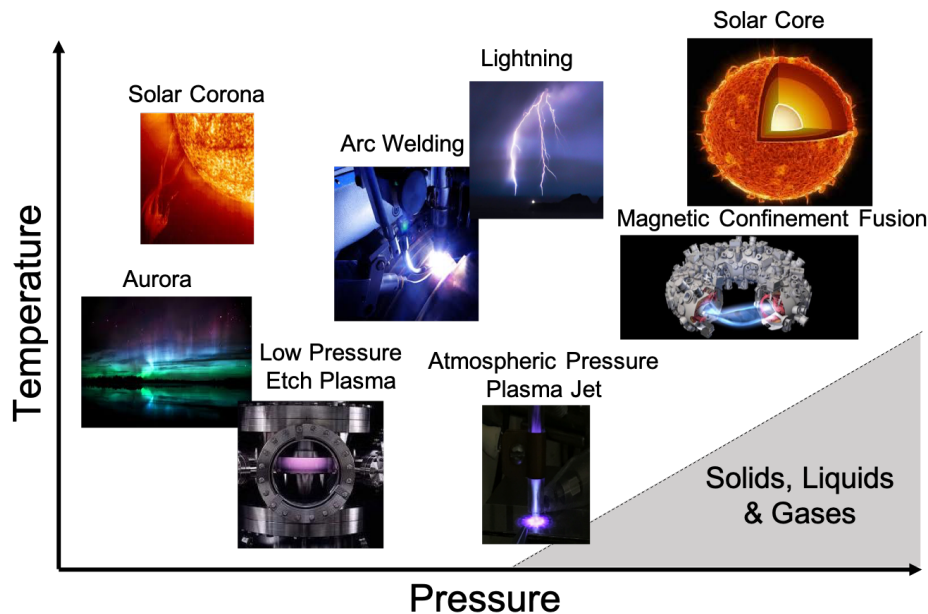
Figure 2.1: Natural and artificial plasmas under different temperature and pressure conditions.

to Earth's magnetic field concentrated at the poles. The charged particles interact with the neutral gas in Earth's atmosphere creating excited states, which then emit visible-range photons. Under the competitively high atmospheric pressure conditions, plasma can be generated as the electrical potential accumulated in clouds is discharged. This, of course, is the familiar phenomenon of the lightning strike.

The active medium of charged and excited particles obtained in the plasma state also make them useful for industrial applications. Artificial plasmas are generated typically by application of electric and/or magnetic fields through a gas. For example, magnetically confined plasmas in fusion reactors are considered for energy generation applications. One common method for generating artificial plasmas is by discharging a capacitor into an electrical circuit with a gap between the electrodes. At sufficiently high voltages, gas in the gap is said to "break down", generating a plasma. These types of plasma are called "gas discharges" [38]. This way electrical energy is efficiently coupled to the charged particles through accelerating them along the electric fields. Gas discharges are widely used industrial applications, most notably for semiconductor manufacturing under low-pressure conditions [39]. Under low pressure, the discharges are well-behaved and take upon the structure of a uniform glow. However, under atmospheric pressure conditions, discharges tend to obtain an arc- and spark-like structures, similar to the lightning bolt. Under this condition, the high collision rates allow energy transfer between the charged particles and the neutral gas. Thus, these types of discharges are used for high-temperature materials processing applications

such as arc welding [40]. It is, however, also possible to generate low-temperature glow-like discharges under atmospheric pressure conditions. These so-called cold atmospheric pressure plasma (CAP) sources allow plasma treatment of heat and pressure sensitive materials including biological targets. An emerging application for plasmas is "plasma medicine" which focuses on the therapeutic effects induced by CAPs. The next sections discuss the details of plasma medicine and the details of the generation of CAP sources with a special focus on the widely-used atmospheric pressure plasma jets (APPJs). A key theme in this chapter is the complexity of the discharge phenomena and the resulting difficulty in their regulation. The consequent variability observed in operation motivates the application of advanced feedback control strategies as demonstrated in the later chapters.

2.2 Plasma Medicine

Medicinal effects of high-frequency currents and associated electrical discharges were first noted in early 20$^{\text{th}}$ century [41]. The increased knowledge and interest in electrical circuits in 19$^{\text{th}}$ century led to the investigation of various effects of alternating and direct currents. Nikola Tesla's designs for high-frequency, high-voltage circuits and his public demonstrations showing that high-frequency currents could interact with living bodies without "apparent harm" pioneered the field [42]. Early adopters such as Arsene d'Arsonval and Paul Oudin innovated on Tesla's design and conducted small-scale trials on patients. d'Arsonval's device reported having medicinal effects including oxidation of blood and increased metabolism [43]. Oudin reported successfully treating a range of ailments with high-frequency current discharges, including focusing on pain relief.[44]

Despite the work of these early investigators, the biological effects of high-frequency currents, at the time, were not well understood. Biological systems and electrical discharges, both complex systems in their own right, give rise to exceedingly complex interactions. In the absence of a good understanding of biology or gas discharge dynamics, the development of electro-therapy applications was outpaced by other contemporary technologies such as X-Ray and radiation [41]. The lack of understanding of the physical principles of electro-therapy also resulted in its association with the metaphysical. Thus, the scientific investigation in this field significantly diminished. This did not stop, however, large scale marketing of gas-discharge based devices to consumers. Known as "Violet Rays", these devices were advertised to have a variety of -unproven- benefits and sold until after World War II. In the late 1940s and early 1950s, a series of cases instigated by the US Food and Drug Administration against various manufacturers resulted in misbranding charges, concluding that the devices did not produce the promised effects [45].

For much of the second half of the 20th century, the research interest in gas discharges primarily focused on comparatively extreme conditions. High temperature and high pressure plasmas for nuclear fusion and low-pressure surface modification applications dominated the field. Notably, with the computer revolution in the 1980s, the demand for semiconductor circuits increased drastically. As one of the primary technologies for manufacturing, use

of gas discharges for "plasma etching" came into prominence both in academia and in industry. This drive resulted in rapid development in the understanding of plasma physics, chemistry, and expertise in diagnostics and device construction [3]. Research efforts in the 1980s focused on atmospheric pressure plasma processes to remove the need for cumbersome and expensive vacuum equipment used in low-pressure processing. By the end of the 1990s, new concepts were developed for atmospheric pressure plasma generation including the use of pointed electrodes, current-limiting dielectric barriers and using pulsed and alternating voltage signals [1], [2], [46].

In parallel to the developments in plasma science, the understanding of biological processes and principles have also rapidly transformed since the 1900s. Notably, the discovery and sequencing of DNA and the development of various assays for metabolites, and gene and protein expression enabled direct and systematic probing of biological systems. In light of these developments, the 2000s saw a re-visiting and re-discovery of the use of electrical discharges for medicinal purposes [47]–[49]. The continued efforts in understanding the medicinal effects of gas discharges and their mechanisms of interactions with biological matter gave rise to the field of "Plasma Medicine" [50], [51].

In the past two decades, the field of Plasma Medicine saw rapid development with increasing number of publications, conference participation and dedicated academic journals. Various medicinal effects are reported with plasma treatment, most prominent of which is the selective deactivation of bacteria [48], [52]–[56]. Other notable applications include:

- Deactivation of biofilms [57]–[59] viruses [60] and fungi [61], [62],

- Dental hygiene [63], [64],

- Surgical ablation [65], [66],

- Treatment of cancers [67]–[71],

- Accelerated wounds healing [72]–[74].

- Assisting drug delivery [75], [76]

- Stem cell differentiation [77], [78]

The majority of plasma medicine research is done *in-vitro* or on animal subjects. At the time of writing, only three plasma devices have obtained clinical certification in Europe; KINPen MED (neoplas tools GmbH), PlasmaDerm (CINOGY GmbH), and SteriPlas (Adtec). The growing clinical experience [13], [79] is poised to provide insight on safety and effectiveness as well as the challenges in *in-vivo* plasma treatment.

In face of the growing interest and research efforts, clarification of the biological mechanisms of plasma therapies, as well as determining the appropriate use cases of plasma devices, are still areas of active research. Efforts of the last decade have provided some significant insight into how plasma devices induce medical effects. Discharges produce a variety of

agents such as reactive oxygen and nitrogen species (ROS), UV and visible range photons, electric fields and thermal effects [80]. Each of these agents is used on their own in medical applications. However, a key advantage of plasma sources is their ability to locally generate and deliver these agents. Particularly ROS are thought to play a key role in inducing biological effects on substrates [10], [80], [81]. These reactive species interact with the cell metabolism inducing proliferation or when the cell is overwhelmed with oxidative and nitrosative stress, cell death [82]. Moreover, short-lived species such as atomic oxygen can induce chain reactions by participating in cell signaling mechanisms, prompting further intracellular production RONs over distances beyond the plasma effects can directly penetrate [12]. The electric fields can result in electroporation, which allows significantly increased transport of the reactive species across cell membranes [20], [83]. UV radiation can have a disinfecting effect on bacteria through inducing dimerization of thymine bases in the DNA strands thereby and interfering with the cell replication processes. Thermal effects of the discharges can also be significant for thermal coagulation applications [84] or for inducing hyperthermia and thermal stress on cell metabolism. The different effects produced by discharges can also act synergistically [19] and induce systemic effects such as oxygenation of the blood [85] and immune response [86]. The complexity of interacting effects produced by discharges is one of the key challenges in understanding the therapeutic effects of plasma devices. This challenge is compounded by the variability observed in operation medically-relevant plasma devices. As a result, the best practices and field standards such as dosimetry, are not yet well-established.

The rest of the chapter overviews the basics of cold atmospheric pressure plasmas, in particular, atmospheric pressure plasma jet configurations and discusses the key sources of variabilities, motivating the need for feedback control.

2.3 Cold Atmospheric Pressure Plasmas

Plasma sources suitable for use in medical applications are necessarily generated under ambient conditions so as to be able to interact with living targets. Moreover, these discharges should be non-thermal, or "cold" exhibiting gas temperatures significantly lower than that of the energetic electrons ($T_g \ll T_e$). CAPs satisfy this requirement by operating outside local thermal equilibrium (LTE). This requirement contrasts with the high temperatures naturally observed in atmospheric pressure discharges such as thermal arcs [87]. Note, however, although termed "cold", the gas temperature in CAPs can still be much higher than room temperature ($\geq 100~^oC$) depending on the operating conditions [88], [89].

This section reviews the basic processes occurring in plasma ignition and steady operation, and thermal equilibrium and presents some common device structures which allow generation of CAPs.

2.3.1 Breakdown and Steady Operation

Electrical breakdown of gases occurs through a process known as Townsend avalanche. This process relies on the presence of a free electron in the discharge gap, accelerated along the applied electric field. Low concentrations of electrons created by cosmic rays are instrumental in initiating this process. As the electron traverses the discharge gap, it collides with neutral atoms, causing them to ionize and to emit electrons. The emitted electrons from these impact reactions are also accelerated in the electric field, further colliding with neutral atoms and causing emission of even more electrons. This chain reaction causes an exponential increase of charged particle in the gap, thereby achieving gas breakdown. [39] The corresponding current during the Townsend process is expressed as

$$I = I_0 e^{\alpha d}, \tag{2.1}$$

where α is the Townsend ionization coefficient, describing the number of ionizing collisions per unit length. This process is also known as the α process. In (2.1) d is the length of the discharge gap and I_0 is the current from the cathode. A key requirement for breakdown is that the mean free path of the electrons is large enough that they can accumulate the necessary energy to ionize the background gas upon impact. With a low mean free path, the electrons lose energy with non-ionizing collisions, preventing ionization. The condition for electrical breakdown is formalized through Paschen's Law which relates the breakdown voltage to the product of gas pressure p and separation distance d for a parallel-plate electrode configuration [90].

In principle, the Townsend avalanche would conclude as the electrons all reach the anode and the ions reach the cathode. The steady-operation of the discharge relies on the so-called secondary or γ process. The γ process involves electron emission from the electrode surface upon bombardment with high energy particles. The Townsend criterion for the self-sustainment of discharge is expressed in terms of both the ionization coefficient α and secondary electron emission coefficient γ as [39]

$$\gamma(e^{\alpha d} - 1) = 1. \tag{2.2}$$

Where the discharge is generated in rare gases (such as He or Ar), a secondary process is known as Penning ionization can also play a significant role in discharge steady operation [91]. This process relies on the emission of secondary electrons from ionization of metastable species instead of emission from the electrode. Note, however, that secondary electron emission processes are not necessary to maintain in all discharges (e.g., radio frequency excited discharges).

2.3.2 Plasma Temperatures and Thermal Equilibrium

The description of a singular "temperature" for plasmas is not straightforward. In fact, plasmas can exhibit several different temperatures at the same time; for example, electrons,

being considerably lighter than ions and neutral particles, can obtain higher velocities in electric fields and therefore can have a higher temperature than the heavier ions. Whether or not the plasma reaches a thermal equilibrium, where all particles have the same velocity, depends on the frequency of collision events which is a function of the pressure and applied electric fields.[37] The deviation of a steady state discharge from thermal equilibrium can be described with the following expression for a group of electrons accelerating in an electric field, moving in a gas [92]

$$\frac{T_e - T_g}{T_e} = \frac{m_g(\lambda_e e E)^2}{4m_e(\frac{3}{2}k_b T_e)^2}. \tag{2.3}$$

Here, T_e is the electron temperature and T_g is the temperature of the surrounding (neutral) gas and the heavy particles. λ_e is the mean free path of electrons, m_g and m_e are the molecular mass of the gas and electron, respectively, E is the electric field, e is the elementary charge and k_b is the Boltzmann constant. The term $\lambda_e e E$ corresponds to the energy accumulated by an electron accelerated in the electric field along its free path, and $\frac{3}{2}k_b T_e$ is the average thermal energy assuming a Boltzmann distribution. Expression (2.3) indicates that large mean-free paths (low pressure or density), large electric fields and low electron energies result in deviations from LTE. Moreover, differences in the mass of an electron and the background gas contribute to this deviation. The lighter electrons can move significantly faster allowing them to respond to changes in electric fields faster than the heavier ions.

Since the mean free path scales with pressure, discharges tend to thermal equilibrium as pressure increases. At low pressures, the mean free path is large; electron-neutral collisions are rare and the energy in electrons is not effectively transferred to the gas. As a result, T_e and T_g diverges, generating a "cold" plasma. This type of discharges is well studied in the field of astrophysics [37] and widely used in materials processing applications for heat sensitive materials [39]. Under atmospheric pressure, however, it is comparatively difficult to generate a non-thermal plasma. The rapid heating of gas when an electrical discharge is ignited can cause the plasma to exhibit "arc" or "spark" behaviors [93]–[95]. In this case, the discharge shrinks into a thin conductive filament with high current density, as the energy in the electrons is transferred to the gas through rapid collisions. A naturally occurring example of this phenomena is the formation of the lightning bolt. While arc and spark type discharges have some industrial uses (e.g., welding, spray casting [40], [96]), the high temperatures they exhibit (on the order of 10,000K) limit their use for interacting with heat sensitive, and living substrates.

Generation of cold plasmas under atmospheric pressure condition can be achieved through the application of *transient* electric fields, the use of current limiting circuitry and gas flow. The discharge, then can be maintained at a sustained state of non-LTE, maintaining the discrepancy between T_e and gas T_g and preventing the transition to an arc. The next section described the generation of such discharges in further detail.

(a) Streamer Discharge   (b) Dielectric Barrier Discharge
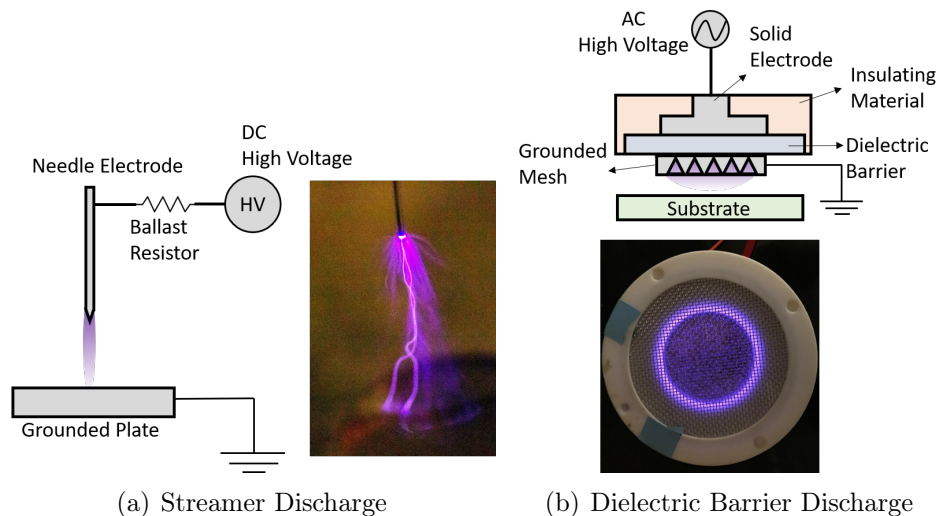
Figure 2.2: Typical configuration of an atmospheric pressure (a) streamer discharge and, (b) a dielectric barrier discharge in air.

2.3.3   Cold Atmospheric Pressure Plasma Devices

The key means of generating non-LTE CAPs is exploiting the distributed timescales of the physical phenomena in discharges [4]. CAP devices are typically ignited by transient electric fields [87]. Figure 2.2 depicts two common types of cold atmospheric pressure plasma sources, a streamer discharge (Figure 2.2(a)) and a dielectric barrier discharge (Figure 2.2(b)). The corona discharge is operated using DC voltage, applied to a needle electrode. The sharp needle tip creates a region of concentrated electric field allowing for an easier breakdown. The steamer discharge exhibits self-pulsing behavior; a large ballast resistor placed between the power supply and the electrode limits the discharge current and causes the discharge to extinguish before it becomes too conductive and transitions to a spark [93]. As a result, corona discharges typically obtain a discrete streamer structure [97]. The self-pulsing behavior allows the corona discharge to remain cold since the discharge is not present for long enough for the background gas to warm up.

The dielectric barrier discharge, as the name implies, relies on a dielectric barrier placed between the electrode to limit the current. The presence of dielectric barrier necessitates the use of AC voltage (few-several kHz) to sustain the plasma. The key advantage of the DBD configuration is the ease of construction of devices with relatively large surface area for comparatively homogeneous treatment. DBDs also have the benefit of being generally arc-free. However, the discharge structure may become filamentary with increasing discharge voltage [98]. The kHz-range excitation also results in discrete breakdown events. These discharges further exhibit a so-called "memory effect" where the effects from one breakdown event are carried over and influence the subsequent breakdowns [99], [100]. This behavior is attributed to charge accumulation in the dielectric and longer-lived metastable species whose

lifetimes can exceed timescales of the electrical excitation, contributing to the repeatability
between the individual breakdown events [101].

Corona and DBD discharges represent examples of typical configurations for CAP sources
ignited in air. A particularly significant enhancement for CAP sources is the incorporation
of gas flow, which can significantly alter discharge phenomena while offering additional flexi-
bility in operation. The CAP sources incorporating gas flow have distinct characteristic and
are often classified separately. The next section focuses on this class of CAP devices termed
atmospheric pressure plasma jets (APPJs).

2.4   Atmospheric Pressure Plasma Jets
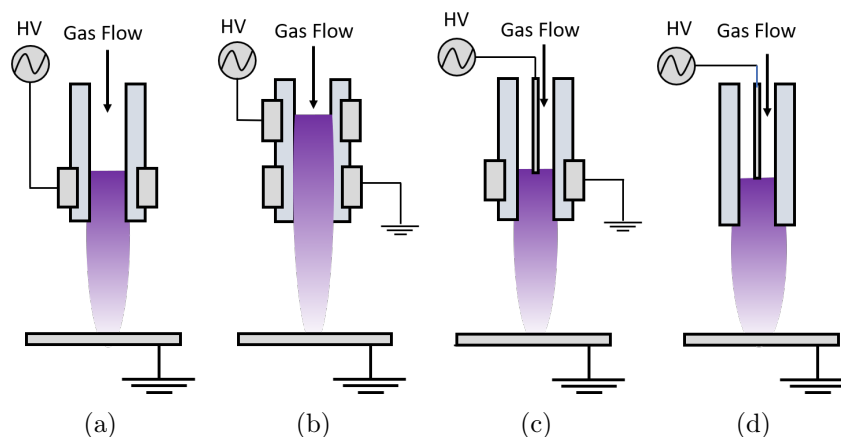
Figure 2.3: Diagrams for atmospheric pressure plasma jets in (a)-(b) DBD-jet and (c)-(d)
DBD-like jet configurations.

APPJs have gained increasing attention in medical [3], [12], [79] and materials process-
ing applications [2], [87], [102] due to their operational flexibility and versatile discharge
chemistry. APPJS are classified based on their electrode geometry and arrangement, the
excitation frequency of the applied voltage, as well as the flow field configuration and com-
position of the working gas [103].

APPJs exhibit similarities to corona and/or DBD discharges based on the shape and
configuration of electrodes. In APPJs, ring and rod (or needle) electrodes are configured
in and around a dielectric tube, which directs the flow of a carrier or operating gas and
usually doubles as a dielectric barrier. To allow breakdown at practical applied voltages, the
dimensions of the dielectric tube is typically kept small (few mms in diameter). Figure 2.3
shows some common electrode geometries for APPJs. When the powered APPJ electrode is
covered by a dielectric the APPJ is referred to as a DBD-jet (Figure 2.3(a)-2.3(b)) whereas
if the powered electrode, typically a needle, is exposed the APPJ is termed a DBD-like jet
(Figure 2.3(c)-2.3(d)). The key difference is that in DBD-like APPJs the discharge directly

runs between the electrode and conductive substrates, with no dielectric barrier to limit
current. This can drastically influence the discharge characteristics and may result in arcing
behavior under certain conditions. The DBD-jet ([25], [104], [105]) and DBD-like jet ([47],
[79], [106]) are the most common APPJ configurations used in medical applications.

Often a distinction is made between direct and indirect treatment with APPJs. Direct
treatment refers to a condition where the plasma is electrically coupled to the substrate,
while in indirect treatment the treated substrate is only in contact with the discharge af-
terglow. Direct plasma treatment allows generation of chemically active species close to the
target substrate and, therefore, can enhance the plasma effects [107]. However, the coupling
between the discharge and substrate under direct treatment also implies that the discharge
properties can change, sometimes drastically, with changing substrate properties [25], [106].
Although some discharge geometries, such as those shown in Figure 2.3(a) and 2.3(d), are
more amenable to direct treatment, electrical coupling to the substrate may occur even
when a grounded electrode is present. The distinction between direct and indirect treat-
ment, therefore, can be non-trivial as it depends on the specifics of the device and operating
conditions.

APPJs can be excited with oscillating electric fields in kHz, RF (MHz) or microwave
(GHz) frequencies. The characteristic frequencies of electrons and heavier ions influence
how the discharge behaves under different frequencies of excitation. Typical characteristic
frequency of ions is on the order of an MHz, while the characteristic frequency of electrons
is on the order of a GHz. As as a result, three distinct behaviors are observed in the
discharge; in kHz range, both electrons and ions respond to the electric field, in RF range
electrons respond to the electric field but the heavier ions cannot, and in microwave-range
neither electrons nor ions can respond to the rapidly changing electric field [87]. kHz range
excitation, be it pulsed or sinusoidal, can result in inherently discrete discharge behavior.
For example in AC kHz-excited APPJs a distinct breakdown events are observed during the
positive and negative half cycle of the applied voltage signal [104]. So-called "plasma bullets"
or guided ionization waves occur under this condition, propagating at speeds of several km/s
[103], [108], [109]. In DBD-jets long-lived metastable species can remain in the discharge
gap between breakdown events, influencing the overall discharge behavior [99], [110]. This
can lead to some distinct mode behavior in kHz-excited APPJs including "continuous" mode
where the discharge appears present throughout the entire period of the applied voltage, and
"filamentar" behavior where multiple secondary breakdown events are observed associated
with an appearance of multiple distinct filaments [110], [111]. In contrast, RF-APPJs are
inherently continuous; the electrons rapidly oscillate in response to the electric field within
a cloud of stationary ions in the bulk discharge. RF discharges are commonly used with
the DBD-like jet configurations [47], [79], [106] and can exhibit the so-called $\alpha - \gamma$ mode
transition where the secondary electron emission processes become dominant over Townsend
ionization [112]. This behavior can lead to arcing, particularly when an APPJ configuration
with an exposed electrode is used. Both RF and kHz-excited APPJs can be further equipped
with a duty cycle or pulse modulation, which involves modulating the applied voltage at a
lower frequency than that of excitation. Duty cycle modulation is sometimes used as a means

for regulating the discharge temperature in RF discharges [106], [113].

The flow rate and composition of the working gas are some of the key parameters which influence APPJ characteristics. Typically APPJs are operated with a noble gas, which allows a lower breakdown voltage. Although it is possible to obtain air or N_2 jets, they are not commonly used in medical applications due to their comparatively high temperature [103]. Common choices of operating gases are He and Ar. The choice of the operating gas can influence the stability region, as defined by the operating region beyond which the discharge becomes unstable and possibly transitions to arc as well as the dissipated power and gas temperatures [88], [114], [115]. Notably, Ar results in higher gas temperatures but higher discharge currents and electron densities and is the working gas of choice for the clinically approved kINPen device [79] as well as for thermal coagulation [84]. In contrast, He jets are associated with larger electron temperatures [115]. Typical flow rates of 1-10 slm are used in APPJ devices. APPJs are constructed in either linear field configuration where the electric and flow fields are parallel, or in cross-flow configuration where the two fields are perpendicular. The geometries depicted in 2.3 are all in linear field configuration. This is desirable as the linear field configuration allows the APPJ to extend beyond the electrode up to several cms outside the tube [116], increasing the flexibility of treatment.

The flow structure in APPJ is coupled to the discharge dynamics, and can significantly influence the discharge characteristics. The flow rate, as well as the laminar and turbulent flow regimes, influence how far the plasma plume extends beyond the electrode as well as the discharge propagation dynamics such as the propagation speed of plasma bullets [103], [117], [118]. The flow rate also influences the extent to which the ambient gas is in-mixed to the jet plume, impacting the spatial profiles of the reactive species delivered to treated substrates [119]–[121]. Small admixtures (few %) of molecular gases such as O_2 [91], [121]–[123], N_2 [47], [124] and H_2O [5], [125] are often used to influence discharge chemistry in generating medically-relevant RONs. The use of so-called shielding gases to change the composition of the ambient gas in contact with the plasma plume can be yet another means of influencing discharge chemistry [126].

2.4.1 Variability in APPJs

The complex physical processes that occur in APPJs are distributed across multiple timescales and result in a broad range of operating conditions for the APPJ. The flexibility in the operating conditions is a key strength in making APPJs attractive tools for medical and materials processing applications. However, the same physical phenomena also result in considerable sensitivity of APPJs to operating and ambient conditions. As a result, APPJs can suffer from considerable variability in operation which can be detrimental to their reliable application, particularly in a medical context.

APPJs typically exhibit steep spatial gradients both in axial (direction of flow) and radial (perpendicular to flow) directions. Concentration gradients of reactive species and gas temperature can be, respectively, on the order of 10^{15} cm^{-3}/cm and 10 K/cm along the plasma plume [8]. This implies that APPJ operation requires considerable precision

for effective treatment. The jet-tip-to-substrate separation distance and the x-y position of the jet over the surface should be manipulated with care. However, the comparatively small dimensions of APPJs (few mm in diameter) often require translation over treated substrates. The small variations in the position of the APPJ which inevitably occur during hand-held translation of APPJs over substrates can cause changes in discharge characteristics resulting in non-uniformity of treatment, with over- and undertreated areas.

Variations in jet-tip-to-substrate separation distance can impact several physical phenomena occurring in APPJs. For example, increased separation distance increases the discharge area exposed to ambient air, increasing the amount of air admixed into the jet plume. This, in turn, influences the temperature dynamics as well as the concentration and spatial distribution of reactive species in the discharge. Moreover, in the case of direct treatment, where the substrate is coupled to the discharge, changing separation distance changes the electric field across the discharge gap and the location of the ground. Therefore changes in separation distance can significantly impact the properties and treatment effects of the APPJs [121], [127].

In case of direct treatment APPJs exhibit sensitivity to properties of the treated substrate. Varying conductivity, electron emissivity and thermal properties of the substrates can dramatically change the APPJ characteristics including electric fields, concentrations of electrons and reactive species concentrations [6], [25]. For example, APPJs are observed to spread out over dielectric substrates while a distinct secondary "re-strik" phenomena are observed over conductive substrates associated with increased power deposition. In a medical context, treated substrates such as healthy skin, wounds or tumors may have varying properties resulting in a different treatment effect. Moreover, APPJs exhibit some inherent variability. Particularly during the start of the operation, the optical and electrical characteristics of APPJ are observed to drift significantly [9], [11].

These sources of variability can significantly impact the safety, effectiveness, and reproducibility of APPJ treatment. Particularly in a medical context, the safety and reproducibility requirements are stringent and sources of variability are compounded by patient-to-patient variability. As a result, the APPJ operating range cannot be fully exploited for safe and effective treatment. Moreover, it can be difficult to isolate and discern the specific effects and underlying physical mechanisms of APPJs in presence of the variabilities making it difficult to compare different discharges and experiments, hampering the research efforts in plasma medicine.

2.4.2   Conclusions

This chapter overviewed the history, basic premise, and devices used in plasma medicine, with a particular focus on APPJs. The potential for plasma devices for a variety of medical application is evident. However, generation and maintenance of discharges suitable for medical treatment can be extremely complex and difficult to regulate. In particular, APPJ devices suffer from various sources of variability in their operation stemming from their sensitivity to the operating condition and their environment.

The main conclusion of this chapter is the pressing need for effective regulation for APPJ characteristics in real time, particularly in the context of plasma medicine. Feedback control strategies can be instrumental in improving the safety of APPJ treatment, broadening the operating region of APPJs and allowing increased flexibility and repeatability of treatments.

Chapter 3

Experimental Setup of a kHz for Real-time Control

Automation of data collection and actuation is necessary for the implementation of process control strategies. However, there is no current practice for automated experimental atmospheric pressure plasma jet (APPJ) setups. As a result, the design and choice of actuators and sensors for automated operation are open questions. This chapter investigates considerations regarding design actuators for voltage and gas flow, as well as the choice and integration of instrumentation for sensing thermal, electrical, and optical characteristics of a kHz-excited APPJ in helium. The details of the hardware and software components of the experimental control setup are presented.

3.1 Introduction

The features of the experimental setup, particularly the instrumentation, can have a significant impact on design and implementation of control strategies. For example, the available measurements and the multiple timescales over which the measurements are acquired may limit what aspects of the system can be controlled. The constitution of the experimental setup (i.e., geometry, excitation frequency, etc.) and the intended use (e.g., stationary vs hand-held setups) can impact the choice of sensors and their placement. Therefore, the design of the experimental setup and the control strategies are coupled undertakings. Some crucial issues pertaining to the design of an APPJ setup for real-time control include:

- construction of the APPJ device,

- design of circuitry for actuation and measurement of electrical signals,

- choice of non-contact measurement methods for discharge characteristics,

- design and implementation of automatic actuation mechanisms for the APPJ position,

- reliable operation of the electrical equipment in presence of interference from the discharge, and

- synchronizing measurements and coordinating actuation signals from different sources.

A single-electrode kHz-excited dielectric-barrier APPJ setup, similar to the configurations investigated in [104], [110], [111], [128]–[131], is chosen for experiments. This APPJ configuration is preferable due to the stable, arc-free operation and simple construction. The APPJ consists of a quartz tube (ID=3 mm, OD=4 mm) which doubles as a flow channel and dielectric barrier. A 1 cm long copper plate, wrapped outside the tube 1 cm away from the nozzle, is used as the powered electrode. An aluminum plate fixed on a gantry acts as the ground. Nominally, a borosilicate microscope cover slip is situated under the APPJ as a dielectric substrate. The APPJ is operated in *direct mode*, where the discharge remains electrically coupled to the treated substrate throughout the operation.

The instrumentation of the setup consists of two distinct parts: (i) an embedded layer managed by microcontrollers (Arduino UNO R3), and (ii) peripheral instruments which collect memory-intensive measurements (images, spectra, etc.). The signals from embedded instruments and peripherals are processed and synchronized in Python, using a single board computer (Raspberry PI 3). The single board computer also governs the actuation by communicating with the embedded layer via USB. The single-board computer is capable of Wi-Fi allowing further communication with the experimental setup using the TCP/IP protocol. The rest of the chapter presents the components of embedded and the peripheral layers and details of the software which allows their coordination.

3.2   Embedded Actuation and Sensing

The embedded layer represents the lowest layer allowing automated interaction with the environment, generation and recording analog and digital signals. The embedded layer consists of actuation circuitry, sensors, and programmable micro-controllers. The micro-controllers are capable of executing code in fast (millisecond) timescales, however, have limited memory and capabilities. For example, they can generate only digital signals (high, low and pulse-modulated) and can access information via limited communication protocols (e.g., analog voltage and i2c communication) and execute relatively simple programs. Therefore the embedded layer is suitable for generating the actuation signals and record comparatively simple, fast-timescale measurements.

A diagram of the embedded measurement and actuation layer for the experimental setup is presented in Figure 3.1. Two Arduino UNO micro-controllers manage actuation and embedded measurements. The "Master Arduino" manages the actuation of the applied voltage signal (applied voltage amplitude, frequency and duty cycle), the flow rates as well as the embedded measurements. The "Complementary Arduino" is solely responsible for managing the x-y-z position of the APPJ. To ensure reliable operation of the micro-controllers in
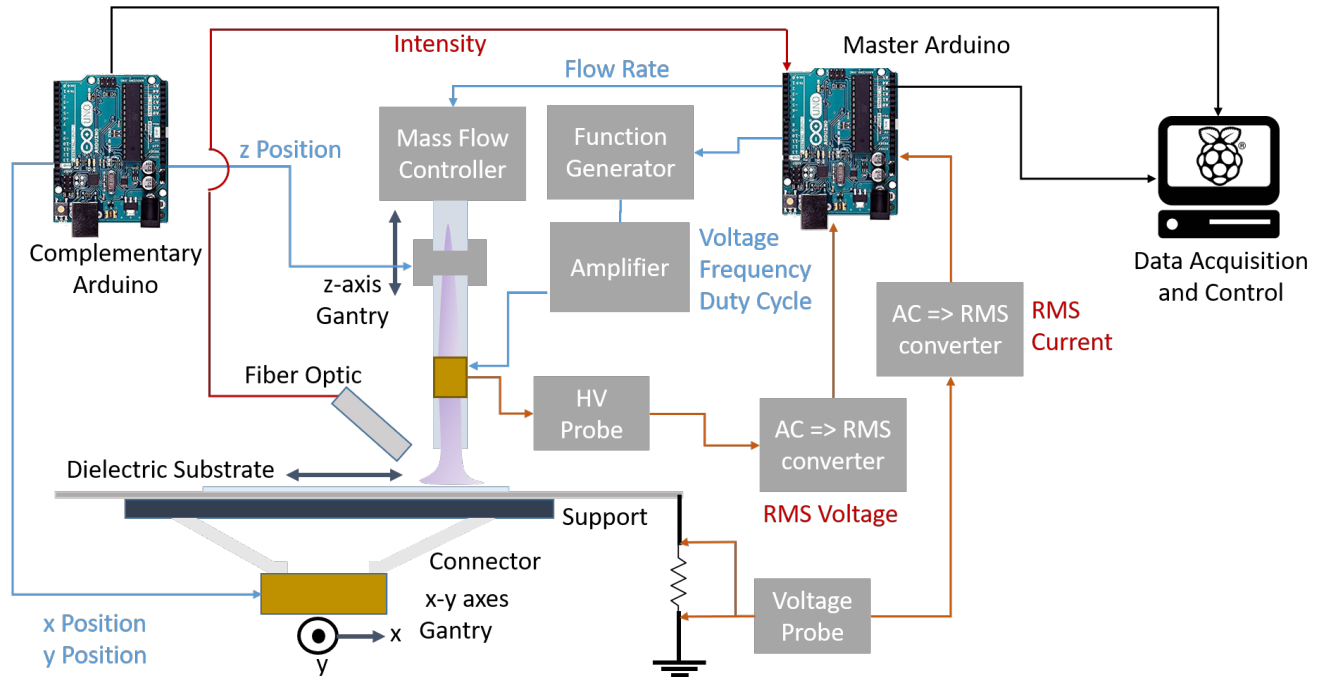
Figure 3.1: Diagram of the embedded sensing and actuation instruments in the experimental APPJ setup. Measurement signals are denoted by red arrows while actuation signals are denoted in blue.

presence of electrical interference, a "watch-dog" algorithm is employed to re-start operation after 500ms of inactivity.

3.2.1 Applied Voltage Signal

The applied voltage is a key input parameter for the APPJ as it is the main means to influence the power deposition in the discharge. In order to ignite the dielectric-barrier type APPJ, a high-voltage AC voltage signal is necessary. As the micro-controller is only capable of generating digital signals, additional circuitry is needed to be able to generate and modify the input voltage signal.

An analog signal generator is designed to generate the sinusoidal voltage signal igniting the discharge. The circuity allows manipulation of three inputs; applied voltage amplitude, frequency, and duty cycle. The circuit diagrams of the different components of the signal generator circuit, as well as the values for the associated circuit elements, are given in Appendix A. The signal generator is based on the monolithic function generator (XR-2206CP) (Figure A.3), configured to generate a sinusoidal signal at a frequency of 8-20 kHz and at an amplitude of 5-10 V peak-to-peak. A 12-bit digital-to-analog converter (MCP4922) (Figure A.1) generates the analog signals necessary to modulate the voltage and frequency.

As the Arduino is capable of generating only a 5 V signal, an operational amplifier (Figure A.2) is used to achieve the range of 5-10 kV peak-to-peak applied voltage. The generated sinusoidal signal is amplified $1000\times$ via a high-voltage amplifier (Trek 10/40A), in order to achieve gas breakdown. A switching circuit is situated between the function generator output and the amplifier (Figure A.4) to allow modulation of the duty cycle of the applied voltage. The switching circuit is controlled by the pulse-width-modulated signal produced by the Arduino UNO at a frequency of 1 kHz.

This circuit design described above is selected for actuation since it provides a robust and reliable means of generating the applied voltage signal. However, using the monolithic function generator allows only a limited range of available waveform shapes (sine, triangular and square wave) and a limited range of excitation frequencies (8-20 kHz). As an alternative, commercial function generators can be adapted for automatic control via digital communication protocols. Waveform generators based on direct digital synthesis (DDS) are often capable of generating various shapes of voltage signals across a large range of frequencies [132]. However, common high voltage amplifiers are often rated for limited ranges of frequencies. Moreover, erratic transient behavior can be observed in fast-timescales with some function generators when voltage changes are applied. Such transients may lead to arcing behavior and are generally undesirable during operation. Nevertheless, utilizing DDS to actuate the voltage signal can open up opportunities for control. For example, discharge properties may be influenced over fast (nanosecond-microsecond) timescales by using custom-generated waveforms.

3.2.2 Flow Rates

Along with the applied voltage, the flow rate of the working gas, helium, and its composition can significantly influence the APPJ behavior [126], [129], [133]. Therefore the ability to manipulate the flow rate helps broaden the operating range of the device. Commercial mass flow controllers (MFC) (UNIT UFC-1200A) are chosen to maintain the flow rate of the working gas, helium, and an admixing gas (O_2 or N_2). Any number of MFCs can be incorporated into the setup via a manifold in order to allow for complicated, multi-component gas mixtures. However, in order to limit the complexity of the setup only two MFCs are incorporated to the setup. The 20-pin connectors between the MFC valves and control boxes are spliced to allow automatic manipulation of the flow setpoints. An analog signal at the range of 0-5 V generated using the digital-to-analog converter (MCP4922), (see A.1)) is utilized to vary the flow rates via the Arduino within the range rated by the individual MFCs (0-10slm for the working gas and 0-20sscm for the admixed gas).

3.2.3 Position

The small diameter of the APPJ requires that the device is translated across substrates for treatment of practical areas ($\sim$ cm^2). The problem of building devices for the automatic positioning of the APPJ position falls in the realm of mechatronics. On its own right, building

(a) z-axis holder side view   (b) z-axis holder in perspective
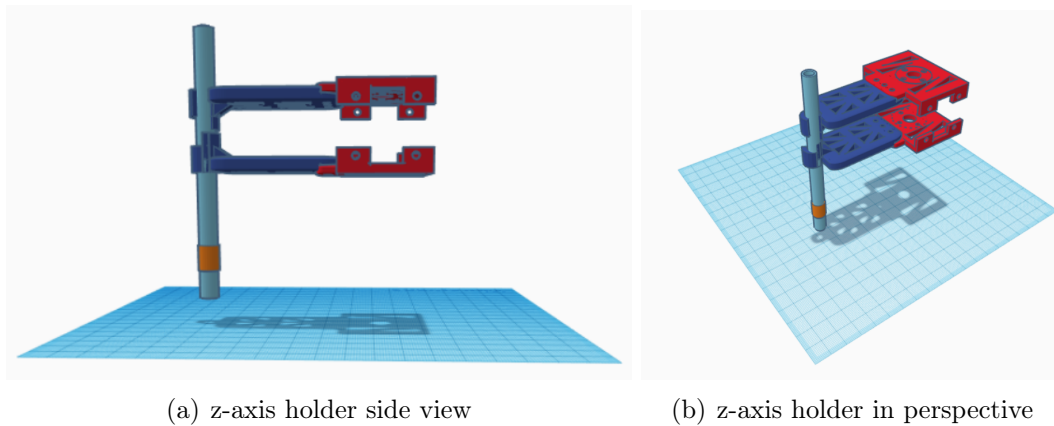
Figure 3.2: Rendering of the holder assembly designed to allow the attachment of the APP tube to the z-axis gantry.

and controlling robotic manipulators for positioning is a complex task [134]–[136]. Various geometries and designs are available each with associated advantages and drawbacks [136]. Two popular choices for robotic manipulators are gantry robots which rely on manipulation in Cartesian geometry, and the so-called articulated or "anthropomorphic" robot arms which mimic the structure of the human arm.

Gantry robots are commonly used in applications such as additive manufacturing and automated liquid handling [137], [138]. A common configuration, also adopted for the experimental setup described in this section, consists of three axes. A gantry (see Figure 3.1) is allowed to slide in the x-y plane. The position is controlled by means of lead screws attached to stepper motors. Another gantry attached a lead screw situated perpendicular to the x-y plane to allow manipulation of the z position. Custom parts are needed to connect the moving parts of the setup (the grounded metal plate and the APPJ tube) to the gantries. The grounded aluminum tube is fixed to the gantry by means two custom designed substrate supports (see Figure A.6). The APPJ tube is attached to the z-axis gantry by means of two copies of a two-part holder assembly (see Figure A.7 and A.8). A rendering of the z-axis assembly is shown in Figure 3.2. The parts are 3D-printed in poly-lactic acid and fixed via 3M screws to the z-axis gantry. The APPJ tube is secured to the holder assembly via zip-ties. The position for each axis is manipulated by stepper motors (NEMA 17) attached to the corresponding lead-screw. The stepper motors are controlled by the complementary Arduino UNO (see Figure 3.1) and two Adafruit Stepper Motor Shields [139]. A photo of the gantry robot setup for manipulating the APPJ position is shown in Figure 3.3(a). As the configuration is set-up in Cartesian coordinates, direct and precise manipulation of the x, y, and z positions is straightforward. Calibration of the number of steps taken by the stepper motors per mm is sufficient to allow for reproducible manipulation of the x,y and z positions. A key drawback of the Cartesian manipulator, however, is the limited working envelope of the device. Since the position of gantries are limited by the lengths of lead screws
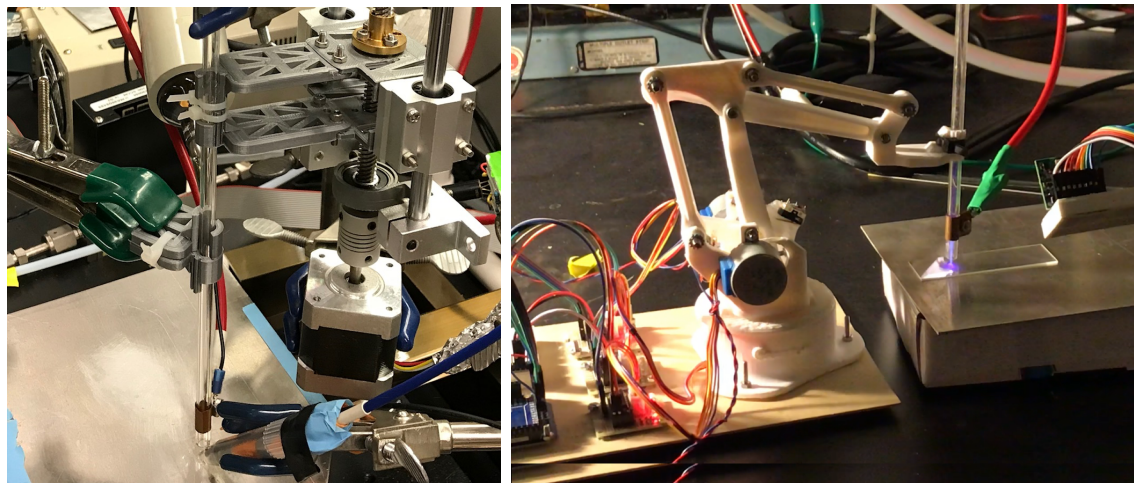
(a) Gantry robot   (b) Robotic arm

Figure 3.3: Example robotic manipulators for the APPJ setup.

and metal rods over which the gantries slide, this configuration results in a comparatively small working envelope and a bulky set-up.

The articulated robotic arm is an alternative configuration which allows for more flexible operation. This type of robotic actuators is attractive as they can be, in some sense, "general purpose", capable of performing a range of tasks. Alongside industrial robotic actuators [140]–[142], various designs of articulated arms ranging from 3- to 8-degrees-of-freedom are made freely available in online communities [143]. A 3D-printed robotic arm configuration, based on one of these designs, holding the APPJ is shown in Figure 3.3(b).

A crucial drawback of the robotic arm configuration is the precise and reproducible manipulation of the position. Derivation of comparatively complex trigonometric relationships is required to relate the movement of the motors to the position of the tip of the arm [136]. A mismatch between the modeled and the realized position can occur due to various sources of error such as mechanical relaxation, small errors in model parameters, or sagging of various parts due to increased torque as the robotic arm extends. As a result, the position of the manipulator may not be reproducible. Although feedback control can aid this issue, their implementation can be a challenging task. Absolute or differential encoders can measure the position of the motors, however, detecting the location of the tip of the arm is a more complicated task. State-of-the-art methods for positioning rely on image processing methods based on artificial neural networks [135]. Due to these complications, a gantry-type robotic actuator is chosen over a robotic arm for experiments. However, the methods developed and demonstrated in the rest of this work can be easily integrated into a robotic arm setup, provided reproducible actuation of position is possible.

3.2.4 Embedded Sensing

Alongside the actuation, the embedded layer is capable of sensing for signals with low memory requirements. The key variables measured in the embedded layer are the total optical emission intensity, root-mean-squared (RMS) voltage and current (see Figure 3.1). The total optical emission intensity is obtained via a photodarlington diode attached to a fiber optic cable pointed towards the APPJ. A signal proportional to the emission intensity is obtained in arbitrary units.

In order to be able to regulate the fast-occurring electrical dynamics of the APPJ, it is necessary to obtain embedded measurements of the voltage and current signals. However, direct-measurement of kHz signals is not possible with the Arduino UNO. Therefore, AC-to-RMS converters (AD536A) (see Figure A.5) are employed to obtain analog measurements of the RMS value of the voltage and current signals. The two signals are multiplied to obtain a measure of the RMS power dissipated in the discharge.

Other sensors based on the digital i2cp communication protocol (e.g., temperature, humidity, time-of-flight distance) can, in principle, be added to the embedded layer. However, it should be noted that the electrical noise created by the discharge poses a significant challenge. Noise in the digital signal can, in effect, block the Arduino UNO, completely halting the operation. Therefore, special care must be taken for sensor positioning and shielding for the incorporation of digital sensors. Similarly, measurements based on optical methods such as IR-based distance sensors can be significantly influenced by the discharge, to the point where their normal function is impaired. As a result, only a limited set of sensors can be readily incorporated to the kHz-excited APPJ setup.

3.3 Peripherals

Specialized instruments are interfaced with the single-board computer in order to obtain more detailed and memory intensive diagnostics. These more detailed measurements involve spatially, temporally and spectrally resolved diagnostics of the APPJ which can be used on their own or to complement and validate the embedded measurements. A diagram of these peripheral instruments are shown in Figure 3.4. Specialized software is required to communicate with these peripheral instruments. As a result, the measurements obtained from these devices are at a significantly slower timescale.

3.3.1 IR Thermal Imaging

Sharp gradients in APPJ dynamics result in spatially distributed temperature profiles on treated substrates. To obtain a measure of the thermal effects of the APPJ, then, a spatially resolved measurement method is necessary. Calibrated thermal images of the substrate are obtained via a radiometric thermal camera (FLIR Lepton 3 [144]) pointed at an angle towards the APPJ (see Figure 3.4). An example of an IR thermal image of the APPJ impinging on the substrate is shown in Figure 3.5.
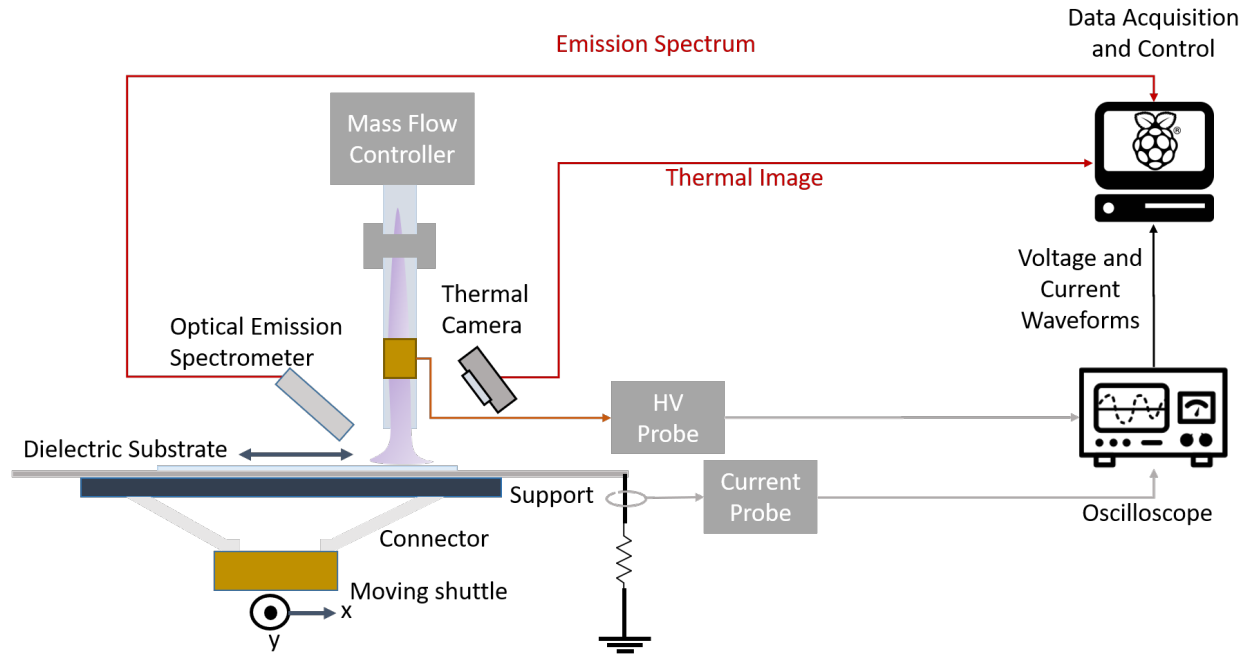
Figure 3.4: Peripheral instruments in the experimental APPJ setup. Measurement signals are shown in red and electrical signals are shown in gray.

Crucial information such as the maximum temperature on the substrate can be easily extracted for thermal images. As the maximum temperature is typically observed to coincide with the jet centerline, with calibration, the thermal images can also provide information regarding the position of the jet. A key advantage of using a non-contact method for measuring substrate temperature is that the sensor can be placed sufficiently far from the discharge to prevent measurements from being affected by electrical noise. Nevertheless, for reliable operation, it is necessary to implement software and hardware level fail-safe mechanisms. Namely, unreasonably high temperature measurements ($\geq$500 K) are discarded, and the thermal camera is forced to re-start if a hang-up is detected (i.e., it is not possible to acquire new measurements).

3.3.2 Oscilloscope

Voltage and current waveforms can provide information about the fast-timescale phenomena of the discharge. Previous work by Walsh et al., [110] and Liu et al., [111] indicate the current signal in APPJs carry important information about the discharge modes. Moreover, the current signal is closely related to the substrate type, since the substrate acts as one of the electrodes for the examined APPJ configuration. An oscilloscope (Rigol DS1054) is used to measure the waveforms of the voltage signal on the powered electrode and the current signal leaving the aluminum ground plate (see Figure 3.4). A typical measurement of a
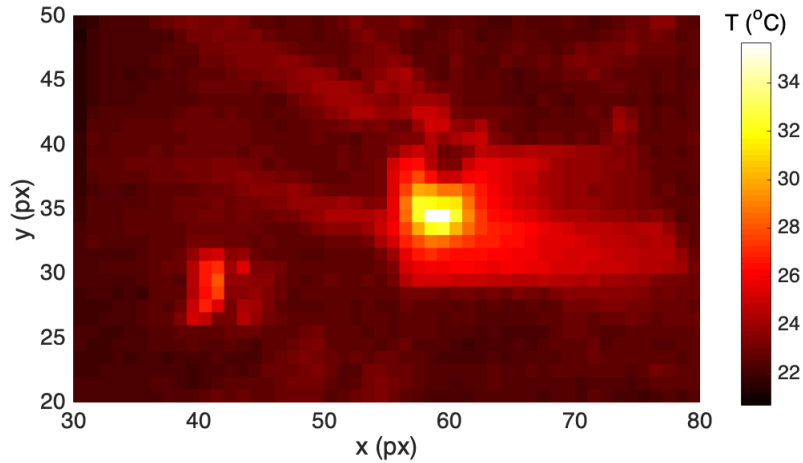
Figure 3.5: Example thermal image of the APPJ at an applied voltage of 6 kV peak-to-peak, 15 kHz, and a flow rate of 1.5 slm.

(a) Example current waveform

(b) Power measurements
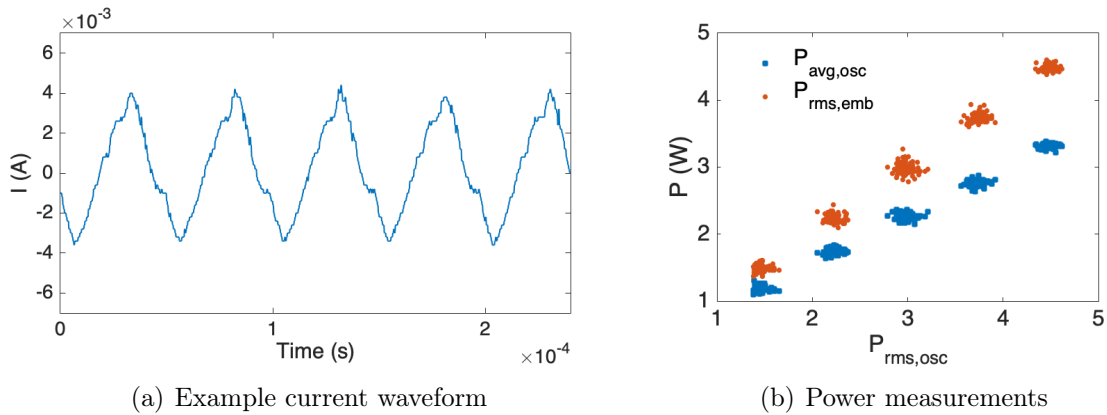
Figure 3.6: Electrical measurements from the APPJ: (a) an example current waveform for applied voltage of 7kV peak-to-peak, frequency of 20 kHz and flow rate of 1.5 slm, and (b) power measurements obtained from the oscilloscope and embedded measurements across the APPJ operating range.

current waveform from the APPJ is shown in Figure 3.6(a). Note that since the current waveform deviates from sinusoidal, the embedded and peripheral measurements of power are not guaranteed to be consistent. Therefore, the measured waveforms are used to obtain a more accurate estimate of the electrical characteristics of the APPJ. For the experimental setup at hand and the investigated operating conditions, the computed RMS discharge power is validated with respect to numerical integration of the product of current and voltage signals obtained from the oscilloscope (see Figure 3.6(b)).
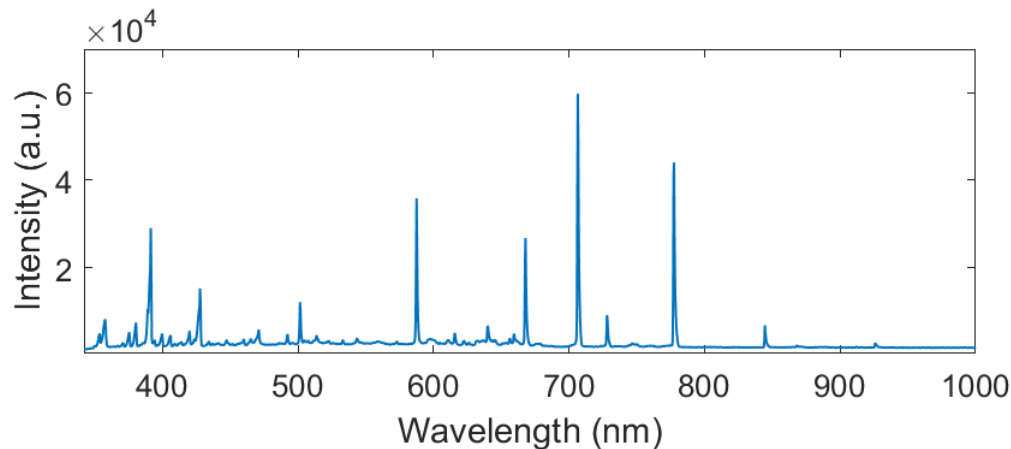
Figure 3.7: Example optical emission spectrum of the APPJ obtained under an applied voltage of 7 kV peak-to-peak, frequency of 20 kHz and a flow rate of 1.5 slm.

(a) OES adaptor side view   (b) OES adaptor in perspective
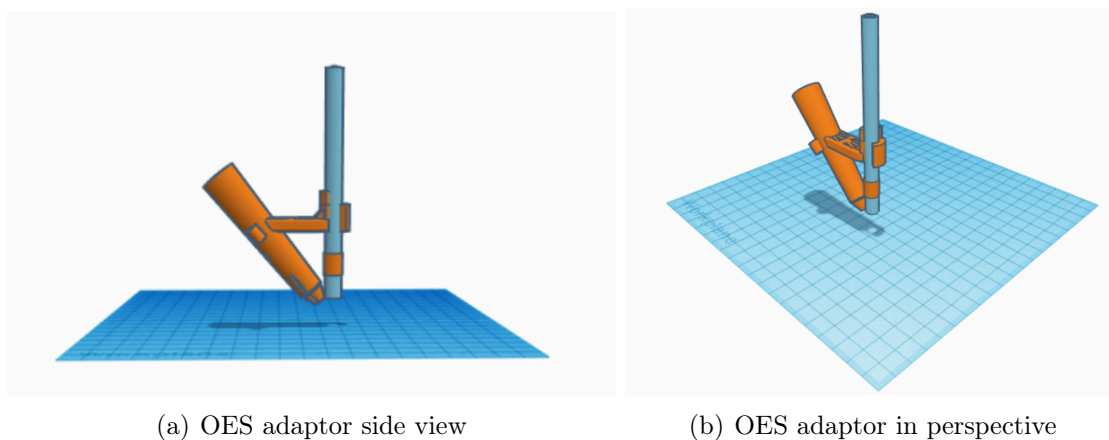
Figure 3.8: Rendering of the designed OES adaptor allowing reliable positioning of the fiber-optic probe.

3.3.3 Optical Emission Spectroscopy (OES)

The optical emission signal can provide important information about the chemical processes occurring the discharge. Relevant thermal characteristics such as rotational and vibrational temperatures of the discharge can be obtained from OES by means of generating and fitting synthetic spectra [145]. Line-ratio methods can help correlate OES measurements to other important discharge variables such as electron temperature [146]. Moreover, OES measurements can be obtained relatively simply and in a non-contact manner, by focusing a fiber-optic towards the discharge area. Therefore, OES is one of the principal sources of information about the discharge characteristics.

Optical emission spectra are obtained via optical emission spectrometer (Ocean Optics USB 2000+). An example spectrum is shown in Figure 3.7. An important consideration here is the positioning of the OES fiber-optic probe. The OES measurement is sensitive to the positioning of the probe, particularly since the discharge area is comparatively small (few mm in diameter). A custom part is designed to ensure the angle of the probe is maintained at a constant angle relative to the substrate (at about 45 degrees). This way, it is possible to ensure the signal is collected from the same position at the substrate-discharge interface. A rendering of this OES adaptor is shown in Figure 3.8 and the dimensions of the part are presented in Figure A.9.

3.4   Software

The development of software is an essential component for enabling automatic experiments and real-time control. There are few major considerations in the development of software; an effective software solution for automation and control should be compatible with all the instrumentation, flexible to allow for modular addition and subtraction of instruments and easy to understand and modify. For this reason, the majority of the software is scripted in Python, which is an open-source coding language with a variety of freely available resources and packages. The software developed for the setup is based on previous work [147] and is presented in Appendix B. The script for automated experimentation and control consists of three parts: (i) the firmware (see B.1) which is compiled in C++ and runs on the micro-controllers, (ii) the coordination software which is coded in Python and runs on the single board computer (see B.2), and (iii) monitoring and supervisory software, also coded in Python, which runs on a standard consumer laptop.

The firmware is responsible for coordinating actuation and displaying the measurements from embedded sensing. The actuation commands are supplied by the user to the serial connection in the format of comma-separated letter-value pairs. The letter specifies the actuated variable to which the value is assigned. For example the command `"v,10"` sets the applied voltage to 10 kV peak-to-peak. The embedded measurements and the current values of the actuated variables are written to the serial USB port at a baud rate of 38400 Bd.

The coordination software is the primary means of running experiments; it collects and records data from the embedded layer and the peripherals. The communication with the embedded layer is achieved with the `pySerial` [148] package, directly communicating with micro-controllers via the serial port, or through the `subprocess` package routing commands through the UNIX terminal. The peripheral instruments are interfaced with Python using preexisting packages; `pylepton` [149] for the thermal camera, `usbtmc` [150] for interfacing with the oscilloscope and `seabreze`[151] for the spectrometer. The measurements are collected using "asynchronous programming". Unlike in conventional synchronous programming, with the asynchronous method, information is collected in parallel from each of the instruments, allowing for a faster sampling rate. The coordination software is also capable of running a web socket server to allow communication over Wi-Fi using TCP/IP protocol.

This allows for monitoring and supervisory software to exercise control over different aspects (set actuate variables, change control setpoints, etc.) of the coordination software.

3.5 Conclusions

This chapter investigated the choice and design of sensing and actuation instrumentation, and their integration via software. The experimental setup design presented in this chapter is by no means definitive. There are various issues related to each aspect of design; for example, the methods for voltage signal generation and the position actuation are chosen primarily based on the relative ease of implementation. Considerable additional effort is required to extend the setup to a commercially viable medical or plasma processing device, re-considering and improving the design and instrumentation choices. Nevertheless, the methods outlined in this chapter presents an open-source, flexible, reliable, and comparatively cheap design for an automated data collection and control test-bed.

The experimental setup described in this chapter is primarily responsible for continuously collecting and recording information. However, the question of how to effectively use the incoming measurements is left open. The next chapters investigate the effective means for utilizing these signals to identify system dynamics and improve the reliability and reproducibility of operation via feedback control.

Chapter 4

Control-Oriented Modeling for Atmospheric Pressure Plasma Jets

Development of dynamic models is crucial for the design and evaluation of effective control strategies. Numerous models of APPJs are developed with the purpose of understanding the physical characteristics of discharges. However, model-based control strategies require so-called "control-oriented" models, which describe the evolution of, preferably measurable, dynamics to be controlled in response to changes in manipulated variables. This chapter aims to bridge this gap with physics-based and data-driven control-oriented modeling strategies

4.1   Introduction

Computational models are useful tools to obtain insight into difficult-to-measure physical phenomena in light of the complexity of the discharge phenomena. Models are also an essential component for the design of both classical and advanced control strategies. Particularly, the optimization-based model predictive control (MPC) strategy directly relies on the real-time solution of a tractable dynamic model of the controlled dynamics [152]. However, requirements of a control-oriented model can significantly differ from models constructed for purposes of investigating discharge physics.

Modeling needs for process control are centered around the end goal of operation; maintaining some discharge property or delivery of a cumulative effect (i.e., a "plasma dose") to a treated substrate. A control-oriented model is then, required to represent the evolution of discharge dynamics as they relate to dose accumulation in the substrate in response to actuated inputs. Moreover, particularly for model predictive control strategies, there is a limitation on model complexity for feasible implementation [152]. The allowable complexity depends on available computational power and the timescale over which the controlled dynamics evolve. The goal of the control-oriented modeling efforts is, therefore, to obtain a simple and adequate description of the relevant dynamics of the APPJs.

The literature on modeling of discharges is extensive. Although control-oriented modeling has significantly different requirements, existing discharge models can be a key source of information for control-oriented models. For example, choice and validation of appropriate assumptions and simplifications in control-oriented modeling can be guided by more complex fluid models. Moreover, some existing modeling practices, such as equivalent circuit modeling, can be readily adopted as a part of a control-oriented modeling strategy.

The rest of this chapter first presents a brief overview of the modeling practices. Then, dose metrics quantifying thermal and non-thermal effects of APPJs on substrates are presented. A simplified fluid model of the APPJ-substrate thermal interactions is developed, which is used to inform a control-oriented lumped-parameter modeling strategy in the following section. Finally, data-driven modeling strategies are presented for obtaining single-input-single-output and multi-variable linear dynamic models based on input-output data. The control-oriented modeling strategies presented in this chapter use simplifications to describe the discharge phenomena. Therefore, the strategies can be readily adapted to accommodate various discharge characteristics such as electrode geometry, excitation frequency, and working gas. The modeling efforts are focused on two main types APPJs; the RF-excited Ar discharge, which is commonly used in plasma medicine and the kHz-excited APPJ setup in helium described in the previous chapter.

4.2   Current Modeling Practices

The most common approach for modeling of APPJs is the development of fluid models which involve solving mass, heat and momentum transport equations coupled with Poisson's equation. Fluid models have the key advantage of capturing the spatial and temporal variation of the discharge phenomena which make them particularly suited for mechanistic studies of physical phenomena. For example, the fluid model of the RF-excited plasma needle in He, reveal the ring-shaped profile of the discharge emission [24], [120]. Several studies use fluid models to investigate temporally resolved phenomena such as the propagation of guided ionization waves (or plasma bullets) in He atmospheric discharges [108], [133], [153], [154]. Such models can reveal significant insight on mechanisms of discharge propagation. Boeuf et. al [108] indicate the importance of the He-air interface in guiding the plasma pullet. Breden et al. examine the importance of photoionization in streamer propagation [154]. Naidis et al. modeled the effect of applied voltage and flow on bullet characteristics [133]. Fluid models have also been developed to investigate the coupling between APPJs and substrate properties, an area of key interest for plasma medicine and plasma processing applications. Studies by Norberg et al. [25] and Breden et al. [155] investigate APPJ dynamics impinging on surfaces with varying electrical properties for timescales of a few tens of nanoseconds. Models developed by Chen et al. [37] and Norberg et al. [156] further investigate the interaction of helium APPJs with biological substrates. Schroder et al. [157] model the thermal effects of an RF-excited He APPJ on the skin. Despite the wealth of information they provide, fluid models of APPJs can be challenging and computationally expensive to solve. Particularly

for MPC applications where the real-time solution of the model is needed, fluid models are often prohibitively complex.

Lower dimensional, 1D and 0D (global) models are also developed in the literature focusing on different aspects of the discharge. These models often focus on uncovering the relationships between the discharge phenomena and the electrical characteristics of the discharge. For example, Mangolini et al. use a 1D model to describe the ionization mechanisms and electrical characteristics of a kHz dielectric barrier discharge (DBD) in He [158]. Golubovskii et al., predict the glow-to-filamentary transition of a kHz-DBD in He using a similar model [99]. Waskoenig et. al, model the reaction chemistry with a focus on atomic O production in RF-APPJ in He [159]. Balcon et al., model the dynamics of an RF-APPJ in Ar using a 1D model, predicting α-γ mode transition. Lazzaroni et al., use a global model to describe the behavior of electron temperature and density in an RF-APPJ in He [160], [161]. Van Gaens et al., [162] investigate the discharge chemistry in an RF-APPJ in Ar using a 0D kinetic model. Schmidt-Bleker et. al., use a similar model to investigate the effect of shielding gas composition to the reaction chemistry of an RF-exited APPJ in Ar [126]. 1D and 0D models can be more conducive to use in conjunction with control strategies. However, these models are still considerably complex. Even 0D models can require comparatively large reaction networks in order to describe the APPJ behavior (see [126], [162]). Moreover, the validation of such models can be challenging as direct measurements of discharge characteristics such as species, electron and ion densities and temperatures may not be readily available.

Circuit models are used to describe the electrical behavior of the plasma circuit, often abstracting the discharge as a variable resistor and/or capacitor. Hofmann et al., use a circuit model of an RF-APPJ in argon to describe its electrical behavior [106]. Kieft et al., describe the electrical properties of an RF-APPJ in He [163]. Fang et al., use equivalent circuit models to differentiate between the operating regimes in a kHz-excited APPJ in He. Naudé et. al, describe the transition between Townsend and filamentary modes using a parametric representation of discharge current [164]. Although circuit models are comparatively easy to construct their use can be limited by their simplicity. Therefore circuit models are often used in a descriptive capacity or, they involve some parametric description of discharge electrical characteristics which relies on a deeper understanding of discharge physics.

4.3 Dose Metrics

A common objective in plasma medicine is delivery of a predefined "plasma dose". However, generally, accurate quantification of therapeutic doses is challenging due to lack of direct measurements for short- and long-term biological effects of a therapy [165]. This challenge is further aggravated in plasma medicine because of the presence of a multitude of different therapeutic effects (e.g., thermal, chemical, and electrical) and their synergistic interactions [19], [80]. Although dose quantification is highly specialized in different therapies, dose metrics share some commonalities: (i) they should describe the cumulative, *non-retractable*

(a)   (b)
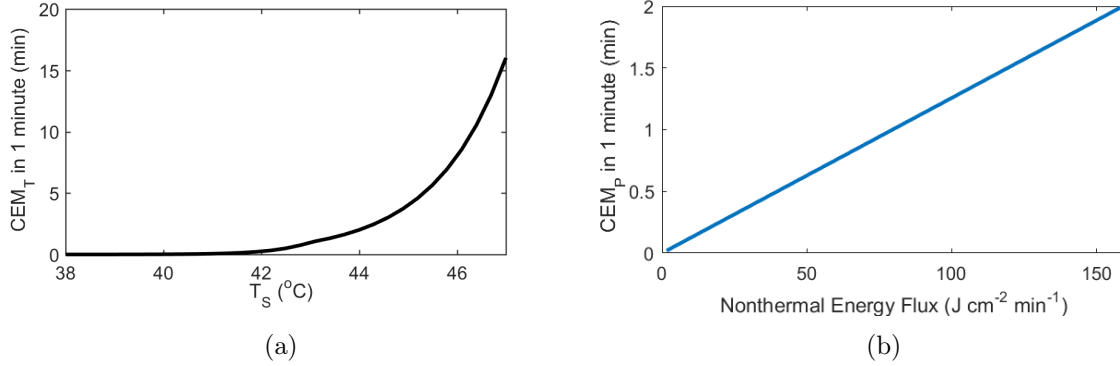
Figure 4.1: (a) Thermal energy accumulation CEM_T during one minute treatment as a function of the substrate temperature T_s; (b) Nonthermal energy accumulation CEM_P during one minute treatment as a function of power deposited onto substrate per area. The dose metrics are nondecreasing and have a time unit (min).

nature of a therapeutic effect, and (ii) they should be defined in terms of a measurable property of a target substrate, which is related to some characteristics of underlying biological processes (e.g., volumetric energy absorbed as ionizing radiation in radiotherapy [165], or substrate temperature in hyperthermia [27]). Additionally, concepts such as *isodose* in radiotherapy [165] or *equivalent dose* in hyperthermia [166] are commonly adopted in order to quantify how therapeutic effects vary under different treatment protocols relative to a reference treatment condition or protocol.

The thermal effects of the APPJ on the substrate is comparatively easy to quantify and important and regulate to ensure safety and comfort of operation. Although APPJs are considered to be "low temperature" the gas temperatures in APPJs can be considerably higher than room temperature ($\geq 100\ ^oC$) depending on the operating conditions [88], [89]. As a result, the APPJ can damage heat-sensitive materials [167] particularly in presence of operational variability. In medical context the well-established metric of cumulative equivalent minutes at 43°C (CEM_T) [18], [27], [168] is used for determining thermal dose for hyperthermia therapies. CEM_T is defined as [27],

$$\text{CEM}_\text{T} = \int_0^t K^{(43-T_s(\tau))}\, \mathrm{d}\tau \tag{4.1}$$

or, equivalently,

$$\frac{d\text{CEM}_\text{T}}{dt} = K^{(43-T_s(t))}, \qquad \text{CEM}_\text{T}(0) = 0, \tag{4.2}$$

where the constant K describes the thermal-stress response of the treated substrate. A

typical value of K is derived derived based on the response of CHO cells to thermal stress,

$$K = \begin{cases} 0 & T_s \leq 39°C \\ 0.25 & 39°C < T_s < 43°C \\ 0.5 & T_s \geq 43°C. \end{cases} \tag{4.3}$$

CEM_T, describes the thermal effects normalized with respect to treatment at 43°C, where each 1^oC increase in temperature doubles the thermal dose. The dose definition 4.1 can be readily extended to describe the spatial distribution of dose, provided a spatial distribution of the substrate temperature $T_s(x, y)$ is available.

To mirror the CEM_T metric, accounting for some non-thermal effect imparted by the plasma to the substrate, the metric CEM_P is defined as the total non-thermal energy absorbed by the substrate. In principle, this metric describes the cumulative energy absorbed by the substrate in the form of UV radiation and as energy stored in various chemical reaction products. CEM_P is calculated as

$$CEM_P = \int_0^t \gamma(1 - \eta)P(\tau)d\tau \tag{4.4}$$

or, equivalently,

$$\frac{dCEM_P}{dt} = \gamma(1 - \eta)P(t), \quad CEM_P(0) = 0, \tag{4.5}$$

where γ is an absorption factor of the substrate. Note that CEM_P takes the units of Joules and, assuming a constant cross-sectional area for the jet, can be used interchangeably with fluence.

4.4 Thermal Model of APPJ in COMSOL

The APPJ interaction with substrates are heavily influenced by the transport phenomena which occur as the flowing gas impinges on the treated substrate [119], [169]–[172]. In order to inform control-oriented modeling strategies a fluid model is constructed, simplifying the APPJ behavior as a hot noble gas jet impinging on a substrate. In this model, the discharge phenomena are neglected and the effect of the plasma on the working gas is reduced to that of a heat source. Although this is an oversimplification, the so-called hot-jet assumption is a useful tool to investigate the transport phenomena which occur in APPJs.

The 2D axisymmetric fluid model describes the behavior of a hot jet of helium flowing through a quartz tube, impinging on a borosilicate cover slip placed on an aluminum plate. The model geometry is shown in Figure 4.2 and the material properties are summarized in Appendix C.1. The heating of the gas due to the plasma is simulated as a uniform heat source adjacent to the electrode. The discharge is observed to not extend radially to fill the tube. Thus the power deposition region is specified to have a smaller radius than that of the tube ($\sim 0.6r$). The deposited power and He flow rate are two inputs to the model. The
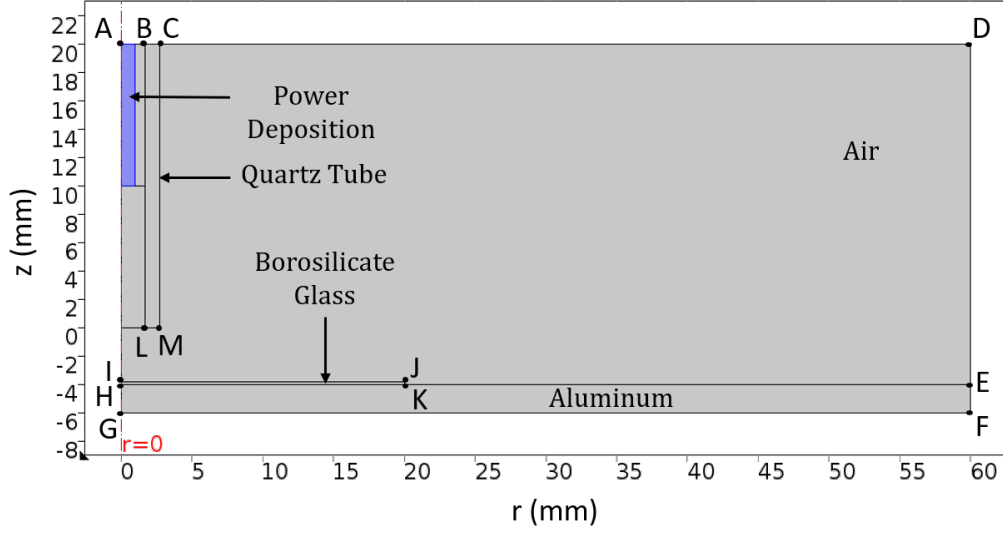
Figure 4.2: The geometry used for the COMSOL model with the different regions labeled.

temperature of the tube and the temperature distribution on the substrate are the outputs of interest.

The model involves the solution of coupled heat, mass and momentum transport equations (4.6)-(4.8), and the continuity equation (4.9) for the gas phase. These equations are coupled with heat transfer in solid bodies of the tube, the substrate (coverslip) and the aluminum plate. For the gas phase, neglecting the viscous heating and pressure work, the heat equation for gas temperature T is expressed as,

$$\rho c_p \frac{\partial T}{\partial t} + \rho c_p \mathbf{u} \cdot \nabla T = \nabla \cdot (k \nabla T) + Q. \tag{4.6}$$

Here, ρ, c_p and k are material density, specific heat capacity, and thermal conductivity, respectively. $\mathbf{u}$ is the velocity vector and Q represents the uniform volumetric heat source. In this case, the flowing gas is heated by the plasma with a contributing fraction of η of the deposited power, giving $Q = \eta P$. The power deposition efficiency η is a fitting parameter, found to be about $\eta = 0.47$ for the APPJ at hand. This is consistent with the results reported by Sobota et al. who determined the power transfer efficiency to a similar He APPJ to be in the order of 0.50 [105]. Two species; helium and air, are considered in the gas phase. Assuming the diffusive flux is the main contribution to the concentration changes in the jet, the mass transport equation for concentration of species i is expressed as,

$$\frac{\partial c_i}{\partial t} + \nabla \cdot (-D_i \nabla c_i) + \mathbf{u} \cdot \nabla c_i) = 0. \tag{4.7}$$

Here, D_i is the mass diffusivity of species i. Under the investigated conditions the Reynolds Number of He is computed to be about 80 indicating the flow is in the laminar regime.

Assuming the fluid is Newtonian, the momentum equation is formulated as follows,

$$\rho\frac{\partial u}{\partial t} + \rho(\mathbf{u}\cdot\nabla)\mathbf{u} = \nabla\cdot\left[-p\mathbf{I} + \mu(\nabla\mathbf{u} + (\nabla\mathbf{u})^{\mathrm{T}}) - \frac{2}{3}\mu(\nabla\cdot\mathbf{u})\mathbf{I}\right]. \tag{4.8}$$

Here, u is the flow speed, p is pressure, μ is material viscosity and $\mathbf{I}$ is the identity matrix. The system of equations are completed with the the continuity equation,

$$\frac{\partial\rho}{\partial t} + \nabla\cdot(\rho\mathbf{u}) = 0. \tag{4.9}$$

The physical properties (ρ, c_p and k) of the jet plume is computed at every point as the sum of the properties of the two components, weighted by their mass fractions as follows:

$$\rho = (w_{He}\rho_{He} + (1 - w_{He})\rho_{Air})\frac{298}{T}, \tag{4.10}$$

$$c_p = w_{He}c_{p,He} + (1 - w_{He})c_{p,Air}, \tag{4.11}$$

$$k = w_{He}k_{He} + (1 - w_{He})k_{Air}. \tag{4.12}$$

A reduced form of the heat equation (4.6) is solved for the solid bodies, with no flow term $\mathbf{u} = \mathbf{0}$, and no volumetric heat sources. The gas-phase simulation volume is initialized as pure air at 18 $^o C$. Constant temperature boundary condition is applied to the top boundary, while the sides of simulation volume and bottom of the aluminum ground plate are assumed to be thermally insulated. The tube inlet is assumed to have an influx of pure helium at a constant mass flow rate. Top and the side boundaries are assumed be constant pressure outlets. The boundary conditions imposed on the system are summarized in Table 4.4. The aluminum plate and the glass coverslip are not in perfect thermal contact. Therefore, the addition of a thin thermally resistive layer on the boundary HK in Figure 4.2 was necessary to reconcile the model with experimental observations. The thermal resistance R_S is a fitting parameter found to be 3.3×10^{-3} Km^{2}W^{-1}.

4.4.1 Results

The COMSOL model is used to obtain steady-state flow, temperature and concentration profiles at nominal input conditions corresponding to a power deposition 3.2 W and an inlet flow rate of 2 slm ($\sim$5 m/s).

The velocity profile and the flow field computed in COMSOL are shown in Figure 4.3. Notably, the flow increases within the tube along the power deposition region. The laminar flow channel extends from the tube nozzle and stagnates as it impinges on the surface. As indicated by the white arrows in 4.3 there is a region of recirculation adjacent to the jet. The size and the distance of this region to the axis of symmetry (jet centerline) is influenced

Boundary	T	c_{He}	u
AB	18 ^oC	41 mol/m^3	$-U_0\mathbf{n}$
BC	18 ^oC	$-$	$-$
CD	18 ^oC	0 mol/m^3	$p=\mathrm{p_{amb}}$
DE	$\textbf{-n}\cdot(-k\nabla T)=0$	0 mol/m^3	$p=\mathrm{p_{amb}}$
EF	$\textbf{-n}\cdot(-k\nabla T)=0$	$-$	$-$
FG	$\textbf{-n}\cdot(-k\nabla T)=0$	$-$	$-$
IJKE	$-$	$\textbf{-n}\cdot(-D_i\nabla c_i+\mathbf{u}c_i)$	0 m/s
BLMC	$-$	$\textbf{-n}\cdot(-D_i\nabla c_i+\mathbf{u}c_i)$	0 m/s

Table 4.1: Boundary conditions for the COMSOL model. The symbols (A-M) correspond to
the vertices labeled in Figure 4.2. $\mathbf{n}$ is the normal vector to the boundary, U_0 is the inlet flow
velocity calculated based on the inlet He mass flow rate and $\mathrm{p_{amb}}$ is the ambient pressure,
equal to 1 atm.
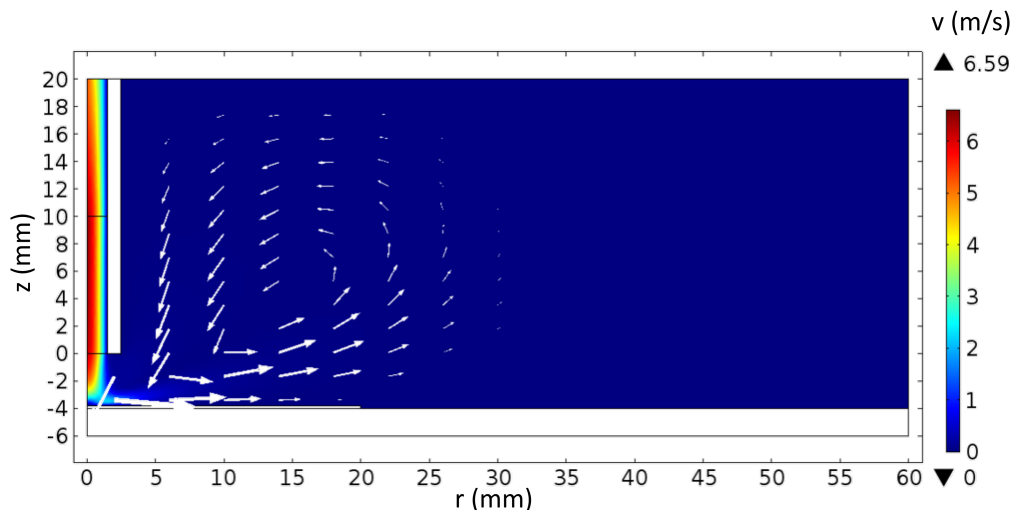
Figure 4.3: Steady-state velocity profile (color surface) and velocity field (white arrows)
obtained from the COMSOL model corresponding to operating power of 3.2 W and inlet He
flow rate of 2 slm.

by the inlet gas flow rate and the deposited power. This observation is consistent with those
reported in the literature for APPJ models [173] and experimental investigation of impinging
gas jets [169].

   The recirculation behavior also significantly influences the heat transport phenomena.
Figure 4.4(a) shows the steady-state temperature profile and total heat flux at the nominal
operating conditions. The glass coverslip is heated by the impinging and recirculating hot
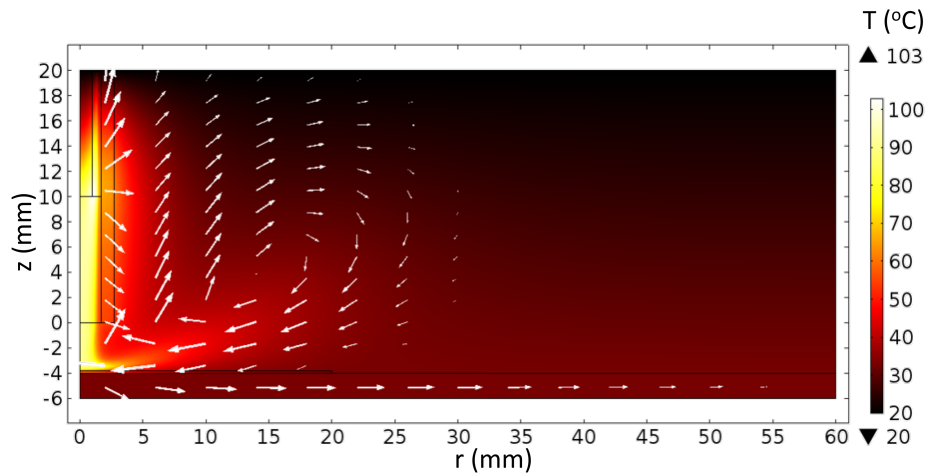
(a) Temperature profile
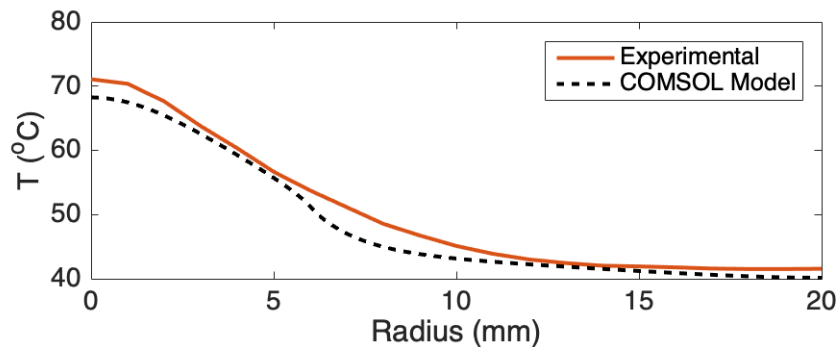
(b) Substrate temperature validation

Figure 4.4: (a) Steady-state temperature profile (color surface) and heat flux (white arrows) obtained from the COMSOL model, and (b) the radial temperature distribution on the substrate compared against experimental measurements, corresponding to operating power of 3.2 W and inlet He flow rate of 2 slm.

gas and is cooled by the aluminum plate which conducts away the heat in the radial direction. The predicted radial distribution of the substrate temperature is validated against spatially resolved substrate temperature measurements. As shown in Figure 4.4(b), the COMSOL model is able to describe the radial distribution of temperature reasonably well. Another significant observation here is that the gas temperature is predicted to be significantly higher than the ambient temperature, reaching up to 100 ^{o}C. Although gas temperatures close the ambient are reported under some operating conditions [174], [175], the gas temperature in APPJ can be relatively high. Indeed, the computed temperature is consistent with some experimental measurements [88], [89] and modeling studies [157] of He APPJs. Figure 4.5(a) shows the modeled profile of He concentration in the APPJ and the total flux of He. The

(a) Concentration profile   (b) Air fraction
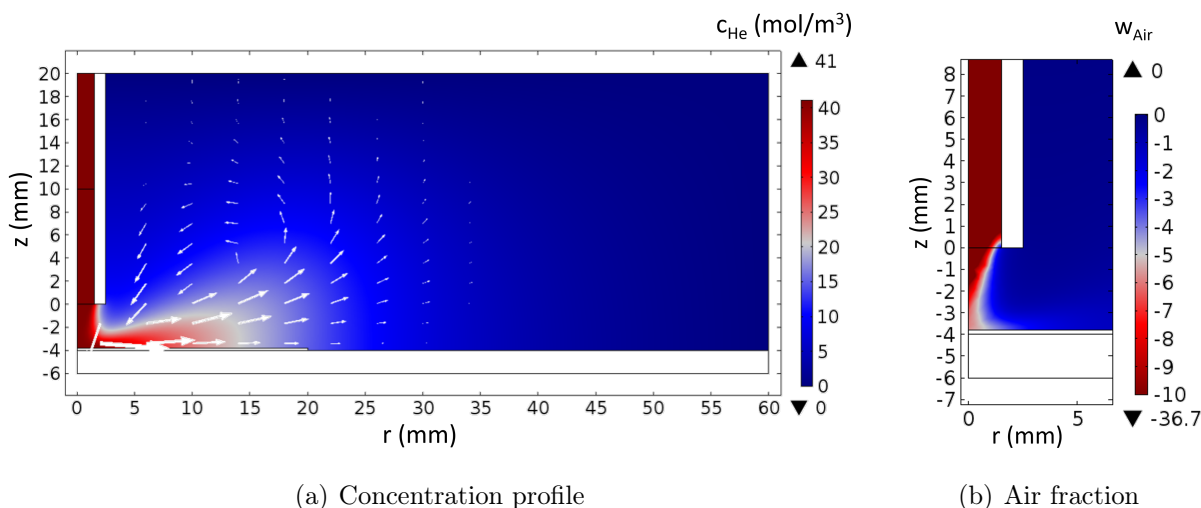
Figure 4.5: Steady-state (a) concentration profile (color surface), total He flux (white arrows),
and (b) air fraction in logarithmic scale obtained from the COMSOL model corresponding
to operating power of 3.2 W and inlet He flow rate of 2 slm.

gas composition appears to remain dominated by He within the tube, and air in-mixing is
observed only after the gas exits the tube nozzle. The impingement and spreading out of
the gas on the surface has a shielding effect, which allows a relatively high concentration of
helium to extend up to 1 cm away from the jet centerline. The centerline of the flow channel
appears to remain close-to-pure helium throughout as the convective flow dominates over
radial diffusion of air. The log-scale plot of air mass fraction shown in 4.5(b), shows that
small amounts of air diffuse up the tube nozzle and into to the centerline of the jet. These
findings are consistent with results reported in the literature [121], [171].

Next, the performance of the COMSOL model is evaluated in predicting the dynamic
behavior of the thermal dynamics of the substrate and the APPJ tube. As direct measure-
ments of the gas temperature are not available, the tube temperature is used as a proxy for
evaluating the thermal dynamics of the flowing gas. Figure 4.6(a) shows the predictions of
the COMSOL model and the experimental measurements of the tube and maximum sub-
strate temperature dynamics, for the range of operating conditions given in Figure 4.6(b).
As shown in Figure 4.6(a), the COMSOL model performs adequately in describing the dy-
namics of maximum substrate temperature and is capable of qualitatively describing the
dynamics of the tube temperature. However, the COMSOL model under-predicts the tube
temperature for high flow conditions (t > 375 s). This behavior is attributed to the chosen
simplified power deposition profile as well to un-modeled phenomena such as changes plasma
radius with changing flow rate.

The COMSOL model described in this section presents a fairly simple but surprisingly
accurate description of the transport phenomena in the APPJ. The spatiotemporal charac-
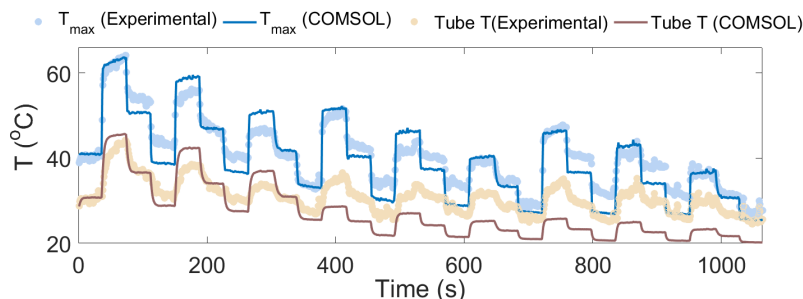
(a) Dynamics of tube and substrate temperatures
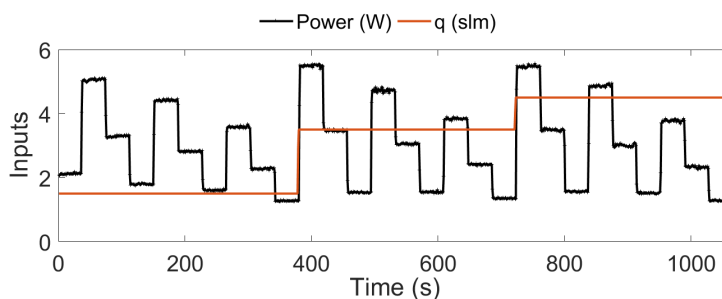
(b) Deposited power and input mass flow rate of He

Figure 4.6: (a) Measured dynamic behavior of maximum substrate temperature and tube temperature compared against dynamics computed from the COMSOL model and (b) corresponding input power and flow sequence.

teristics of the substrate temperature, in contact with the APPJ, is well-captured by the model for the investigated operating conditions. The fluid model provides useful information for construction of physics-based control-oriented models; simplifying assumptions can be validated and lumped-parameters such as averaged heat and mass transfer coefficients can be estimated based on the COMSOL model.

4.5   Physics-Based Control-Oriented Modeling

A physics-based control-oriented model of the kHz-APPJ in He depicted in Figure 4.7 is developed for use in conjunction with MPC strategies. In addition to transport phenomena, a lumped-parameter model is developed to describe the electrical behavior of the APPJ, relating the voltage amplitude and frequency to the power deposition in the jet. This allows for the lumped-parameter model to be readily extended to include the cumulative effects of the APPJ on the substrate, i.e., dose delivery, as described by the metrics is presented in Section 4.3. The principle of timescale separation is used to develop the control-oriented lumped-parameter model of the APPJ. Figure 4.8 depicts the modeling framework, which
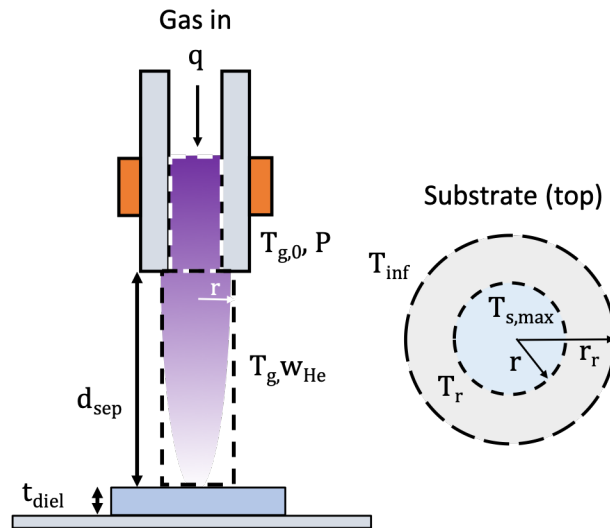
Figure 4.7: Diagram of the APPJ with the regions corresponding to the power deposition and gas heating, heat and mass transfer in separation distance, and substrate heating labeled in dashed lines.

consists of three coupled modules — power deposition and gas heating within the dielectric tube, heat and mass transfer in the separation distance between the tip of the tube and the substrate, and substrate heating and dose accumulation.

The electrical power deposition in the plasma and the associated heating of the flowing gas are assumed to occur adjacent to the electrode in the dielectric tube, as in the COMSOL model. The dynamics of power deposition and gas heating within the tube are neglected and, therefore, this module of the model is assumed to be at steady state. The spatial variations within the dielectric tube are also neglected in order to obtain a 0-dimensional equivalent circuit model for the plasma. Under these assumptions, the plasma electrical properties can be described by a parametric expression intended to capture aspects of the nonlinear behavior of the plasma electrical properties. Note that gas heating in the dielectric tube is coupled with the plasma electrical properties. This is due to the dependence of the plasma resistance on the gas number density (see Section 4.5.1). Modeling the APPJ as a 0D system inevitably introduces a number of approximations. The goal of this model is to provide a computationally efficient and sufficiently accurate description of the thermal dynamics of the APPJ for process control applications.

The radial mixing of air and heat in the free jet region between the tip of the tube and the substrate are approximated by lumped mass and heat transfer coefficients, respectively. The latter coefficients are obtained from the 2D axisymmetric COMSOL fluid model of mass and heat transfer in the distance between the tip of the tube and the substrate. The length of the plume is assumed to be equivalent to the separation distance between the tube nozzle and the substrate. Note that this distance can change during hand-held operation of the
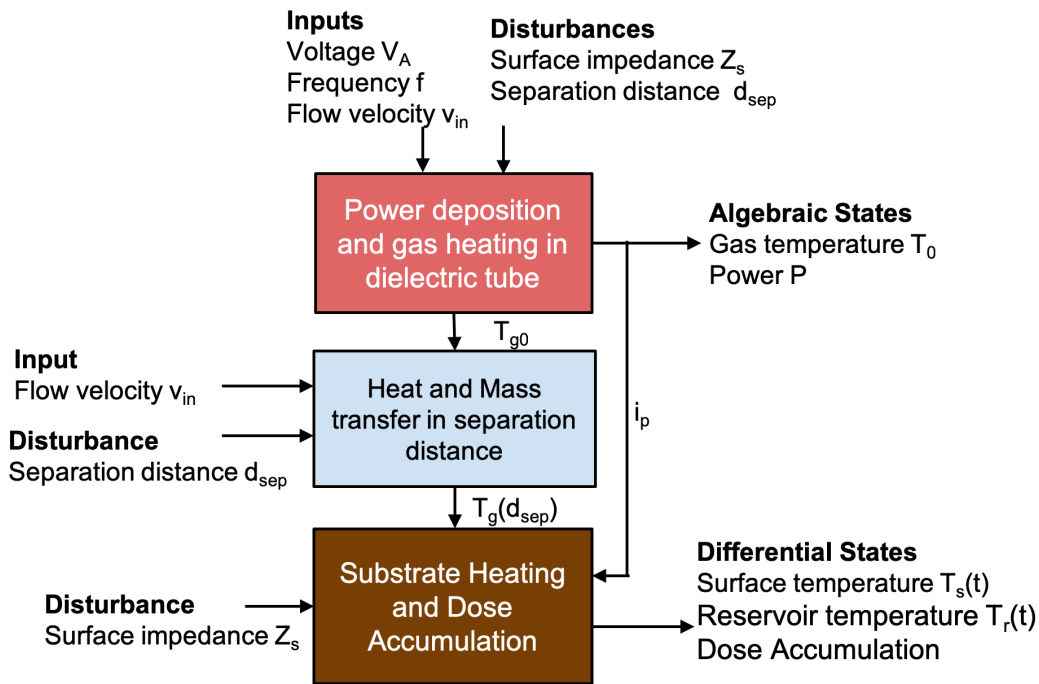
Figure 4.8: Framework of the physics-based model of the RF-APPJ coupled with a substrate. Input variables include applied voltage V_A, frequency f and gas flow velocity v_{in} with disturbances associated with substrate impedance Z_s and jet-tip-to-substrate distance d_{sep}. The model consists of three coupled modules: power deposition and gas heating in the dielectric tube (top); heat and mass transfer in the jet separation distance (middle); and substrate heating and dose accumulation (bottom).

APPJ.

The lumped-parameter model includes the thermal and electrical effects of the plasma on the target substrate. The heat transfer coefficient between the incident jet and the substrate is obtained from the 2D axisymmetric COMSOL fluid model, assuming that the substrate properties are spatially averaged. The dynamics of substrate effect are considerably slower than that of the plasma dynamics within the dielectric tube and the heat and mass transfer in the separation distance. In the following, the physics-based model equations are presented for the kHz-APPJ in He. The same modeling strategy is applied to an RF-APPJ in Ar, under slightly different assumptions. The equations corresponding to this configuration are presented in Appendix C.2. The parameters and material properties for the lumped-parameter model for kHz-APPJ in He described in the following section can be found in Appendices C.3 and C.1, respectively.
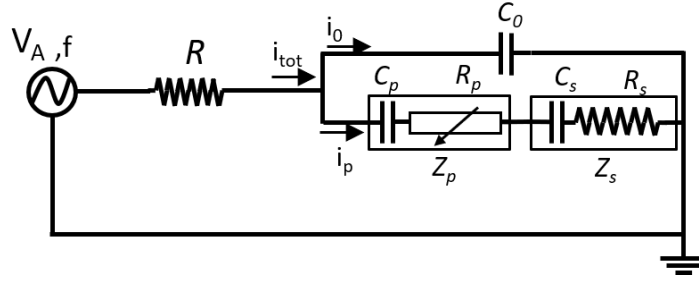
Figure 4.9: Equivalent circuit for the APPJ. The circuit elements corresponding to the discharge (R_p and C_p) and to the substrate (R_p and C_p) are indicated with boxes.

4.5.1 Power Deposition and Gas Heating

Figure 4.9 shows an equivalent circuit for the APPJ, where R is the external circuit resistance, C_0 is the parasitic capacitance, Z_p is the plasma complex impedance consisting of the bulk plasma resistance R_p and plasma capacitance C_p, and Z_s is the surface impedance with the resistive and capacitive components C_s and R_s, respectively. At steady state, the equivalent circuit can be modeled by Kirchhoff's second law,

$$V_A - |Z_{ip}|i_p = 0, \tag{4.13}$$

where the overall impedance Z_{ip} relates the plasma current i_p to the applied voltage V_A. The expression for Z_{ip} is derived from the circuit structure as

$$Z_{ip} = Z_p + Z_s + Z_c + Z_c\frac{(Z_p + Z_s)}{Z_0}, \tag{4.14}$$

where Z_c is the impedance associated with the external circuit, and Z_0 is the impedance associated with the parasitic capacitance C_0.

A key issue in describing the electrical characteristics of the APPJ with the equivalent circuit model is capturing the variable plasma resistance R_p. The discharge resistance is a spatially and temporally varying quantity, therefore the choice of a valid parametrization of the plasma resistance is not trivial. Depending on the discharge type R_p can depend on gas temperature, plasma current, separation distance, and other factors. Based on knowledge of physics and experimental observation, the plasma resistance R_p is expressed in a parametric form.

The plasma resistance can be related to other discharge quantities through the relation [39]

$$R_p = \frac{V_p}{i_p} = \frac{d_{sep}}{S_e}\frac{m_e}{e^2}\frac{\bar{\nu}_{eH}}{n_e}, \tag{4.15}$$

where V_p is the plasma potential, i_p is the plasma current, S_e is the surface area of electrodes, m_e and e are the electron mass and charge, respectively, n_e is the electron density, and $\bar{\nu}_{eH}$

is the electron-heavy particle collision frequency. Due to direct treatment of the substrate, the inter-electrode distance in the APPJ is equivalent to the separation distance between the tip of the dielectric tube and the substrate. Thus, the plasma resistance depends on the separation distance d_{sep}. The plasma resistance is also dependent on the gas temperature through the electron-heavy particle collision frequency

$$\bar{\nu}_{eH} = k(T_e, n_e)n_0, \tag{4.16}$$

where k is the collision rate constant, that is a function of the electron temperature T_e and electron density n_e, and n_0 is the neutral density. The dependence of the plasma resistance R_p on the gas temperature arises from the neutral density n_0, which is assumed to obey the ideal gas law

$$n_0 = \frac{P_{atm}}{k_b T_{g,0}}, \tag{4.17}$$

where k_b is the Boltzmann constant and P_{atm} is atmospheric pressure. Notice that (4.16)-(4.17) indicate that the plasma resistance R_p is inversely related to the gas temperature exiting the tube nozzle $T_{g,0}$.

For the kHz excited APPJ, the following parametrization was found to effectively describe the plasma resistance:

$$R_p = R_{p,0} \frac{340 \ K}{T_{g,0}} \frac{d_{sep}}{4 \ mm}. \tag{4.18}$$

Here, $R_{p,0}$ is the constant resistance fitted from experimental measurements. The constant values 340 K and 4 mm represent nominal values of gas temperature and separation distance, used as normalization factors. $T_{g,0}$ is computed by solving an energy balance for the gas within the tube. From COMSOL simulations, the axial variations of temperature is observed to primarily occur within the tube (see Figure 4.4(a)). Since the temperature dynamics of the gas within the tube is faster than the thermal dynamics of the substrate, $T_{g,0}$ is calculated at steady-state. The axially varying temperature within the tube is, then, expressed as,

$$\frac{dT}{dz} = \frac{1}{\rho c_p v} \left[\eta P(z) - \frac{U_I}{r}(T - T_{inf}) \right], \quad T(z = 0) = 298K. \tag{4.19}$$

Here, U_I represents a lumped heat transfer coefficient and r is the tube internal radius. As in the COMSOL model, the power is assumed to be deposited uniformly adjacent to the electrode, The spatial power deposition is described by the piecewise function,

$$P(z) = \begin{cases} \frac{1}{2}|i_p|^2 |Z_p|cos(\phi) & 0 \text{ mm} < z \leq 10 \text{ mm} \\ 0 & \text{otherwise} \end{cases} \tag{4.20}$$

where ϕ is the angle between the sinusoidal plasma current and voltage across the discharge. Note, since air fraction is negligible within the tube (see Figure 4.5(b)), (4.19) can be solved analytically. In this region, ρ and c_p refer to the density and heat capacity of pure helium. Equation (4.19) is coupled with the circuit solution (4.13) setting gas temperature
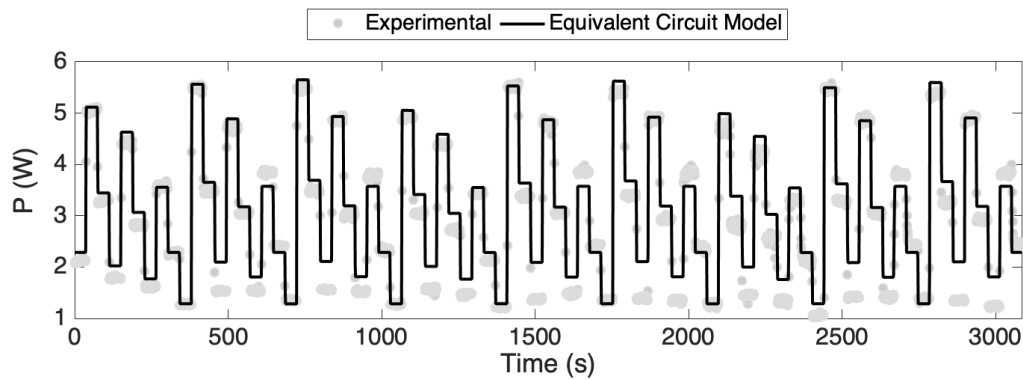
(a) Outputs
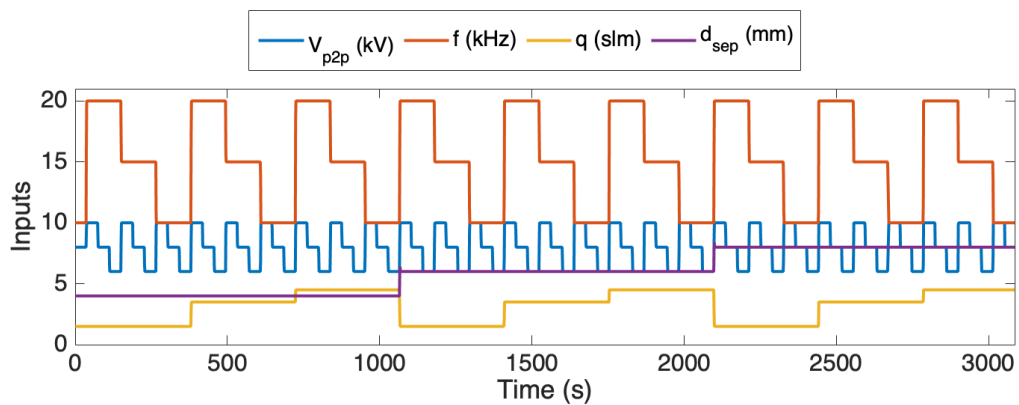
(b) Inputs

Figure 4.10: (a) Predictions of the plasma power compared against measurements over (b) a range of operating conditions.

at the nozzle $T_{g,0} = T(z = 2cm)$. The predictions of this model are compared against experimental data. Figure 4.10 shows that the measured APPJ power is reasonably captured over a range of operating conditions.

4.5.2 Heat and Mass Transfer in the Separation Distance

As the gas plume extends to the substrate, it exchanges heat and mass transfer with the surrounding air due to radial heat losses and in-mixing of air. Based on the COMSOL simulations, the temperature of the jet exposed to air does not vary significantly in the axial direction within the distance between the tube nozzle and the substrate (see Figure 4.4(b)). Thus, the temperature dynamics as well as the in-mixing of air into the stream is described
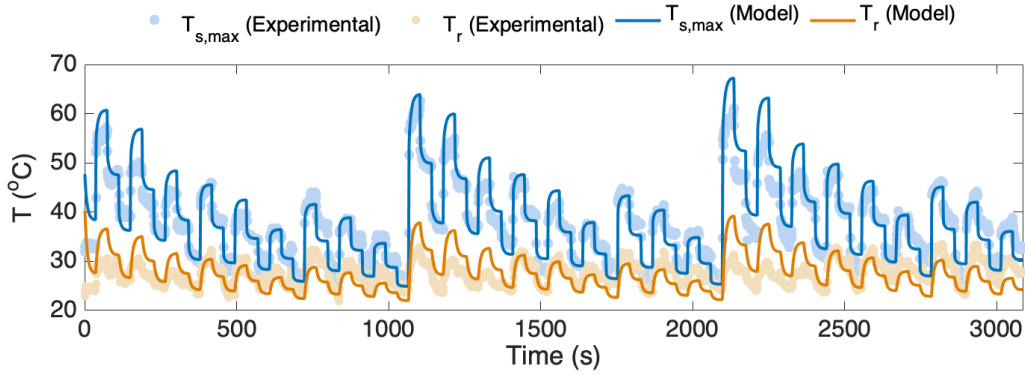
Figure 4.11: Substrate temperature measured and calculated from the lumped-parameter physics based model over operating conditions shown in Figure 4.10(b).

by spatially averaged differential equations,

$$\frac{dT_g}{dt} = \frac{\rho v A c(T_{g0} - T_g) - U_{II} 2\pi r d_{sep}(T_g - T_{inf})}{\rho C_p A_c d_{sep}}, \quad T_g(0) = 298\,\text{K}. \quad (4.21)$$

$$\frac{dw_{He}}{dt} = \frac{\rho v A c(1 - w_{He}) - K 2\pi r d_{sep} \rho(w_{He} - w_{inf})}{\rho A_c d_{sep}}, \quad w_{He}(0) = 0. \quad (4.22)$$

Here, U_{II} and K are lumped heat and mass transfer coefficients respectively. d_{sep} is the jet-tip-to-substrate separation distance, A_c is the jet cross-sectional area and v is the flow velocity. Density ρ and heat capacity c_p of the gas in this region are calculated as in (4.10) and (4.11). Continuity equation (4.9) reduces to

$$\frac{d(\rho v)}{dz} = 0, \quad v(z = 0) = v_{in}, \quad \rho(z = 0) = \rho_{in}, \quad (4.23)$$

4.5.3   Substrate Temperature

The substrate temperature during plasma treatment is characterized by a sharp spatial gradient with peak temperature at the axis of symmetry (see Figure 4.4(b)). The key output of the lumped-parameter model is the peak substrate temperature. In order to capture the radial distribution of the temperature to some extent, the substrate is modeled as two concentric circles with uniform temperature. The center corresponds to the maximum temperature, and the surrounding area acts as a reservoir. $T_{s,max}$ is described by,

$$\frac{dT_{s,max}}{dt} = \frac{A_c U_{III}(T_g - T_{s,max}) - 2\pi r t_s \frac{2k_s}{r+r_r}(T_{s,max} - T_r)}{\rho_s C_{p,s} A_c t_s}, \quad T_{s,max}(0) = 298\,\text{K}, \quad (4.24)$$

where U_{III} represents a lumped heat transfer coefficient between the jet and the substrate, ρ_s, $c_{p,s}$, k_s and t_s are the density, specific heat capacity and thermal conductivity and the thickness of the substrate, respectively. The time-evolution of the reservoir temperature is given by.

$$\frac{dT_r}{dt} = \frac{2\pi t_s k_s}{U_{IV}\rho_s C_{p,s}\pi(r_r - r)^2 t_s}\left(\frac{2r}{r + r_r}(T_{s,max} - T_r) - \frac{2r_r}{r_r}(T_r - T_{inf})\right), \quad T_r(0) = 298\,\text{K}. \quad (4.25)$$

Here, the lumped parameter U_{IV} is the scaling factor for the thermal inertia of the reservoir, and r_r is the reservoir radius. The model equations constitute a system of differential algebraic equations (DAE). Equations (4.13) and (4.19) make-up the algebraic equations while equations (4.21)-(4.25) represent the differential component of the lumped-parameter model. The model equations can be expressed in terms in state space form,

$$\begin{aligned} \tfrac{dx}{dt} &= f(x, z, u, \theta), & x_0 &= x(0) \\ 0 &= g(x, z, u, \theta), \end{aligned}$$

with algebraic states $z = [P, T_{g,0}]^\top$, differential states $x = [Tg, w_{He}, T_{s,max}, T_r]^\top$, inputs $u = [V_{p2p}, f, q]^\top$ and model parameters $\theta = [R_{p,0}, U_I, U_{II}, U_{III}, U_{IV}, K]$. Note the peak-to-peak voltage V_{p2p} relates trivially to voltage amplitude $V_{p2p} = 2V_A$ and mass flow rate q relates to the inlet flow velocity with $q = \rho_{in}A_c v_{in}$. Figure 4.11 shows that the substrate dynamics of the substrate at the center line $T_{s,max}$ as well as the substrate temperature further out at $r \sim 5$ mm (T_r) are well-described by lumped-parameter model.

4.6 Data-Driven Modeling

As the name implies, data-driven modeling strategies only rely on input-output data collected from the experimental setup. While there is an obvious drawback to discarding knowledge of the system physics, data-driven models can allow for simplified representations of complicated dynamic systems [176]. Moreover, the behavior of physical variables which are difficult to model with physics-based approaches can be captured with data-driven models. Since the complexity of APPJs presents numerous challenges for physics-based modeling, data-driven models can provide an advantage particularly in the context of control applications.

This section focuses on linear parametric data-driven models to describe the dynamics of the kHz-APPJ and the treated substrate. These models represent a limited, and arguably the simplest, subset of data-driven modeling strategies. To this end, first, a linear operating region is established with respect to two outputs, maximum substrate temperature $T_{s,max}$ and total optical emission intensity measured at the surface I. The total optical emission I contains information about the chemical processes occurring in the discharge and requires considerable effort to model with a physics-based approach. Each of the inputs are excited individually around the nominal operating point (V_{p2p}=8 kV, f=16 kHz, q=1.2 slm) and the corresponding steady state values of the two outputs from their nominal values ($T_{s,max}$=58

(a) Deviations in maximum temperature

(b) Deviations in optical intensity
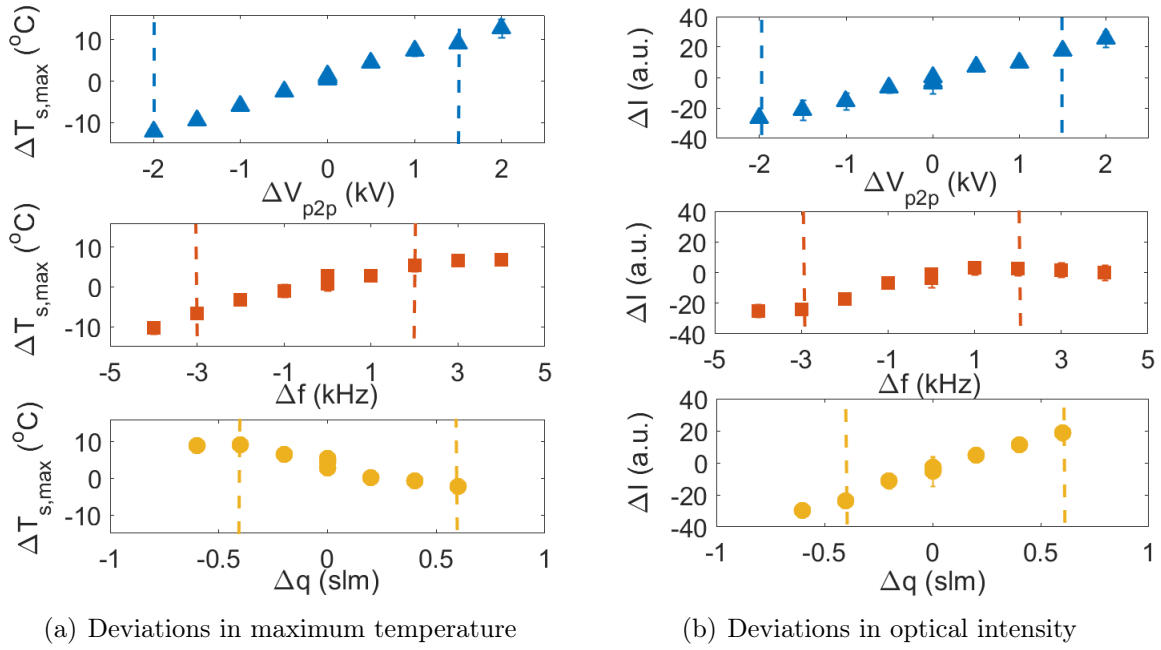
Figure 4.12: Steady-state deviations from the nominal operating condition observed through single-input step tests of different magnitudes: (a) deviations in the maximum temperature $T_{s,max}$ and (b) deviations in the total optical intensity I at the surface.

°C, I=87 a.u.) are recorded. The resulting trends plotted in Figure 4.12 are used to determine the linear operating range,

$$6 \text{ kV} \leq V_{p2p} \leq 9.5 \text{ kV}$$
$$13 \text{ kHz} \leq f \leq 18 \text{ kHz}$$
$$0.8 \text{ slm} \leq q \leq 1.8 \text{ slm}.$$

4.6.1   Transfer Function Models

Transfer function models are useful in describing single-input-single-output (SISO) system models in frequency domain. Their properties and use are well-established in classical control theory for design and evaluation of proportional-integral (PI) and feedforward controllers [30]. Although the thermal dynamics of substrates in contact with APPJs result from complicated physical processes coupled across multiple timescales, the behavior of the maximum substrate temperature can be described with a first-order transfer function using only two parameters: a gain and a time constant. Figure 4.13(a) shows the measured dynamics of maximum substrate temperature in response to changing applied voltage in terms of deviation variables. Similarly, transfer functions can be useful in describing disturbance response
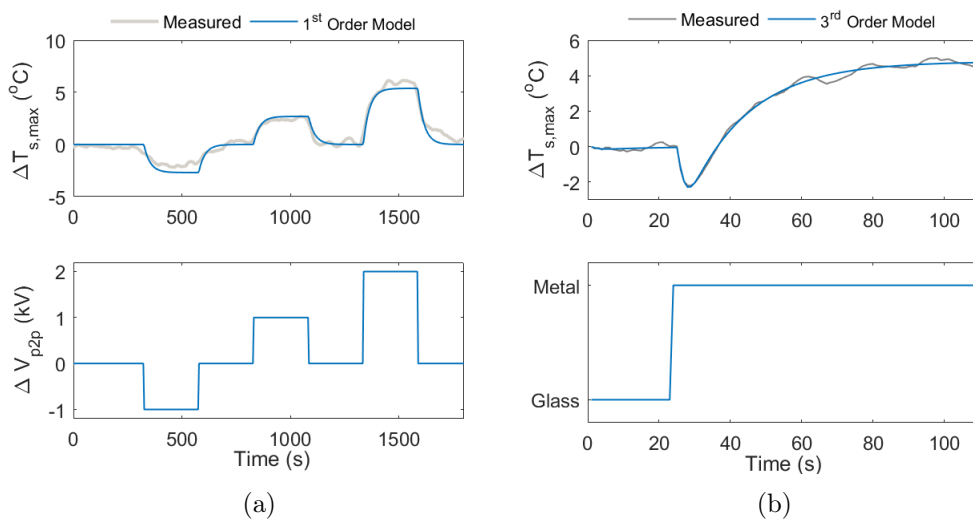
Figure 4.13: Deviation in maximum substrate temperature ($\Delta \mathrm{T}_{s,max}$) (a) in response to deviations in applied peak-to-peak voltage ($\Delta \mathrm{V}_{p2p}$), compared to a 1$^{\text{st}}$ order transfer function, and (b) in response to changing substrate temperatures compared to a 3$^{\text{rd}}$ order transfer function. The transfer functions shown in (a) and (b) are given in Appendix C.4.

of temperature dynamics. The physical phenomena occurring in the APPJ changes considerably with changing electrical and thermal properties of the substrate [6], [25], [127], [177], [178]. For example, the APPJ tends to spread on dielectric substrates and a so-called discharge restrike is observed when the APPJ is in contact with conductive substrates [6], [25], [178]. Physics-based modeling of this behavior can be particularly challenging. In contrast, as shown in Figure 4.13(b), a third order transfer function model can describe the response of maximum substrate temperature to changing substrate type with reasonable accuracy.

4.6.2 Linear Subspace Identification

[1]Despite the usefulness of transfer functions, it can be challenging to extend them to describe multiple-input-multiple-output (MIMO) dynamics. It is more convenient, instead, to use the so-called state space representation in the time domain. In discrete form, the linear state-space model is written generally as

$$
\begin{aligned}
x_{k+1} &= Ax_k + Bu_k \\
y_k &= Cx_k + Du_k,
\end{aligned}
\tag{4.27}
$$

where k is the time index; x denotes the states; u denotes the manipulated inputs, and y denotes the outputs. Although it is possible to convert between linear state space models

---

[1]Results in this section are published in [179]

(a) Model predictions (b) Inputs
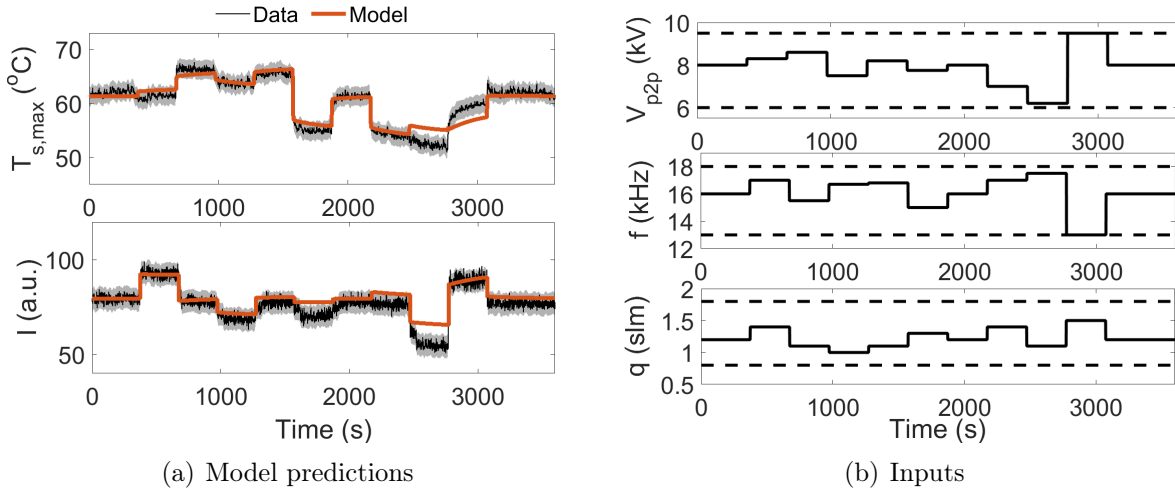
Figure 4.14: Model predictions compared against a validation data set: (a) outputs — maximum temperature $T_{s,max}$ and total optical intensity of plasma I at the surface and (b) manipulated inputs — peak-to-peak voltage V_{p2p}, frequency of excitation f, and He mass flow rate q. The shaded regions in (a) show standard deviations of the measured outputs computed based on the three validation data sets.

and transfer function models, the mapping between transfer function and state space is not unique. Therefore, subspace identification methods are used as a means for directly identifying state space models with robust numerical properties. These methods rely on projecting the measured data into a space of "states" that are not necessarily physically meaningful but mathematically characterize the modes of system dynamics. The relationship between the inputs, the states and the outputs are then determined via a least squares estimation [26].

Note that the SISO step tests broadly describe the linear operating region (see Figure 4.12) however, they do not capture the effects of coupling between the multiple inputs. To fully characterize the APPJ dynamics, multi-input step excitation tests are conducted where two or more inputs are excited simultaneously. The input-output data obtained as a result of these tests are used to identify a linear system model using the canonical variable algorithm (CVA) for subspace identification [26]. The subspace model identification was performed in MATLAB (MathWorks®) using the `n4sid` function. The identified model is of the discrete-time form (4.27). $x \in \mathcal{R}^7$ denotes the states; $u = [V_{p2p} \ f \ q]^\top \in \mathcal{R}^3$ denotes the manipulated inputs; $y = [T_{s,max} \ I]^\top \in \mathcal{R}^2$ denotes the measured outputs; and A, B, and C and D are time-invariant system matrices of appropriate dimension. The system matrices are given in Appendix C.5.

The descriptive capability of the identified model was examined based on independent validation data, generated using a different multi-step input profile than that used in the identification experiments. The validation experiments were repeated three times to ensure

reproducibility of the data. Figure 4.14 shows the model validation results. The identified model exhibits adequate performance in capturing the dynamics of the maximum substrate temperature $T_{s,max}$ and the total optical intensity of plasma I at the surface (see Figure 4.14(a)). As expected, the model predictions can more adequately describe the data when the system operation remains closer to the nominal operating condition. The quality of the identified model deteriorates as the inputs are pushed farther away from the nominal values after time 2500 s (see Figure 4.14(b)).

4.7 Conclusions

Two main strategies are demonstrated for control-oriented modeling of APPJs; lumped-parameter physics-based, and data-driven modeling. The main conclusion of this chapter is that it is possible to obtain reasonably accurate descriptions of APPJ characteristic for process control applications using relatively simple models. The choice of the method relies on the specific needs of the control application e.g., how difficult it is to obtain input-output data or to describe the controlled variables using fundamental physical laws. Both of the methods have certain challenges. Lumped-parameter physics-based models require tractable representations of the complex plasma physics with few parameters; selecting and validating appropriate assumptions for these models is a key barrier. Data-driven models, on the other hand, allow the use of input-output data for modeling APPJ characteristics, such as emission intensity, which are challenging to model using a physics-based approach. However, in the absence of knowledge of physics choice of model structure can be complicated. Particularly, the restriction of the model structure to linear introduces considerable drawbacks in describing the APPJ behavior over a large range of parameters (see Figure 4.14). A potential path forward may involve so-called grey-box modeling, combining the two methods: leveraging the knowledge of physics to inform model structures and using data to determine the appropriate model parameters.

Another challenge for control-oriented modeling pertains to the definition of dose metrics. The metrics provided in Section 4.3 are tentative definitions whose usefulness in a clinical context remain unclear. In contrast, effective regulation of plasma treatment relies on the ability to effectively represent relationships between APPJ characteristics (such as current, emission intensities, reactive species concentrations and thermal effects), the substrate response (such as tissue oxygenation, cell death, extent of metabolic up-regulation) and biological effects (such as wound healing response, extent of cancer reduction, systemic immune response). Although some preliminary efforts are present in the literature [180], there is no widely accepted definition for a "plasma dose". Obtaining more clinically-relevant plasma dose models to replace those presented in Section 4.3 is likely a multi-disciplinary and multi-year effort requiring input form plasma scientists as well as medical professionals.

As dictated by choice of the dose metrics, the control-oriented modeling of APPJs, in this chapter, has focused on primarily thermal and to a lesser extent electrical and optical characteristics. The chemical effects of the APPJs are largely left out of the discussion.

This is due to two related reasons: (i) difficulties in measuring the chemical species concentrations in gas-phase in the APPJ and their subsequent effect on surfaces in real-time, and (ii) the consequent lack effective dose definitions based on chemical effects of APPJs. Direct measurement of species concentrations often relies on methods requiring expensive and cumbersome equipment such as laser-induced fluorescence [181] and mass spectrometry [182] which are also difficult to adopt for real-time measurements. Some potential methods to mitigate these challenges are presented in Chapter 10.

Chapter 5

Basic Control of Atmospheric Pressure Plasma Jets

Basic control strategies such as proportional-integral (PI) control and feedforward control can be a powerful means of regulating the electrical characteristics and thermal effects of APPJs. This chapter demonstrates use cases of basic controls strategies for regulation of electrical properties of the APPJ and their thermal effects on the substrate. In single-input-single-output context, basic control strategies can enable effective rejection of a variety of disturbances including run-to-run variability, change in separation distance, substrate impedance among others. The basic control strategies shown in this chapter can reduce variability in atmospheric pressure plasma jets in a single-input-single-output context and, as shown in later chapters, may be used in conjunction with advanced control strategies to aid dose delivery.

5.1   Introduction

APPJ characteristics are impacted by the intrinsic variability of the discharge and the exogenous disturbances acting on the APPJ such as ambient temperature, jet position, jet-tip-to-surface separation distance, substrate impedance and the admixture of molecular gases. Basic feedback control strategies such as proportional-integral (PI) and feedforward controls can aid in the rejection of disturbances as well as in reducing the variability in APPJ characteristics and their effects on substrates.

The goal of this chapter is to motivate the need for feedback control for APPJs, particularly under disturbances, and to demonstrate the effectiveness and shortcomings of basic control strategies for regulating APPJ effects. To this end, PI and feedforward control strategies are implemented on the kHz-APPJ setup in He described in Chapter 3 in order to control the electrical characteristics of the APPJ and their thermal effects on substrates.
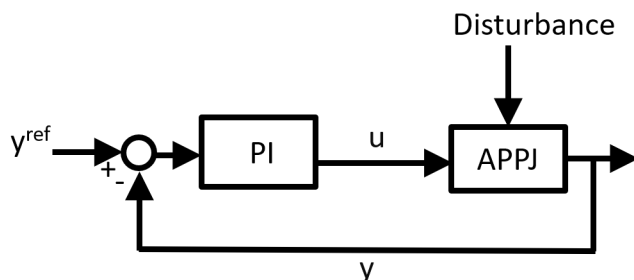
Figure 5.1: Block diagrams for basic PI feedback control; y is the output, y^{ref} is the setpoint, and u is manipulated input.

5.2 Proportional-Integral Control

Proportional-integral (PI) control is the workhorse of process control systems [183]. PI control uses the difference between a single output y and its prespecified setpoint, or reference y^{ref} to determine the value of a single control input u that eliminates the setpoint tracking error $e(t) = y^{\text{ref}} - y(t)$, in the face of setpoint changes and system disturbances. A block diagram of a simple PI control loop is shown in 5.2. The mathematical expression for the PI controller is given as

$$u(t) = k_p \left(e(t) + \frac{1}{\tau_i} \int_0^t e(\tau)d\tau \right), \tag{5.1}$$

which consists of a proportional-error action (first term) and an integrating-error action (second term). The proportional term allows the controller to respond proportionally to instantaneous error, and the integral term allows elimination accumulated errors for offset-free setpoint tracking. The proportional gain k_p and the integral-time constant τ_i are the tuning parameters of a PI controller. Due to its simplicity and ease of design, PI control can be a powerful tool. Most modern control systems employ PI-type controllers, at some level, to allow for rapid rejection of disturbances [36], [184].

The design of PI control strategies relies on the selection of the tuning parameters of the controller (see (5.1)). PI tuning methods are typically based on modeling and analysis of the dynamics of the closed-loop system arising from feedback control [29], [30]. The Internal Model Control (IMC) method allows the systematic selection of PI tuning parameters. Developed by Morari et al., IMC method makes use of a transfer-function representation of the controlled dynamics to obtain analytical expressions for controller tuning parameters. The various analytical expressions for controller optimal turnings for dynamic models of different levels of complexity are tabulated [185]. The IMC control strategy involves a single user-defined parameter λ which relates to the response time of the closed-loop system dynamics. Note here, that for the simplest, first order system dynamics the IMC procedure results in a PI-type controller. For more complicated transfer function models, the inclusion of a

derivative-action term to the controller is recommended. Tuning of the various PI controllers implemented in this section is reported in Appendix D.

Another key consideration in the implementation of PI strategies is enforcing bounds on the manipulated variables. Instruments are often capable of manipulating inputs only over a limited range, whereas the input values computed by the PI controller, as given by (5.1), are unbounded. Simply clipping (i.e., saturating) the input values computed by the PI controller can give rise to the so-called windup effect. When the input saturates at the bounds, the error continues to accumulate and due to the integrating action "winding up" the controller. Once the input is no longer saturated, the PI controller overcompensates giving rise to undesirable behavior. In order to avoid this behavior, an anti-windup strategy is applied to the PI controllers implemented in this section [186].

5.3   Disturbance Rejection with Single-Loop PI Control

In this section, the effectiveness of PI control strategies in regulating the thermal effects of the APPJ on the substrate in the presence of key disturbances is investigated. Common disturbances arising in APPJ operation; variations due to ambient temperature and jet translation, changes in jet-tip-to-surface separation distance, and substrate characteristics can drastically affect the electrical and thermal phenomena occurring in the APPJ and treated substrates.

The APPJ has multiple input variables available for use in feedback control loops. Applied peak-to-peak voltage, frequency, and duty cycle influence the substrate temperature through the effecting the power dissipated in the discharge, changing the electrical properties of the APPJ. The input He flow rate influences the substrate temperature affecting the transport phenomena in the jet. This investigation focuses on the effectiveness of two manipulated variables relating to electrical properties of the APPJ (the peak-to-peak voltage V_{p2p}) and He flow rate q in rejecting disturbance. The effect of the disturbances and the PI control strategies on the electrical properties of the discharge, as quantified by dissipated power P, and the thermal effects on the substrate, as quantified by maximum substrate temperature $T_{s,max}$, are investigated.

5.3.1   Run-to-Run Variability of Substrate Temperature

Variations in the ambient temperature, as well as run-to-run variability observed in APPJs, can make reliable operation challenging [9], [11]. Figure 5.3 shows experimental observations of the maximum substrate temperature, $T_{s,max}$, as the APPJ is translated across a glass substrate following the trajectory given in Figure 5.2, under (a) no feedback control (i.e., constant applied peak-to-peak voltage V_{p2p}), and (b) PI control. For each case, two sets of experiments are carried out on different days under different ambient temperature, where each run is replicated three times.
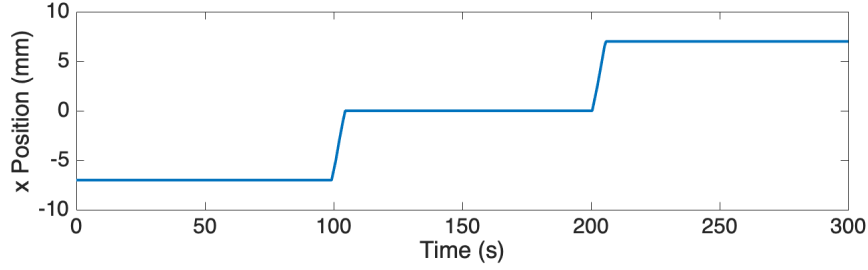
Figure 5.2: Position profile used to perturb the APPJ operation for disturbance rejection studies.

(a) No Control
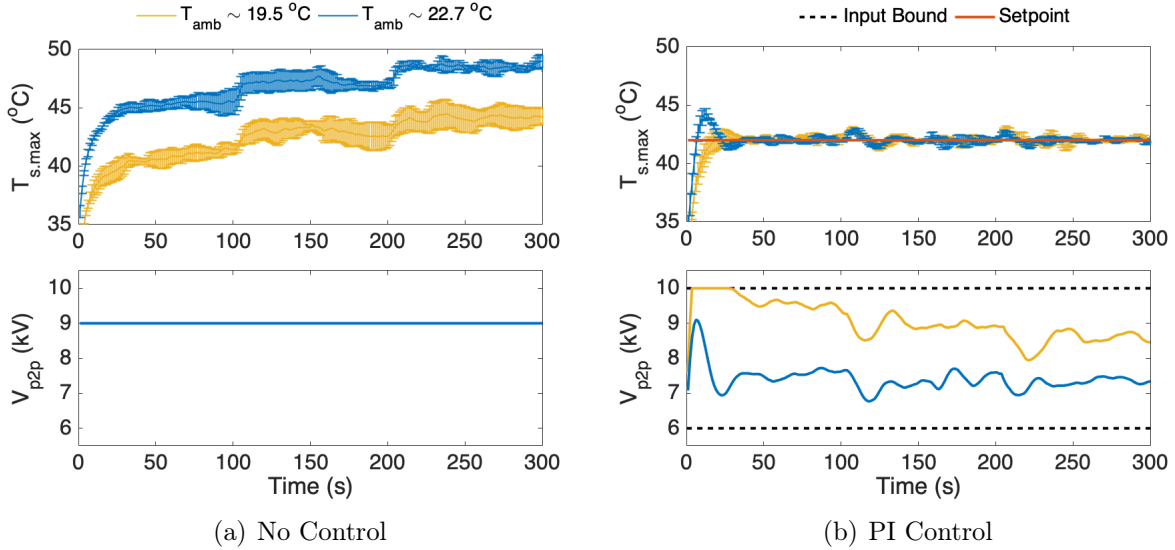
(b) PI Control

Figure 5.3: Maximum substrate temperature $T_{s,max}$ and applied peak-to-peak voltage V_{p2p} under the APPJ translation profile 5.2 under (a) no feedback control and (b) PI control with the reference maximum substrate temperature $T_{s,max}^{\text{ref}} = 42\ °C$. Two sets of experiments are carried out for each case under different ambient temperature T_{inf}. The error bars show the standard deviation of temperature measurements based on three replicate runs.

In the case of no feedback control, Figure 5.3(a) suggests that $T_{s,max}$ is sensitive to ambient temperature, and there is considerable run-to-run variability over the three replicate runs. The effect of the APPJ translation is also reflected in the $T_{s,max}$ profile, where abrupt changes at t=100 s and t=200 s are observed – consistent with the APPJ translation shown in Figure 5.2. The timescale of APPJ translation is on par with that of the substrate temperature dynamics. Thus, when the APPJ is translated to a new point (e.g., at t=100 s), that point has already been exposed to thermal energy due to the spatial distribution of substrate temperature along the target region x. This presents one possible explanation for
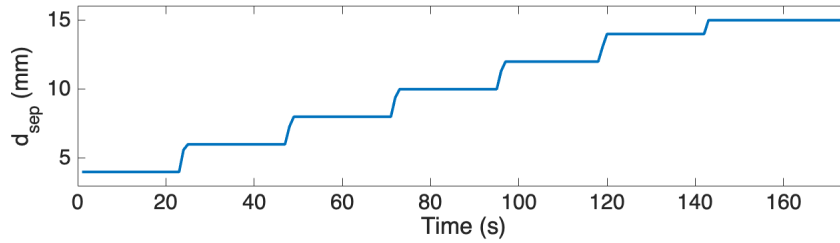
Figure 5.4: Disturbance profile used to investigate the effect of jet-tip-to-substrate separation distance, d_{sep}, on APPJ operation.

the observed increase in $T_{s,max}$ as the APPJ is translated over the target region. Since the discharge is very sensitive to external conditions, other disturbances such as inhomogeneity in substrate properties or small changes in separation distance along the movement direction can also affect thermal behavior. This behavior demonstrates the need for feedback control for regulation thermal effects of the APPJ on the substrate even under relatively mild disturbance conditions investigated here.

On the other hand, Figure 5.3(b) suggests that the PI controller can effectively maintain $T_{s,max}$ at its arbitrarily chosen reference $T_{s,max}^{\text{ref}} = 42 \text{ °C}$. The PI controller is able to maintain the user-specified reference temperature under both ambient temperatures, while significantly reducing the variability of $T_{s,max}$ across the replicate runs. This is achieved by manipulating the applied peak-to-peak voltage V_{p2p} based on real-time substrate temperature measurements. In order to maintain constant that $T_{s,max}$, the input V_{p2p} varies considerably during the operation.

5.3.2 Separation Distance

Changes in jet-tip-to-surface separation distance d_{sep} can occur due to variations in substrate topology or during hand-held treatment. The substrate temperature is particularly sensitive to changes in separation distance. Since the investigated APPJ is of single electrode configuration, changing separation distance impacts some key discharge parameters. Changes in the position of the ground, the electric field strength, as well as the amount of in-mixing from the ambient air all, vary with separation distance causing significant variability in discharge characteristics [7], [127], [187]. Figure 5.3.2 shows the behavior of the maximum substrate temperature and dissipated discharge power in the absence of feedback control as the separation distance is gradually increased. The dissipated power decreases with increasing separation distance. However, $T_{s,max}$ does not follow this trend. Instead, the maximum substrate temperature increases by about 10 ^{o}C as d_{sep} is increased from 4 to 10 mm, after which it starts to decrease. As the APPJ is pulled away from the grounded surface beyond a separation distance of 10 mm (t > 100 s), the visual appearance of the discharge becomes unstable. The spikes observed in P during this time period are accompanied by fluctuations
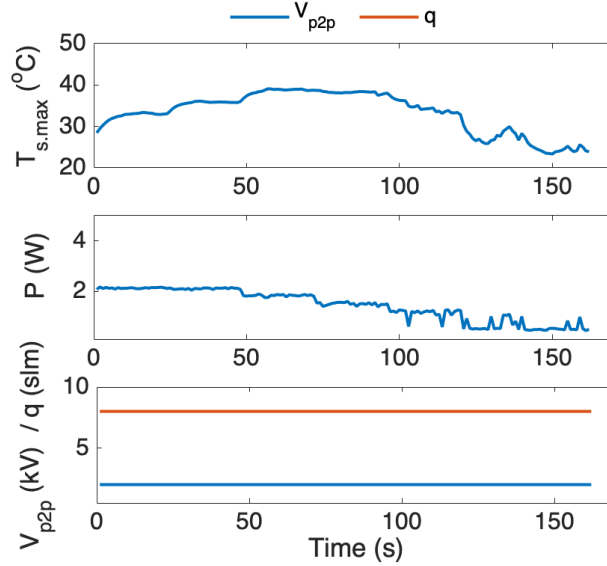
Figure 5.5: Maximum substrate temperature, $T_{s,max}$ and discharge power P under the separation distance profile in Figure 5.4 in absence of feedback control; applied voltage V_{p2p} and helium mass flow rate q are maintained at their constant values.

of the discharge. Eventually, at d_{sep}=15 mm, the discharge is decoupled completely from the surface.

Two PI control strategies are tested in their ability to mitigate the effect of the disturbance in d_{sep}. $T_{s,max}$ is controlled with two different manipulated variables; the applied voltage V_{p2p} and the helium mass flow rate q. Figure 5.6(a) shows the control performance with manipulated V_{p2p}. Initially, with this strategy, $T_{s,max}$ cannot reach the setpoint, on account of the saturation of the input. However, as d_{sep} is increased beyond 6 mm (t > 25 s) the PI controller tracks the setpoint in maximum substrate temperature effectively, until d_{sep} reaches 14 mm (t = 120 s). After this time, as in the no control case, spikes are observed in P and $T_{s,max}$ starts to decline as the discharge starts to decouple from the surface. Figure 5.6(b) shows the control results obtained with q as the manipulated variable. The control performance is noticeably better compared to results obtained using V_{p2p} as the manipulated variable. The setpoint in $T_{s,max}$ is tracked well throughout the operation as q increases with increasing separation distance. Moreover, P remains comparatively constant with no indication of the spiking behavior associated with discharge instability and decoupling from the surface. Visually, the discharge also remains more stable as the APPJ is drawn away from the surface. One explanation for the comparative advantage of using q as the manipulated variable may pertain to in-mixing of ambient air species into the discharge plume. Increasing separation distance allows increased in-mixing of air. This, in turn, results in increased temperature, as both N_2 and O_2 have significantly shorter mean free paths resulting in more frequent collisions, quenching the plasma. Increasing q causes the convective flow in the axial
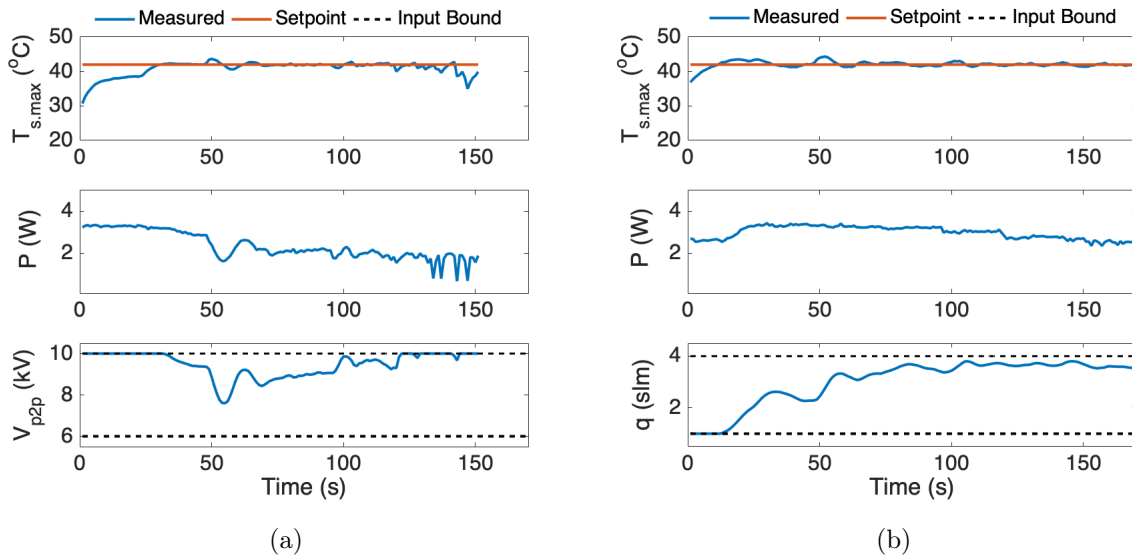
Figure 5.6: Maximum substrate temperature $T_{s,max}$, discharge power P, and applied input profiles with the varying separation distance profile in Figure 5.4, under PI control with (a) applied peak-to-peak voltage V_{p2p} and (b) helium mass flow rate q as the manipulated variable.

direction to dominate over the radial diffusion of air, allowing the discharge to be sustained in a stable manner over large separation distances. This is similar to reported behavior of the APPJ increasing length with the increased flow when operated as a free jet, de-coupled from the ground [117], [133], [188].

Although use of q as manipulated variable appears to be advantageous over using V_{p2p} to mitigate the effect of the disturbances in separation distance, both methods appear to be adequate in maintaining $T_{s,max}$ over a reasonably broad range of disturbances (d_{sep} 4-10 mm) in separation distance, offering considerable improvement over the no control case.

5.3.2.1 Substrate Properties

Since the APPJ is electrically coupled to the substrate, variations in substrate characteristics such as impedance or thermal properties can drastically impact the APPJ properties and its effects on treated substrates [6], [25], [177]. This, in turn, complicates the reliable operation of APPJs over a range of substrates. For example, in a medical context, thermal and electrical properties of the treated location may vary between healthy and wounded tissue, or between patients. To investigate the effect of the substrate impedance on the substrate temperature, up to four borosilicate microscope coverslips are stacked on top of one another under the APPJ. The APPJ is translated across the substrates of varying property (different number of stacked coverslip) and finally onto a bare aluminum substrate. The corresponding disturbance profile is shown in Figure 5.7. Note that it is often not possible to de-couple
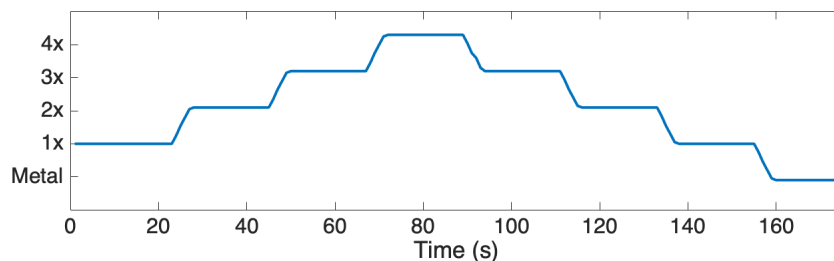
Figure 5.7: Disturbance profile used to investigate the effect of substrate impedance; labels 1x, 2x, 3x and 4x indicate the number of borosilicate cover slip stacked under the APPJ, whereas Metal indicate the APPJ is on the bare grounded aluminum plate.
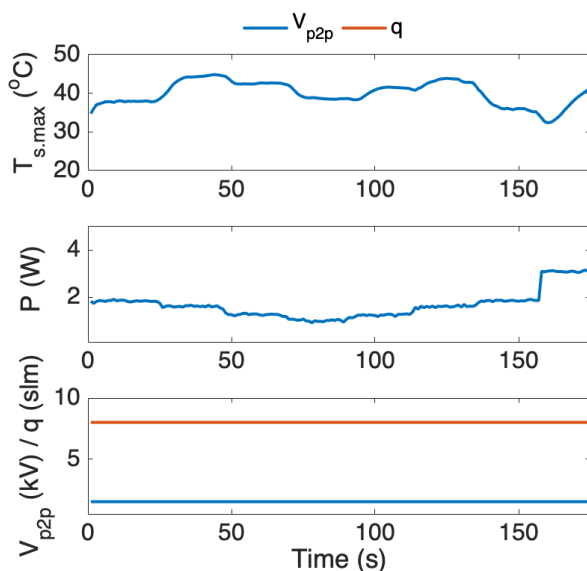
Figure 5.8: Maximum substrate temperature, $T_{s,max}$ and discharge power P under the disturbance in substrate properties in Figure 5.7 in absence of feedback control, with applied voltage V_{p2p} and helium mass flow rate q are maintained at their constant values.

changing substrate impedance from changes in other properties of the substrate such as heat capacity and thermal conductivity. For example, borosilicate and aluminum substrates differ not only in their impedance but also have significantly different thermal conductivity.

Figure 5.8 shows the response of the maximum substrate temperature and dissipated power to the changes in substrate properties following the profile is given in Figure 5.7. P appears to steadily decrease as the jet is translated over an increasing number of coverslips. This can be explained by the increase in substrate impedance with the number of coverslips stacked. $T_{s,max}$, however, follows a different trend; it first appears to increase as the jet is translated over 2x stacked coverslips and then declines as the number of stacked coverslips
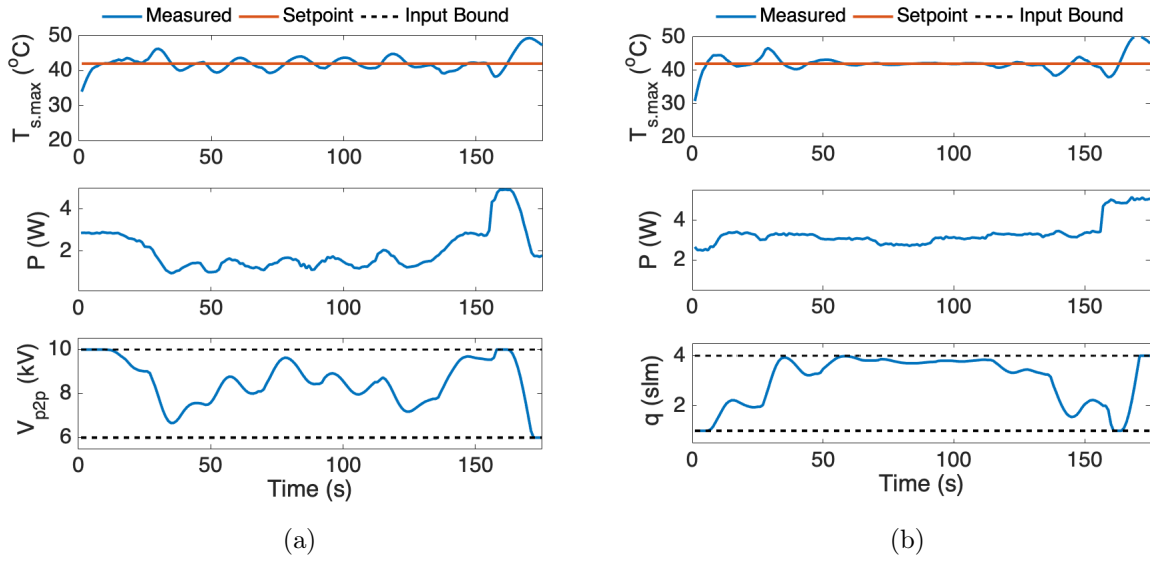
Figure 5.9: Maximum substrate temperature $T_{s,max}$, discharge power P, and applied input profiles under the varying substrate characteristics following the profile in Figure 5.7, with PI control with (a) applied peak-to-peak voltage V_{p2p} and (b) helium mass flow rate q as the manipulated variable.

increase. This counter-intuitive behavior in $T_{s,max}$ can be attributed to the competing effects of the additional thermal resistance associated with the non-perfect thermal contact between coverslips, and the decreasing P. The increased thermal resistance can allow the substrate temperature to increase despite the decreasing power. Lastly, at the end of the operation, P significantly increase as the APPJ is translated over the metal substrate. Correspondingly, $T_{s,max}$ takes on an increasing trend, although it does not reach steady state within the allowed time. The response of P and the dynamics of the $T_{s,max}$ clearly demonstrate the sensitivity of APPJ operation substrate characteristics.

Two PI control strategies are tested for mitigating the effect of the disturbance in substrate characteristics, controlling $T_{s,max}$ with two different manipulated variables; V_{p2p} and q. Figure 5.9(a) shows the measured $T_{s,max}$ and P under PI control with V_{p2p} as manipulated variable. $T_{s,max}$ tracks the setpoint reasonably well initially. However, oscillations are observed as the APPJ is translated over 2x, 3x and 4x coverslips. The oscillatory behavior of temperature may be attributed, at least in part, to the fact the PI controller is tuned under the nominal substrate condition of 1x coverslip. As the substrate properties change, the PI tuning may end up being too aggressive giving rise to the observed oscillations.

Figure 5.9(b) show measured $T_{s,max}$ and P under PI control with q as the manipulated input. As in the previous case, some oscillations are observed in $T_{s,max}$ although the controller appears to give rise to comparatively smooth behavior, particularly as the APPJ is translated over 3x and 4x stacked coverslips (t = 50–140 s). During this time, q increases close to the

upper bound and appears to remain fairly stationary. Note that the dissipated power profile in Figure 5.9(b) is very similar to that of the no control case (Figure 5.8). This indicates that the flow and electrical effects are somewhat decoupled, save for the slight variation in P observed at the beginning of the operation corresponding to a particularly low flow rate of 1 slm. As the APPJ is translated onto metal at the end of the operation, both strategies in Figure 5.9 appear to perform poorly. Regardless of which manipulated variable is used, $T_{s,max}$ considerably overshoots setpoint. This indicates a potential shortcoming of the naive single-loop PI strategy in handling the drastic disturbance of glass-to-metal transition.

As in the case of changing separation distance, the results indicate some advantage in using q to $T_{s,max}$. However, the advantage is less clear in this case. Using flow as the manipulated variable leaves the electrical properties of discharge, as quantified by P, to freely fluctuate in response to disturbances. This is undesirable as power dissipation is a key discharge property which can impact discharge chemistry and effects on the substrate. This behavior indicates the need for more complex strategies beyond single-loop PI to effectively regulate the APPJ characteristics as well as thermal effects in the presence of disturbances. One possible approach to allow this is presented in the next section.

5.4 Cascade Control of Substrate Temperature

Cascade control is a so-called "enhanced single-loop" control strategy which involves connecting multiple PI controllers in serial manner [29]. Figure 5.4 depicts a block diagram of a cascade control strategy with two PI controllers. In cascade control, the input value calculated by the controller in the outer loop is fed to a controller in the inner loop as the setpoint. The APPJ is particularly amenable to cascade control strategies due to the separation of timescales between the dynamics of the electrical phenomena in the APPJ ($\sim$ ms) and the thermal response of the substrate ($\sim$ s). The cascade control structure allows leveraging this separation of timescales for rapid disturbance rejection. The electrical properties of the APPJ can be controlled by an embedded PI controller at a faster timescale, while the thermal properties can be controlled at a slower timescale. This section first investigates the embedded control of electrical properties of the APPJ via control of the applied peak-to-peak voltage V_{p2p} and dissipated power P. Then, the capability of a cascade control strategy in setpoint tracking and disturbance rejection is demonstrated.

5.4.1 Embedded Control of Electrical Properties of APPJ

5.4.1.1 Voltage Control

The applied voltage (V_{p2p}) is one of the key input variables that influence the APPJ characteristics. In current practice, APPJs are operated at constant applied voltage and frequency. However, conventional high voltage amplifiers have frequency-dependent behavior [189], [190] which can cause the voltage across the discharge to vary considerably with changing frequency. Figure 5.4.1.1 shows experimental results collected from the kHz-APPJ setup in He.
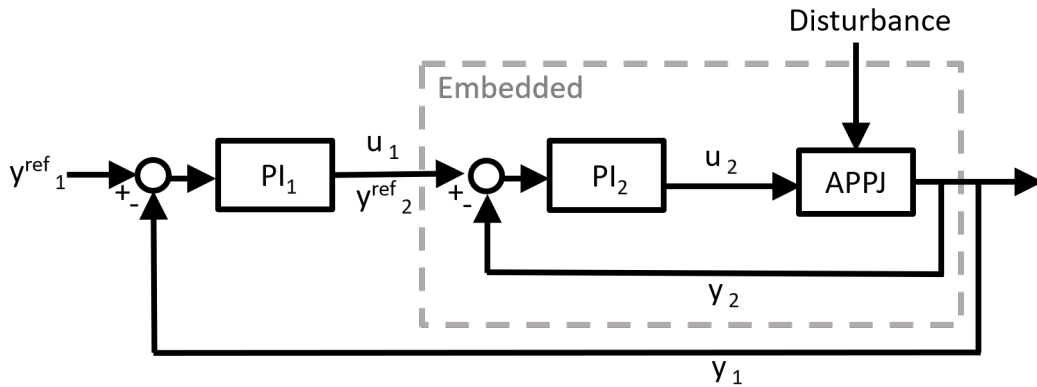
Figure 5.10: Block diagram for cascade control, y^{ref}, y and u refer to the setpoint, output and input associated with the PI controller with the corresponding subscript; the input computed by the controller in the outer loop u_1 is the setpoint to the controller in the inner loop y_2^{ref}.

(a) No control

(b) Embedded voltage control
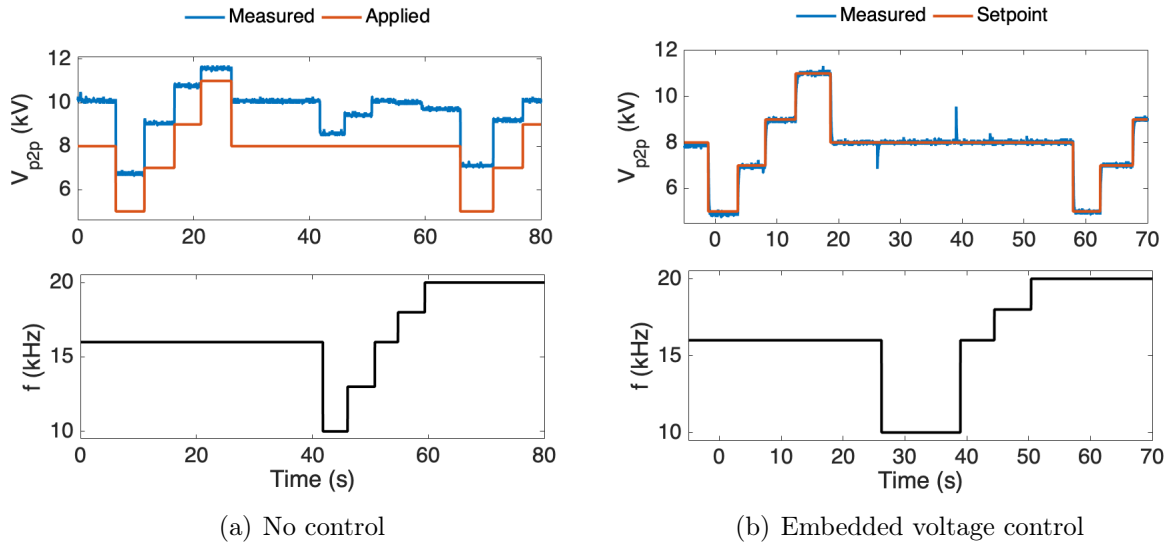
Figure 5.11: Measured peak-to-peak voltage (V_{p2p} in presence of varying discharge frequency f under (a) no feedback control and (b) embedded voltage control.

Figure 5.11(a) shows the clear mismatch observed between the measured peak-to-peak voltage (V_{p2p}) across the discharge and the amplifier input. Evidently, the frequency response of the amplifier presents a disturbance to the voltage signal; measured V_{p2p} considerably varies with changing frequency. This behavior motivates the need for embedded control strategies for reliably controlling the voltage measured across the APPJ. Indeed, an embedded PI

(a) Setpoint tracking

(b) Disturbance rejection
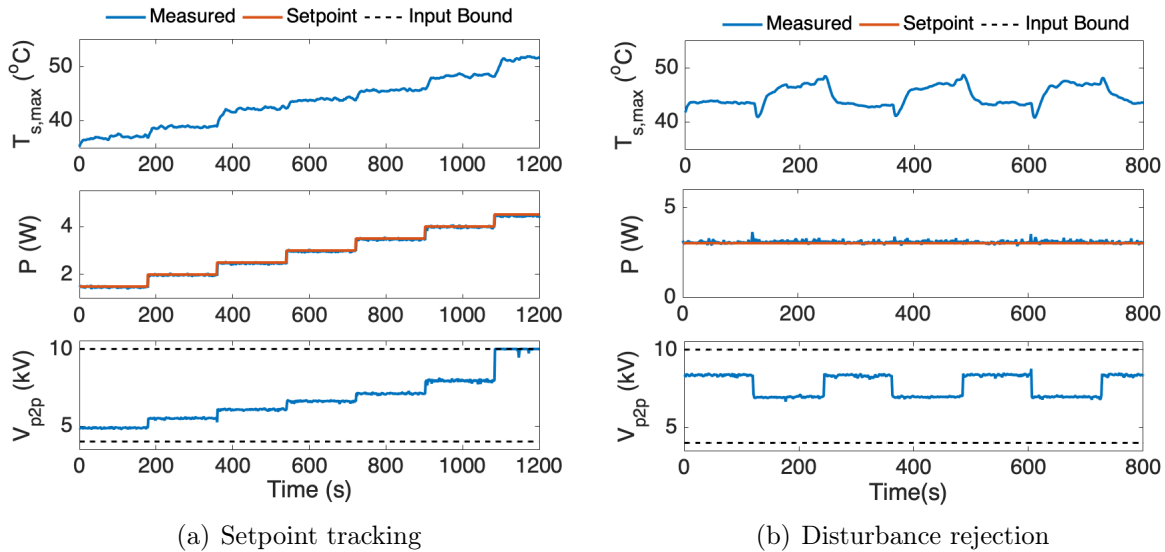
Figure 5.12: Measured power P, maximum substrate temperature $T_{s,max}$ and applied peak-to-peak voltage V_{p2p} under PI control for (a) setpoint tracking, and (b) rejection of disturbance in changing substrate type.

controller implemented in the ms timescale allows the regulation of the measured voltage (Figure 5.11). The effects of disturbance arising from changes in frequency are mitigated effectively by the PI controller except for small and short timescale excursions at t = 27 s and t = 39 s. The embedded PI controller, therefore, ensures that the desired input value of peak-to-peak voltage is reliably applied to the setup.

5.4.1.2 Power Control

The dissipated power depends not only on the applied voltage but also on the properties of the discharge such as discharge geometry and the substrate the discharge is in contact with. Moreover, the dissipated power directly influences the thermal end chemical processes occurring in the discharge, impacting the APPJ effects delivered to the substrate. Therefore, directly controlling the discharge power of key interest. An embedded PI controller is configured to maintain the dissipated power by manipulating the applied peak-to-peak voltage V_{p2p}. As described in Chapter 3, the embedded power is computed as the product of analog measurements of root-mean-squared (RMS) voltage and current. Figure 5.12 shows the experimental results concerning the embedded PI control of power. Figure 5.12(a) indicates that the controller is able to accurately track the power setpoint by manipulating the applied voltage. The input, V_{p2p}, appears to vary in a similar manner with P indicating a constant V_{p2p}, for the most part, can allow maintaining a constant power in the absence of disturbances. Notably, the final change in setpoint from 4 to 4.5 W results in a sharper rise in V_{p2p} compared to the previous changes. This behavior indicates an advantage of PI control
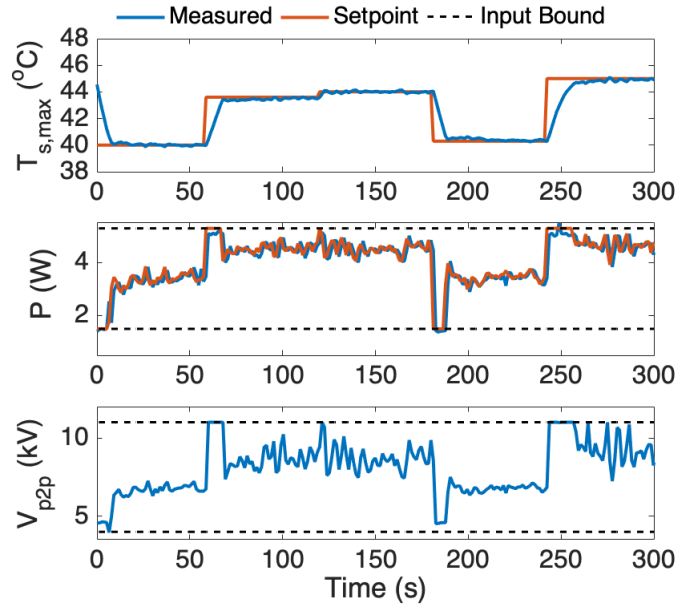
Figure 5.13: Temperature setpoint tracking using cascaded control strategy; the lower level embedded controller regulates P by manipulating V_{p2p} is cascaded to a controller for $T_{s,max}$.

in reliably maintaining P, beyond simply controlling the applied voltage. Moreover, $T_{s,max}$ appears to vary in a similar manner with P, indicating P can allow regulation of $T_{s,max}$ in a similar manner as voltage.

The advantage of PI control of dissipated power is more evident in the presence of disturbances. Figure 5.12(b) shows the performance of the embedded PI power controller in maintaining power in presence of a periodic disturbance in substrate type; the operation is started on a glass substrate and the APPJ is transitioned between a dielectric and conductive substrate every 120 s. Dielectric and conductive substrates can result in drastically different electrical behavior in the discharge [6], [25]. The experimental observations verify the sensitivity of electrical and thermal characteristics of to substrate type. The input profile clearly indicates that a considerably lower V_{p2p} is needed to maintain the dissipated power on the conductive substrate. The advantage of embedded PI control is clear in this case, as the dissipated power is effectively regulated in the presence of the disturbance in the presence of disturbances.

5.4.2 Setpoint Tracking with Cascade Control

While the embedded PI control allows effectively regulating the electrical properties of the APPJ, it does not necessarily allow maintaining of the thermal effects of the substrate as shown in Figure 5.12(b). Therefore, a cascade control strategy is adopted for regulation of maximum substrate temperature. The embedded power controller described in Section
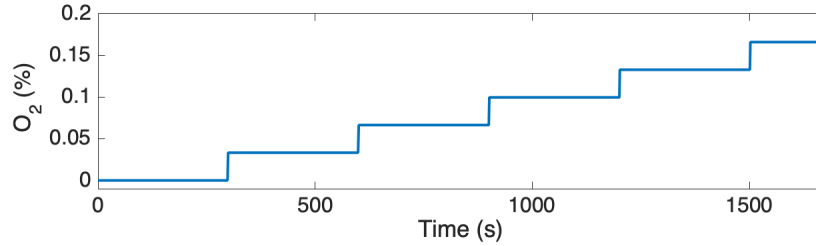
Figure 5.14: Disturbance profile used to investigate the effect of O_2 admixture on APPJ operation.
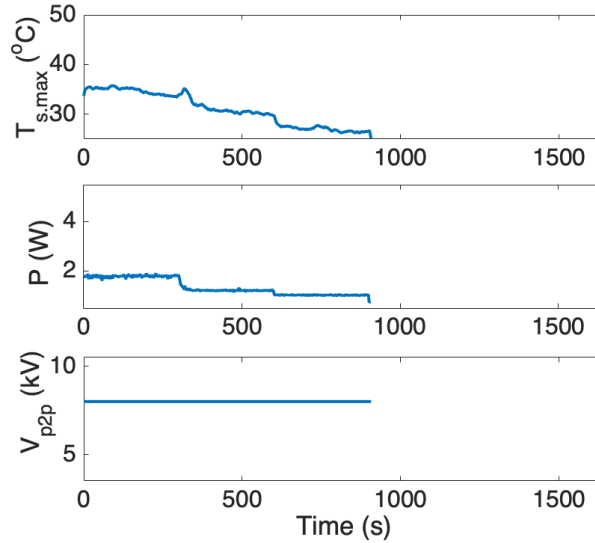
Figure 5.15: Maximum substrate temperature, $T_{s,max}$ and discharge power P under the disturbance in admixed O_2 concentration in Figure 5.4.3 in absence of feedback control, with constant applied voltage V_{p2p}.

5.4.1.2 is used in the inner loop (PI_1 in Figure 5.4). A PI controller regulating $T_{s,max}$ by manipulating the power setpoint is configured for the outer loop (PI_2 in Figure 5.4).

Figure 5.13 shows results obtained for setpoint tracking with the cascade control strategy. The results indicate that the cascade control strategy is able to track the $T_{s,max}$ set point adequately. Moreover, the embedded power controller in the inner loop effectively tracks the setpoints computed by the controller in the outer loop. Note that it takes considerable time for $T_{s,max}$ to reach the setpoint, however, P reaches its setpoint almost instantaneously due to the faster timescale of the embedded control.
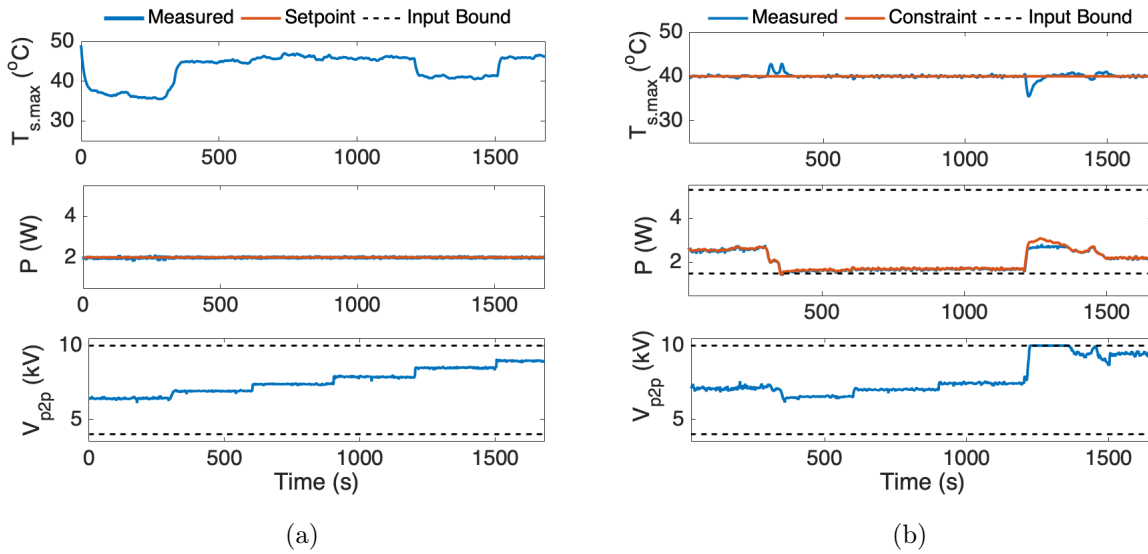
Figure 5.16: Maximum substrate temperature, $T_{s,max}$ and discharge power P under the disturbance in admixed O_2 concentration in Figure 5.4.3 with (a) embedded control of power (b) cascade control of maximum substrate temperature.

5.4.3 Disturbance Rejection with Cascade Control

APPJs are often operated with small amounts of molecular gases (N_2, O_2 and H_2O) admixed into the working gas in order to enhance the discharge chemistry [5], [121]–[123], [126]. However, molecular gases can significantly impact both thermal and electrical characteristics of the APPJ. While addition molecular gases allow production of biologically active reactive oxygen and nitrogen species in greater quantities, they also quench the discharge making it more difficult to sustain the discharge. To investigate the effect of molecular gas admixing, small quantities of O_2 are added to the working gas. Figure 5.4.3 shows the measured $T_{s,max}$ and P in response to O_2 admixture following the profile given in Figure 5.4.3. At constant V_{p2p}, both P and $T_{s,max}$ steadily decline with increasing O_2 concentration. As the O_2 concentration is increased to 0.1% at t = 900 s, the discharge is extinguished.

Figure 5.16(a) shows measured $T_{s,max}$ and P in presence of embedded power control. As in Figure 5.12(b), embedded PI controller is able to regulate P effectively, however $T_{s,max}$ fluctuates. A clear benefit to embedded power control is that the discharge remains ignited up to an O_2 concentration of 0.17%. The behavior in $T_{s,max}$; an initial decrease, followed by a stationary period and another period of decrease, is difficult to explain in simple terms. However, clearly, a strategy beyond embedded power is needed to regulate $T_{s,max}$. Figure 5.16(b) show the performance of the cascade control strategy in rejecting the disturbance in O_2 concentration. Note that in order to obtain acceptable performance with the cascade control strategy the tuning of the outer PI controller is re-visited based on dynamics observed with 0.1 % O_2 admixture (see D.2). The measured profile of $T_{s,max}$ under cascade control
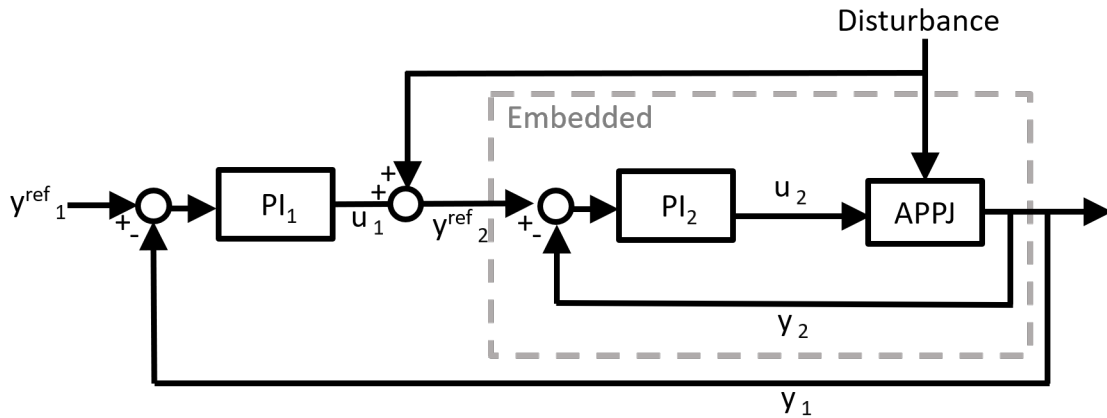
Figure 5.17: Block diagram for cascade control with feedforward (FF) action, y_{ref}, y and u refer to the setpoint, output, and input associated with the PI controller with the corresponding subscript; setpoint to the controller in the inner loop y_2^{ref} is is computed by adding the controller input u_1 to the feedforward action.

in Figure 5.16(b), indicates that the disturbance is effectively rejected. Note at t = 1200 s as O_2 concentration increases to 0.13%, it is not possible for the embedded power controller to reach the setpoint determined by the cascade temperature controller, as the input V_{p2p} saturates. Overall the cascade control strategy is able to effectively reject the disturbance in O_2 admixture disturbance, allowing regulation of both electrical properties of the APPJ and the thermal effects on the substrate.

5.5   Feedforward Control

PI control strategies may not, on their own, be effective in rejecting particularly drastic disturbances effectively. In particular, feedback control cannot directly take advantage of the knowledge of disturbance dynamics. Feedforward strategies can be used to take predictive action, leveraging knowledge of the disturbance response of the system dynamics. In feedforward control, the effect of the disturbance is directly compensated for based on a model of the dynamic of the disturbance response [29]. The feedforward action is combined additively with action computed by the feedback control as shown in the block diagram in Figure 5.5. In order to demonstrate this strategy, the particularly drastic disturbance of the transition between a dielectric and conductive substrate is revisited.

Results shown in Figures 5.9(a), 5.9(b), and 5.12(b) indicate the disturbance in glass-to-metal transition is challenging to handle with single-loop control strategies. Figure 5.18(a) shows the performance of the cascade temperature controller, tuned based on a transfer function model of the thermal dynamics on the glass substrate. As the disturbance acts at t = 120 s, the aggressive tuning of the controller gives rise to oscillations. One method to

(a)   (b)
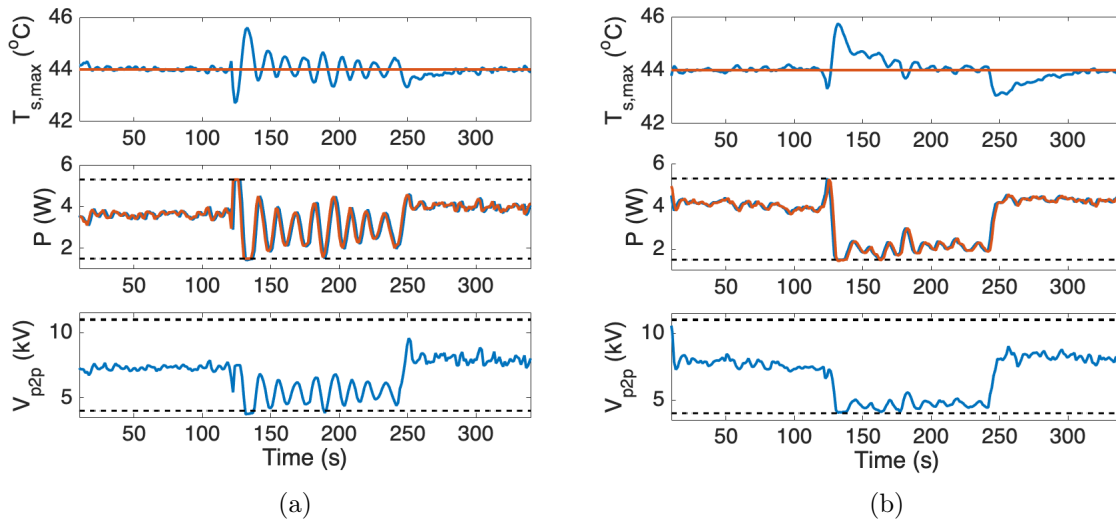
Figure 5.18: Maximum substrate temperature, $T_{s,max}$ and discharge power P as the APPJ is translated from a dielectric to a conductive substrate (t = 120 s) and back (t = 240), under cascade PI controller (a) tuned based on observed dynamics on glass and (b) de-tuned

deal with this behavior is to de-tune the controller by increasing the λ parameter, in effect increasing the response time of the control loop. Figure 5.18(b) shows the performance of the de-tuned cascade control strategy. The measured $T_{s,max}$ profile indicates that de-tuning prevents the oscillatory behavior, at the expense of a considerably slower response. As a result, $T_{s,max}$ overshoots the setpoint significantly and takes a comparatively long time to recover during transitions from both glass-to-metal (t = 120 s) and metal-to-glass (t = 240 s).

Figure 5.19 shows the effectiveness of the feedforward controller in rejecting the disturbance in substrate type. The overshoot observed when the disturbance acts are considerably smaller, allowing for the temperature to return to the desired setpoint rapidly. The difference between the profiles of P and V_{p2p} in Figures 5.19 and 5.18(b) is subtle. Noticeably, the peak observed in P following the glass-to-metal transition at t = 120 s is sharper in Figure 5.19, spanning a shorter duration. Although small, this difference allows for a considerably less drastic overshoot as $T_{s,max}$ recovers from its initial drop. Another peak in P is observed in Figure 5.19 when the APPJ is translated back onto the dielectric, which is absent in Figure 5.18(b). This behavior allows for $T_{s,max}$ to recover more rapidly from the undershoot observed when the APPJ is back on the glass. Note that a crucial aspect of the design and implementation of feedforward strategies is the measurement of the disturbance. In particular, the direct measurement of the substrate type can be challenging. The method used in this section to discriminate between dielectric and conductive substrates is described in the later chapters (see 10.2.2).
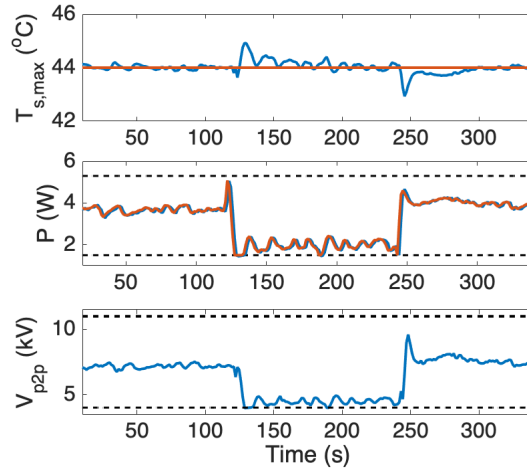
Figure 5.19: Measured voltage in presence of varying discharge frequency under (a) no feedback control and (b) embedded voltage control.

5.6 Conclusions

Results presented in this section demonstrate the effectiveness of basic control strategies, namely, single-loop and cascade PI control and feedforward control, in regulating electrical characteristics of the APPJ and their thermal effects on substrates. Basic control strategies allow rejection of a range of disturbances which may arise in APPJ operation, including, variability in environment and change in APPJ position (Figure 5.3), changes in separation distance (Figure 5.6), varying substrate properties (Figures 5.6 and 5.19), and molecular gas admixing (Figure 5.16(b)). Therefore, a key conclusion of this chapter is that basic control strategies can provide a significant advantage in mitigating effects of disturbances on APPJ operation.

However basic control strategies have some limitations. For example, it is challenging to address multi-variable dynamics with basic control strategies. This issue is touched upon in Sections 5.3 and 5.4. Single loop control of $T_{s,max}$ indicates the advantage of using q as a manipulated variable. However, manipulating only q has the disadvantage of leaving the electrical characteristics of the APPJ unregulated. The cascade control strategy allows regulation of both P and $T_{s,max}$, although, not independently. With the cascade strategy, choice of setpoint in P is dictated by the outer PI controller for $T_{s,max}$. Therefore, a strategy is required for manipulating multiple inputs to regulate multiple outputs simultaneously to fully exploit the operating region of the APPJ. Moreover, basic control strategies cannot systematically address nonlinear and spatially distributed dynamics which arise, for example, in dose delivery problems. The use of advanced, optimization-based control strategies to address these issues are investigated in the following chapters.

Chapter 6

Linear Model Predictive Control Based on a Data-Driven Model

Atmospheric Pressure Plasma Jets (APPJs) are inherently multiple-input-multiple-output (MIMO) systems. Moreover, the input-output relationships amongst the different operating variables in APPJs are interdependent and difficult to decouple. As a result, the problem of controlling the multiple effects produced APPJs is difficult to address with the classical proportional-integral (PI) control strategies. This chapter demonstrates the drawbacks of using PI control on a multivariate problem and contrasts them with a linear model predictive control (MPC) strategy. Real-time control experiments reveal the MPC strategy can more effectively regulate the multivariable dynamics of the APPJ for effective setpoint tracking and constraint handling in the face of disturbances.[1]

6.1   Introduction

The ability to influence the discharge properties over a broad range of conditions is one of the key properties of APPJs that make them attractive tools for bio-chemical processing and medicine. The broad range of operating conditions observed in APPJs, however, hinge on the ability to manipulate a number of process inputs (applied voltage amplitude, frequency, flow rate, molecular gas admixtures...) over relatively large ranges. The electronic, physical and chemical processes that govern the discharge are highly coupled across multiple timescales, resulting in tight coupling of the APPJ dynamics. As a result, each output is often influenced by multiple variables, making it difficult to control with PI control strategies. Individual PI controllers can only control a single output using a single input variable, disregarding the possible interactions occurring between various inputs and outputs in APPJs.

This chapter investigates the application of the optimization-based model predictive control (MPC) strategy to the APPJ for a mutlivariable setpoint tracking problem. A compara-

---

[1]This section is adapted from previously published work [179]

tively simple MPC formulation, based on a linear-data-driven model of the APPJ dynamics (see Chapter 4.6.2) is investigated. The use of a linear system model allows formulation of the MPC optimization as a quadratic problem, which is easy to solve. However, the use of a linear model also significantly limits the accessible operating range for the APPJ. Moreover, nonlinear aspects of operation such as dose delivery, is neglected to retain the linearity of the system dynamics. Nevertheless, the results shown in this chapter demonstrate that the MPC strategy has a clear advantage for regulating multiple APPJ effects over PI control strategies.

In this chapter, the performance of the linear MPC strategy is compared to that of multi-loop PI controls. The control objective is to regulate the maximum substrate temperature $T_{s,max}$ and intensity of plasma at the target surface I in the presence of step disturbances in the device tip-to-surface separation distance d_{sep}, while constraining the APPJ operation within an acceptable operating range. For consistent comparison with the PI strategy, the issue of input-output pairing of the APPJ is systematically addressed. The same linear-data driven model is used in the MPC scheme is adopted for tuning the PI controllers using the internal model control (IMC) method [185].

6.2 Multi-loop PI Control Design

6.2.1 Input-output Pairing

To design the PI controllers for the APPJ at hand, it was necessary to first choose the most effective pairings between the manipulated inputs and measured outputs. The APPJ system has three inputs, applied peak-to-peak voltage V_{p2p}, excitation frequency f, and He flowrate q; and two inputs, maximum substrate temperature $T_{s,max}$, and total optical intensity I. Two PI controllers are designed independently for regulating $T_{s,max}$ and I. Relative gain array (RGA) and singular value decomposition (SVD) analyses [29], [191] were performed using the subspace identified model to systematically determine the most effective input-output pairings.

Relative gain array is constructed based on the steady-state gains K_{ij}, between each input-output pair $i - j$, The steady state gains are organized in the so-called steady-state gain matrix K which is used too determine the RGA as

$$RGA = K \otimes (K^{\#})^{T}, \tag{6.1}$$

where $\otimes$ is the element-by-element multiplication operation (the Schur product), and $\#$ denotes the pseudo-inverse operation, generalizing the inversion operation to non-square matrices. This is necessary as in the APPJ system is non-square. Using the linear subspace identification model (see Section 4.6.2) the RGA is calculated as

$$RGA = \begin{bmatrix} 0.5083 & 0.0947 & 0.3971 \\ 0.3461 & 0.0511 & 0.6028 \end{bmatrix}. \tag{6.2}$$

Here, the rows correspond to the outputs ($T_{s,max}$ and I respectively), and the columns correspond to the inputs (V, f and q respectively). The recommended pairing corresponds to the largest positive elements of the RGA that are closest to one. In (6.2), the elements 0.5081, and 0.6028 are the these two elements, revealing that the maximum temperature $T_{s,max}$ and total optical intensity of plasma I are most sensitive to the peak-to-peak voltage V_{p2p} and He mass flow rate q, respectively. The third input f is dropped for the PI strategy as it is the least significant manipulated variable for both of the inputs.

Further insight can be obtained about the multi-variable dynamics of the system using SVD analysis. Unlike RGA, SVD analysis considers the system dynamics as well as the scaling of the inputs and outputs. For SVD the inputs and outputs are scaled with respect to their allowable range (i.e., inputs u_i is scaled by u_i^{max}-u_i^{min}) [29] and the scaled gain array K_s is computed,

$$K_s = \begin{bmatrix} 0.4258 & 0.2586 & -0.3137 \\ 0.3732 & 0.2195 & 0.4799 \end{bmatrix}. \tag{6.3}$$

This matrix is then de-composed to obtain the singular values,

$$K_s = U\Sigma V^T, \tag{6.4}$$

where Σ is the diagonal matrix of the singular values; columns of U are are the output singular vectors and columns of V are the input singular vectors. These matrices are calculated as follows assuming the system is at steady state,

$$U = \begin{bmatrix} 0.5103 & 0.8600 \\ 0.8600 & -0.5103 \end{bmatrix} \tag{6.5}$$

$$\Sigma = \begin{bmatrix} 0.6756 & 0 & 0 \\ 0 & 0.5549 & 0 \end{bmatrix} \tag{6.6}$$

$$V = \begin{bmatrix} 0.7967 & 0.3167 & 0.5147 \\ 0.4748 & 0.1990 & -0.8573 \\ 0.3739 & -0.9274 & -0.0081 \end{bmatrix} \tag{6.7}$$

The metric of interest in SVD is the conditioning number (CN) defined as the ratio of the largest and smallest non-zero singular values. The calculated steady-state Σ shows that CN is close to 1, indicating the system is well-conditioned. An important observation based on SVD pertains to the U matrix. Notably, the singular output vectors have components in similar magnitude in the two outputs, indicating that they are coupled. The first vector, the so-called strong output direction that is easy to control, corresponds to simultaneous increase of $T_{s,max}$ and I. The second vector indicates the weak input direction that is difficult to control. The matrix U indicates that it is challenging to reduce I while increasing $T_{s,max}$. The SVD analysis also gives information about the process dynamics. Figure 6.1 shows the frequency response of the two singular values of the data-driven linear APPJ model. The trends indicate at higher frequencies the second singular value decreases significantly, which may cause the system to become ill-conditioned (i.e., large CN). This poses a potential issue as the outputs would be difficult to control with any control strategy in this case.
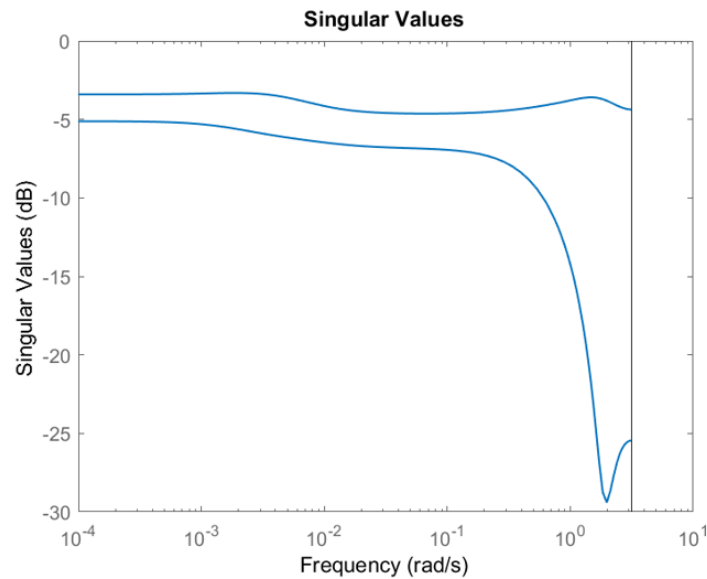
Figure 6.1: The frequency behavior of the two singular values of the multiple-input-multiple-output linear data-driven APPJ model (See 4.6.2).

6.2.2 Multi-loop Control Structure

A block diagram depicting the multi-loop PI control scheme is shown in Figure 6.2. The linear subspace identified model is used for tuning of the PI controllers based on the internal model control (IMC) method [185]. To this end, the first-order response of each output to its paired input was characterized using the linear subspace model. The first-order transfer functions mapping each input to each output were then used to explicitly derive expressions for each controller. The tuning parameters of both PI controllers are given in Appendix
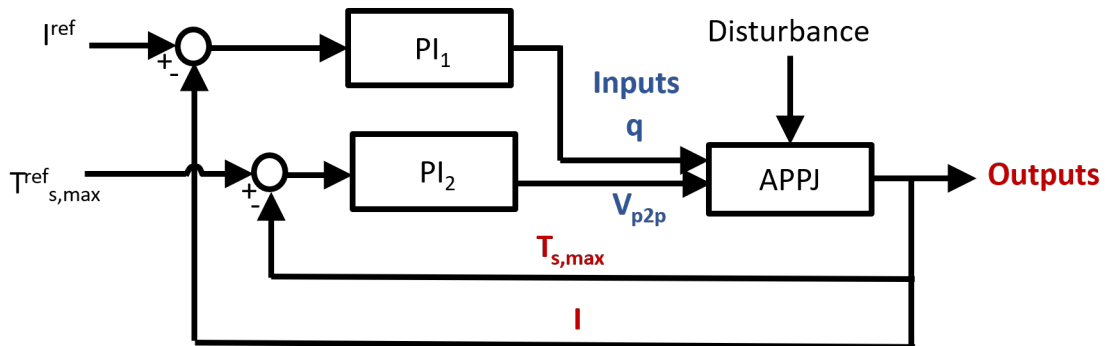
Figure 6.2: Block diagram of the PI control scheme

(a) Outputs   (b) Inputs
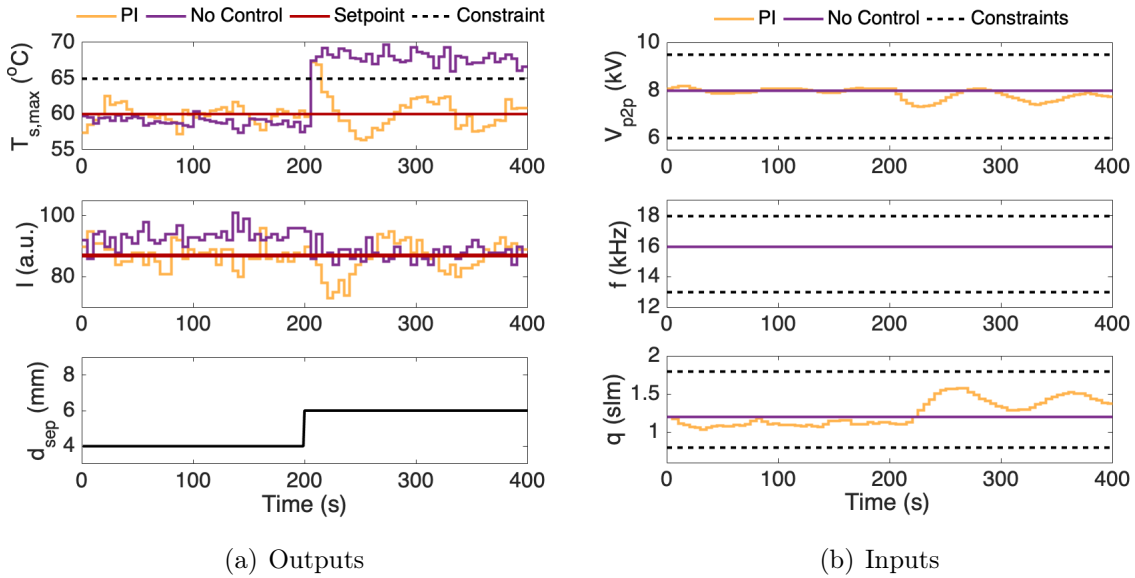
Figure 6.3: The APPJ behavior in presence of a step change in the device tip-to-surface separation distance at 200 s with no feedback control and with feedback control using the PI scheme: (a) outputs — maximum temperature $T_{s,max}$ and total optical intensity of plasma I at the surface and (b) manipulated inputs — peak-to-peak voltage V_{p2p}, frequency of excitation f, and He mass flow rate q.

D, Table D.4. Input saturation was implemented to the PI controllers through addition of antiwindup effect [183], so that the manipulated inputs would always remain within the bounds of the linear operating region.

6.2.3   Results

First, the performance of the multi-loop PI control strategy in rejecting the disturbance in jet-tip-to-substrate separation distance is demonstrated. Two APPJ runs were performed: no feedback control was applied in the first run, while the PI control scheme of Figure 6.2 was implemented in the other run. In both experiments, the APPJ was allowed to settle nearly at the nominal operating condition reported in Section 4.6.2 before marking the onset of the runs. The manipulated inputs were kept at their nominal values in the run with no feedback control. The results of APPJ runs are shown in Figure 6.3. A step change of magnitude 2 mm was applied to the device tip-to-surface separation distance d_{sep} at 200 s. That is, the APPJ was moved away from the target surface at 200 s. The step change in d_{sep} leads to a sharp increase in the maximum temperature $T_{s,max}$ and a sharp decrease in the total optical intensity I (see Figure 6.3(a)). This somewhat counter-intuitive behavior can be attributed to radial contraction of the plasma, resulting in an increase in $T_{s,max}$, which is associated with increased in-mixing of the surrounding air that apparently contributes to the decrease

in emission intensity I.

Figure 6.3(a) shows that the PI control scheme can follow setpoints of $T_{s,max}$ and I closely throughout the run. In particular, after the step change in d_{sep} perturbed the APPJ operation, the PI controller was able to bring both $T_{s,max}$ and I back to their respective setpoints. On the other hand, when the manipulated inputs were kept constant at their nominal values in the APPJ run with no control (see Figure 6.3(b)), the step change in d_{sep} steered temperature away from its setpoint to an extent that can be unacceptable, for example, for safe operation of the APPJ. In the run with no control, the temperature consistently violated the chosen constraint of 65 °C after 200 s. However, note after the disturbance is applied the PI control scheme results in an oscillatory response. This can be partially ascribed to controller tuning but also to the interference of the two independently designed PI control loops with each other. This is a result of the tightly coupled nature of the APPJ dynamics, i.e., both manipulated variables influence both of the controlled outputs.

A notable observation in Figure 6.3(a) is the difference in the initial behavior (i.e., first few seconds) of the two runs despite applying identical inputs to the APPJ. This can be ascribed to the intrinsic variability of the plasma characteristics and/or unknown exogenous disturbances, which can impede reproducible operation of the APPJ. The results in Figure 6.3(a) suggest that the multi-loop PI control strategy can allow significant improvement over operation in absence of control. However, the multi-loop PI control strategy also has some shortcomings, particularly the interference between the two controllers resulting in the observed oscillatory response can be problematic.
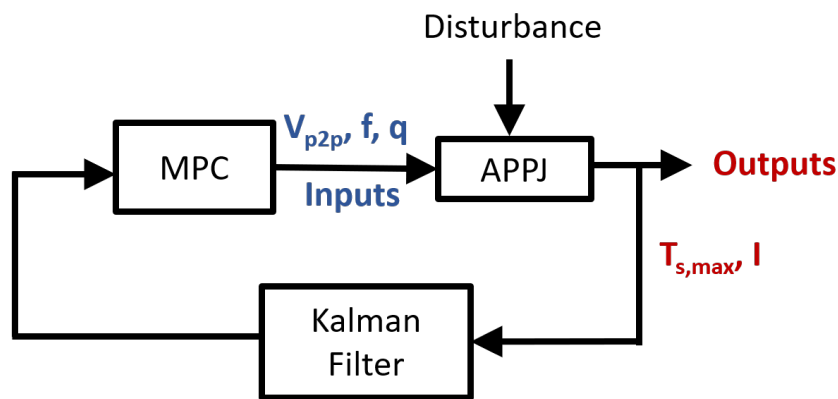
Figure 6.4: Block diagram of the MPC control scheme.

6.3 Offset-free Linear MPC Design

MPC is widely used for advanced control of multivariable systems with constraints and multiple (possibly competing) control objectives (e.g., see [184], [192]). The key notion of MPC is to optimize the predicted behavior of a system over a horizon in terms of some user-specified performance criteria, while imposing constraints on the system state and input variables [34], [35]. To incorporate measurement feedback into MPC, the online system information obtained at every measurement sampling time is used to initialize the underlying system model in MPC. This is known as *receding-horizon control*, which provides MPC with some degree of robustness to system uncertainties and unmeasured disturbances.

The optimal control problem is commonly formulated to drive the system to desired input and output targets $(\bar{u}, \bar{y})$. If the system model were perfect, keeping the inputs constant at $\bar{u}$ would ensure that the system goes to $\bar{y}$ at steady state. However, due to model uncertainties and unmeasured system disturbances, integral action (leading to zero $e(t)$) is not guaranteed in the standard formulation of MPC.

An MPC scheme with integral action, commonly referred to as *offset-free MPC* [193], is adopted for the APPJ to ensure adequate disturbance rejection. The offset-free MPC scheme requires the system model be updated with measurement feedback information through two mechanisms: (i) incorporation of an integrating disturbance model and (ii) state and disturbance estimation based on measured outputs. The disturbance model in offset-free MPC takes the form

$$
\begin{aligned}
\begin{bmatrix} x_{k+1} \\ d_{k+1} \end{bmatrix} &= \begin{bmatrix} A & B_d \\ 0 & I \end{bmatrix} \begin{bmatrix} x_k \\ d_k \end{bmatrix} + \begin{bmatrix} B \\ 0 \end{bmatrix} u_k \\
y_k &= \begin{bmatrix} C & C_d \end{bmatrix} \begin{bmatrix} x_k \\ d_k \end{bmatrix},
\end{aligned}
\tag{6.8}
$$

where d_k is the unknown integrating disturbance and the matrices B_d and C_d define the disturbance model — often chosen to be $(B_d = I, C_d = 0)$ or $(B_d = 0, C_d = I)$ corresponding to the pure input or output disturbance models, respectively. Note that estimates of the states and disturbances, denoted by $\hat{x}_{k|k}$ and $\hat{d}_{k|k}$, respectively, are needed to initialize the MPC at every measurement sampling time. Subscript $k|k$ denotes the estimate at time instant k, given the information at the same time instant. For the estimation, a Kalman filter was used in this work [194]; see the MPC block diagram in Figure 6.4.

The desired input and output targets $(\bar{u}, \bar{y})$ should be updated based on the disturbance estimates. Constraints on inputs and outputs, described by

$$
\begin{aligned}
F u_k &\leq f \\
H y_k &\leq h,
\end{aligned}
$$

with matrices F and H casting the respective linear combinations of inputs and outputs below the vectors f and h, may prevent the system from reaching the desired steady state. Thus, a *target calculator* was used to find a feasible steady state (y_s, x_s, u_s) such that y_s and u_s are, respectively, as close to $\bar{y}$ and $\bar{u}$ as possible. The target calculator can be formulated

as the following mathematical program with a least-squares objective

$$\min_{y_s, x_s, u_s} \quad (y_s - \bar{y})^\top \tilde{Q}_s (y_s - \bar{y}) + (u_s - \bar{u})^\top \tilde{R}_s (u_s - \bar{u})$$

$$\text{s.t.} \quad \begin{bmatrix} A - I & B \\ C & 0 \end{bmatrix} \begin{bmatrix} x_s \\ u_s \end{bmatrix} = \begin{bmatrix} -B_d \hat{d}_{k|k} \\ y_s - C_d \hat{d}_{k|k} \end{bmatrix} \tag{6.9}$$

$$Fu_s \leq f$$

$$Hy_s \leq h,$$

where $\tilde{Q}_s$ and $\tilde{R}_s$ are (user-specified) weight matrices. The optimization problem (6.9) is a quadratic program (QP), which can be solved using standard methods. To drive the system toward the input and output targets computed from (6.9), the optimal control problem in the designed MPC was formulated in terms of the deviation variables

$$w_j = \hat{x}_{k+j|k} - x_s, \qquad v_j = u_{k+j|k} - u_s. \tag{6.10}$$

Here, j refers to the time index of the MPC prediction, whereas k is the time index of the operation i.e., the real time. Using the fact that $x_s = Ax_s + Bu_s + B_d \hat{d}_{k|k}$, the system dynamics can be described by

$$\hat{x}_{k+j+1|k} - x_s = A\hat{x}_{k+j|k} + Bu_{k+j|k} + B_d \hat{d}_{k|k} - x_s$$

$$\longrightarrow w_{j+1} = Aw_j + Bv_j, \tag{6.11}$$

so that the optimal control problem takes the form of the following regulator problem

$$\min_{v_0, v_1, \dots, v_{N-1}} \quad \sum_{j=0}^{N} w_j^\top Q w_j + v_j^\top R v_j \tag{6.12a}$$

$$\text{s.t.} \quad w_{j+1} = Aw_j + Bv_j \tag{6.12b}$$

$$w_0 = \hat{x}_{k|k} - x_s \tag{6.12c}$$

$$Fv_j \leq f - Fu_s \tag{6.12d}$$

$$HCw_{j+1} \leq h - H(Cx_s + C_d \hat{d}_{k|k}) \tag{6.12e}$$

$$\forall j = 0, 1, \dots, N - 1.$$

In the optimal control problem, the objective function (6.12a) is the sum of weighted output deviations from their target and weighted input deviations from their target over the prediction horizon N. Q is defined by $Q = C^\top \bar{Q}C$, where $\bar{Q}$ specifies the output penalty weight. R represents the input penalty weight. The system dynamics are enforced through the equality constraints (6.12b) and (6.12c). Lastly, the input and output constraints are enforced over the prediction horizon through (6.12d) and (6.12e), respectively. The MPC algorithm can be summarized as follows:

1. Obtain state/disturbance estimates $\Longrightarrow (\hat{x}_{k|k}, \hat{d}_{k|k})$.
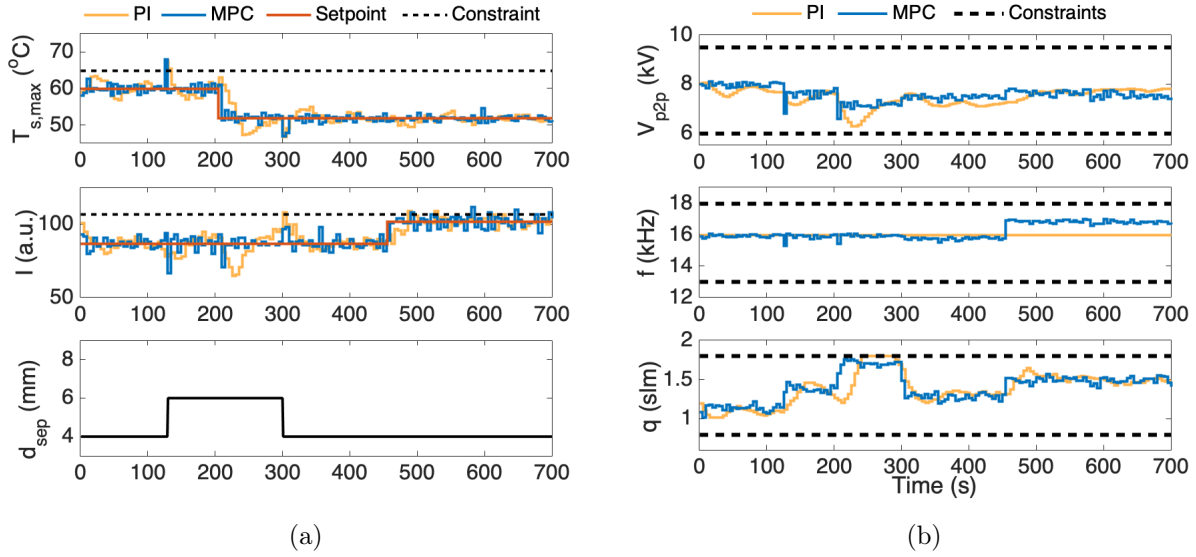
Figure 6.5: The APPJ behavior under feedback control with the PI control and MPC schemes in the presence of setpoint changes as well as a temporary step change of magnitude 2 mm in the device tip-to-surface separation distance: (a) outputs — maximum temperature $T_{s,max}$ and total optical intensity of plasma I at the surface and (b) manipulated inputs — peak-to-peak voltage V_{p2p}, frequency of excitation f, and He mass flow rate q.

2. Determine steady-state target from (6.9) $\implies (y_s, x_s, u_s)$.

3. Solve the regulation problem (6.12) $\implies (v_0^\star, \ldots, v_{N-1}^\star)$.

4. Apply first optimal input to system $\implies u_k = v_0^\star + u_s$.

5. Repeat for $k \leftarrow k + 1$.

Here, the input and output constraints are defined as $y_k \leq y_{max}$ and $u_{min} \leq u_k \leq u_{max}$ through proper choice of F, f, H, and h in (6.12). The maximum temperature and the total optical intensity of plasma at the surface are constrained by setting $y_{max} = [65\,°C, 107\,\text{a.u.}]^\top$. The input bounds $u_{min} = [6\,\text{kV}, 13\,\text{kHz}, 0.8\,\text{slm}]^\top$ and $u_{max} = [9.5\,\text{kV}, 18\,\text{kHz}, 1.8\,\text{slm}]^\top$ are selected to ensure that the APPJ operation remains within the linear region for which the system model is developed (see Section 4.6.2). The MPC parameters are given in Appendix D, Table D.7. The MPC algorithm is implemented using the CasADi interface [195] with the qpOASES solver [196]. Both the PI control and MPC schemes were implemented on the single-board computer in Python, with a measurement sampling rate of 5 s.

6.3.1   Results: PI Control versus Linear MPC

The performance of the PI control and MPC schemes are evaluated in terms of setpoint tracking for the maximum temperature $T_{s,max}$ and the total optical intensity of plasma I at the surface, while accommodating the effects of step changes in the device tip-to-surface separation distance d_{sep}. The step changes in d_{sep} can be viewed as deterministic disturbances perturbing the APPJ operation. In all the real-time control experiments, the APPJ nearly reached the nominal operating condition before marking the onset of runs. All experiments are repeated three times to examine the reproducibility of results. Figure 6.5 shows the results of the PI control and MPC runs in which d_{sep} increased by 2 mm at 130 s, followed by a decrease of 8°C in the temperature setpoint at 200 s, a decrease of 2 mm in d_{sep} at 300 s, and finally an increase of 15 a.u. in the total optical intensity setpoint at 450 s. The designed setpoint trajectory represents a clinically relevant scenario, where it is typically desired to lower the thermal effects of the APPJ while increasing its non-thermal effects (characterized by I in this work). The singular value decomposition analysis performed using the linear subspace identified model (see Section 4.6.2) indicated that moving $T_{s,max}$ and I in opposite directions presents an operational challenge due to the high degree of coupling between the temperature and the intensity of plasma at the surface.

Figure 6.5(a) shows that the increase in the separation distance d_{sep} at 130 s instantaneously leads to spikes in $T_{s,max}$ and I in opposite directions. The spike in $T_{s,max}$ violated the constraint of 65 °C. The slow rejection of the step change in d_{sep} by both control schemes at 130 s can be attributed to the slow measurement sampling rate (i.e., 5 s) relative to the system dynamics. As soon as new measurements becomes available, both control schemes take corrective action to drive $T_{s,max}$ and I back to their respective setpoints, even though the MPC scheme showed a faster response. For the remainder of the run, Figure 6.5(a) suggests that the MPC scheme exhibits a faster and a smoother response to the setpoint changes as well as to the step changes in d_{sep} than the PI control scheme. This can be ascribed to the fact that MPC uses a system model to systematically account for the interactions between all the APPJ inputs and outputs. However, the two PI controllers were designed independently and thus disregard the coupling between the outputs $T_{s,max}$ and I, leading to undesired closed-loop interactions that manifested itself in terms of a somewhat oscillatory response. While detuning the PI controllers can partly reduce their closed-loop interactions, the controllers would become less aggressive in rejecting disturbances, which can be undesirable in practice. The performance of the PI control and MPC schemes for setpoint tracking are quantified in terms of the setpoint tracking error

$$\int_0^{t_f} \left(y(\tau) - y^{\mathrm{ref}} \right) d\tau,$$

where y^{ref} denotes the setpoint trajectory. The analysis reveal that the MPC scheme resulted in approximately 44% improvement in setpoint tracking for $T_{s,max}$ and I as compared to the PI control scheme. In particular, the plasma intensity I at the surface deviates as much as 20 a.u. from its setpoint under PI control, which can be detrimental to safe and

(a)   (b)
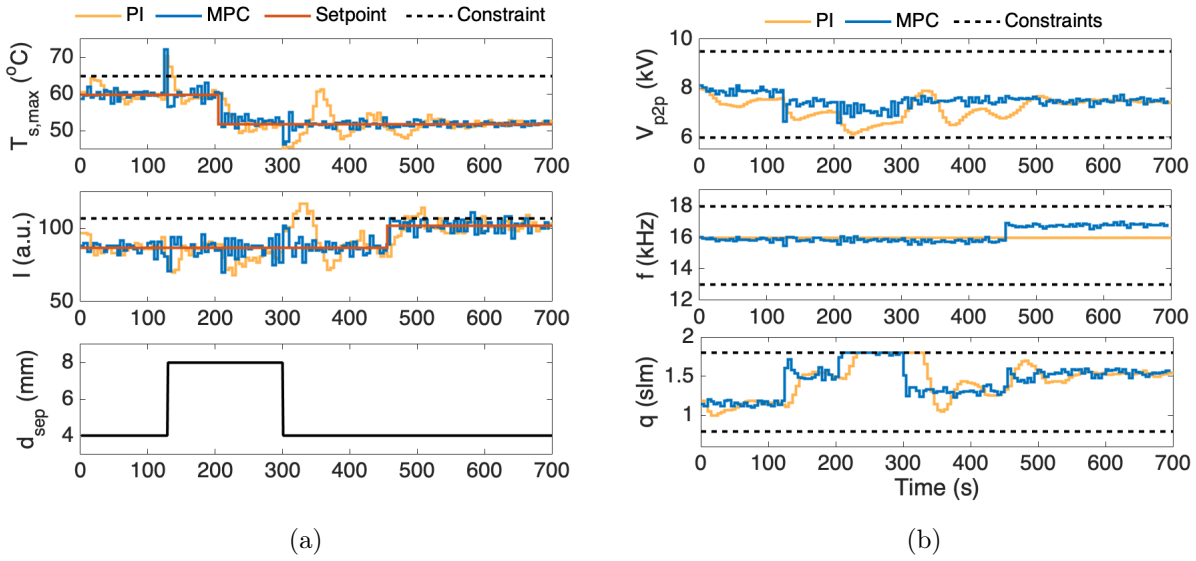
Figure 6.6: The APPJ behavior under feedback control with the PI control and MPC schemes in the presence of setpoint changes as well as a temporary step change of magnitude 3 mm in the device tip-to-surface separation distance: (a) outputs — maximum temperature $T_{s,max}$ and total optical intensity of plasma I at the surface and (b) manipulated inputs — peak-to-peak voltage V_{p2p}, frequency of excitation f, and He mass flow rate q.

effective application of the APPJ. Under the setpoint changes and disturbances considered in Figure 6.5, both control schemes show comparable performance in handling the (arbitrarily chosen) constraints on $T_{s,max}$ and I, even though PI control generally cannot account for constraints. Due to the proximity of the setpoint of I to its constraint after 450 s, a slight degree of constraint violation is observed in both control runs. This can be attributed to process and measurement noise, which are not accounted for in the deterministic formulations of the control schemes designed in this work. As expected, Figure 6.5(b) indicates that both the PI control and MPC schemes keep the manipulated inputs within their specified bounds at all times during the run.

In order to further evaluate the performance of the PI control and MPC schemes, a larger step change of magnitude 3 mm in the separation distance d_{sep} is applied between 130 s to 300 s while the setpoints for $T_{s,max}$ and I are kept the same as in the previous case. Note that the d_{sep} in hand-held APPJs is likely to constantly fluctuate during the operation. Figure 6.6 shows the results of the PI control and MPC runs. As in the previous case shown in Figure 6.5, the step change in d_{sep} leads to spikes in I and particularly in $T_{s,max}$, but with larger magnitudes and with a more significant temperature constraint violation (see Figure 6.6(a)). Increasing the measurement sampling rate (i.e., shorter sampling intervals) may enable both controllers to more effectively accommodate the step increases in the separation distance, especially when their magnitude is large. After the decrease in the separation distance to
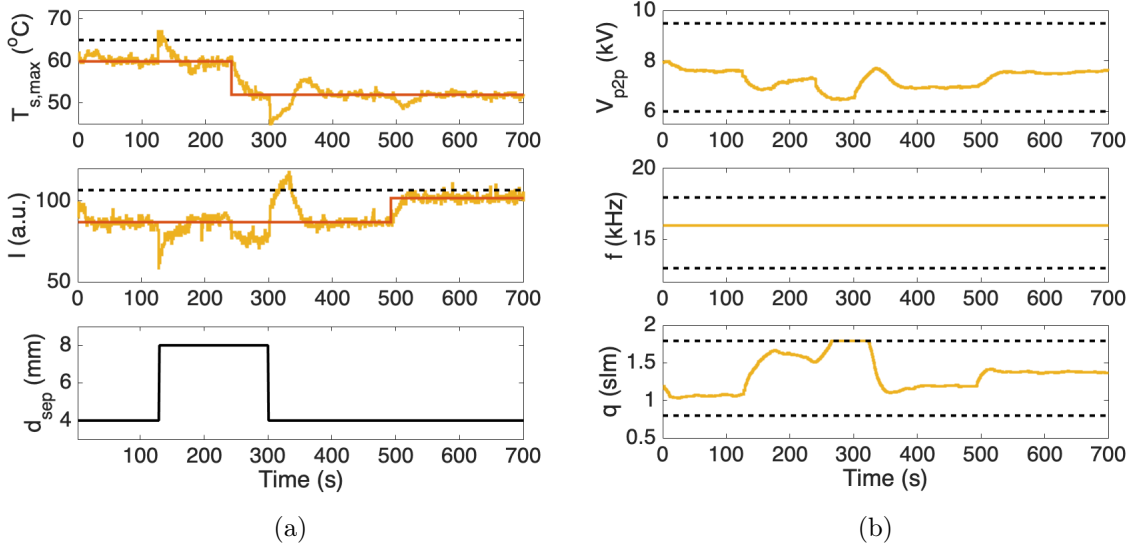
Figure 6.7: The APPJ behavior under feedback control with the PI control and MPC schemes in the presence of setpoint changes as well as a temporary step change of magnitude 3 mm in the device tip-to-surface separation distance: (a) outputs — maximum temperature $T_{s,max}$ and total optical intensity of plasma I at the surface and (b) manipulated inputs — peak-to-peak voltage V_{p2p}, frequency of excitation f, and He mass flow rate q.

its original value at 300 s, the MPC scheme is able to adequately handle the step change in d_{sep} and maintain $T_{s,max}$ and I at their setpoints. The PI control scheme however exhibits sharp variations in $T_{s,max}$ and I, followed by a notable oscillatory behavior in both outputs. After 300 s, the optical intensity I at the surface increases by as much as 35 a.u. under PI control, violating the intensity constraint by approximately 15 a.u.. In the context of medical applications, such a drastic violation of the permitted operating range can lead to over-exposure of the target surface to the plasma, potentially causing irreversible damage. Likewise, the temperature $T_{s,max}$ deviates from its setpoint for as much as 10°C under PI control, which can cause discomfort during the treatment. Figure 6.6 suggests that the MPC scheme considerably outperforms the PI control scheme both in terms of setpoint tracking and constraint handling, with fast and smooth response to all changes in the setpoints and the separation distance (except the d_{sep} change at 130 s). The MPC scheme result in 48 % improvement in setpoint tracking, while the PI control scheme leads to approximately 70 % more constraint violations of larger magnitudes. Even when a faster measurement sampling rate of 1 s was used for the PI control scheme, as shown in Figure 6.7, the control performance is inferior to that of the MPC scheme with the sampling rate of 5 s.

6.4 Conclusions

The results in this chapter indicate that even a carefully designed proportional-integral control system using a sophisticated model-based tuning as IMC method may not be adequate for dealing with the complex dynamics of APPJs. PI controllers cannot account systematically for the multivariable dynamics of APPJs that arise from using multiple manipulated inputs for inducing multiple plasma effects. The design of individual PI controllers relies on pairing the system inputs and outputs based on the open-loop response of the system, which cannot capture the closed-loop interactions of the PI controllers and therefore may lead to reduced closed-loop performance.

On the other hand, model predictive control provides a versatile framework for feedback control of APPJs. MPC directly incorporates a system model and therefore can systematically account for the interactions between the multiple inputs and multiple outputs of the system. In addition, MPC can explicitly handle system constraints, so that it can be ensured that the system remains within an acceptable operating range during the operation. This can be a particularly important consideration for medical applications of APPJs, as the stringent requirements on safe and consistent APPJ operation can be explicitly defined and enforced through constraints. Moreover, as discussed in the following chapters, the MPC framework can be readily extended to accommodate nonlinear and integrating dynamics, such as those arise in the problem of dose delivery. For the model kHz-excited APPJ used in this work, MPC consistently showed a superior performance to PI control in terms of setpoint tracking and constraint handling in the presence of step disturbances.

A key component of any MPC design is a system model that can adequately describe the system dynamics relevant to the control problem while being computationally amenable to online computations. The complexity of MPC largely depends on the complexity of its underlying system model. This chapter focused on the relatively basic MPC design based a data-driven, linear system model that is valid over a narrow operating range of the APPJ at hand. The use of the linear model allowed a consistent performance comparison with PI control, which is an inherently linear control method. However, the linear model limits the potential effectiveness of MPC. The next chapter focuses on MPC design using nonlinear lumped-parameter, physics-based models.

Chapter 7

Nonlinear Model Predictive Control based on Physics-Based Lumped-Parameter Models

APPJ characteristics and their effects on the substrate give rise to nonlinear dynamics. Therefore, linear models can describe APPJ behavior only over narrow operating regions. Particularly, the problem of dose delivery has nonlinear characteristics that are challenging to address with linear control strategies. In this chapter, a nonlinear model predictive control (NMPC) strategy is developed based on lumped-parameter physics-based descriptions of the APPJ. The effectiveness of the NMPC strategy is investigated in simulations and experimental studies for setpoint tracking and multicomponent dose delivery.[1]

7.1   Introduction

The linear MPC strategy investigated in the previous chapter used a data-driven linear model to describe APPJ dynamics over a relatively narrow range of operating conditions. However, nonlinear behavior is prevalent in APPJs and and their applications. For example, depending on the Reynolds number of the gas flow, the flow can become turbulent thereby introducing nonlinear hydrodynamic fluctuations [117]. The plasma electrodynamics also introduce significant nonlinearities. In presence of small admixtures of H_2O, He APPJs are shown to exhibit as many as five different modes of operation depending on the gas flow and composition and, in particular, the magnitude of the applied voltage [111]. Moreover, the biological responses of treated substrates to APPJ effects can be nonlinear. The thermal dose metrics defined in Section 4.3 exemplifies this behavior. Therefore, use of nonlinear models in conjunction with MPC can enable capturing the behavior of some key variables such

---

[1]Part of the results presented in this chapter is adopted from published work [197]

as discharge current and power, and systematically addressing the nonlinear dose delivery
problem.

   This chapter presents a nonlinear model predictive control (NMPC) [34], [35] strategy,
for setpoint tracking and delivery of a multicomponent dose with the APPJs while ensuring
safe operation of the jet (e.g., arc-free) in the presence of disturbances. NMPC seeks to
optimize the APPJ performance for multicomponent dose delivery using the knowledge of
the system dynamics, described by a mathematical model (see Section 4.5), as well as system
constraints. NMPC can explicitly account for the nonlinear (often cumulative) nature of
plasma dose mechanisms and systematically trade-off between multiple (possibly conflicting)
dose delivery mechanisms. In addition, the inclusion of system constraints into NMPC will
allow for restricting the APPJ operation within a predetermined operating range to ensure
safe and reproducible dose delivery.

   The, NMPC strategy is first studied in simulations for feedback control of a radio-
frequency (RF) APPJ in pure argon. NMPC is then applied to the experimental kHz-APPJ
setup He. To address the computational requirements of online optimization in NMPC,
physics-based, lumped-parameter models are used in conjunction with NMPC (see Section
4.5 and Appendix C.2). These models describe the electrical properties of plasma as well
as the mass and heat transfer along the gas plume. Provisional dose metrics (see Section
4.3) are used to quantify the thermal and nonthermal energy effects delivered to a tar-
get substrate. The closed-loop performance of the NMPC is compared to that of a basic
proportional-integral (PI) control system, which is designed using the internal model control
(IMC) method. [185]. Two case studies are considered in simulations and experiments: (i)
rejection of disturbances in jet-tip-to-surface separation distance, and (ii) multicomponent
dose delivery.

7.2 Simulation Study: NMPC on an RF-APPJ in Ar

7.2.1 State-space representation of the lumped-parameter model

The physics-based, lumped-parameter model of the RF-APPJ with the target substrate is
described by the set of nonlinear, differential algebraic equations given in Appendix C.2;
see Figure 4.8. For the NMPC design, the system model is compactly represented by a
discrete-time, state-space description

$$
\begin{aligned}
x_{k+1} &= f(x_k, z_k, u_k, \theta), \quad x_0 = x(0) \\
0 &= g(x_k, z_k, u_k, \theta),
\end{aligned}
\tag{7.1}
$$

where k is the time index, $x_k = [T_{s,max} \ \mathrm{CEM_T} \ \mathrm{CEM_P}]^\top$ is the vector of differential state
variables with the initial conditions x_0, $z_k = [T_{g0} \ i_p \ P \ T_g(z) \ m_{\mathrm{Ar}}(z)]^\top$ is the vector of
algebraic state variables, $u = [V_A \ v_{in}]^\top$ is the vector of RF-APPJ inputs, θ is the vector of
model parameters (given in C.2.4), and f and g are the nonlinear differential and algebraic
model equations, respectively. Variations in the separation distance between the tip of the

tube and the substrate (d_{sep}) act on the system as unmeasured disturbances. In the next
section, the nonlinear state-space model (7.1) is used for designing the NMPC.

7.2.2   Nonlinear Model Predictive Control

NMPC involves solving the following optimal control problem at every time instant k that
the system states x_k are measured [35]:

$$\min_{\mathbf{u}} J(x_k, \mathbf{u})$$

$$\begin{aligned}
\text{subject to:} \quad & \bar{x}_{i+1} = f(\bar{x}_i, \bar{z}_i, u_i, \theta), & i = 0, ..., N_p - 1 & \quad (7.2\text{a}) \\
& 0 = g(\bar{x}_i, \bar{z}_i, u_i, \theta), & i = 0, ..., N_p & \quad (7.2\text{b}) \\
& l(\bar{x}_i, u_i, \bar{z}_i, \theta) \le 0, & i = 1, ..., N_p & \quad (7.2\text{c}) \\
& u_i \in \mathcal{U}, & i = 0, ..., N_c - 1 & \quad (7.2\text{d}) \\
& \bar{x}_0 = x_k, & & \quad (7.2\text{e})
\end{aligned}$$

where $\mathbf{u} = [u_0, ..., u_{N_c-1}]^\top$ is the control policy over the control horizon N_c, which comprises
the decision variables of the optimization problem (7.2); N_p is the prediction horizon over
which the system behavior is predicted ($N_c \le N_p$); (7.2a)-(7.2b) represent the system model,
with $\bar{x}$ and $\bar{z}$ denoting the predicted differential and algebraic state variables, respectively
(see (7.1)); J is the objective function, defined in terms of the control objective(s); l denotes
(possibly nonlinear) functions representing the state constraints; and $\mathcal{U}$ is a convex, compact
set defining the input constraints. The optimal control policy, the optimal solution to (7.2),
is denoted by $\mathbf{u}^*$. The prediction and control horizons N_p and N_c are commonly treated as
the tuning parameters of NMPC.

In this section, two NMPC controllers are designed for the RF-APPJ, as described in the
following case studies.

Case Study I (disturbance rejection): The goal of this case study is to maintain
the substrate temperature $T_{s,max}$ and the plasma power P at user-specified setpoints, while
counteracting the effects of a step change in the separation distance d_{sep}. In this case study,
the control objective function in the optimization problem (7.2) is defined by

$$J = \sum_{i=0}^{N_P} \left(T_{s,max,i} - T_{s,max}^{\text{ref}}\right)^2 + w\left(P_i - P^{\text{ref}}\right)^2, \qquad (7.3)$$

where N_P is the prediction horizon, $T_{s,max}^{\text{ref}} = 315$ K and $P^{\text{ref}} = 5$ W are the setpoints for the
substrate temperature and plasma power, respectively, and w is a constant chosen such that
both setpoint tracking objectives have an equal weight in the objective function (7.3). The
prediction and control horizons in the optimization problem (7.2) are chosen as 20 and 3,
respectively. State constraints are imposed to maintain the plasma current and power below
critical values in order to avoid potentially damaging conditions (e.g., arcing) as well as to

keep the substrate temperature within a comfort level. Accordingly, the state constraints
are defined by

$$\begin{bmatrix} T_{s,max} \\ i_p \\ P \end{bmatrix} \leq \begin{bmatrix} 316 \text{ K} \\ 2.5 \text{ mA} \\ 10 \text{ W} \end{bmatrix}. \tag{7.4}$$

In addition, the APPJ input values must be maintained within the following bounds

$$\begin{bmatrix} 100 \text{ V} \\ 8 \text{ m/s} \end{bmatrix} \leq \begin{bmatrix} V_A \\ v_{in} \end{bmatrix} \leq \begin{bmatrix} 700 \text{ V} \\ 35 \text{ m/s} \end{bmatrix}, \tag{7.5}$$

where the lower input bounds correspond to the minimum input values required for sustain-
ing the plasma and the upper input bounds correspond to the physical limitations of the
equipment. The rates of input change are also bounded as

$$\begin{bmatrix} \Delta V_A \\ \Delta v_{in} \end{bmatrix} \leq \begin{bmatrix} 300 \text{ V} \\ 13.5 \text{ m/s} \end{bmatrix}. \tag{7.6}$$

Case Study II (dose delivery): The goal of this case study is to safely deliver pre-
scribed thermal and nonthermal energy doses to the substrate within a given treatment
time of 150 s, without inflicting damage on the substrate. The control objective function is
formulated as

$$J = \left(\text{CEM}_{\text{T},N_t} - \text{CEM}_{\text{T}}^{\text{ref}}\right)^2 + w\left(\text{CEM}_{\text{P},N_t} - \text{CEM}_{\text{P}}^{\text{ref}}\right)^2, \tag{7.7}$$

where the time index N_t corresponds to the total treatment time 150 s, $\text{CEM}_{\text{T}}^{\text{ref}} = 9$ min and
$\text{CEM}_{\text{P}}^{\text{ref}} = 3$ min (corresponding to an equivalent fluence of 225 J/cm^2) are the prescribed
setpoints for the thermal and nonthermal energy doses, respectively, and w is a constant
weight. The control objective function (7.7) implies that the dose delivery problem requires
that the thermal and nonthermal energy dose accumulation reach their prescribed target at
the end of the treatment time. To ensure safe dose delivery, not only the plasma current
and power must be constrained to prevent mode transition, but also the dose accumulation
CEM_{T} and CEM_{P} must remain below prescribed limits at all times to avoid inflicting damage
on the substrate. Thus, the following state constraints are imposed

$$\begin{bmatrix} T_s \\ i_p \\ P \\ \text{CEM}_{\text{T}} \\ \text{CEM}_P \end{bmatrix} \leq \begin{bmatrix} 319 \text{ K} \\ 3.7 \text{ mA} \\ 12 \text{ W} \\ 10 \text{ min} \\ 5 \text{ min} \end{bmatrix}. \tag{7.8}$$

The input bounds and the bounds on the rates of input change in this case study are defined
as in (7.5)-(7.6). The interior-point optimization algorithm IPOPT [198] is used to solve
the optimization problem (7.2) in both case studies. The closed-loop performance of the
NMPC controllers in Case Studies I and II is compared to that of a more conventional
proportional-integral (PI) control system, as demonstrated in Section 7.2.4.[2]

---

[2]In this case study, the NMPC controller is implemented using a *shrinking* prediction horizon.

7.2.3 PI Controls

Sensitivity analysis is performed to assess the effect of each input on each output of the APPJ. Accordingly, the plasma power P is paired with the input voltage V_A and the substrate temperature $T_{s,max}$ is paired with the inlet flow velocity v_{in}. Since the dynamics of power deposition and gas heating in the dielectric tube are neglected relative to the substrate and dose accumulation dynamics (see 4.5), a proportional-only controller (excluding the integrating action) is used for regulating the plasma power. To enable a consistent comparison with the NMPC controllers, the internal model control (IMC) method [185] is used for optimal tuning of the PI controllers. To this end, the nonlinear state-space model (7.1) is used to characterize the first-order-plus-deadtime dynamics between the paired inputs and outputs. Thus, the same system model is used for designing the NMPC and PI controllers. The tuning parameters of the PI controllers are given in Appendix D.3. *Antiwindup* [183] is incorporated into the PI controllers to handle the input bounds considered in the NMPC controllers.

For Case Study I, the same setpoints as expressed in the control objective function (7.3) are used to design the PI controllers. On the other hand, the dose metrics CEM_T and CEM_P used in Case Study II cannot be readily incorporated into the PI controllers due to their non-decreasing, cumulative nature. Thus, the target doses CEM_T^{ref} and CEM_P^{ref} in (7.7) are translated into, respectively, their corresponding substrate temperature setpoint $T_{s,max}^{ref} = 318$ K and plasma power setpoint $P^{ref} = 6$ W for the prescribed treatment time 150 s (see (4.1) and (4.4)). The latter setpoints are then used for designing two PI controllers for substrate temperature and plasma power setpoint tracking. The closed-loop simulation results are discussed next.

7.2.4 Closed-loop Simulation Results and Discussion

The closed-loop control systems with the NMPC and the PI controllers are shown in Figure 7.1. In the closed-loop control simulation studies presented below, the nonlinear state-space model (7.1) is used to represent the true system.[3] In all simulations, the measurement sampling time is 5 s, that is, the measured system outputs are fed to the controller every 5 s.

Case Study I (disturbance rejection): This case study is designed to assess the ability of the NMPC controller and the PI control system to achieve setpoint tracking for the substrate temperature and plasma power while counteracting the effects of a step change in the separation distance between the tip of the tube and the substrate (i.e., d_{sep}). The separation distance undergoes a step change from 7.5 mm to 3 mm at time 50 s, as in [199]. The state constraints (7.4) are incorporated into the NMPC controller to ensure that the plasma properties remain within some prespecified thresholds. This can be important when the plasma has a tendency to transform into a spark or some other undesirable mode.

---

[3]In closed-loop control simulation studies, the model used as the true system is typically different from that used in the controller.

(a) NMPC controller
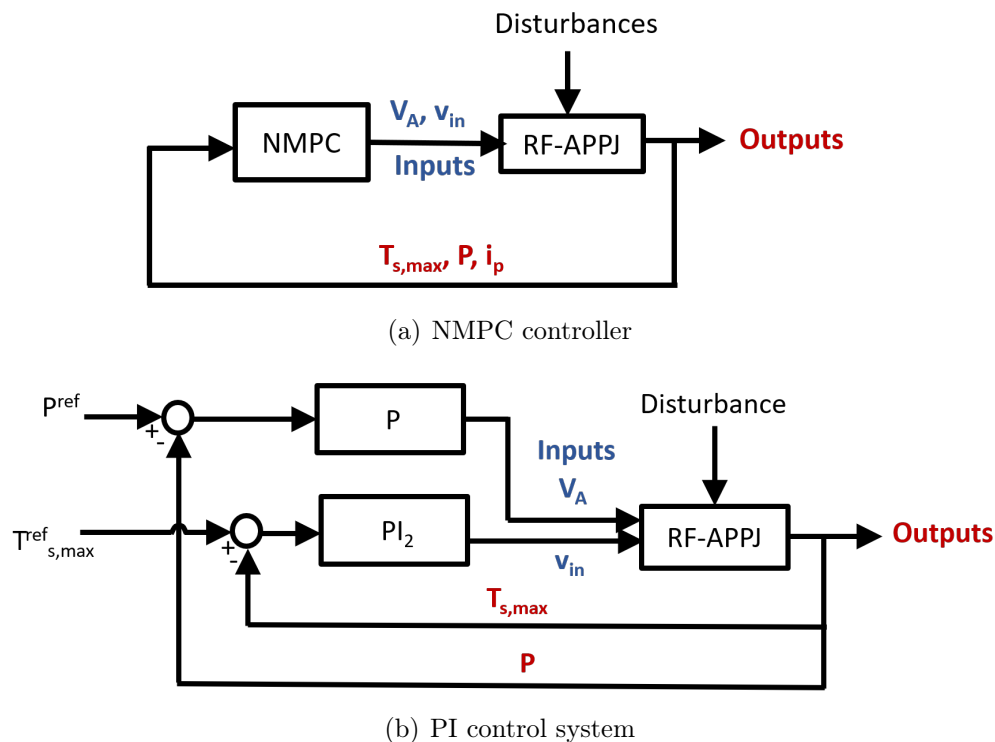
(b) PI control system

Figure 7.1: Block diagram of the closed-loop control systems for the RF-APPJ: (a) the
NMPC controller which uses measurements of maximum substrate temperature, plasma
current, and plasma power for manipulating applied voltage and inlet gas velocity, and
(b) the PI control system which is designed to achieve the same goals using two single-
input-single-output proportional (P) and proportional-integral (PI) controllers operating in
parallel.

The closed-loop simulation results are shown in Figure 7.2. The step change in d_{sep} at
50 s results in an increase in the plasma current (Figure 7.2(a)). The PI control system
can effectively maintain the substrate temperature and plasma power at their respective
setpoints after the step change in d_{sep} (Figure 7.2(a)). However, the plasma current exceeds
the specified current constraint of 2.5 mA. PI controllers cannot handle state constraints
to retain the jet operation within a desired operating region. Thus, when disturbances act
on the APPJ (in this case, the step change in d_{sep}), safe operation of the APPJ may be
compromised. The APPJ inputs (i.e., voltage amplitude and inlet gas velocity) computed
by the PI controllers are shown in Figure 7.2(b). The antiwindup property of the PI con-
trollers enables retaining the inputs within their admissible bounds. However, the PI control
system cannot systematically exploit the mutlivariable dynamics of the APPJ as the two PI
controllers operate independently from each other.

(a) Outputs

(b) Inputs
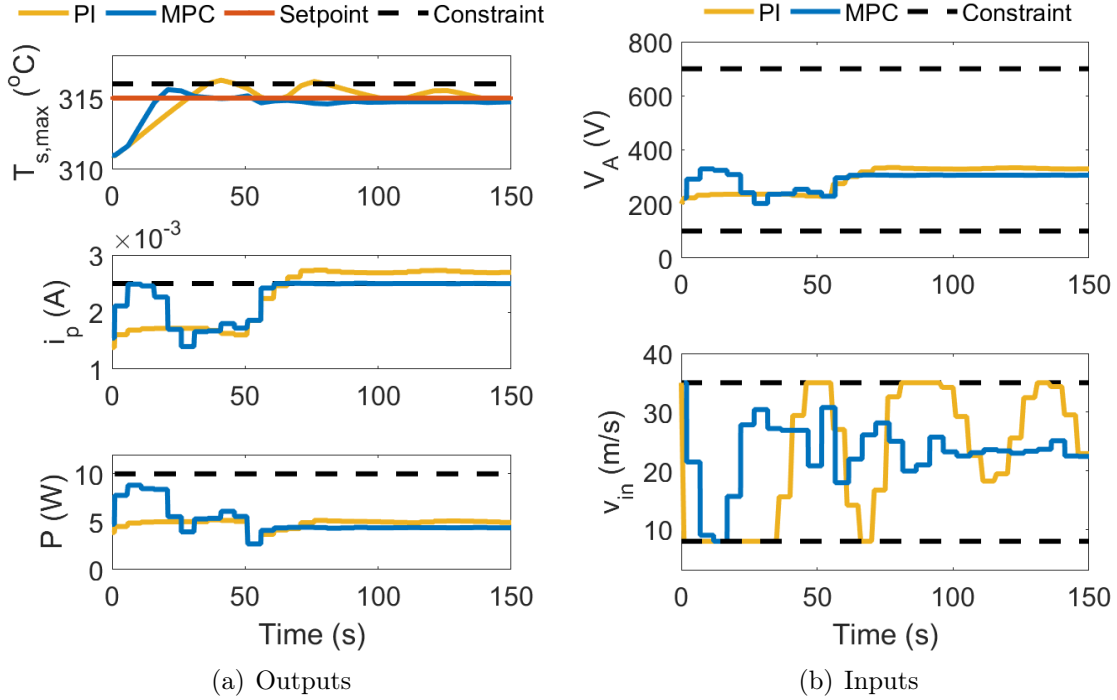
Figure 7.2: Closed-loop simulation results for the NMPC and the PI control system in Case Study I: (a) maximum substrate temperature, plasma current and, plasma power; and (b) voltage amplitude, and inlet gas velocity.

On the other hand, NMPC exploits the multivariable nature of system dynamics to achieve the control objectives. The NMPC controller simultaneously modulates both APPJ inputs V_A and v_{in} to achieve the setpoint tracking objective for the substrate temperature and plasma power (as defined in (7.3)). In comparison with the PI control system, the NMPC controller leads to more effective setpoint tracking for substrate temperature until the separation distance is changed at 50 s (see Figure 7.2(a)). After the step change in the separation distance, the performance of the NMPC controller slightly degrades due to the offset in setpoint tracking for $T_{s,max}$ and P. However, as shown in Figure 7.2(a), the NMPC controller can effectively fulfill the constraint on the plasma current in the presence of the step change in the separation distance (i.e., disturbance). The ability to handle state constraints is paramount for safe and reliable operation of the plasma jets, particularly in safety-critical applications such as in plasma medicine. State constraints can be motivated by various considerations for safe APPJ operation such as avoiding plasma mode transition via restricting the plasma state to a prespecified operating window, or accounting for requirements of the target substrate (e.g., a temperature range for comfortable treatment). Even though not demonstrated in this work, the slight offset in the setpoint tracking in Figure 7.2(a) can be completely eliminated using standard offset-free NMPC techniques, as
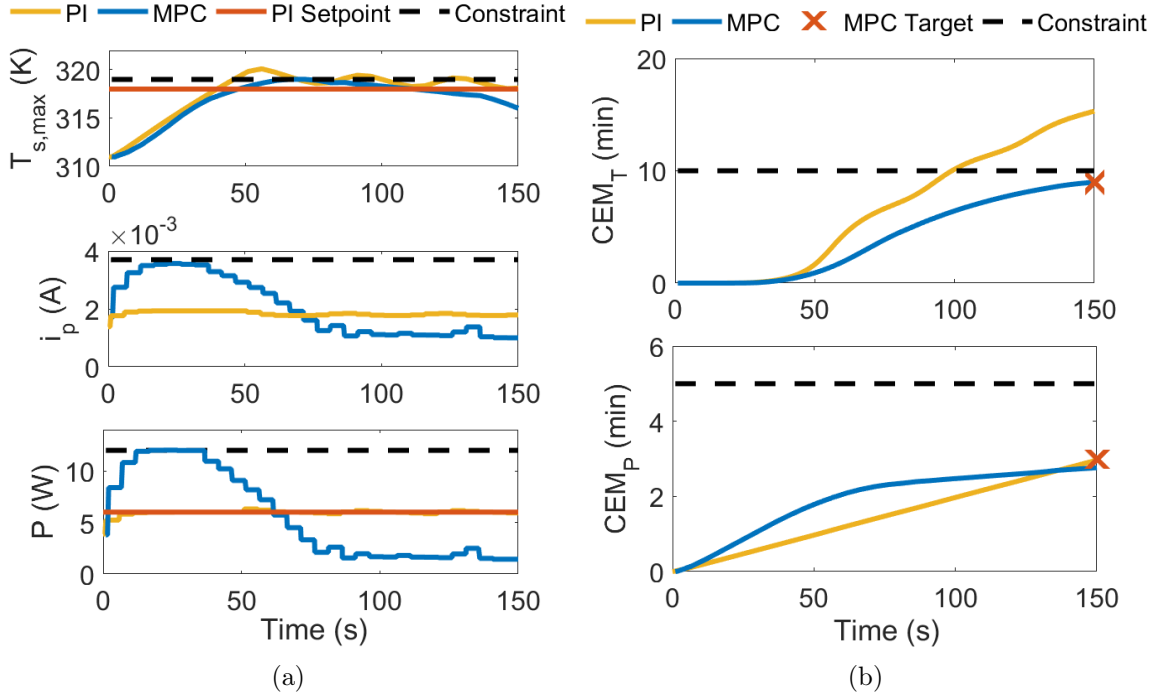
Figure 7.3: Closed-loop simulation results for the NMPC controller and the PI control system in Case Study II: (a) substrate temperature, (b) plasma current, (c) plasma power, (d) thermal dose CEM_T, and (e) nonthermal energy dose CEM_P.

in the previou chapter [193]. The key advantage of NMPC in this case study lies in its ability to realize multiple control objectives (setpoint tracking for $T_{s,max}$ and P) while handling constraints on the system variables (constraint on i_p) and bounds on the system inputs (bounds on V_A and v_{in}).

Case Study II (dose delivery): This case study aims to demonstrate the importance of advanced feedback control for safe and effective dose delivery. The objective is to deliver a target thermal dose CEM_T and nonthermal energy dose CEM_P to the substrate by the end of the treatment time 150 s. To avoid inflicting damage on the substrate, for example, due to undesired mode transition or arcing, the plasma power and current are constrained in the NMPC controller to remain below a certain threshold at all times during the APPJ operation (see expression (7.8)). In addition, upper constraints are imposed on CEM_T and CEM_P to prevent excessive dose delivery during the plasma treatment. The substrate temperature is also constrained, for example, to ensure comfort of a patient being treated. Note that the latter state constraints cannot be handled in the PI control system.

The closed-loop simulation results for the NMPC controller and the PI control system are shown in Figure 7.3. As discussed in Section 7.2.3, the PI controllers cannot readily accommodate the cumulative dose metrics (4.1) and (4.4). Consequently, the dose delivery
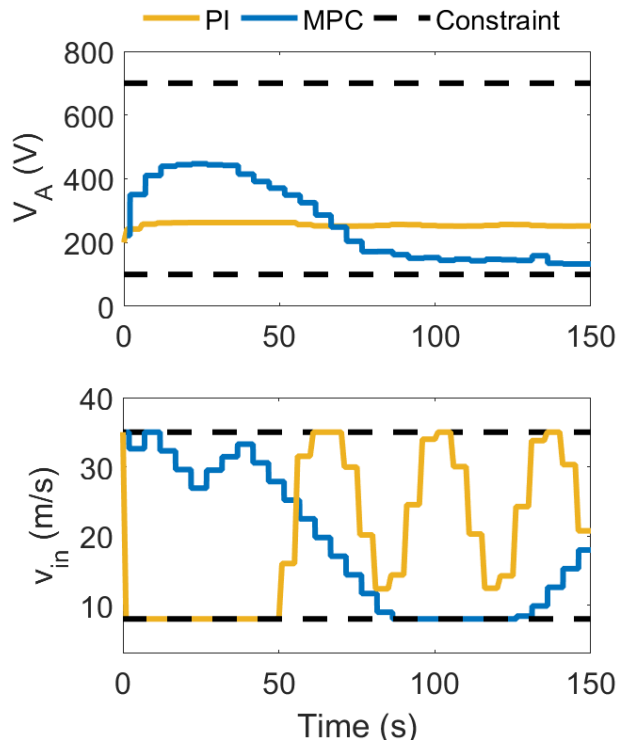
Figure 7.4: Input profiles computed by the NMPC controller and the PI control system in Case Study II: (a) applied voltage and (b) inlet gas velocity.

problem for the PI controllers is defined in terms of setpoint tracking for the substrate temperature $T_{s,max}$ and the plasma power P, the setpoints of which were determined based on the target dose levels for CEM_T and CEM_P to be delivered over 150 s. Figure 7.3(b) indicates that the PI control system fails to realize the dose delivery objective since the dose metric CEM_T exceeds its target level and constraint. While the nonthermal energy dose CEM_P is delivered in 150 s, the violation of the safety threshold on CEM_T can result in severe thermal damage to the substrate. Figure 7.3(a) shows that the constraint on the substrate temperature is also violated when the PI control system is used.

On the other hand, Figure 7.3 shows that the NMPC controller can effectively achieve the dose targets at 150 s while satisfying the comfort and safety constraints on the substrate temperature, plasma current, and plasma power. In the NMPC controller the dose requirements are defined in the objective function (7.7). Hence, they can be viewed as soft constraints, suggesting that their fulfillment is not guaranteed (in contrast to the safety constraints on states that are enforced at all times). This leads to a slight offset in the nonthermal dose CEM_P with respect to its target value (less than 10%). It is worth noting that it may not be possible to deliver any arbitrary combination of thermal and nonthermal dose due to the tight coupling between the thermal and nonthermal dose delivery mechanisms. However, NMPC enables achieving a trade-off between the two dose delivery mechanisms through

selection of the weight constant w in (7.7).

This case study demonstrates that NMPC can handle multiple cumulative (in this case, linear and nonlinear) dose metrics. This is likely to be paramount in plasma medicine, particularly in light of the time-integral nature of the dose metrics. Note that dose delivery is an intrinsically "integrating process" because once a part of the dose is delivered it cannot be removed from the substrate. NMPC allows for seeking trade-offs between multiple (possibly conflicting) dose delivery mechanisms in a systematic manner. The constraint handling ability of NMPC (Figure 7.3(a)) is crucial for ensuring safe and reliable operation of the APPJ since the plasma state can be restricted to a prespecified operating range. The control input profiles computed by the NMPC controller and the PI control system are shown in Figure 7.4. The NMPC and PI controllers result in different input profiles. However, both control strategies can effectively retain the control inputs within their bounds (see expression (7.5)), which were defined based on the physical limitations of the APPJ.

7.3 Experimental Investigation of NMPC on the kHz-APPJ in He

The simulation studies conducted on the RF-APPJ in the previous section are now adapted for the kHz-APPJ setup in He (see Chapter 3). The physics-based lumped-parameter model developed in Section 4.5 is used in conjunction with the NMPC. The performance of NMPC and PI control strategies are tested in real-time control experiments.

7.3.1 PI Controls

Two separate classical controllers are designed for control of $T_{s,max}$ and P. Using the physics-based lumped parameter model, sensitivity analysis was conducted to determine the appropriate input/output pairing. mass flow rate is found have little effect on power while both outputs are most sensitive to the applied voltage. Thus, helium mass flow rate (q) is coupled to the maximum substrate temperature ($T_{s,max}$) and applied voltage (V_{p2p}) is coupled to the power deposition (P). Both controllers are designed using IMC tuning rules [185] and were equipped with antiwindup [186]. The controller tuning used in experiments are given in Appendix D.5.

7.3.2 Nonlinear Model Predictive Control

As pointed out in Section 6.3, the system model does not perfectly capture the real system due to presence of unmeasured disturbances and uncertainties in the system model. Consequently, standard MPC formulations are not guaranteed to track setpoints in an offset-free manner. To deal with this mismatch, integrating action is conferred via an offset-free MPC strategy, based on an integrating disturbance model [193]. As the system dynamics are nonlinear an Extended Kalman Filter (EKF) is used to estimate unmeasured states and the

disturbances. EKF relies on a local linearization of the nonlinear system model for obtaining
estimates of the unmeasured states. The lumped-parameter physics-based model of the kHz-
APPJ in He, described in Section 4.5, is used in conjunction with the NMPC. The system
model is modified to include the noise and integrating disturbance on the measurements. The
following system of differential algebraic equations (DAE) describe the system dynamics,

$$\frac{dx}{dt} = f(x, z, u, d, \theta) + w, \quad x_0 = x(0), \tag{7.9a}$$

$$0 = g(x, z, u, d, \theta), \tag{7.9b}$$

$$y = h(z, x) + v. \tag{7.9d}$$

with algebraic states $z = [P, T_{g,0}]^\top$, differential states $x = [T_g, w_{He}, T_{s,max}, T_r]^\top$, inputs
$u = [V_{p2p}, f, q]^\top$ and model parameters θ. The output function h designates the measured
subset of the states, i.e., $y = [P, T_{s,max}]^\top$ and d is the 2×1 vector of integrating disturbances,
added to P and $T_{s,max}$ to allow offset-free behavior as in Section 6.3. w and v denote
independent Gaussian white noise with known covariance matrices Q and R.

For compact representation, augmented sates are defined to include the dynamic and al-
gebraic states as well as the disturbance. With the augmented state vector $x^{aug} = [x, z, d]^\top$,
the augmented dynamic model is defined as $f^{aug} = [f, g, \mathbf{0}]$. To estimate unmeasured states a
discrete-continuous variant of EKF is implemented for the DAE system [200], [201]. The lin-
earized dynamic and algebraic components of the model are computed based on the Jacobian
matrices,

$$F = \frac{\partial f^{aug}}{\partial x^{aug}} \quad \text{and} \quad \Gamma = \begin{bmatrix} \mathbf{I} \\ -\left(\frac{\partial g}{\partial z}\right)^{-1}\frac{\partial g}{\partial[x,d]} \end{bmatrix} \tag{7.10}$$

respectively. The linearized measurement model is obtained from the Jacobian of the mea-
surement function,

$$H = \frac{\partial h}{\partial x^{aug}} \tag{7.11}$$

The EKF algorithm consists of a prediction and correction stages. The prediction stage
involves the following steps at time instant k:

- Predicted estimates $\hat{x}^{aug}_{k+1|k}$ are obtained by propagating previous estimates of the aug-
  mented states $\hat{x}^{aug}_k$ forward using the system model 7.9a and the current inputs u_k.

- The covariance matrix P in differential states is propagated computing the following
  integral over the sampling period

$$P_{k+1|k} - P_k = \int_0^{\Delta t} (FP + PF^\top + \Gamma Q)dt\Gamma^\top \tag{7.12}$$

Then the following steps are used to correct the predictions of the state and covariance
estimates:

- The Kalman gain is computed from

$$K_{k+1} = P_{k+1|k}H(HP_kH^\top + R)^{-1} \tag{7.13}$$

- Updated state estimates are obtained using the Kalman gain and current measurements y_{meas}

$$\hat{x}_{k+1|k+1}^{aug} = \hat{x}_{k+1|k}^{aug} + K_{k+1}(y_{meas} - H\hat{x}_{k+1|k}^{aug}) \tag{7.14}$$

- Finally, the covariance matrix is updated as,

$$P_k = (\mathbf{I} - K_{k+1}H)P_{k+1|k}. \tag{7.15}$$

Recursively executing the EKF algorithm, state estimates $\hat{x}_k$ are obtained at each time steps in order to initialize the optimal control problem. The control problem takes a similar form as (7.2). The control objective is defined as the deviation of the outputs from their respective setpoints,

$$J = \sum_{i=0}^{N_P} \left(T_{s,max,i} - T_{s,max}^{\text{ref}}\right)^2 + W\left(P_i - P^{\text{ref}}\right)^2. \tag{7.16}$$

The input constraint set $\mathcal{U}$ is defined such that the manipulated variables are retained within the ranges allowed by the experimental setup,

$$\begin{bmatrix} 6 \text{ kV} \\ 10 \text{ kHz} \\ 1.5 \text{ slm} \end{bmatrix} \leq \begin{bmatrix} V_{p2p} \\ f \\ q \end{bmatrix} \leq \begin{bmatrix} 10 \text{ kV} \\ 10 \text{ kHz} \\ 5 \text{ slm} \end{bmatrix}. \tag{7.17}$$

The output constraints, denoted with l in (7.2), are defined as

$$\begin{bmatrix} 30^oC \\ 0 \text{ W} \\ 0 \text{ min} \end{bmatrix} \leq \begin{bmatrix} T_{s,max} \\ P \\ CEM_T \end{bmatrix} \leq \begin{bmatrix} 47 \ ^o\text{C} \\ 4.7 \text{ W} \\ 10 \text{ min} \end{bmatrix}, \tag{7.18}$$

to represent safety and comfort during treatment.

7.3.3 Soft-Sensing for Dose Delivery

PI controllers cannot systematically account for the nonlinear and integrating nature of the dose definitions, as demonstrated in Section 7.2.4. However, using a so-called soft sensing technique it is possible to convert the dose delivery problem to a setpoint tracking problem, which is tractable for PI strategies. The soft sensing method relies on pre-defining the *rate* of dose delivery using a parametric expression, such as a linear or quadratic function. With soft sensing, the necessary temperature setpoint to achieve the incremental increase in dose can be computed at each sampling instant by inverting the nonlinear dose definition [28]. A description of the soft sensor algorithm for an assumed linear rate of dose delivery follows.

Given at time instant k, a dose of $CEM_{T,k}$ is previously accumulated, the necessary linear rate of dose delivery to achieve the desired final dose CEM_T^{ref} at the end of operation t_f, is computed as

$$\alpha_k = \frac{CEM_T^{ref} - CEM_{T,k}}{t_f - t_k}. \tag{7.19}$$

Then, the reference thermal dose for the next time point to achieve a linear delivery rate can be computed from,

$$CEM_{T,k}^{set} = CEM_{T,k} + \alpha_k[t_{k+1} - t_k]. \tag{7.20}$$

The temperature setpoint $T_{s,max,k}^{ref}$ corresponding to the incremental increase in dose can be further computed by inverting the dose metric (4.5),

$$T_{s,max,k}^{ref} = \begin{cases} \mathcal{M}(CEM_{T,k}^{set} - CEM_{T,k}) & \alpha_k \geq 0 \\ 30 \ ^oC & \text{otherwise} \end{cases} \tag{7.21}$$

Here, the function $\mathcal{M}$ denotes the inverse of the dose metric function. Since the inverse of the dose metric is not real-valued when α_k is less then 0, (i.e., the delivered dose exceeds the reference), the $T_{s,max,k}^{ref}$ is set to its lower bound. An analogous procedure is used for the non-thermal dose metric CEM_P. Using this method, control objectives defined in terms of dose metrics are translated into setpoint tracking problems in $T_{s,max}$ and P. Note for the MPC strategy, instead of a single setpoint, a future *trajectory* of setpoints are computed. At each time point, predicted delivered dose is computed, which in turn allows computing future setpoints in $T_{s,max}$ over the MPC prediction horizon.

7.3.4 Experimental Results and Discussion

The block diagrams of the PI and MPC strategies, including soft sensing are shown in Figure 7.5. An embedded voltage controller is implemented in both strategies to ensure that the applied V_{p2p} is accurately implemented, not shown in the block diagrams (see Section 5.4.1.1). Two cases are investigated experimentally; In Case Study I, the ability of PI and MPC strategies are evaluated for rejection of disturbances. In this case, soft sensing is not used, and the disturbances are applied to the system while the outputs $T_{s,max}$ and P are controlled at setpoints chosen close to the system constraints. In Case the Study II, the effectiveness of the two control strategies in multicomponent dose delivery are compared in presence of disturbances. Both control strategies are implemented with a sampling time of 3 s.

Case Study I (disturbance rejection): The ability of the PI control and NMPC strategy to reject disturbances is tested in real-time control experiments. Two disturbances are investigated; an increase in jet-tip-to-surface separation distance (d_{sep}), and an increase in substrate impedance via stacking additional cover slips under the APPJ. For this case study, the setpoints in maximum substrate temperature $T_{s,max}$ and dissipated power P are intentionally chosen to be close to the respective constraints, in order to evaluate control
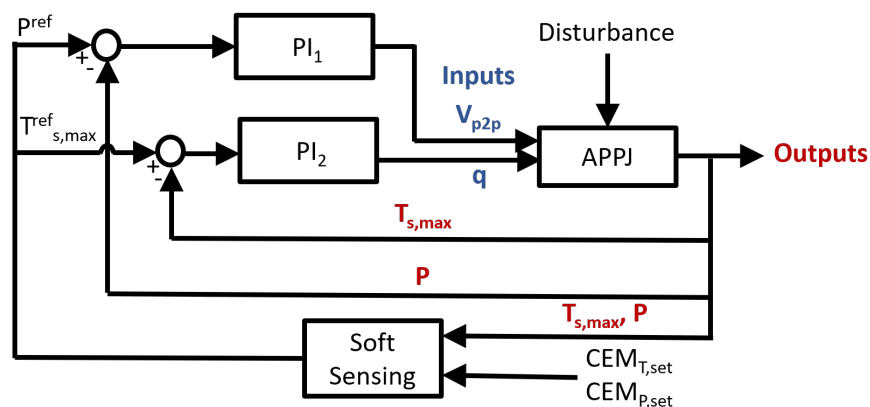
(a) PI Control Strategy with Soft Sensing
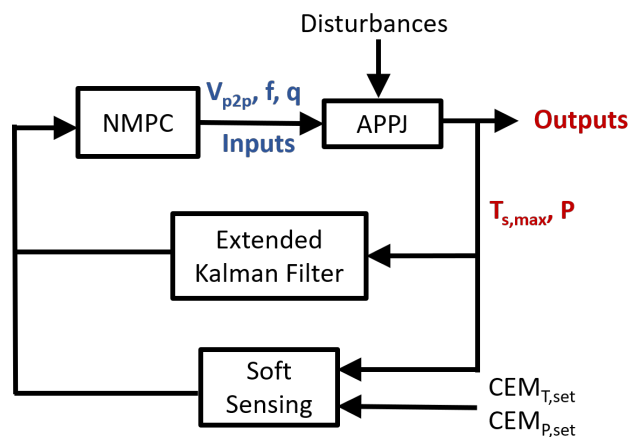
(b) NMPC with Soft Sensing

Figure 7.5: Block diagrams depicting the PI and NMPC control schemes used in the dose delivery experiments. The Integrator computes the delivered dose based on outputs and the Soft Sensing block computes the setpoints based on the delivered dose and the control objective.

performance close to the limits of the operating range. Figure 7.6 shows the performances of the two control strategies in rejecting a disturbance in d_{sep}. The jet is pulled away from the substrate at t = 60 s, increasing d_{sep} from 4 to 12 mm. The disturbance is removed after 180 s. Figure 7.6(a) shows the measured $T_{s,max}$ and P. Evidently, the PI control strategy results in larger excursion from the setpoint. With PI, the constraint in $T_{s,max}$ is violated both when the disturbance acts and when it is removed. In contrast, the NMPC strategy is able to more effectively reject the disturbance. Although the $T_{s,max}$ constraint is violated when the disturbance acts initially, NMPC strategy is able to mitigate the effect of the disturbance rapidly. This constraint violation can be attributed to the comparatively long

(a) Outputs   (b) Inputs
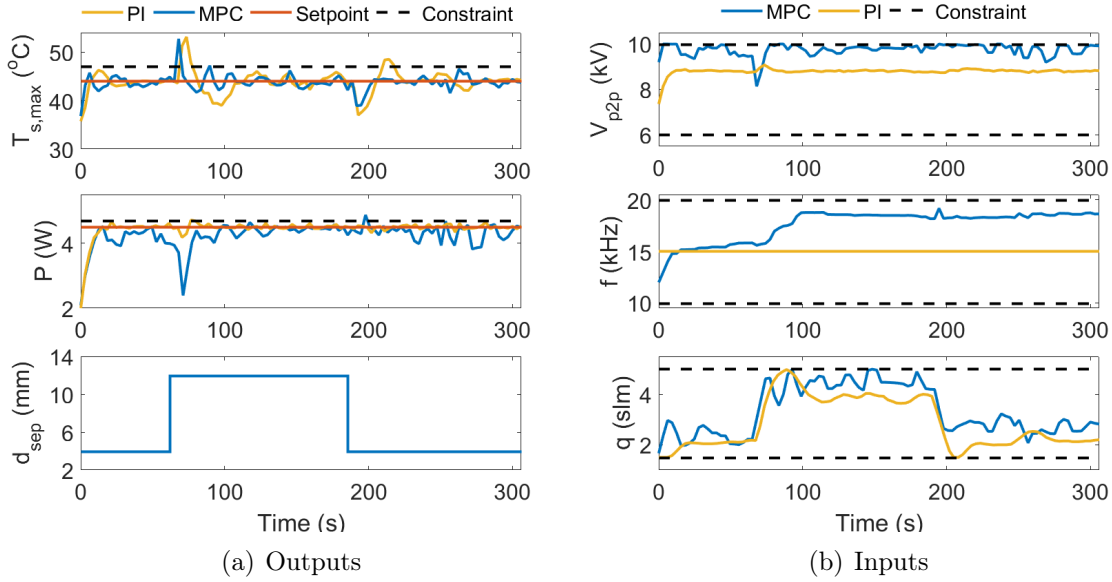
Figure 7.6: The APPJ behavior under feedback control with the PI control and NNMPC schemes in presence of a temporary step change of magnitude 8 mm in the device tip-to-surface separation distance: (a) maximum temperature $T_{s,max}$ and dissipated power P and the disturbance profile in d_{sep} (b) peak-to-peak voltage V_{p2p}, frequency of excitation f, and He mass flow rate q.

sampling time, not allowing NMPC to act rapidly enough. In contrast, the constraint is not violated under NMPC when the disturbance is removed, as the NMPC effectively regulates the dynamics to prevent overshoot. A key advantage of the NMPC strategy for effective disturbance rejection is the ability account for the full multivariable dynamics of the APPJ. As seen in Figure 7.6(b), the applied voltage V_{p2p} is decreased under NMPC immediately after the disturbance acts, in order to help decrease $T_{s,max}$ back to the setpoint. This is done at the expense of a deviation in P away from the setpoint (see Figure 7.6(a)). Since PI strategy consists of two independent controllers, however, the PI controller for P is unaware of the dynamics of $T_{s,max}$. Thus, under the PI strategy, the setpoint in P is maintained in spite of undesirable behavior in $T_{s,max}$, i.e., larger magnitude deviations of setpoint and more sustained violations of constraints.

Figure 7.7 shows experimental results obtained with PI and NMPC control strategies in presence of a disturbance in substrate impedance, imparted by increasing the number of cover slips stacked under the APPJ from 1x to 3x at t = 60 s. The disturbance is then removed at t = 180 s. Notably, an offset in P setpoint is observed in presence of the disturbance, under both control strategies. This behavior is attributed to the fact that the setpoint in P is not easily reachable when substrate impedance is increased. The offset from setpoint in P observed under PI control is somewhat larger, as V_{p2p} saturates. The NPMPC strategy

(a) Outputs

(b) Inputs
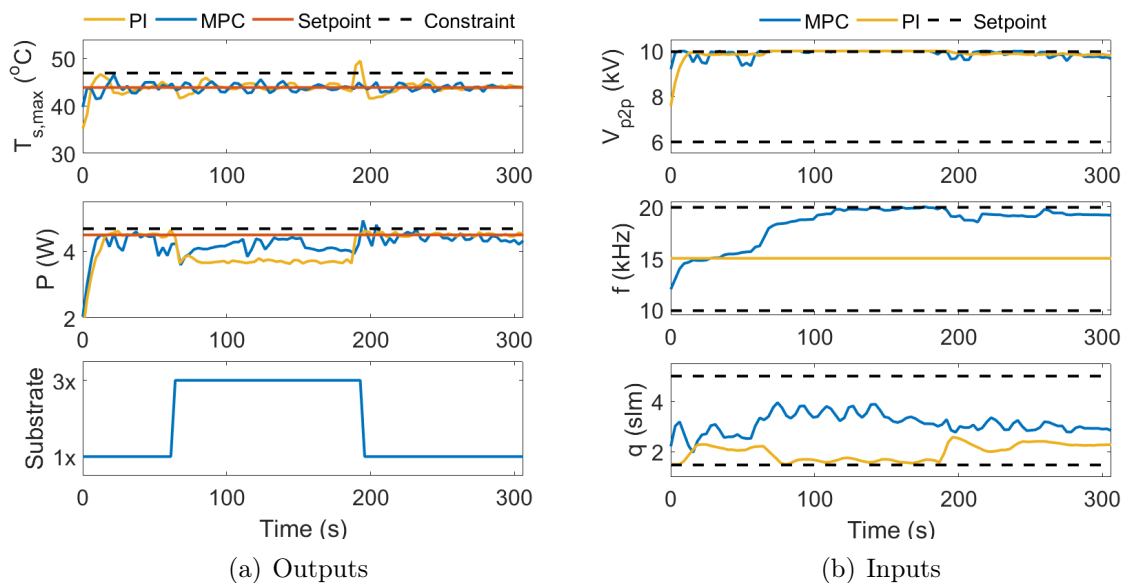
Figure 7.7: The APPJ behavior under feedback control with the PI control and MPC schemes in presence of a temporary change in substrate impedance, imparted by increasing the number of cover slips stacked under the APPJ from 1x to 3x: (a) maximum temperature $T_{s,max}$, dissipated power P, and the disturbance profile in substrate characteristics and (b) peak-to-peak voltage V_{p2p}, frequency of excitation f, and He mass flow rate q.

performs slightly better, with a smaller deviation from the setpoint in P, on account of the ability of the NMPC to manipulate the discharge frequency f as an additional manipulated variable. This behaviour underlines the advantage of NMPC in its ability to account for multivariable dynamics. The requirement for single-input single-output pairing limits the PI strategy in this case, preventing the use of f as a manipulated variable. The PI control strategy further results in a sharp increase and a consequent constraint violation in $T_{s,max}$ when the disturbance is removed. This behaviour is attributed, again, to the independent design of the two PI controllers. As the PI controller tracks P setpoint faithfully, once the disturbance is removed, $T_{s,max}$ sharply increases causing the excursion and consequent constraint violation observed in Figure 7.6(a). NMPC, in contrast is able to mitigate this disturbance without constraint violations in $T_{s,max}$. However, small excursions and constraint violations are observed in P. This is due to the fact that the NMPC is not designed to be robust against noise and uncertainty in system dynamics.

These two studies demonstrate the advantage of the NMPC strategy for rejection of disturbances. Notably, the interaction between the two controlled outputs $T_{s,max}$ and P, necessitate some systematic strategy to allow trade-off between the competing objectives and respecting constraints. NMPC strategy is precisely capable of this, yielding improved control performance. Figure 7.3.4 summarizes the control performance of PI and NMPC
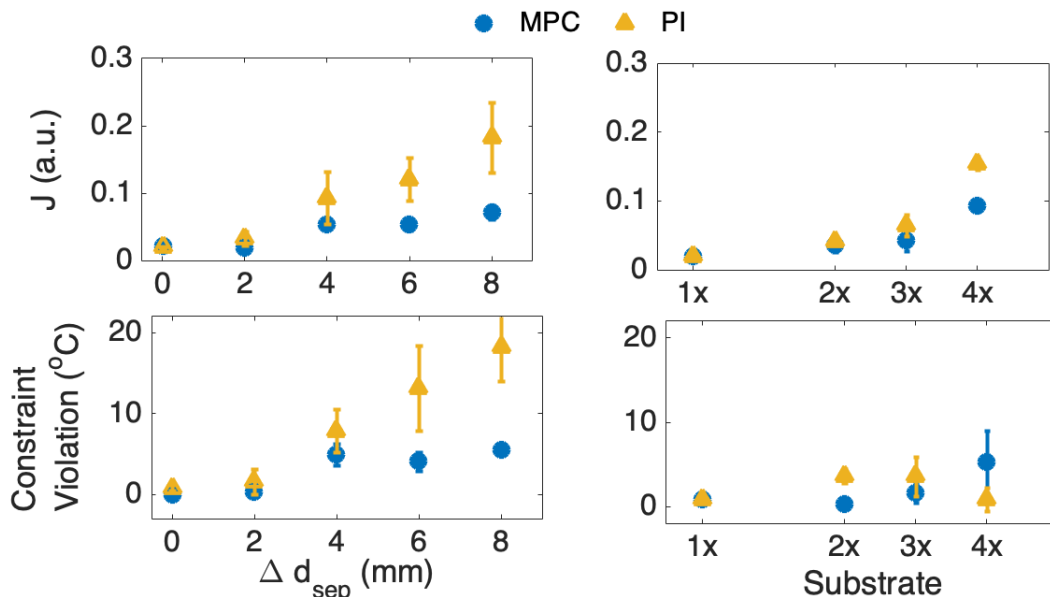
Figure 7.8: Summary of performance of the PI and NMPC control strategies for rejection of disturbances of different magnitude, quantified in terms of the value of the objective function (7.16) and magnitude of constraint violation in $T_{s,max}$. Experiments are conducted in sets of triplicates and error bars are indicate the a single standard deviation computed over each set.

control strategies in terms of the value of the objective function 7.16 and the magnitude of the constraint violation in $T_{s,max}$ in presence of disturbances of different magnitudes. The two strategies preform similarly in absence of disturbances. However, control performance with NMPC is superior to that of the PI control strategy in presence of disturbances, in terms of both the value of the objective function and the magnitude of constraint violation. Notably, with increasing disturbance magnitude in d_{sep}, NMPC preforms more than 2x better than the PI strategy. The performance increase with NMPC is less pronounced with change in substrate properties as the inputs can easily saturate and setpoints can become inaccessible with changes in substrate properties (see Figure 7.7). A notable exception is when the substrate properties are changed with 4x coverslips inserted under the APPJ. This results in a significantly larger constraint violation with NMPC indicating the limitation of the strategy. One explanation for this observation is that the mismatch between the dynamics and the model increases beyond tolerance in presence of this disturbance.

Case Study II (Dose Delivery): The differences in performance between PI and MPC strategies can result in drastically different dose delivery performances. In particular, the nonlinearity in dose metrics can exacerbate relatively minor performance differences between the two control strategies. This case study investigates the delivery of a multicomponent dose combination in presence of disturbances in d_{sep} and substrate characteristics. The control

(a) Outputs   (b) Inputs
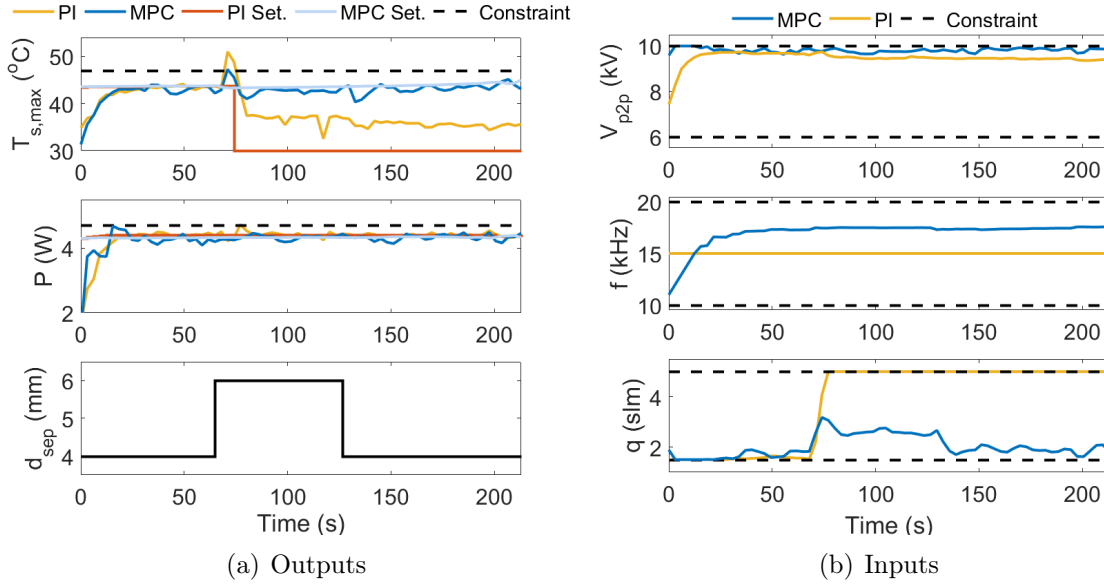
Figure 7.9: The APPJ behavior for dose delivery with the PI control and NMPC schemes in the presence of a temporary step change of magnitude 2 mm in the device tip-to-surface separation distance: (a) maximum temperature $T_{s,max}$ and dissipated power P and the disturbance profile in d_{sep} (b) peak-to-peak voltage V_{p2p}, frequency of excitation f, and He mass flow rate q.

objective is defined in terms of delivery of a fixed combination of thermal and non-thermal dose, quantified by CEM_T and CEM_P, respectively (see Section 4.3), over a fixed treatment time of 200 s. The dose delivery problems are converted to setpoint tracking problems using soft sensing, assuming a linear dose delivery rate as described in Section 7.3.3. For the NMPC strategy, although a trajectory of future setpoints are calculated with soft sensing, for ease of visualization only the current setpoint is plotted at each sampling time.

Figure 7.9 shows the time courses of the measured variables and the setpoints computed by soft sensing, during multicomponent dose delivery in presence of a disturbance in separation distance. d_{sep} is increased by 2 mm at t = 60 s and its reverted back to its original position at t = 120 s. As seen in Figure 7.9(a) under PI control $T_{s,max}$ considerably exceeds its setpoint and constraint when the disturbance acts. This behavior, in turn, results a drastic spike in the delivered CEM_T profile as shown in Figure 7.10; the delivered thermal dose under the PI strategy drastically exceeds the target value as well as the imposed safety constraint. In practice, this behavior may correspond to imparting some thermal damage (i.e., burning) on the treated substrate. Note that, as CEM_T exceeds its target value, the PI setpoints computed by the soft sensor drop sharply, indicating failure of the PI control strategy. In contrast, the NMPC strategy is able to effectively track the setpoint computed by the soft sensor (see Figure 7.6(b)). With NMPC The disturbance is more effectively rejected.
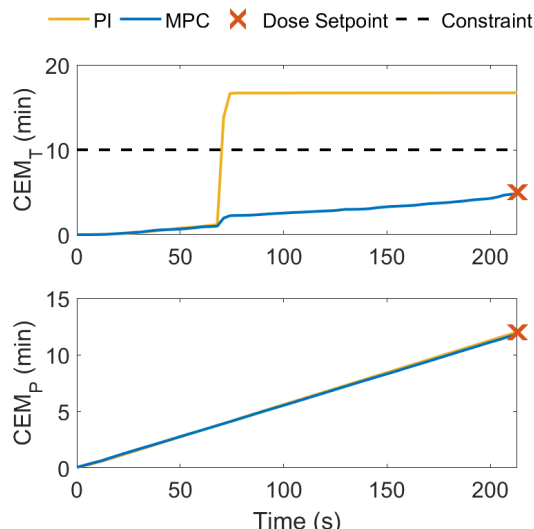
Figure 7.10: Delivered dose profiles under PI and NMPC strategies in presence of a disturbance in jet-tip-to-substrate separation distance, corresponding to time courses given in Figure 7.9.

A significantly smaller excursion is observed in $T_{s,max}$ which remains below the constraint. As a result, the MPC strategy is able to reliably deliver the desired multicomponent dose (see Figure 7.10).

Figure 7.11 shows the measured time courses of outputs and corresponding setpoints under PI and NMPC strategies for multicomponent dose delivery in presence of a disturbance in substrate impedance. The disturbance is imparted by increasing the number of coverslips under the APPJ from 1x to 3x at t = 60 s. The disturbance is then removed at t = 120 s. Figure 7.11(b) show the profiles of $T_{s,max}$ and P under the two control strategies. Under PI control the $T_{s,max}$ setpoints calculated via soft sensing continue to increase throughout the operation. Once the disturbance is removed at t = 120 s, the PI controller appears to be incapable of tracking the setpoint as the input q saturates at the lower bound (Figure 7.11(b)). This is is attributed to the independent nature of the two PI controllers designed. In this case the power setpoint, which is tracked well by the PI, results in a situation where the setpoint in $T_{s,max}$ becomes inaccessible by manipulating q alone. The inability of the PI strategy to handle the multivariable nature of APPJ dynamics, in this case, results in a significant undershoot in the delivered CEM_T (see Figure 7.12). This may correspond to ineffective treatment with the APPJ as the desired dose target is not reached. In contrast, NMPC is able to deliver the desired multicomponent dose effectively (see Figure 7.12). Notably, the under the NMPC strategy, P initially deviates from its setpoint (see Figure 7.11(b)), presumably in order to achieve effective setpoint tracking in $T_{s,max}$. Once the disturbance acts, a significant fluctuation in $T_{s,max}$ is observed under NMP,C corresponding to a large increase in CEM_T (see Figure 7.12). However, the NMPC strategy is able to

(a) Outputs
(b) Inputs
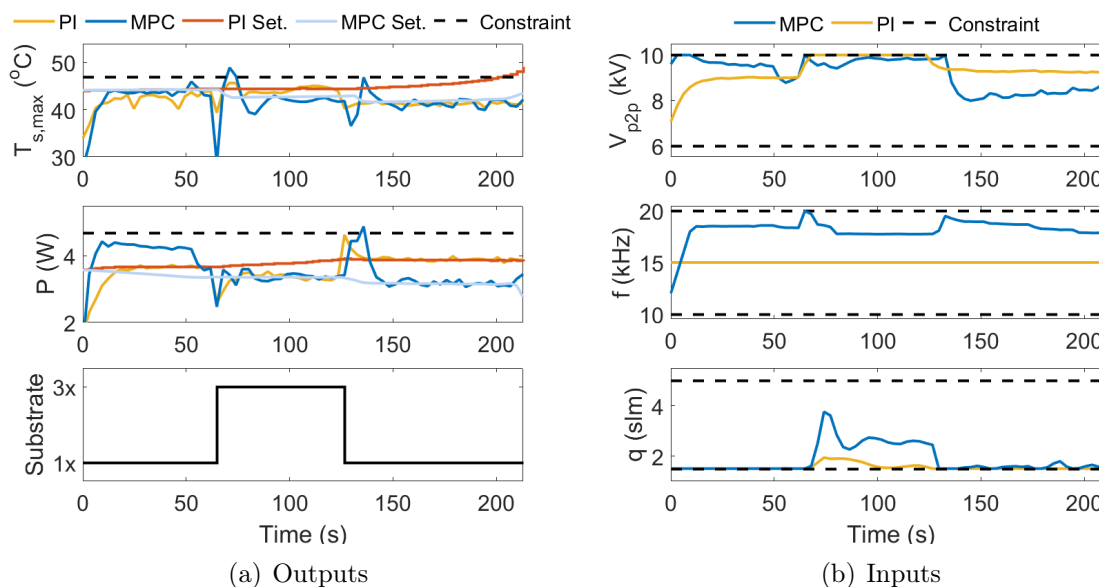
Figure 7.11: The APPJ behavior for dose delivery with the PI control and NMPC schemes
in the presence of a temporary change in substrate impedance, imparted by increasing the
number of cover slips stacked under the APPJ from 1x to 3x: (a) maximum temperature
$T_{s,max}$ and dissipated power P and the disturbance profile in d_{sep} (b) peak-to-peak voltage
V_{p2p}, frequency of excitation f, and He mass flow rate q.

recover later in the operation as the setpoints in $T_{s,max}$ and P, calculated by the soft sensor,
are effectively followed.

The two examples investigated in this case study demonstrate the advantage of NMPC
over the PI strategy for multicomponent dose delivery under disturbances. A notable obser-
vation here is that the PI strategy, under both cases is able to deliver the nonthermal dose
component CEM_P reliably. This can be attributed to the linear nature of the CEM_P metric
(see Section 4.3) as well as the effectiveness and rapid response of the PI controller between
V_{p2p} and P. However, as demonstrated above, faithful tracking of setpoints in P alone can
be detrimental for overall performance, especially in presence of disturbances. As a result,
the PI control strategy may be unable to regulate the thermal dose, either overshooting or
undershooting the CEM_T target. Even when the somewhat complex soft sensing strategy
is used to aid its performance, the PI controls cannot systematically and reliably address
the multicomponent dose delivery problem. For this purpose, the NMPC strategy appears
advantageous. Note, however, that targets for CEM_P and CEM_T and the disturbance pro-
files in this case study, are picked specifically to demonstrates the shortcomings of the PI
strategy. The key factors impacting the control performance are found to be the magnitude
and the timing of the disturbances. If a disturbance realization causes an extreme overshoot
(for example in Figure 7.9(b) under PI) or if the disturbance acts close to the end of the
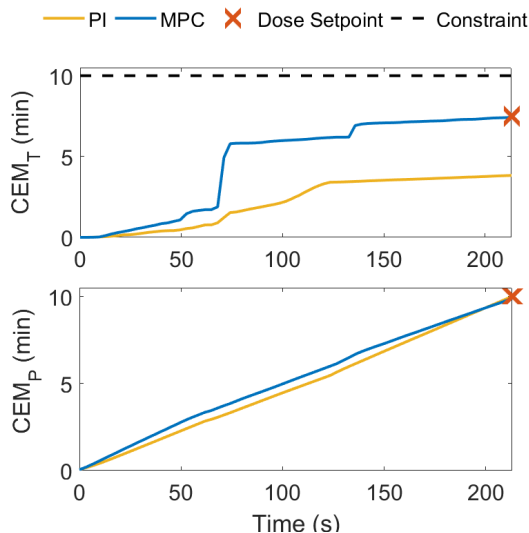
Figure 7.12: Delivered dose profiles under PI and NMPC strategies in presence of a change
in substrate impedance, corresponding to time courses given in Figure 7.11.

operation, when most of the dose have already been delivered, it may simply be not possible
for either control strategy to recover.

7.4   Conclusions

This chapter demonstrated the effectiveness of NMPC for multivariable setpoint tracking and
multicomponent dose delivery in presence of disturbances. Both simulations and experimen-
tal studies indicate the clear advantage of the NMPC over PI control strategies. Simulation
studies indicate that integrating and nonlinear metrics are difficult to readily regulate with
PI control strategies. In contrast, CEM_T and CEM_P dose definitions can be readily incorpo-
rated to the NMPC strategy as a part of the system model. The end-point control objectives
are systematically addressed though the "shrinking-horizon" implementation demonstrated
in dose delivery simulations. The ability to systematically incorporate constraints and the
multivariate and nonlinear aspects of the system dynamics appear to be a key advantage for
regulating the complex behavior of APPJs.

   The nonlinear and integrating nature of the dose metrics, as well as the nonlnearities
in APPJ behavior necessitate the use of nonlinear system models over linear ones. Indeed,
the NMPC strategy demonstrated experimentally in this chapter is capable of exploiting a
broader operating range and rejecting disturbances of larger magnitude compared to the lin-
ear MPC in Chapter 6. The key conclusion of this chapter is that NMPC is uniquely capable
of addressing the challenges of the APPJ dose delivery problem, where safety constraints are
of paramount importance, and dynamics are integrating and nonlinear.

The effectiveness of the NMPC strategy relies on the descriptive capability and the computational efficiency of the underlying model. The system of differential-algebraic equations obtained from the lumped-parameter model (see Section 4.5) are a particularly stiff set of equations. In turn, solving optimal control problems based on this model takes up to 3 - 5 seconds. This in turn, limits the timescales over which the NMPC strategy can be applied. Fast optimization methods for non-linear optimization may aid this issue.

Another issue pertains to he descriptive capability of the models used for NMPC. For example, certain aspects of the physics-based model, such as the equivalent circuit, rely on empirical parametrizations. Moreover, a key aspect of APPJ treatment, the spatial distribution of the APPJ effects on the substrate are not considered here. In contrast, dose delivery is fundamentally a spatially distributed problem. The next chapter investigates how the NMPC strategy can be extended to the spatially distributed dose delivery problem.

Chapter 8

Spatially Uniform Dose Delivery with Model Predictive Control in 1D

The effects of the APPJs on substrates are spatially and temporally distributed. Moreover, to treat practical treatment areas APPJs must often be translated across treated substrates. This results in the complex problem of regulating the spatial dose delivery with APPJ while the jet is moving. This chapter experimentally investigates spatially uniform delivery of thermal effects in 1D and including issues pertaining to the translation of the APPJ. The thermal dose metric CEM_T is extended to quantify the cumulative, nonlinear thermal effects of the APPJ along a translation trajectory. An optimization-based feedback control strategy is proposed for real-time regulation of thermal dose delivery using spatial measurements of substrate temperature.[1]

8.1   Introduction

In the absence of reliable dosimetry and online diagnostics, the common practice is to devise treatment protocols offline, largely based on the user's experience and device characteristics. The primary challenges in this approach arise from quantifying the complex interactions between plasma and target substrate and achieving the delivery of a therapeutically effective plasma dose across a substrate in the face of inherent variabilities of plasma dynamics, exogenous disturbances, and uneven substrate characteristics.

Previous chapters demonstrated the usefulness of advanced control strategies for mitigating the effects of variabilities and disturbances on APPJ operation. However, these demonstrations were limited to regulation of instantaneous APPJ characteristics and point-wise dose delivery. On the other hand, the APPJ treatment is inherently a spatially distributed problem. Hence, this chapter focuses on spatially uniform thermal dose delivery in atmospheric pressure plasma jets (APPJs) in 1D. A key consideration in spatial dose delivery with APPJ is the translation of the device. The small dimensions of APPJs often necessi-

---

[1]This chapter is adapted from published material in [202]

tate that the device is translated over substrates in order to fully treat the target area. The
APPJ translation introduces further variability in plasma characteristic, that can compromise the reproducible and effective operation of APPJs. Moreover, the systematic choice of
a translation trajectory which allows effective spatial dose delivery is not a trivial task.

This chapter addresses the problem of uniform delivery of a thermal dose of the kHz-excited APPJ in helium along its translation trajectory in 1D. First, the thermal dose metric
is re-visited to quantify spatial thermal effects of the APPJ using spatially-resolved measurements of substrate temperature. An optimization-based advanced control strategy is then
proposed for real-time regulation of thermal dose delivery as the APPJ is translated over
a dielectric substrate. The performance of the advanced control strategy is demonstrated
under different APPJ translation trajectories, where experimental investigations indicate
the critical role of real-time regulation of dose delivery and feedback control for achieving
spatially uniform dose delivery.

8.2   Thermal Dose Delivery

Treatment protocols in plasma medicine are commonly designed based on user's experience
in terms of some reference operating parameters of a hand-held plasma device, treatment
time, and *translation rate* of the plasma device on a target substrate [13]. Ideally, however,
the objective of plasma treatment is to deliver a predetermined plasma dose to a target
substrate within a prespecified treatment time frame as the plasma device is translated over
the substrate. This suggests that effective plasma dose delivery hinges on (i) quantifying
the cumulative effects of plasma on the target substrate in terms of tempo-spatial variations
of substrate properties that are intimately related to the plasma effects and (ii) systematic
translation of the plasma device over the substrate. Here, the notion of spatial dose delivery
for the thermal effects of the APPJ in Chapter 3 is demonstrated when the APPJ is translated
along the x-direction.

8.2.1   Spatial Metric for Thermal Dose

Controlling the thermal effects of plasma in medical therapies is important for patient safety
and comfort [167]. Thermal dosimetry is fairly well-established in hyperthermia treatment,
where the thermal dose is commonly quantified point-wise using the *Cumulative Equivalent
Minutes* (CEM$_\text{T}$) metric that is defined at a reference treatment temperature of 43°C [18],
[27], [168] (see Section 4.3). The dose metric CEM$_\text{T}$ can be readily extended for any target
point x,

$$\text{CEM}_\text{T}(\tau, x) = \int_0^\tau K^{(43-T(t,x))} \, \mathrm{d}t, \tag{8.1}$$

Table 8.1: Four cases for the translation rate of the APPJ, which are specified in terms of characteristic time Δt and length Δx.

	$\Delta x \, (mm)$	$\Delta t \, (s)$
Case I	7	100
Case II	2	30
Case III	1	7.8
Case IV	0.5	1.3

where τ is a prespecified treatment time and the constant K characterizes the substrate response to thermal stresses

$$
K = \begin{cases} 0 & T(t,x) \leq 39°\text{C} \\ 0.25 & 39°\text{C} < T(t,x) < 43°\text{C} \\ 0.5 & T(t,x) \geq 43°\text{C}. \end{cases}
$$

This metric is adopted for quantifying the tempo-spatial thermal effects of the APPJ along the translation trajectory x. Based on empirical observations of substrate temperature shown in Figure 8.1, a Gaussian parameterization is used to describe the spatial distribution of substrate temperature along x

$$
T(t,x) = (T_{\max}(t) - T_{\inf})e^{-\frac{(x-\mu(t))^2}{\sigma^2(t)}} + T_{\inf}. \tag{8.2}
$$

Expression (8.2) suggests that substrate temperature at any point along the translation trajectory $x \in [-L, \, L]$ can be described in terms of: (i) the maximum substrate temperature $T_{\max}(t)$ at the centerline of the APPJ, which determines the highest rate of dose accumulation according to the CEM_T metric in (8.2), (ii) the spatial variance of substrate temperature around the APPJ centerline $\sigma^2(t)$, and (iii) the position of the APPJ centerline $\mu(t)$, which is governed by the APPJ translation rate. $T_{\inf}$ denotes the ambient temperature in (8.2) and is used to normalize the temperature distribution. As discussed in Section 8.3, the parameters $T_{\max}(t)$, $\sigma^2(t)$, and $\mu(t)$ can in principle be controlled for regulation of the thermal dose delivery along x.

8.2.2   Translation Rate

To treat areas larger than the dimensions of the APPJ, it is necessary to translate the APPJ over the target substrate. The common practice in plasma medicine is to translate the APPJ in a "meandering pattern" to achieve an average treatment rate of approximately 1 cm^2/min [13], [79]. Generally, prespecifying the APPJ translation rate systematically to achieve a desired spatial dose profile across the treatment area is not trivial. In radiotherapy, the device translation is typically specified in terms of either discrete translation steps (i.e., *step-and-shoot* strategy), or continuous translation with some velocity (i.e., *moving window*

strategy) [203]. Inspired by the step-and-shoot strategy, a discrete translation scheme is adopted for the APPJ. The APPJ translation rate is defined in terms of discrete steps of size Δx, where the APPJ is held for a time interval of Δt at each step. Δx and Δt can be chosen based on the characteristic time and length scales of the APPJ dynamics. Under nominal APPJ operation ($V_{\text{p2p}} = 8$ kV and $q = 1.5$ slm), the characteristic time of the substrate temperature dynamics is 30 s, whereas the spatial distribution of substrate temperature has a variance of approximately 7 mm (i.e., $\sigma^2 = 7$ mm in (8.2)). However, due to the exponential nature of the dose metric (8.1), $\sigma^2(t)$ is considerably larger than the region over which dose accumulates (see Figure 8.1). This characteristic length of dose accumulation is observed to be similar to the radius of the visible area the plasma spreads across on the substrate.

Table 8.1 lists the time- and length-scale characteristics of four cases for the translation rate of the APPJ, as considered in the remainder of this article. Note that Cases I and IV correspond to two extreme translation rates: a discrete translation with few long steps in Case I and a "continuous" translation with many short steps in Case IV.

8.3 Real-time Regulation of Thermal Dose Delivery

The goal of this chapter is to investigate uniform delivery of thermal dose $\text{CEM}_\text{T}(\tau, x)$ along the APPJ translation trajectory $x \in [-L, L]$ under the APPJ translation rates listed in Table 8.1. A schematic of spatially uniform thermal dose delivery is given in Figure 8.2.
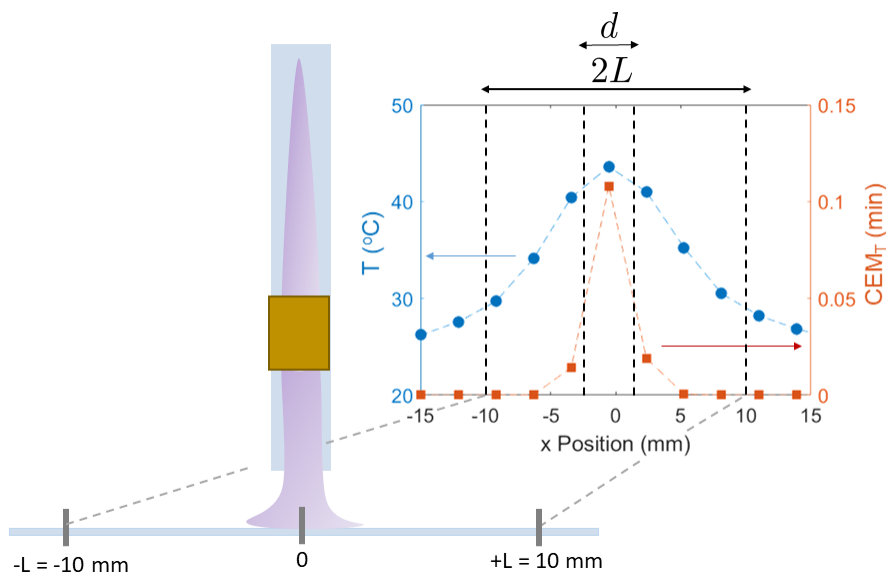
Figure 8.1: A representative measurement of the substrate temperature obtained from the IR thermal images and its corresponding thermal dose CEM_T delivered over 1.3 s along the translation trajectory $x \in [-L, L]$. d denotes the tube diameter of the APPJ.

To achieve uniform thermal dose delivery, a hierarchical, feedback control strategy shown in Figure 8.3 is proposed to control the spatial distribution of substrate temperature along the translation trajectory. At the lower level of the control strategy, a proportional-integral (PI) controller is used to control the maximum substrate temperature $T_{\max}$ at the centerline of the APPJ via manipulating the applied peak-to-peak voltage V_{p2p}. The PI controller computes the control input V_{p2p} every 1.3 s as $T_{\max}$ is measured. Physical bounds of the control input V_{p2p} are incorporated into the PI controller via addition of antiwindup effect [29]. The controller tuning is given in Appendix D.1.

The PI controller enables tracking the reference temperature $T_{\max}^{\mathrm{ref}}$ in the presence of exogenous disturbances acting on the APPJ as shown in Chapter 5. However, the PI controller cannot account for the cumulative, nonlinear nature of the thermal dose $\mathrm{CEM_T}(\tau, x)$. Thus, an optimization-based supervisory controller (i.e. an NMPC strategy) is adopted for determining the reference temperature $T_{\max}^{\mathrm{ref}}$ (see Figure 8.3). Given the accumulated thermal dose $\mathrm{CEM_T}(t_k, x)$ up to sampling time t_k over $x \in [-L, L]$, the supervisory controller solves
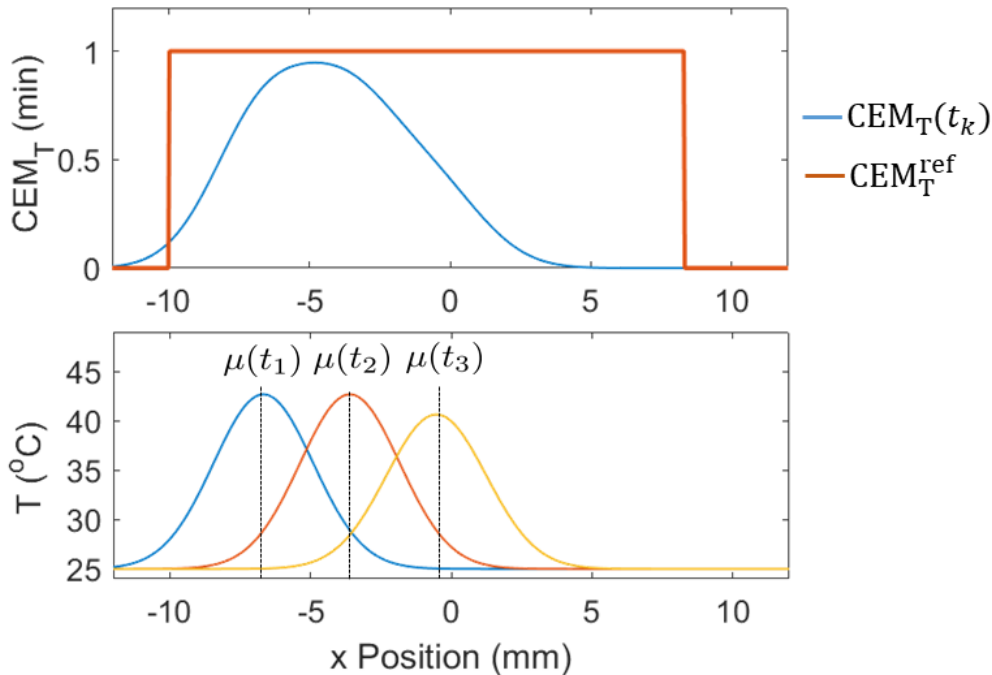
Figure 8.2: Depiction of thermal dose delivery along the APPJ translation trajectory $x \in [-L, L]$ at an arbitrary time point t_k. The accumulated thermal dose $\mathrm{CEM_T}$ (top) is quantified in terms of spatial measurements of the substrate temperature obtained in real time along the translation trajectory x (bottom). μ denotes the centerline of the APPJ, which shifts along the translation trajectory.

the dynamic optimization problem

$$\min_{T_{\max}^{\text{ref}}(t)} \quad \int_{-L}^{L} \|\text{CEM}_{\text{T}}(\tau, x)dx - \text{CEM}_{\text{T}}^{\text{ref}}(\tau, x)\|^2 + \int_{t_k}^{\tau} \|dT_{\max}^{\text{ref}}(t)\|_w^2 dt \tag{8.3a}$$

$$\text{s.t.} \quad \frac{d\text{CEM}_{\text{T}}(t, x)}{dt} = K^{(43-T(t,x))}, \tag{8.3b}$$

$$T(t, x) = (T_{\max}^{\text{ref}}(t) - T_{\inf})e^{-\frac{(x-\mu(t))^2}{\sigma^2(t)}} + T_{\inf}, \tag{8.3c}$$

$$T_{\max}^{\text{ref}}(t) \leq 45°\text{C}, \tag{8.3d}$$

$$t \in [t_k, \tau], \quad x \in [-L, L],$$

where $T_{\max}^{\text{ref}}(t)$ over the time horizon $[t_k, \tau]$ is the decision variable of the optimization problem, τ is the user-specified treatment time in the thermal dose metric (8.1), $\text{CEM}_{\text{T}}^{\text{ref}}(\tau, x)$ is the user-specified *reference* thermal dose at the end of the treatment time τ along the translation trajectory $x \in [-L, L]$, and w is a user-specified constant weight. In the optimization (8.3), the first term of the objective function (8.3a) describes the integral of squared deviations between the predicted and reference thermal dose at τ. The second term in (8.3a) penalizes excessive changes in the decision variable $T_{\max}^{\text{ref}}(t)$ to avoid abrupt changes in the substrate temperature. Expressions (8.3b) and (8.3c) describe the time evolution of thermal dose accumulation in terms of the dose metric (8.1) and the Gaussian parameterization of distribution of substrate temperature along x (see expression (8.2)). The thermal dose accumulation predicted by (8.3b) is dependent on the initial thermal dose $\text{CEM}_{\text{T}}(t_k, x)$ and the translation rate of the APPJ centerline $\mu(t)$. The constraint (8.3d) ensures that the maximum substrate temperature remains below some user-specified threshold, for example, to ensure patient safety and comfort.

The dynamic optimization problem (8.3) is solved repeatedly in real time every 6 s to enable *closed-loop* thermal dose delivery planning . This entails re-initializing (8.3) at every sampling time t_k based on the thermal dose $\text{CEM}_{\text{T}}(t_k, x)$ accumulated up to time t_k (i.e., inferred by integrating the substrate temperature measurements), solving the optimization, and subsequently applying the optimal value for $T_{\max}^{\text{ref}}(t_k)$ to the lower-level PI controller as its reference. The repeated solution of the optimization confers a measurement feedback action to the thermal dose delivery planning in order to provide some degree of robustness to unmeasured disturbances affecting the dose delivery. Alternatively, the optimization (8.3) can be solved offline – only once, before the treatment – to determine an optimal trajectory for $T_{\max}^{\text{ref}}(t)$ over the treatment time $[0, \tau]$. This strategy is hereinafter referred to as *open-loop* thermal dose delivery planning. In this work, the optimization (8.3) is solved using automatic differentiation software CasADi [195] and the interior point optimization library IPOPT [198] in Python.

It follows from above that the PI controller enables fast rejection of disturbances acting on the APPJ, whereas the optimization-based supervisory controller allows for planning the thermal dose delivery in terms of the treatment time τ, the reference thermal dose $\text{CEM}_{\text{T}}^{\text{ref}}(\tau, x)$ along the translation trajectory $x \in [-L, L]$, and the APPJ translation rate as
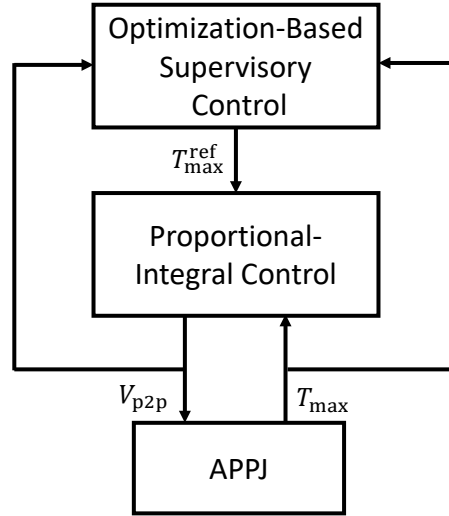
Figure 8.3: The hierarchical, feedback control strategy for real-time regulation of thermal dose delivery using the APPJ. The control strategy consists of: (i) a proportional-integral (PI) controller that regulates the maximum substrate temperature $T_{\max}$ at the APPJ centerline via manipulating the applied peak-to-peak voltage V_{p2p} every 1.3 s, and (ii) an optimization-based supervisory controller that plans the thermal dose delivery every 6 s via determining the optimal values for the reference maximum substrate temperature $T_{\max}^{\mathrm{ref}}$ in the PI controller based on the user-specified treatment time, the reference thermal dose along the translation trajectory, and the APPJ translation rate.

specified in Table 8.1. Note that other parameters characterizing the spatial distribution of substrate temperature in expression (8.2) – namely the spatial variance of substrate temperature around the APPJ centerline, σ^2, and the APPJ position, μ – can be considered in the optimization (8.3) as decision variables. To the extent that σ^2 can be measured and manipulated effectively, the distribution of the substrate temperature can be controlled to realize a desired spatial distribution of the reference thermal dose $\mathrm{CEM}_{\mathrm{T}}^{\mathrm{ref}}(\tau, x)$. Optimizing for μ in the optimization (8.3), on the other hand, can allow for determining an optimal translation trajectory. Although these alternative formulations for the optimization (8.3) can introduce further computational and/or implementation complexities (e.g., increased solution time of optimization, or a multivariable lower-level control structure), the hierarchical, optimization-based control strategy in Figure 8.3 provides a versatile framework for real-time regulation of spatial dose delivery.

8.4 Results and Discussion

The proposed feedback control strategy is implemented on the APPJ shown in Chapter 3, where the objective is to deliver a thermal dose of 1 min uniformly over a translation
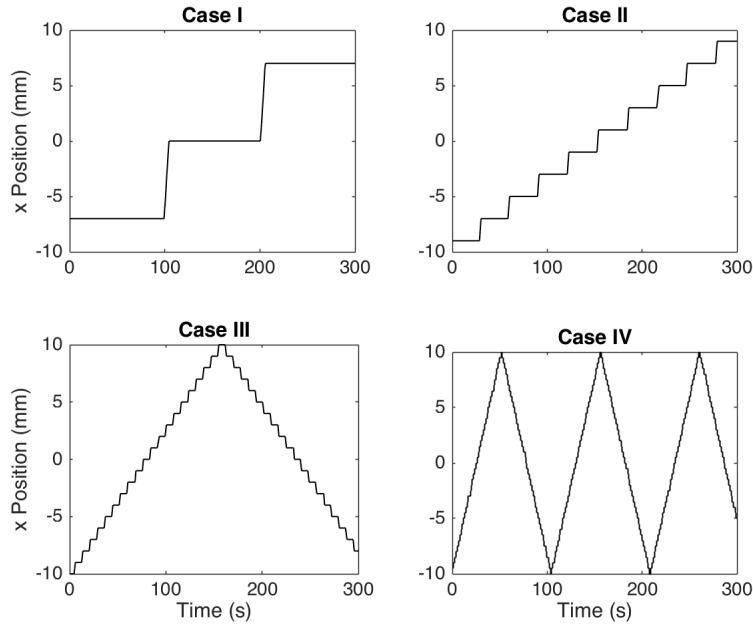
Figure 8.4: The translation trajectories of the APPJ under the four translation rates given in Table 8.1. The translation rate increases from Case I to Case IV while the target region and treatment time remain fixed at 20 mm and 5 min, respectively.

distance of 20 mm during treatment time of $\tau = 5$ min. Thus, the reference thermal dose in the optimization problem (8.3) is defined as

$$\text{CEM}_\text{T}^\text{ref}(5, x) = \begin{cases} 1 & -10\,\text{mm} \leq x \leq 10\,\text{mm} \\ 0 & \text{otherwise.} \end{cases} \tag{8.4}$$

Figure 8.4 shows the APPJ translation trajectories corresponding to the four APPJ translation rates given in Table 8.1. Note here, that the translation direction of the APPJ is reversed during the treatment in Cases III and IV. This is because the APPJ translation rate in these two cases is high – relative to that in Cases I and II – for the target region be treated in a "single pass" given the fixed treatment time of 5 min.

In the remainder of this section, the performance of the hierarchical, optimization-based control strategy for real-time regulation of thermal dose delivery is investigated under the APPJ translation trajectories depicted in Figure 8.4.

8.4.1 Spatially Uniform Thermal Dose Delivery

As described in Section 8.3, the dynamic optimization problem (8.3) enables designing the reference temperature T_max^ref for the PI controller directly in terms of the desired thermal

dose delivery objective specified in (8.4). The offline and online solution of the optimization problem (8.3) is considered respectively for, open-loop and closed-loop dose delivery planning under the four translation trajectories shown in Figure 8.4. For the translation trajectory of Case III, Figure 8.5 shows the spatial thermal dose delivered at the end of the treatment time 5 min, the $T_{\max}$ profile, and the V_{p2p} profile for the cases of: (a) no feedback control and dose delivery planning, (b) the open-loop dose delivery planning strategy, and (c) the closed-loop dose delivery planning strategy. As seen in Figure 8.5(a), $T_{\max}$ exhibits high variability and sensitivity to the APPJ translation when no feedback control is used for regulating $T_{\max}$. The inability to plan the dose delivery in this case, along with the variabilities in $T_{\max}$, leads to significant non-uniformity in the spatial dose delivery along the target region. For example, the thermal dose delivered at $x = -5$ mm is significantly lower than the desired thermal dose reference (i.e., $\mathrm{CEM}_{\mathrm{T}}^{\mathrm{ref}}(5, x) = 1$ min), whereas at $x = 5$ mm the delivered thermal dose is approximately twice the reference. Thus, the results suggest that the safety and effectiveness of dose delivery can be severely compromised in the case of no feedback control and dose delivery planning.

Figure 8.5(b) shows the results obtained using the open-loop dose delivery planning strategy, where the reference of the PI controller is determined by solving the optimization problem (8.3) once, offline. As expected, the PI controller can effectively track the offline-computed reference profile for the maximum substrate temperature, $T_{\max}^{\mathrm{ref}}$, while mitigating the variabilities that stem from the APPJ translation and possibly other unknown sources of disturbances. Yet, even though a significantly more uniform thermal dose is achieved relative to the case of no feedback control, there is an offset between the delivered thermal dose and the reference dose. This can be attributed to the discrepancy between the planned dose and the actual thermal dose delivered due to the fact that the reference profile $T_{\max}^{\mathrm{ref}}$ is determined offline and thus it is blind to the actual state of dose delivery during APPJ treatment. On the other hand, the closed-loop dose delivery planning strategy mitigates this discrepancy via the real-time solution of the optimization problem (8.3). In this case, the actual thermal dose delivered to the substrate is inferred from temperature measurements every 6 s and is fed back to the supervisory controller (see Figure 8.3). This allows online computation of the reference temperature $T_{\max}^{\mathrm{ref}}$ sent to the PI controller. Figure 8.5(c) suggests that the closed-loop dose delivery planning enables achieving a close to uniform thermal dose along the target region at the end of the treatment time while maintaining high reproducibility and low variability in the dose delivery.

Next, the effect of the APPJ translation rate on the spatial thermal dose delivery is investigated. Figure 8.6 shows the delivered thermal dose using the open-loop and closed-loop dose delivery planning strategies under the APPJ translation rates of Cases I to IV given in Table 8.1, which correspond to the four APPJ translation trajectories shown in Figure 8.4. APPJ translation along the prespecified trajectories perturbs the substrate temperature dynamics, thus acting as a disturbance on the thermal dose delivery. Figure 8.6(a) suggests that neither the open-loop nor the closed-loop dose delivery planning strategy enables achieving spatially uniform thermal dose delivery in Case I. This can be attributed to the large, discrete
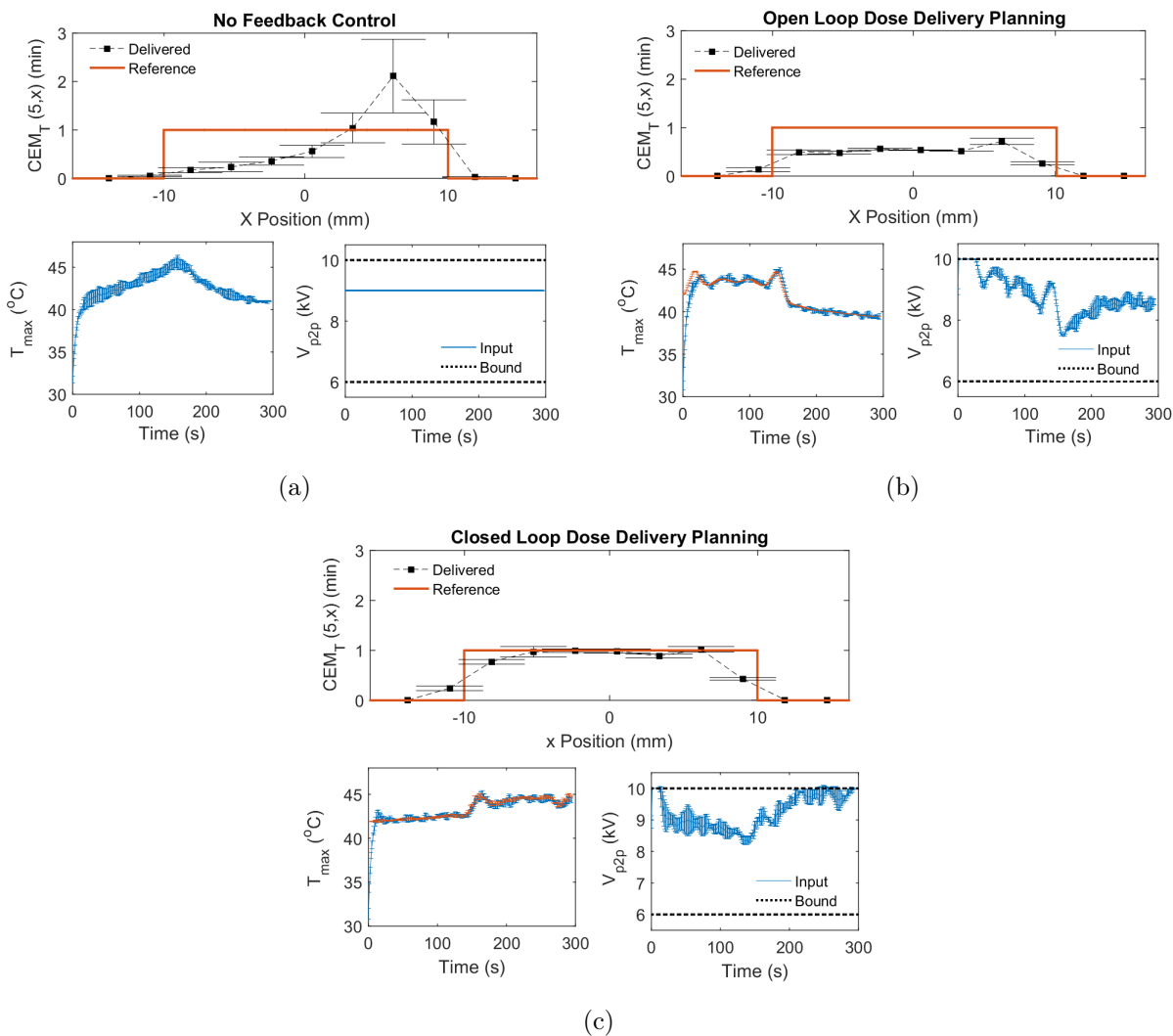
Figure 8.5: Delivered thermal dose $CEM_T(5, x)$ along $x \in [-10, \, 10 \, \mathrm{mm}]$, maximum substrate temperature $T_{\max}$, and applied peak-to-peak voltage V_{p2p} under the APPJ translation trajectory of Case III in Figure 8.4 for: (a) no feedback control and dose delivery planning, (b) the open-loop dose delivery planning strategy, and (c) the closed-loop dose delivery planning strategy. The error bars show the standard deviation of variables based on three replicate runs.

steps of the APPJ translation, which prevent the substrate from being uniformly treated.[2] Figure 8.6 shows that a fairly uniform dose delivery can be achieved along the target region as the APPJ translation rate is increased in Cases II to IV. Higher translation rates result

---

[2]Note that similar nonuniformity in treatment is also observed in the case of discrete device translation strategies in radiotherapy applications [204].
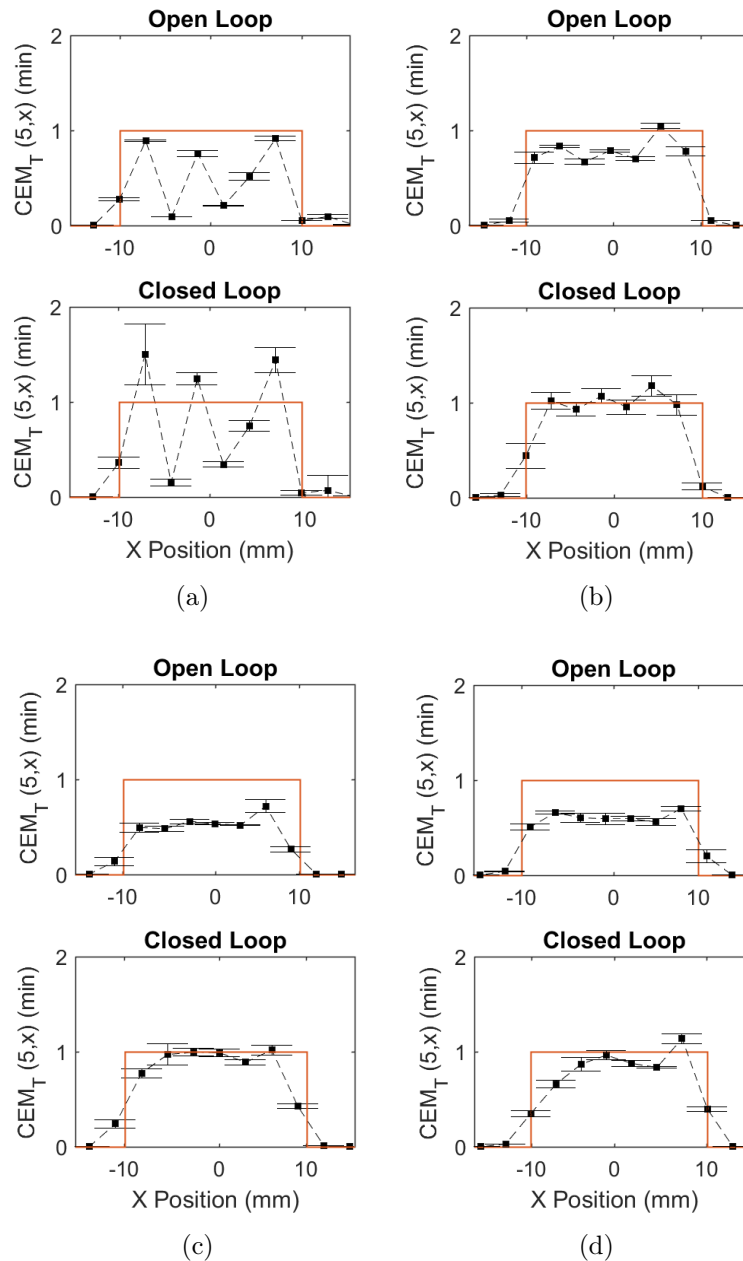
Figure 8.6: Delivered thermal dose $CEM_T(5, x)$ along $x \in [-10,\ 10\,\text{mm}]$ using the open-loop and closed-loop dose delivery planning strategies under the APPJ translation rates of (a) Case I, (b) Case II, (c) Case III, and (d) Case IV. The red profiles depict the reference thermal dose $CEM_T^{\text{ref}}(5, x)$. The error bars show the standard deviation of the delivered thermal dose based on three replicate runs.
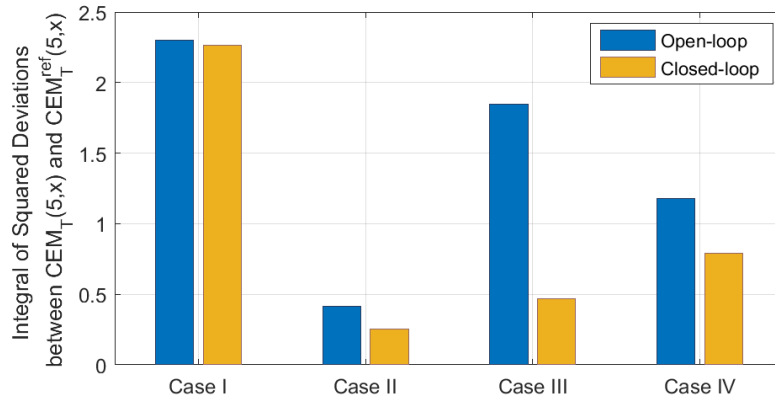
Figure 8.7: Performance comparison of the open-loop and closed-loop dose delivery planning strategies under the different APPJ translation rates. The dose delivery performance is quantified as the integral of squared deviations between the delivered, $\mathrm{CEM_T}(5, x)$, and reference, $\mathrm{CEM_T^{ref}}(5, x)$, thermal dose.

in smaller discrete translation steps, toward continuous APPJ translation in Case IV (see Figure 8.4). This observation suggests there should exist a minimum translation rate below which uniform dose delivery is impractical.

Furthermore, Figure 8.6 shows that irrespective of the APPJ translation rate, the open-loop dose delivery planning strategy leads to an offset in dose delivery with respect to the reference thermal dose. On the other hand, the closed-loop strategy enables realizing the reference thermal dose level of $\mathrm{CEM_T^{ref}}(5, x) = 1$ fairly uniformly along the target region. The performance comparison of the open-loop and closed-loop strategies under the different APPJ translation rates is summarized in Figure 8.7, where the dose delivery performance is quantified as the integral of squared deviations between the delivered and reference thermal dose, i.e.,

$$\int_{-10}^{10} \|\mathrm{CEM_T}(5, x)dx - \mathrm{CEM_T^{ref}}(5, x)\|^2 dx.$$

Note that the expression above is, in fact, the first term in the objective function of the optimization problem in the supervisory controller (see (8.3a)). Figure 8.7 indicates that the closed-loop dose delivery planning strategy consistently outperforms the open-loop strategy under the four translation rates. However, as the translation rate increases from Case II to IV, the performance of the closed-loop dose delivery planning strategy slightly deteriorates. This can be attributed to the fact that a higher rate of the APPJ translation will perturb the spatial distribution of the delivered thermal dose more significantly.
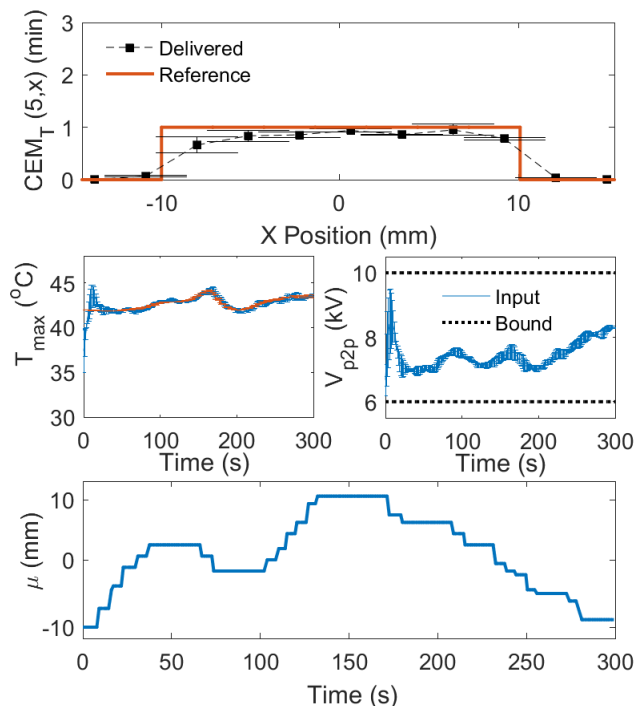
Figure 8.8: Delivered thermal dose $CEM_T(5, x)$ along $x \in [-10, \, 10 \, \text{mm}]$, maximum substrate temperature T_{max}, and applied peak-to-peak voltage V_{p2p} for the closed-loop dose delivery planning strategy under the offline-computed optimal APPJ translation trajectory μ. The error bars show the standard deviation of variables based on three replicate runs.

8.4.2 Thermal Dose Delivery under Optimal APPJ Translation Trajectory

The dynamic optimization problem (8.3) can be modified to include the APPJ translation trajectory $\mu(t)$ as a decision variable, along with the reference temperature $T_{\text{max}}^{\text{ref}}$. Figure 8.8 shows the delivered thermal dose using the closed-loop dose delivery planning strategy when the optimal APPJ translation trajectory is computed offline. Interestingly, the optimal APPJ trajectory has some resemblance to the translation trajectory of Case III (see Figure 8.4) in that the APPJ is translated to the end of the target region and back. In comparison with the thermal dose delivery under the trajectories of Cases II and III (see Figure 8.4), the optimal translation trajectory results in slight improvement in the dose delivery.

8.5 Conclusions

This chapter investigated the usefulness of advanced feedback control methods for real-time regulation of thermal dose delivery using the kHz-APPJ in He. To this end, a hierarchical, feedback control strategy is proposed, which consists of a proportional-integral controller for fast disturbance rejection and a supervisory, optimization-based controller for online planning of the thermal dose delivery. Although this work focuses only on thermal effects, the proposed strategy can be readily extended to include multiple plasma effects. As demonstrated in Chapters 6 and 7, optimization-based control strategies can accommodate multivariable dynamics. The key challenges remaining in the development of practical and comprehensive control strategies for APPJ are effective sensing and tractable modeling of complex plasma effects including chemistry. Particularly, models of plasma dose in terms of measurable plasma properties is an essential component for the regulation of dose delivery.

The real-time control experiments demonstrated that the supervisory controller enables achieving close-to-uniform dose delivery along the one-dimensional target region under different translation rates of the APPJ. However, the implementation here is limited to a single output variable and 1D. Moreover, the dynamics that arise from the closed-loop system (that is APPJ and the PI controller for T_{max}) are neglected here. Next chapter focuses on extending this to approach to address these issues for uniform thermal dose delivery on two-dimensional surfaces with non-uniform electrical and thermal characteristics and in the presence of disturbances.

Chapter 9

Spatially Uniform Dose Delivery with Model Predictive Control in 2D

The regulation of dose delivery in 2D in presence of disturbances is demonstrated. A hierarchical control strategy is employed composed of a basic proportional-integral control layer for rapid disturbance rejection and a supervisory nonlinear model predictive control (NMPC) layer for regulating the spatial thermal dose delivery in 2D. The closed-loop dynamics of the lower-level basic control layer is identified and incorporated into the NMPC strategy to allow effective dose regulation in the presence of disturbances. Experimental results demonstrate drastically improved dose delivery performance with the hierarchical control strategy in the presence of disturbances in jet tip-to-surface separation distance and in electrical and thermal properties of the treated substrate.[1]

9.1 Introduction

As outlined in the previous chapters, the end-goal of APPJ treatment is the reliable and effective delivery of a cumulative and spatially distributed effect, or a spatial plasma dose to the target substrate. This can be a challenging task due to the sensitivity of APPJs to disturbances (i.e., disturbance), which can drastically impact dose delivery. The sharp spatial gradients in APPJ characteristics can easily result in non-uniformity in delivered dose distributions. Moreover, hand-held operation relies on the operator to maintain the jet-tip-to-substrate separation distance, variation of which can result in drastic changes in APPJ characteristics and the delivered cumulative effects [7], [123], [179], [187]. Similarly, changing electrical and thermal properties of the substrate can considerably influence the APPJ characteristics, particularly when the substrate is electrically coupled to the discharge [6], [25], [127], [177].

The previous chapter demonstrated that optimization-based advanced control strategies can significantly improve reliable, reproducible and effective spatially distributed dose de-

---

[1]This chapter is adapted from material submitted for publication in [205].

livery with APPJs in 1D. This chapter extends the spatial dose delivery approach to 2D. Specifically, the effects of the disturbances on key characteristics of APPJ-substrate system (e.g., discharge power, substrate temperature) and on spatiotemporal dose delivery is investigated. The separation of timescales of physical phenomena in the APPJ and the target substrate can guide the development of a control architecture capable of achieving this task. Fast phenomena such as the response of discharge electrical properties ($\sim$ms) and substrate thermal response ($\sim$s) to exogenous perturbations should be addressed rapidly. In contrast, the dose accumulation is considerably slower ($\sim$min), allowing for the time needed for the complex task of treatment planning. Hence, a hierarchical (i.e., multi-level) control structure is well-suited for this problem: basic proportional-integral (PI) controller implemented in the lower level (i.e., fast timescales) can allow fast rejection disturbances. An optimization-based nonlinear model predictive control (NMPC) strategy, acting in a supervisory capacity, can plan dose delivery accounting for the nonlinear and spatially varying nature of dose accumulation as well as the APPJ translation trajectory. There are two key differences between the strategy proposed here and the strategy presented in the previous chapter. First, a cascade control strategy is employed in the lower level including an embedded power controller for fast disturbance rejection (see Section 5.4). Second, the closed-loop dynamics of the basic control layer is identified and incorporated into the MPC optimization.

The hierarchical control strategy is experimentally demonstrated to enable spatially uniform thermal dose delivery in 2D in the presence of two key disturbances in APPJ operation: (i) changes in separation distance, which can arise during hand-held treatment or treatment of uneven surfaces and (ii) abrupt changes in substrate properties, which can arise when thermally and electrically heterogeneous substrates are treated. Using the experimental setup described in Chapter 3, dose delivery performance is investigated under comparatively drastic disturbance realizations in order to examine the limits of the proposed control strategy. The results indicate that the proposed hierarchical control strategy with NMPC is crucial for reproducible and effective spatial dose delivery.

9.2 Thermal Dose Delivery

As in previous chapters. the thermal dose metric of Cumulative Equivalent Minutes ($\mathrm{CEM_T}$) at a reference temperature of 43 ^{o}C is adapted to quantify the nonlinear thermal effects of the APPJ on a substrate (see Section 4.3). [27]. The spatially-varying $\mathrm{CEM_T}$ is defined as

$$\mathrm{CEM_T}(\tau, x, y) = \int_0^\tau K^{\left(43 - T(t,x,y)\right)} \, \mathrm{d}t. \tag{9.1}$$

Recall here, that the parameter K describes the response of the substrate to thermal stress. The reference temperature and the value of K can be chosen according to the properties of the target heat-sensitive substrate. In this chapter, the expression reported in Section 4.3 is employed, which describes the thermal stress-response of biological substrates based on the

response of CHO cells to thermal stress. The dose definition (9.1) is widely used clinically
for dosing hyperthermia treatments [18], [27], [168].

(a)   (b)
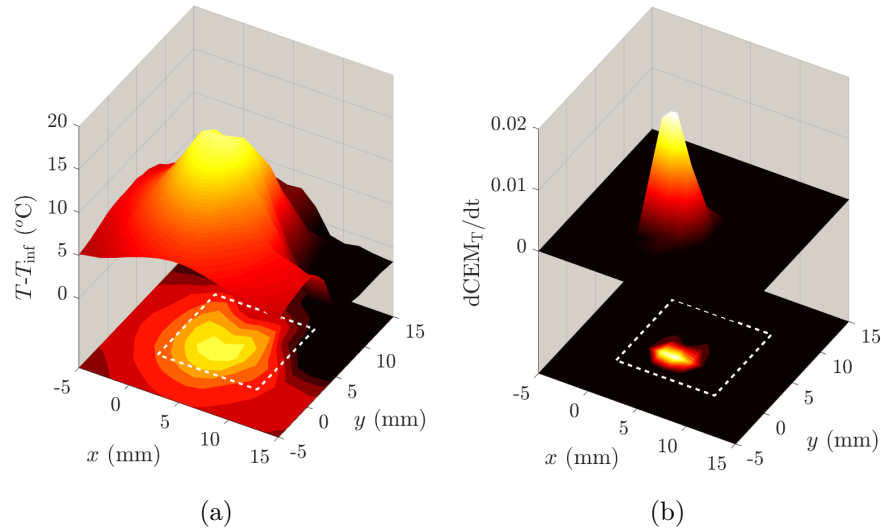
Figure 9.1: Spatial distribution of the thermal effects of the APPJ across the x-y plane.
Surface plots and projected contour plots of (a) the temperature distribution on a glass
substrate and (b) the corresponding rate of the thermal dose accumulation. APPJ is operated
with dissipated power of 3 W and He flow rate of 1.5 slm. The dashed lines circumscribe a
treatment area of 1 cm^2.

The spatial nature of the dose definition (9.1) requires a description of the spatial distri-
bution of temperature on the substrate. A typical measurement of the substrate temperature
for the APPJ at hand is shown in Figure 9.1(a). The spatial distribution of the substrate
temperature is approximated by a bivariate Gaussian distribution as

$$T(t, x, y) = (T_{\max}(t) - T_{\inf})e^{-\frac{\left([x,y]-[\mu_x(t),\mu_y(t)]\right)^2}{\sigma(t)^2}} + T_{\inf},\qquad(9.2)$$

where, $T_{\max}$ is the the maximum substrate temperature, $T_{\inf}$ is the ambient temperature,
σ^2 is the spatial variance of the temperature distribution, and μ_x and μ_y are the $x-$ and
$y-$position of the jet centerline. An important observation here is that the exponential
nature of CEM$_T$ (see (9.1)) results in a spatial distribution for the thermal dose delivered
to the substrate that is sharper (i.e., a smaller variance) than that of the temperature, as
shown in Figure 9.1(b).

The time-evolution of the two variables $\mu_x(t)$ and $\mu_y(t)$ constitutes the translation trajec-
tory of the APPJ, chosen by the user. The translation trajectory is generally a function of the
desired dose delivery objective, the thermal dynamics of the substrate, the total treatment
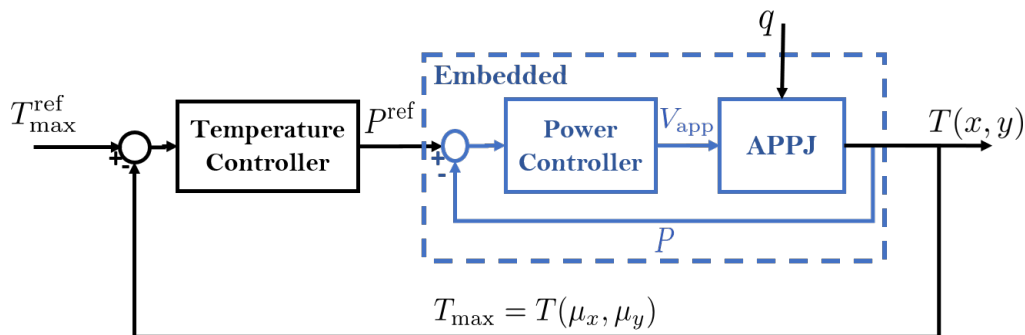
Figure 9.2: The basic control layer. The dashed box shows the embedded proportional-integral controller for the plasma power, which is implemented in the ms timescale. The proportional-integral controller for the maximum substrate temperature is cascaded to the embedded controller.

time, and the spatial distribution of the dose. In the next section, an open-loop "optimal" approach for computing the translation trajectory is presented.

9.3 Hierarchical Control Strategy for Thermal Dose Delivery

Based on the separation of timescales between the APPJ dynamics and the thermal dynamics of the target substrate, a hierarchical control strategy is proposed for regulating the 2D spatial distribution of the delivered thermal dose. The hierarchical control strategy, consists of (i) a basic control layer that enables fast rejection of disturbances acting on the substrate temperature dynamics, and (ii) NMPC layer that computes the "optimal" setpoint for the maximum substrate temperature at the APPJ centerline, supplied to the basic control layer. In addition, a feedforward controller is designed to mitigate measured variations in the type of the substrate. Each of the components of the hierarchical control structure are discussed below.

9.3.1 Basic Control Layer

Figure 9.2 depicts the basic control layer consisting of two proportional-integral (PI) controllers: an embedded controller for the plasma power and a cascade controller for the maximum substrate temperature. The embedded power controller is used to maintain the plasma power at the desired setpoint P^{ref} in the presence of unknown (i.e., unmeasured) disturbances acting on the APPJ by manipulating the applied voltage V_{app} in ms timescale. Note that the dissipated power in the APPJ is one of the main plasma outputs that influence the substrate thermal dynamics. The cascade temperature controller, thus, aims to control the maximum substrate temperature measured at the jet centerline (T_{max}) by manipulating
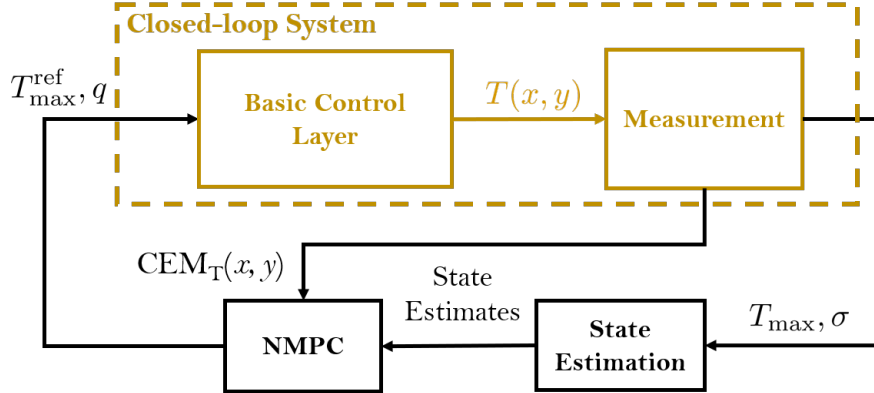
Figure 9.3: The hierarchical control strategy with NMPC. The dashed box shows the closed-loop system consisting of the basic control layer and the measurement The NMPC is tasked to predict and accordingly plan the spatial dose delivery by computing the "optimal" setpoints for the temperature controller.

the power setpoint (P^{ref}) of the embedded controller. $T_{\max}$ is a key state variable governing the spatial distribution of the substrate temperature, as described by (9.2). Both PI controllers in the basic control layer are designed using the internal model control (IMC) tuning rules [185]. The tunings for the PI controllers are given in Appendix D.

9.3.2 Nonlinear Model Predictive Control

Figure 9.3 depicts the hierarchical control strategy with NMPC. The NMPC is tasked to determine the "optimal" setpoints of the cascade temperature controller in the basic control layer, accounting for the spatially distributed and nonlinear nature of the dose delivery problem. For planning dose delivery, MPC relies on predictions of the dose distribution based on a model of the spatiotemporal behavior of the substrate temperature. As the spatial temperature distribution is parametrized with (9.2), it is necessary to first model the dynamics of $T_{\max}$ and σ^2 in response changes to actuated variables. Thus measurement block in Figure 9.3 extracts the values of $T_{\max}$ and σ^2 from spatially resolved temperature measurements $T(x,y)$. The other function of the measurement block is to keep track of the delivered dose by integrating $T(x,y)$ according to (9.1), which is also necessary for predictions of the dose distribution. We describe the dynamics of $T_{\max}$ and σ^2 as "closed-loop dynamics" as they rely on the basic control layer (Figure 9.2). We employ a linear state-space model to describe the closed-loop dynamics

$$\mathbf{x}_{i+1}^{\text{cl}} = A\mathbf{x}_i^{\text{cl}} + B\mathbf{u}_i \tag{9.3}$$
$$\mathbf{y}^{\text{cl}} = C\mathbf{x}_i^{\text{cl}},$$

where $\mathbf{x}^{\text{cl}}$ are a-physical states describing the time evolution of the dynamics, the outputs $\mathbf{y}^{\text{cl}}$ are the mean (i.e., maximum substrate temperature) and variance of the spatial distribution

of the substrate temperature $\mathbf{y}^{\mathrm{cl}} = [T_{\max}, \sigma]^{\top}$; and inputs $\mathbf{u}$ are the maximum temperature
setpoint and the flow rate of He $\mathbf{u} = [T_{\max}^{\mathrm{ref}}, q]^{\top}$. The state-space model (9.3) is identified
from experimental data collected using only the basic control, exciting q and $T_{\max}^{\mathrm{ref}}$. The
subspace identification routine routine `n4sid` (the canonical variable algorithm) is used in
MATLAB (MathWorks®) for model identification. The model identification and validation
results for the closed-loop model are presented in Appendix C.6.

To predict the thermal dose accumulation on the substrate, the closed-loop dynamics
(9.3) are coupled with a discrete-form of the $\mathrm{CEM}_{\mathrm{T}}$ expressions (9.1)-(9.2), which describe the
thermal dose delivery in terms of the spatiotemporal dynamics of the substrate temperature.
Accordingly, the dynamics of the dose delivery are described by a set of nonlinear ordinary
differential equations of the discrete-time form

$$\mathbf{x}_{i+1} = f(\mathbf{x}_i, \mathbf{u}_i, \boldsymbol{\theta}) \tag{9.4}$$
$$\mathbf{y}_i = h(\mathbf{x}_i, \mathbf{u}_i, \boldsymbol{\theta}),$$

where the states are $\mathbf{x} = [\mathbf{x}^{\mathrm{cl}}, \mathrm{CEM}_{\mathrm{T}}(x, y)]^{\top}$, the outputs are $\mathbf{y} = [\mathbf{y}^{\mathrm{cl}}, \mathrm{CEM}_{\mathrm{T}}(x, y)]^{\top}$, and
the parameters are $\boldsymbol{\theta} = [A, B, C, D, K, \mu_x, \mu_y]^{\top}$.[2] Note here that CEM_T also depends on the
$T_{\max}$ and σ^2 which are the outputs of the closed-loop model (9.3).

The 2D thermal dose delivery problem is formulated in terms of minimizing the square
of 2-norm of the difference between the thermal dose distribution at the end of the treat-
ment time $\mathrm{CEM}_{\mathrm{T}}(\tau, x, y)$ and a user-specified spatial thermal dose $\mathrm{CEM}_{\mathrm{T}}^{\mathrm{ref}}(x, y)$. Thus, the
objective function of the NMPC, discretized in time and space, takes the form of

$$J = \sum_{x}^{L} \sum_{y}^{L} \|\mathrm{CEM}_{\mathrm{T}}(\tau, x, y) - \mathrm{CEM}_{\mathrm{T}}^{\mathrm{ref}}(x, y)\|^2 + \sum_{i=1}^{N_c} \|\Delta \mathbf{u}_i\|_Q^2, \tag{9.5}$$

where τ denotes a user-specified treatment time, L denotes the length of the square-shaped
treatment area, $Q = 0.01$ is the relative weights assigned to input changes, and N_c is the
control horizon over which the decision variables $\mathbf{u_i}$ are designed. Here, the the treatment
area of dimensions $L \times L$ is discretized into a grid of 2×2 mm squares (see Figure 9.1).

To account for practical considerations such as the operational limitations of the APPJ
or the reliability and reproducibility of the plasma treatment, the objective function (9.5) is
minimized subject to the following constraints on the inputs $\mathbf{u}$ and outputs $\mathbf{y}$

$$\mathcal{Y} = \left\{ \mathbf{y} \mid 30\ ^o\mathrm{C} \le T_{\max} \le 46\ ^o\mathrm{C} \text{ and } 5 \text{ mm} \le \sigma^2 \le \infty \right\}, \tag{9.6}$$

$$\mathcal{U} = \left\{ \mathbf{u} \mid 30\ ^o\mathrm{C} \le T_{\max}^{\mathrm{ref}} \le 45\ ^o\mathrm{C} \text{ and } 1.5 \text{ slm} \le q \le 3.5 \text{ slm} \right\}. \tag{9.7}$$

The upper bound on $T_{\max}$ in (9.6) represents a critical temperature above which the heat-
sensitive substrate can be damaged. On the other hand, σ^2 is a proxy for the width of

---

[2]Note that boldface $\mathbf{x}, \mathbf{y}$ are the vectors of states and outputs while italic x, y are spatial coordinates

the incident discharge. The discharge shrinks as it tends toward extinguishment, causing a sharper temperature distribution on the substrate and thus a smaller value of σ^2 . Hence, the lower bound σ^2 ensures the discharge is ignited and stable. The input constraints (9.7) correspond to the limits of the operating region for which the closed-loop model (9.3) remains valid.

Dose delivery is implemented in a feedback fashion. This implies that the objective (9.5) should be minimized subject to the constraints (9.6)-(9.7) and the nonlinear dose delivery dynamics (9.4), given the most recent state of the system, and more specifically the current dose delivered. The feedback implementation, therefore, requires knowing the states of the nonlinear system (9.4). However, the closed loop states $\mathbf{x}^{cl}$ cannot be directly measured. Thus a Luenberger observer [206] is used to estimate the closed-loop states based on measurements of the closed-loop outputs $\mathbf{y}^{cl}$. On the other hand, the delivered dose $CEM_T(x, y)$ is directly inferred from spatially resolved temperature measurements $T(x, y)$ (see Figure 9.3). Once the states $\hat{\mathbf{x}}_k$ are estimated from measurements, at every sampling time k the NMPC solves the following optimal control problem

$$\min_{\boldsymbol{\pi}} \quad J(\boldsymbol{\pi}, \hat{\mathbf{x}}_k) \tag{9.8a}$$

$$\mathbf{x}_{i+1|k} = f(\mathbf{x}_{i|k}, \mathbf{u}_i, \boldsymbol{\theta}) \qquad\qquad i = 0, \dots, N_{p-1} \tag{9.8b}$$

$$\mathbf{y}_{i|k} = h(\mathbf{x}_{i|k}, \mathbf{u}_i, \boldsymbol{\theta}) \qquad\qquad i = 0, \dots, N_p \tag{9.8c}$$

$$\mathbf{u}_{i|k} \in \mathcal{U} \qquad\qquad i = 0, \dots, N_{c-1} \tag{9.8d}$$

$$\mathbf{y}_{i|k} \in \mathcal{Y} \qquad\qquad i = 0, \dots, N_p \tag{9.8e}$$

$$\mathbf{x}_{0|k} = \hat{\mathbf{x}}_k, \tag{9.8f}$$

where N_p and N_c are prediction and control horizons, respectively, and $\boldsymbol{\pi} = [\mathbf{u}_0, \dots, \mathbf{u}_{N_c-1}]^\top$ is the vector of decision variables. First element of the vector of the optimal decision variables, the solution to (6.12), is applied to the APPJ. One of the inputs, T_{max}^{ref}, is the setpoint to the cascade substrate temperature controller in the basic control layer. The other input, the He flowrate q, is directly applied to the jet (see Figure 9.2. Since the objective (9.5) is defined in terms of the final dose distribution $CEM_T(\tau, x, y)$, the predictions of spatial dose delivery (9.8b)-(9.8c), are carried out until the end of the operation time. Thus, the prediction horizon N_p spans the time interval between the current operation time and the total treatment time τ. Thus N_p gets smaller, i.e. shrinks as the treatment progresses. This implementation is termed shrinking-horizon. Recall N_c describes the interval over which the inputs are designed, chosen here as $N_c=N_p$. The measurement sampling time in this study is 1.3 s, limited by the time required to acquire and process the measurements from the IR thermal camera and optical emission spectrometer (see Figure Chapter 3). The optimal control problem (9.8) is solved in Python using the automatic differentiation toolbox CasADi [195] and the interior-point optimization solver IPOPT [198].

9.3.3 Feedforward Control

The thermal dose delivery is investigated in the presence of an abrupt change in the electrical properties of the substrate, which is mimicked by the transition between glass (dielectric) and metal (conductive) substrates. This change in the type of the substrate can be considered as a drastic disturbance perturbing the thermal dose delivery. To mitigate the effect of this disturbance, a feedforward controller is added to the basic control layer. The key challenge in designing this feedforward controller arises from lack of real-time measurement for the disturbance. To this end, a *soft sensor* based on k-means clustering [207] is utilized to classify the optical emission signal from the APPJ into two distinct categories corresponding to the glass and metal substrates. The details of the k-means clustering and the feedforward control strategy are presented in Sections 5.5 and 10.2.2, respectively.

9.4 Results

The proposed hierarchical control strategy based on NMPC is now tested on the APPJ. The goal is to uniformly deliver a CEM_T of 0.25 minutes over an area of 1 cm^2 within a treatment time of 1 minute. The chosen translation rate of 1 cm^2/min is relatively fast compared to thermal dynamics of the substrate which have a time constant of approximately 30 s. This rate of translation is inspired by medical applications where the time available for treatment is limited [13], [79]. Note that the APPJ translation presents a disturbance to the thermal dynamics of the substrate and thus, a fast translation rate can complicate spatial dose delivery. The magnitude of the reference thermal dose is chosen according to what is achievable given the thermal dynamics of the substrate in the APPJ setup at hand as well as the predetermined treatment time of 1 min. Four different strategies are investigated for dose delivery: (i) no control (constant voltage), (ii) embedded power control only, (iii) basic control including the cascade temperature controller in Figure 9.2, and (iv) the hierarchical control strategy including the NMPC for spatial thermal dose delivery planning in Figure 9.3. The control strategies are tested under three different operating scenarios: (i) no disturbances (base case), (ii) step changes in jet-tip-to-substrate separation distance (iii) changing substrate type. The time-course profiles of the main state variables and the delivered thermal dose are presented. However, since dose delivery results are generally poor under no control (constant voltage), the corresponding dose distributions are not reported. Prior to implementing the control strategies, a translation trajectory should be selected to allow for the treatment of the desired area. The next section describes the computation of an "optimal" translation trajectory for uniform dose delivery.

9.4.1 Translation Trajectory

The choice of the translation trajectory of the APPJ is one of the key components of the spatial dose delivery problem as it can drastically effect the dose distribution. However, selection of an appropriate translation trajectory is not trivial. The spatial distribution of

(a)   (b)
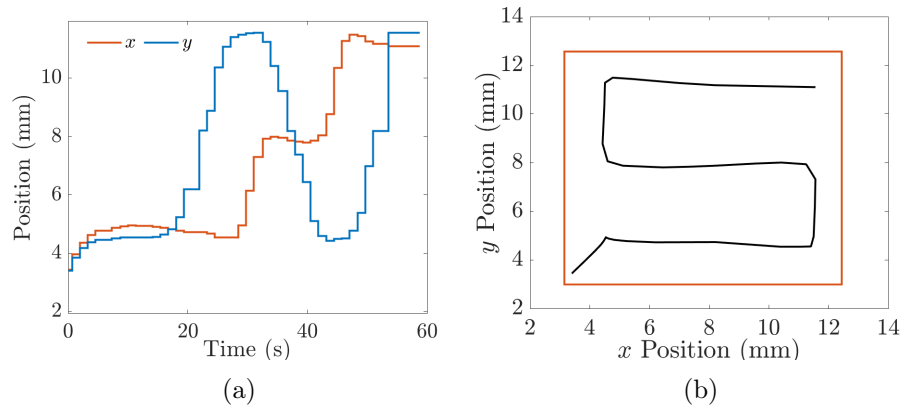
Figure 9.4: The APPJ translation trajectory utilized in control experiments. (a)Time evolu-
tion of the APPJ centerline in x- and y- coordinates and, (b) the treatment area (red square)
and the meandering shape of the translation trajectory (solid black line).

the substrate temperature, the treatment time, and the thermal response of the substrate
generally influence the choice of the translation trajectory. To address the complexities of
this problem, we formulated an offline optimization to determine the "optimal" translation
trajectory in an open-loop sense (i.e., in the absence of any measurement feedback). The
optimal control problem (9.8) is modified to include the translation trajectory (μ_x, μ_y) as
additional decision variables. Solving the optimization problem result in multiple optima,
which implies multiple possible translation trajectories which can correspond to a similar dose
delivery performance. It should be noted that solving the modified optimization problem
is both computationally expensive, and the solution is sensitive to initial guesses for the
translation trajectory. The increased computation time for the problem can make the online
computation of an optimal translation trajectory prohibitive. Depending on the supplied
initial guesses, the optimal translation trajectories are observed to follow either spiraling
or meandering patterns. No apparent advantage is observed for using one pattern over the
other in the control experiments discussed below. Thus, the meandering optimal translation
trajectory, shown in Figure 9.4 is chosen for control experiments. Figure 9.4(a) depicts the
time evolution of the $x-$ and $y-$ position of the APPJ centerline is shown. Notably, the
APPJ remains somewhat stationary between the treatment times 5 and 15 seconds. This
behavior is likely to account for the initial transient of the temperature dynamics as the
surface warms-up. The meandering pattern of the translation trajectory is illustrated in
Figure 9.4(b). The number and spacing of the back and forth strokes are dictated by the
spatial distribution of the CEM_T (Figure 9.1(b)).

(a) No control - constant voltage

(b) Embedded power control

(c) Cascade temperature control

(d) Hierarchical control with NMPC
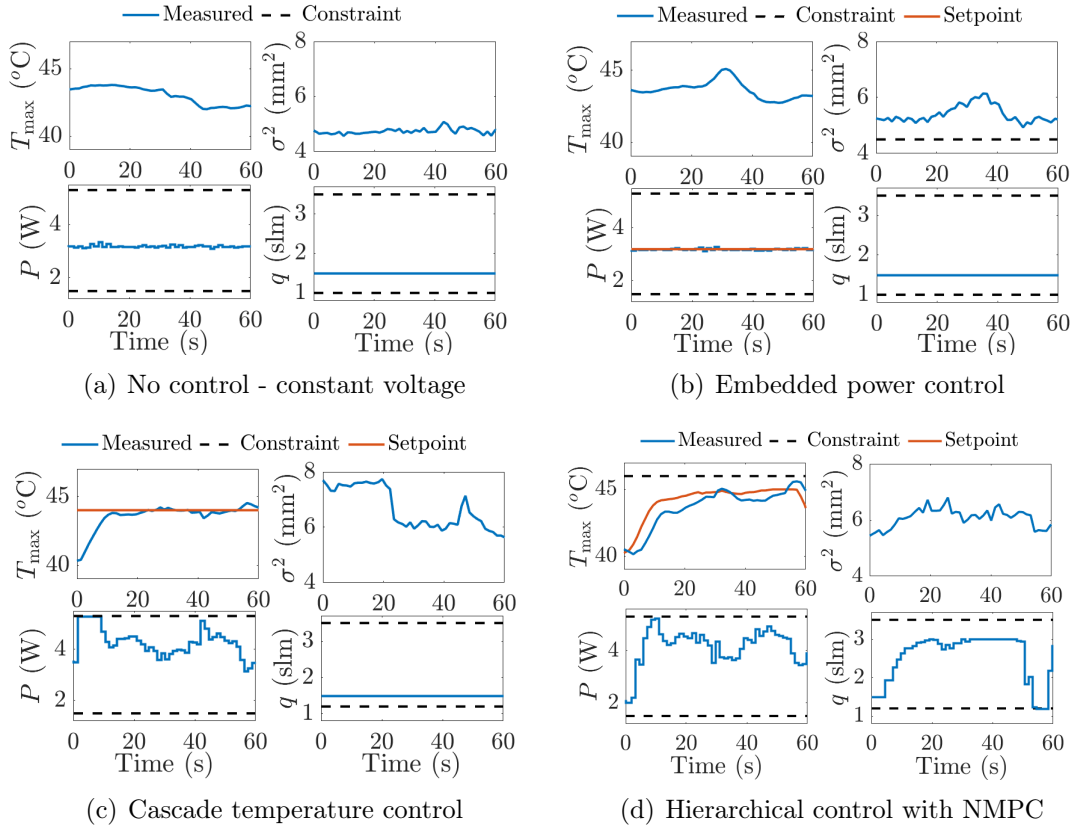
Figure 9.5: Base case control experiments in the absence of measured disturbances acting on the APPJ. The time evolution of the maximum substrate temperature T_{max} and, the variance of the temperature distribution on the substrate σ^2 and the APPJ inputs applied power P and flow rate q.

9.4.2 Base Case

First, a base case is established for comparing the effectiveness of the spatial thermal dose delivery achieved using the four control strategies in the absence of any measured APPJ variations or disturbances. Figure 9.5 the time evolution of the APPJ inputs and outputs for the four investigated strategies: no control (Figure 9.5(a)), constant power P maintained by the embedded power controller (Figure 9.5(b)), constant maximum substrate temperature T_{max} maintained by the cascade temperature controller (Figure 9.5(c)), and, the hierarchical control strategy that uses the NMPC control to regulate the 2D thermal dose delivery. (Figure 9.5(d)). The 2D spatial distribution of the thermal dose delivered at the end of the treatment time using each strategy is shown in Figure 9.6.

Figure 9.5(a) suggests that, in the absence of known/measured disturbances, the plasma power can be retained at the desired level fairly effectively by applying a constant voltage V_{app} to the APPJ. Note that the embedded power controller used in 9.5(b) to maintain a

(a) Reference

(b) Embedded power control

(c) Cascade temperature control

(d) Hierarchical control with NMPC
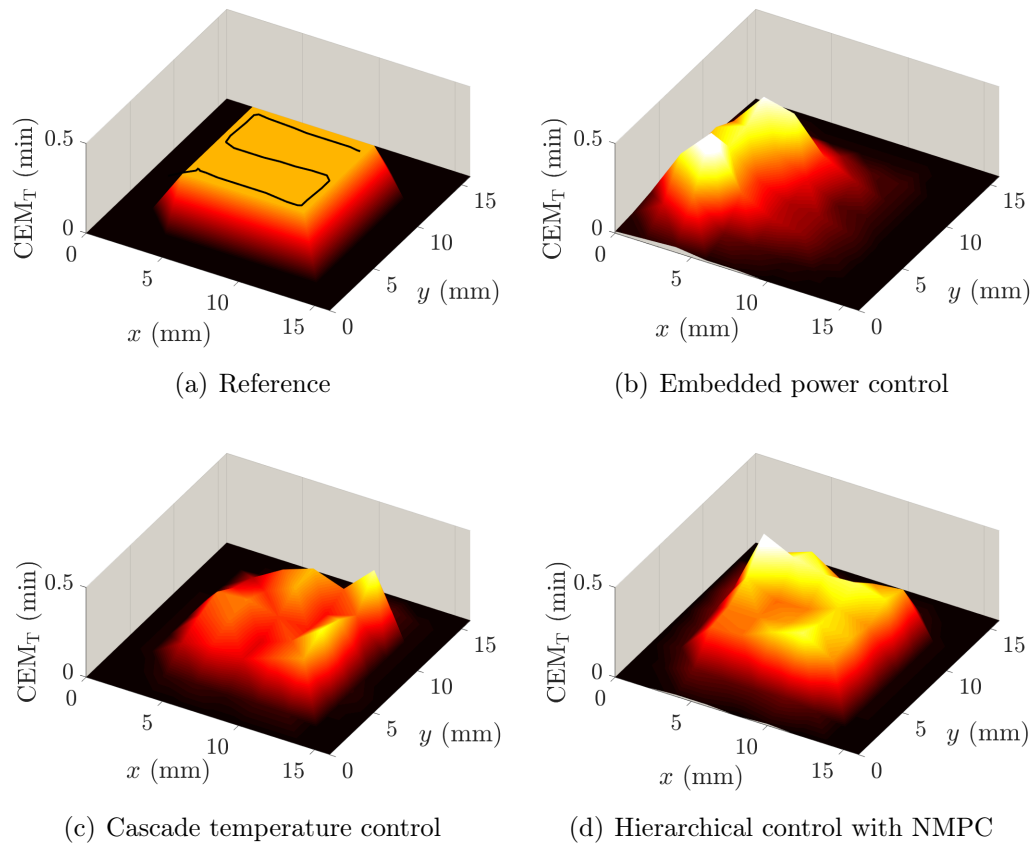
Figure 9.6: The spatial distribution of the delivered CEM_T across the $x - y$ plane at the end of the treatment in the absence of measured disturbances. In subplot (a) the translation trajectory (black) superimposed on the reference dose distribution.

constant power enables rejection of unknown disturbances acting on the APPJ. However, the maximum substrate temperature T_{max} and the variance of the spatial temperature distribution σ^2 cannot be kept constant by maintaining the power (Figures 9.5(a) and 9.5(b)). As a result, the delivered thermal dose with the embedded power controller is spatially non-uniform (Figure 9.6(b)). This indicates the importance of directly controlling the substrate temperature for regulating the thermal dose delivery, even in the absence of known disturbances.

Figure 9.5(c) shows that the cascade temperature controller enables controlling the maximum substrate temperature to remain constant. It is evident that the cascade temperature controller can effectively reject the unmeasured disturbances that upset the thermal dynamics of the substrate (e.g., due to the translation of the APPJ), whereas such disturbances lead to variations in the variance of the temperature distribution that is uncontrolled. Although the cascade temperature control strategy offers an improvement upon the embedded

power control, the delivered thermal dose distribution is still not spatially uniform (Figure 9.6(c)). Specifically, determining the appropriate maximum substrate temperature setpoints that correspond to a desired final spatially distributed thermal dose distribution remains a challenge with the basic control strategy. On the other hand, the NMPC controller in the proposed hierarchical control strategy is capable of systematically determining the optimal sequence of setpoints for the cascade temperature controller, allowing for a close-to-uniform spatial dose delivery (Figure 9.6(d)). Under the hierarchical control strategy, the "optimal" setpoint is evaluated at every sampling time based on the current measurements of dose and estimates of the system states. This allows combining fast disturbance rejection, handled by the basic control layer, with optimal dose planing achieved by the NMPC. Note that in Figure 9.5(d) the optimal setpoints in $T_{\max}$ are not tracked particularly closely. However, since the closed-loop dynamics of the basic control layer in Figure 9.2 are explicitly identified and incorporated ((9.3)) in the optimal control problem (9.8), temperature response of the closed-loop system results in a desirable final thermal dose distribution. Noticeably, Figure 9.6(d), shows overshoot at the APPJ position $x=5$, $y=10$. This is attributed to the fact that the objective is fairly difficult to achieve, considering the characteristic timescale of the thermal response of the substrate is about 30 seconds, half of the total treatment time.

9.4.3 Step Change in the Separation Distance

A common source of disturbance in the operation of APPJs results from variations in the separation distance between the tube nozzle and the substrate. This can typically occur in hand-held treatments or in treatment of substrates with non-uniform topology. Since portable and hand-held operation of APPJs is one of the key considerations in allowing their flexible use, it is crucial that disturbances in separation distance can be rejected effectively.

The effectiveness of the spatial thermal dose delivery is investigated using the four control strategies in the presence of a relatively large disturbance: the separation distance is increased from 4 mm to 10 mm when approximately half of the substrate is treated. At a separation distance of 10 mm, the APPJ is on the verge of decoupling from the substrate, giving rise to fluctuations and erratic behavior. The time evolution of the APPJ inputs and outputs along with the 2D spatial distribution of the delivered thermal dose are shown in Figures 9.7 and 9.8, respectively. Figure 9.7(a) suggests that in the absence of feedback control the increase in the separation distance results in a sharp decrease in the maximum substrate temperature, coupled with a drop in the dissipated power. The time profile of the variance of the temperature distribution σ^2 indicates that the treatment area shrinks at a separation distance of 10 mm. With control, on the other hand, the effects of the separation change on the dissipated power can be rejected rapidly and effectively (Figure 9.7(b)). However, the step change in the separation distance leads to an increase in $T_{\max}$ and, in turn, to a drastic overshoot in the delivered thermal dose (i.e., more than 500-fold relative to the reference thermal dose CEMT$^{\text{ref}}$), as shown in Figure 9.8(b). Such a drastic overshoot results from the nonlinear nature of the thermal dose definition (9.1).
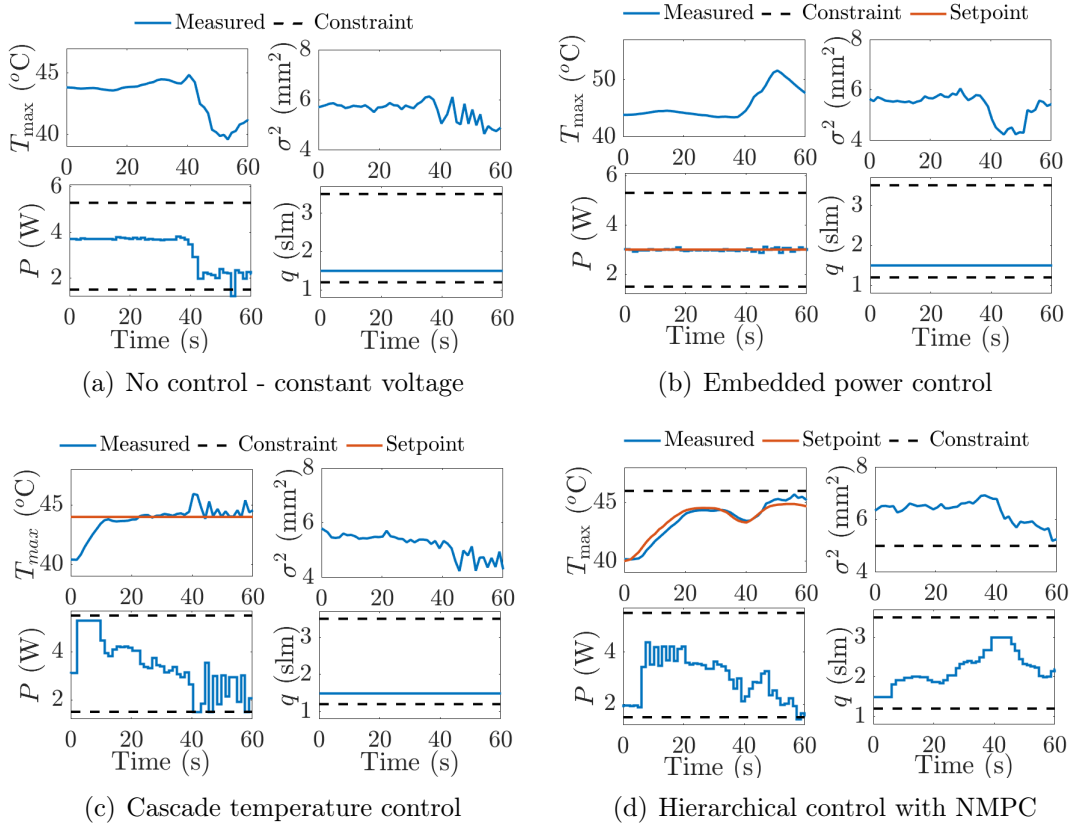
Figure 9.7: Control experiments under a step change of magnitude 6 mm in the jet-tip-to-substrate separation distance. The time evolution of the maximum substrate temperature T_{max}, the variance of the temperature distribution on the substrate σ^2, and the APPJ inputs applied power P and flow rate q.

The cascade temperature control also exhibits some limitations in effectively rejecting the step disturbance in the separation distance. Figure 9.7(c) shows an oscillatory behavior in the maximum substrate temperature T_{max} and rapid changes in the applied power P after the separation distance is increased. Moreover, flickering behavior is observed in the visual appearance of the APPJ, which manifests as spikes in the measurement of σ^2. The still images of the APPJ shown in Figure 9.9(a) indicate that the plasma considerably shrinks and dims during the operation. This behavior indicates that the plasma is unstable, which can impede effective and reproducible thermal dose delivery. As a result, the delivered thermal dose distribution under cascade temperature control is jagged and considerably lower than the reference thermal dose CEMT$^{\text{ref}}$ across the target area once the disturbance occurs. (Figure 9.8(c)).

The effectiveness of the thermal dose delivery is significantly improved using the hierarchical control strategy with NMPC (Figure 7.6). A key advantage of the NMPC is the ability

to handle multiple manipulated variables simultaneously. In this case, by manipulating q and the T_{max}^{ref} at the same time, the NMPC allows for mitigating the effect of the change in separation distance. In this case, no oscillations are observed in the T_{max} (Figure 9.7(d)), and the visual appearance of the APPJ remains stable as shown in Figure 9.9(b). Similarly, the σ^2 remains consistently above the imposed lower bound, indicating the discharge does not shrink or flicker (Figure 9.7(c)). However, there remains an untreated region on the substrate (Figure 7.6). This may have resulted from actuation limitations. Note that there is a trade-off between the achievable combination of T_{max} and σ^2 with increasing q; higher q is associated with a decrease in T_{max} and an increase in σ^2. This implies that it may not be possible to achieve the necessary temperature distribution required for uniform dose delivery.

(a) Reference

(b) Embedded power control

(c) Cascade temperature control

(d) Hierarchical control with NMPC
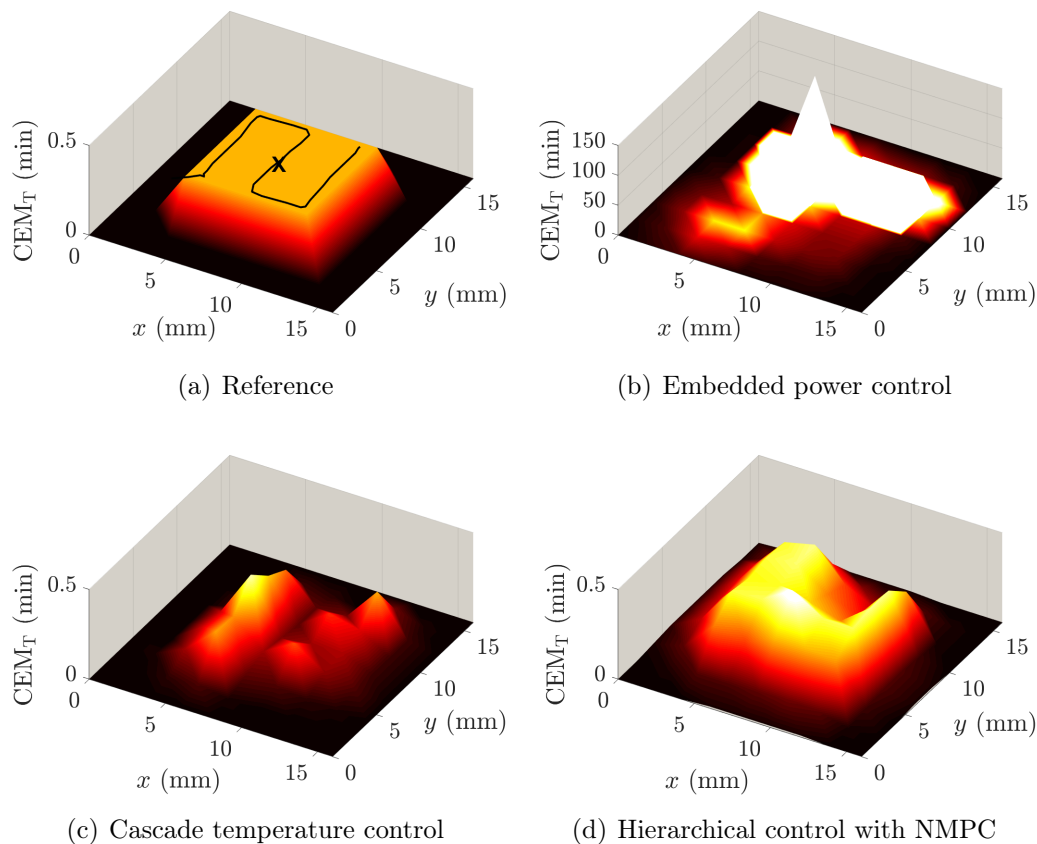
Figure 9.8: The spatial distribution of the delivered CEM_T across the $x - y$ plane at the end of the treatment in presence of a step change in separation distance. In subplot (a) the translation trajectory (black) and the location of the applied disturbance (marked with X) is superimposed on the reference dose distribution.

(a) Cascade temperature control   (b) NMPC
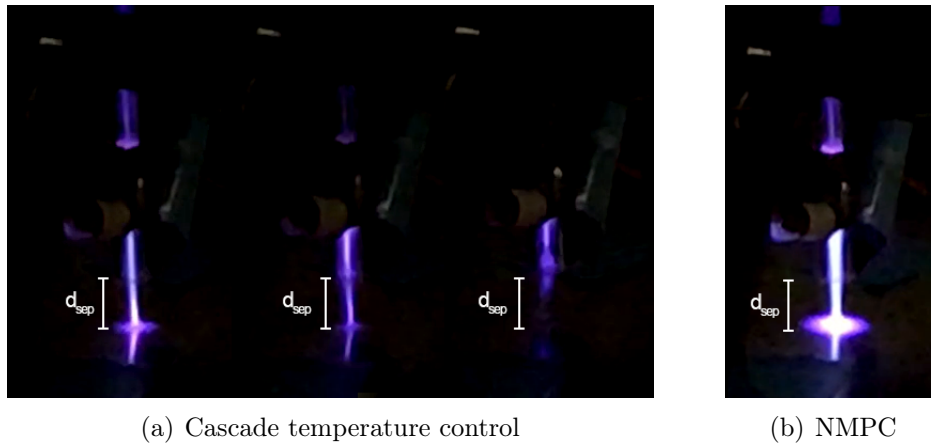
Figure 9.9: Still images of the APPJ at a separation distance of 10 mm under (a) the cascade temperature control and (b) hierarchical control strategy with NMPC.

9.4.4 Abrupt Change in Substrate Type

Abrupt changes in the electrical and thermal characteristic of the substrate can drastically influence plasma properties [6], [25], [127], [177]. Hence, different operating parameters are typically are required to accommodate different substrate types. This can significantly hampers the operational flexibility of APPJs, particularly when the properties of the substrate vary during operation. To investigate the effect of variations in the substrate characteristics on the dose delivery, the APPJ is translated across the a dielectric (glass cover slip) and a conductive (grounded aluminum plate) substrates during treatment (see Figure 9.11(a)). Note that this disturbance is particularly drastic as the electrical properties (e.g., substrate impedance) and thermal properties (e.g., conductivity, heat capacity) of the two substrates are considerably different.

Figure 9.10(a) shows that transitioning the APPJ from a dielectric to a conductive substrate results in the case of constant voltage (i.e., no feedback control) in a sharp increase in P and $T_{\max}$. This can be attributed to the lower impedance of the conductive substrate. In the case of the embedded power control (Figure 9.10(b)), the disturbance in the electrical properties of the substrate is mitigated effectively since the plasma power can be maintained at its setpoint. However, the disturbance in the thermal properties of the two substrates leads to a drastic increase in $T_{\max}$ which cannot be accommodated with the embedded power control strategy. The increase in $T_{\max}$, in turn, results in a large overshoot of approximately 4-fold in the delivered thermal dose relative to the reference $\mathrm{CEM}_{\mathrm{T}}^{\mathrm{ref}}$ (Figure 9.11(b)).

On the other hand, the cascade temperature control strategy can mitigate the disturbance in the substrate type to a considerable extent (Figure 9.10(c)). However, an overshoot in $T_{\max}$ is observed after the substrate transition, which results in a sharp overshoot in the delivered thermal dose distribution (Figure 9.11(c)). Therefore, the cascade temperature control strategy is not capable of effective dose delivery on its own. Note that the cascade

(a) No control - constant voltage

(b) Embedded power control

(c) Cascade temperature control

(d) Hierarchical control with NMPC and feed-forward
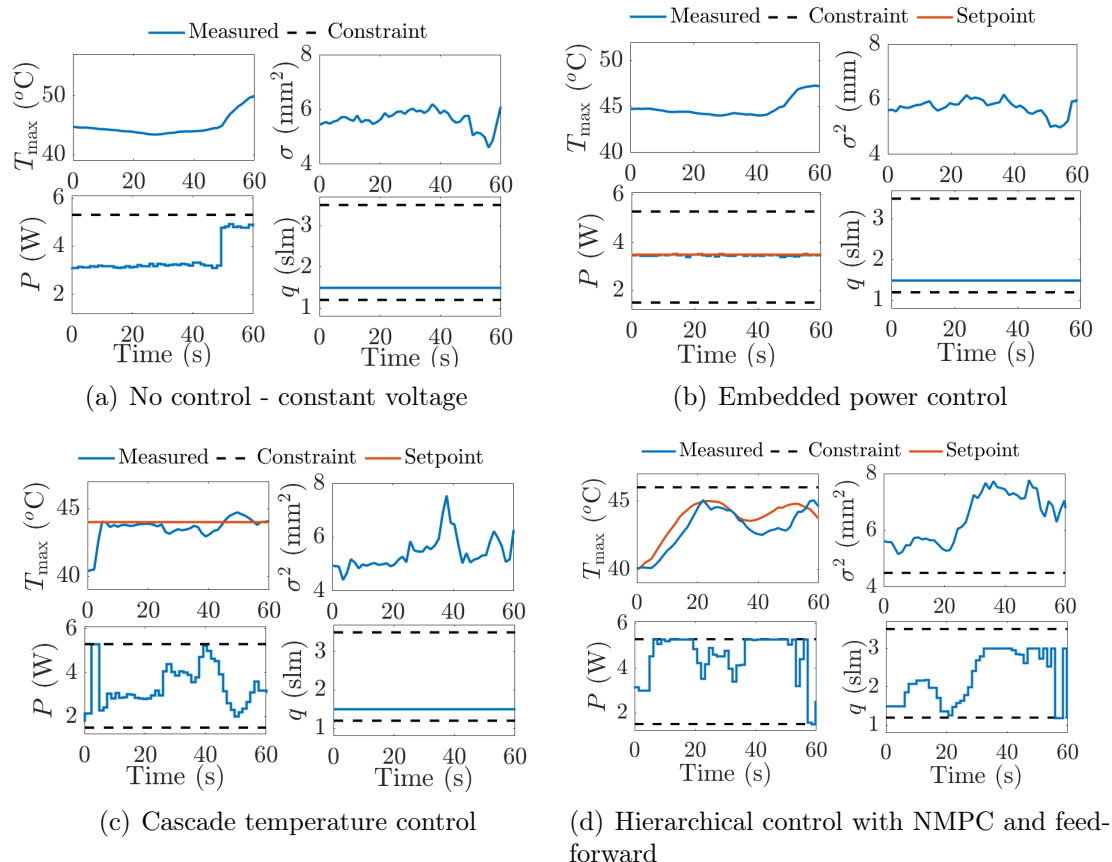
Figure 9.10: Control experiments under an abrupt change in the substrate type when the APPJ transitioned from a glass to a metal substrate at 48 s. The time evolution of the maximum substrate temperature $T_{\max}$, the variance of the temperature distribution on the substrate σ^2, and the APPJ inputs applied power P and flow rate q.

temperature control results reported here are in the absence of feedforward control.

To enhance the ability to handle the change in the substrate type, the hierarchical control strategy combined with a feedforward controller is implemented, leading to a considerable improvement in thermal dose delivery (Figure 9.11(d)). As in the case of the step change in separation distance, actuation limitations can limit the effectiveness of spatially uniform thermal dose delivery. The physical phenomena occurring at the plasma-substrate interface are fundamentally different for conductive and dielectric substrates [6], [25], [178]. For example, charge accumulates on dielectric substrates, allowing the plasma to spread over the treated region. The interaction of the plasma with conductive substrate results in distinct physical phenomena such as the "discharge restrike" [6], [25], [178], leading to a considerable change in the plasma characteristics. It may not be possible to fully mitigate these effects by actuating the given manipulated variables. Moreover, the APPJ has a tendency to couple onto the lower impedance (metal) substrate when it is sufficiently close, making it challenging

to treat the interface of the metal and dielectric substrates.

9.4.5 Summary of Thermal Dose Delivery Results

Finally, in order to quantify the dose delivery performance under the investigated strategies and disturbances, the score metric is defined,

$$
\text{Score} = 1 - \frac{\sum_{x}^{L}\sum_{y}^{L}\|\text{CEM}_\text{T}(\tau, x, y) - \text{CEM}_\text{T}^\text{ref}(x, y)\|^2}{\sum_{x}^{L}\sum_{y}^{L}\text{CEM}_\text{ref}(x, y)}. \tag{9.9}
$$

(a) Reference

(b) Embedded power control

(c) Cascade temperature control

(d) Hierarchical control with NMPC and feedforward
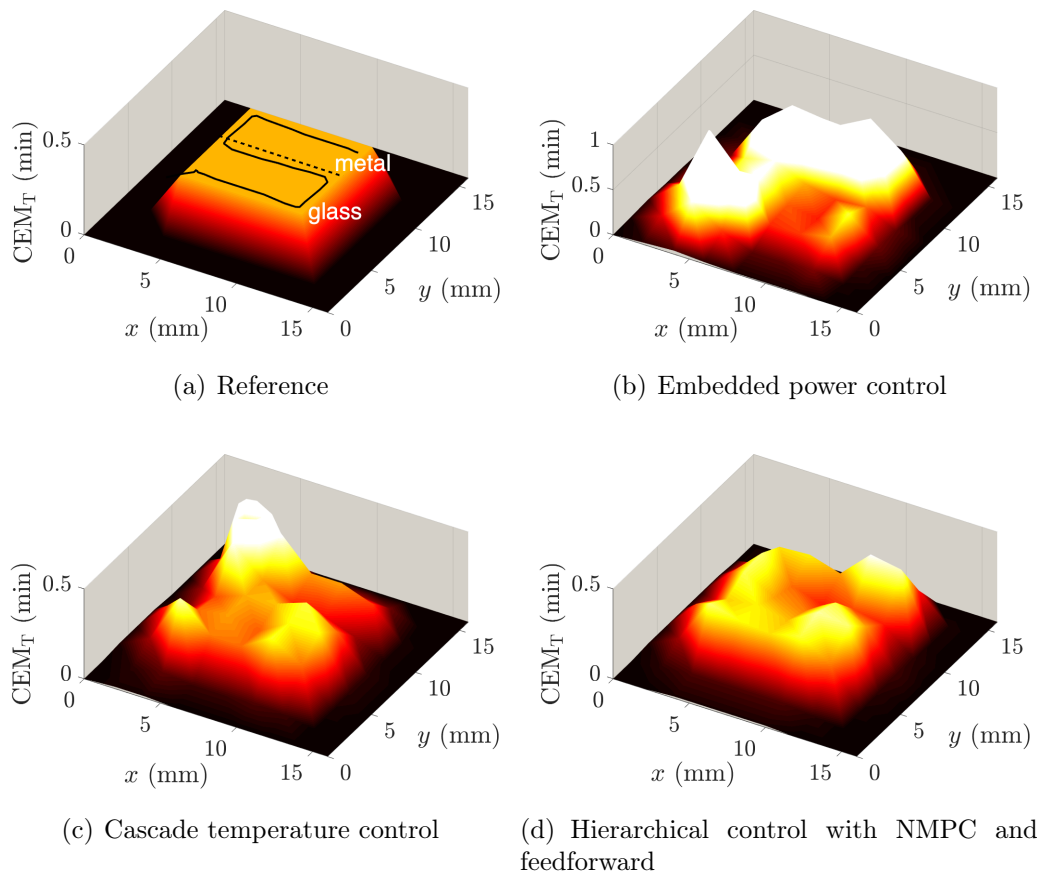
Figure 9.11: The spatial distribution of the delivered CEM_T across the $x-y$ plane at the end of the treatment in an abrupt change in the substrate type. In subplot (a) the translation trajectory (black) and the location of the applied disturbance (dashed line) is superimposed on the reference dose distribution.
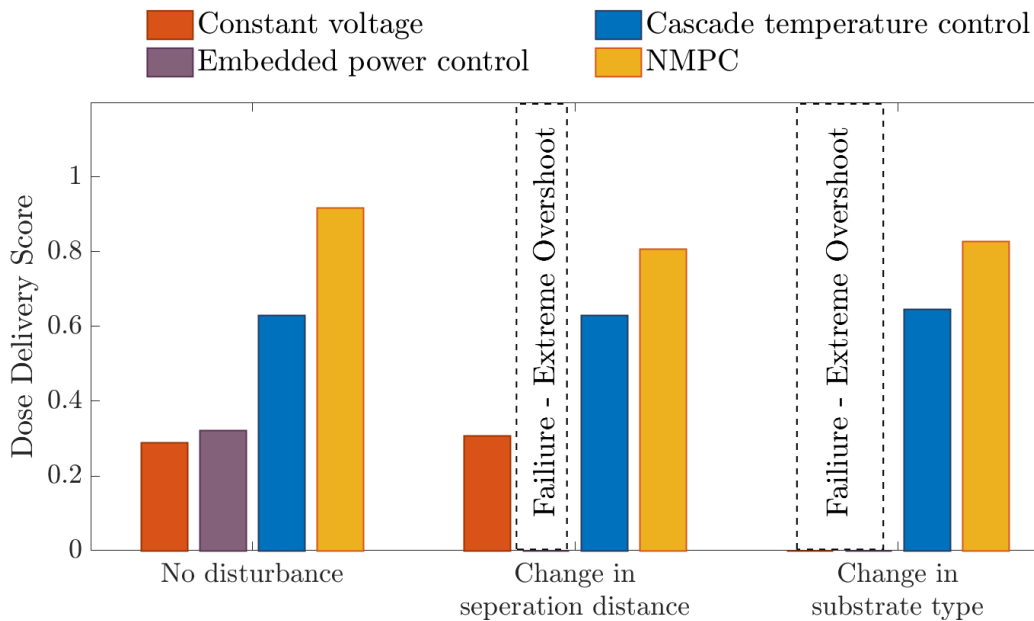
Figure 9.12: Summary of the effectiveness of the four control strategies for uniform dose
delivery CEM_T of 0.25 min across an area of 1 cm^2 at the final treatment time of 1 min. The
hierarchical control strategy with NMPC is superior to other control strategies. In contrast,
using no control (constant voltage) and the embedded power control strategies can result in
failure with extreme overshoot.

With (9.9), perfect dose delivery corresponds to a score of 1, whereas a score of 0 corresponds
to no treatment. The scores calculated using (9.9) for the conditions investigated above are
summarized in Figure 9.12. As expected, dose delivery performance under no control is
generally poor. Even under embedded power control the dose delivery score remains consis-
tently below 0.5, even in absence of disturbances. In presence of disturbances, critical failure
of the treatment is observed, with extreme overshoot in delivered dose distribution under
constant voltage (for changing substrate type) and embedded power control strategies (for
both disturbances). With cascade temperature control, the dose delivery score increases to
about 0.6. and critical failures are avoided. However, this performance is not acceptable for
applications where precise treatment is required, for example, in case of medical applications.
Under the hierarchical control strategy with NMPC, the dose delivery score can reach above
0.9 in absence of disturbances and remains consistently above 0.8 even in presence of the
comparatively drastic disturbances offering a significant increase in performance.

9.5 Conclusions

The results demonstrate the effectiveness of the proposed hierarchical control strategy for the regulation of dose delivery in APPJs under disturbances. Dose planning achieved with NMPC, combined with the rapid disturbance rejection achieved with the basic control layer allows reliable and effective dose delivery. Limitations inherent to the discharge physics and the actuated variables can complicate the uniform delivery of dose under drastic disturbances such as during transition between dielectric and conductive substrates. However, even under such conditions, the proposed control strategy can be instrumental in avoiding drastic failure of operation i.e., thermal damage to the substrate.

A key parameter affecting dose delivery performance is the translation trajectory. In this work, an optimal translation trajectory is determined a priori solving an offline optimization problem. However, our results indicate that real-time trajectory planning can help further improve the control performance, and mitigate some of the shortcomings of the proposed control strategy. For example, untreated regions observed in the presence of changing separation distance can be re-visited with real-time trajectory planning. Another important direction for future work involves substrates with time-varying properties. Substrates can respond to APPJ treatment in various ways (such as drying, coagulation, etc.) which can impact physical properties of the substrate and the discharge-substrate interaction. Obtaining models and developing control strategies which can adapt to the time-varying, nonlinear substrate dynamics during APPJ treatment is a key challenge to be addressed to extend the reliability and capabilities of APPJs.

Chapter 10

Machine Learning for Real-Time Diagnostics

Real-time diagnostics of cold atmospheric plasma (CAP) sources are a key requirement for effective control. However, direct diagnostics of CAPs can be challenging due to the requirement for expensive equipment and complicated analysis. Data analytics that relies on machine learning methods can help address this challenge. In this chapter, the application of several machine learning methods for real-time diagnosis of CAPs is demonstrated using information-rich optical emission spectra and electro-acoustic emission. Data analytics based on machine learning can provide a simple and effective means for estimation of operation-relevant parameters such as rotational and vibrational temperature and substrate characteristic in real time. The results indicate a great potential promise for machine learning for real-time diagnostics of CAPs.[1]

10.1   Introduction

Previous chapters demonstrated the importance and potential of advanced process control in CAPs for safe and reliable operation. A key requirement for effective control is the ability to monitor variabilities in plasma characteristics in real time, for both understanding and minimizing irreproducible plasma effects. The demonstrated control strategies in the previous chapters focused on easily-measured characteristics of the substrates such as temperature and optical emission intensity. However, several potentially important discharge properties such as gas temperatures, species concentrations, and electric fields are not discussed. This is due to the fact that direct quantitative diagnostics of CAP sources can pose a considerable challenge. Methods such as laser-induced fluorescence (LIF) [181], mass spectrometry [182], and spontaneous Raman scattering [209], for example, rely on sophisticated instrumentation and specially designed experimental setups. This is in stark contrast with the current practice of CAP operation in plasma medicine that relies on the flexibility of hand-held treatment

---

[1]This chapter is adapted from published material in [208]

in the absence of plasma diagnostics [13]. Spectral information from various sources such as optical and electro-acoustic emission can be used for plasma diagnostics. Emission signals are often easy to acquire and typically contain a wealth of implicit information about the plasma characteristics [145], [210], [211]. However, this information is often indirect and requires computationally expensive analysis to extract physical quantities such as gas and electron temperatures or reactive species concentrations [211]. This can make the use of spectral information for real-time diagnostics impractical.

Investigation of spectral information for real-time diagnostics of CAP sources has received some attention in the literature. Most notably, O'Connor et al. reported on a multivariate method based on principal component analysis for correlating various optical emission spectrum (OES) peaks to electrical properties and electron density for a dielectric barrier discharge in helium [212]. In contrast to the well-established method of analyzing OES by generating and fitting synthetic spectra to measurements [145], [213], these authors note the potential for developing correlations across large data sets for novel applications

Electro-acoustic emission also contains useful information on plasma characteristics. Diagnostics based on electro-acoustic emission is commonly used in high-temperature materials processing applications such as arc welding [96] and plasma anodizing [214]. Law et al. investigated the application of electro-acoustic emission for process monitoring and control in a DC pulse-modulated APPJ in air [215]. These authors point to the usefulness of spectrally-resolved electro-acoustic emission as a diagnostic tool for various plasma characteristics including surface properties, dissipated power, and the separation distance between the jet nozzle and substrate. O'Connor et al. investigated the electro-acoustic emission of a non-thermal helium plasma jet for process monitoring [216]. They utilize wavelet transforms of electro-acoustic emission for detection of flow modes and anomalies in operation such as sparking phenomena.

In addition, the voltage-current signal is easily available in most plasma setups. Utilization of these signals for diagnostics has been investigated by Walsh et al. in the context of mode behavior of a non-thermal kHz-excited APPJ in helium [110]. These authors demonstrate that phase-space representations of current signals can help distinguish between the three identified modes, although later work by Liu and Kong indicates the detection of mode behavior may be more complicated in the presence of humidity [111]. In [217], Law et al. review the potential application of electro-acoustic emission and current signals for real-time diagnostics and process control.

Data analytics can present an alternative to the commonly used purely physics-based approaches for extracting information from spectra. With the increasing size of available data sets, automated algorithms for discovering patterns in data, broadly referred to as ML methods, have found success as data analytics tools [218], [219]. Some notable applications of ML for data analytics, among many others, include gene discovery [220], remote sensing [221], natrual language processing [222], [223], object recognition in images [224], as well as real-time diagnostics and modeling of low-pressure plasma etch processes [225]–[229]. The availability of easy-to-use software packages such as the open source package scikit-learn [230] and Google's Tensor Flow [231] has made ML methods more accessible, contributing

to their popularity.

This chapter demonstrates the potential of data analytics for real-time diagnostics of CAP sources. Through the use of ML methods, physical quantities, which are otherwise difficult to obtain in real-time due to limitations of instrumentation (e.g., optical setup required for LIF) or time required for analysis (e.g., fitting OES spectra), can be inferred by utilizing the raw spectral information. Three case studies are presented to demonstrate the application of data analytics tools for real-time CAP diagnostics: (i) determination of rotational and vibrational temperature from OES; (ii) discrimination between a conductive and an insulating substrate from OES; and (iii) determination of discharge gap distance from electro-acoustic emission. The rest of the chapter first presents an overview of selected machine learning methods, then describes the utilized experimental setup, and finally presents results pertaining to each of the three investigated cases.

10.2   Machine Learning Methods

In this section the ML methods used in this chapter are reviewed (see, e.g., [218], [219], [232], [233] for a detailed description).

The selection of a suitable ML method relies on two principal considerations related to the output data: (i) whether the output variables are continuous or discrete, and (ii) whether they are used for training a model. When a ML method uses the output data for training, it is known as *supervised* learning, where the goal is to predict continuous (e.g., *regression*) or discrete (e.g., *classification*) output variables. On the other hand, *unsupervised* learning only uses the input data to discover patterns in the data. For example, clustering methods are used to separate data into discrete bins.

Data sets used for ML consist of inputs denoted by $X \in \mathcal{R}^{N \times n}$ and, where applicable, outputs denoted by $Y \in \mathcal{R}^{N \times m}$. Here, n and m are the dimensions of the inputs and outputs, respectively, and N is the number of samples in the data set. One sample of inputs is denoted by $\mathbf{x} \in \mathcal{R}^n$ and one sample of outputs by $\mathbf{y} \in \mathcal{R}^m$. Predictions of a ML are further denoted by $\hat{Y} \in \mathcal{R}^{N \times m}$ and a single instance of prediction by $\hat{\mathbf{y}} \in \mathcal{R}^m$. Data are typically divided into *training*, *validation*, and *test* sets. In general, the majority of the data set (50-90%) is used for training and validation [219]. During *training*, mathematical descriptions of the relationships among the data are inferred. Training typically involves a parametric or non-parametric fitting process. In order to systematically assess the quality of inferences made by an ML model, a *validation* procedure is employed. A common approach is k-fold cross-validation procedure in which the training data are partitioned into k complementary training and validation subsets or *folds* [218]. $k-1$ of the subsets are used for training and the remaining subset is used for validation. To overcome the inherent randomness of arbitrarily partitioning a data set, this process is systematically repeated for different partitioned sets [218]. Furthermore, ML models often have some *hyperparameters*, whose values cannot be directly estimated from data and thus are fixed prior to training. The models are often trained using different values of hyperparameters and subsequently, the appropriate values

are selected based on the model performance in the validation step. Finally, in the *testing* stage, the capability of the ML model is assessed against an independent data set. The performance of the ML model is quantified in terms of some error metrics such as *root mean squared error (RMSE)* and *error fraction* when the output variables are continuous and discrete, respectively. These error metrics are defined as

$$\text{RMSE}(Y, \hat{Y}) = \frac{1}{N} \sum_{i=1}^{N} \sqrt{(\hat{\mathbf{y}}_i - \mathbf{y}_i)^2}, \tag{10.1}$$

and

$$\text{Error Fraction}(Y, \hat{Y}) = \frac{1}{N} \sum_{i=1}^{N} \mathbb{1}(\hat{\mathbf{y}}_i \neq \mathbf{y}_i). \tag{10.2}$$

In expression (10.2), the indicator function $\mathbb{1}$ takes the value 1 when the condition $\hat{\mathbf{y}}_i \neq \mathbf{y}_i$ is met and 0 otherwise.

In Section 10.4, the use of supervised methods for determination of rotational and vibrational temperatures (linear regression) and discharge gap distance (Gaussian process regression), and unsupervised learning methods for discrimination between glass and metal substrates (k-means clustering) are explored. An overview of the adopted ML methods is presented in the remainder of this section.

10.2.1   Linear Regression

Linear regression is widely used in statistical analysis [234]. In linear regression, output variables are described by a linear combination of some (nonlinear) function of the inputs [218]. For a scalar output, a regression model can be written as

$$\hat{y} = \sum_{j=1}^{O} w_j \phi_j(\mathbf{x}), \tag{10.3}$$

where $\mathbf{w} = [w_1, \ldots, w_O]$ is the vector of weights, $\mathbf{x}$ is the vector of inputs, and $\phi_j(\mathbf{x})$ denotes basis functions. Note that expression (10.3) readily generalizes to higher output dimensions. A common choice for the basis functions, which is utilized in this work, is powers of the inputs defined as

$$\phi_j(\mathbf{x}) = \mathbf{x}^j. \tag{10.4}$$

In this case, O, the highest order of the polynomial basis functions in (10.4), comprises the *order* of the regression model. O is treated as a hyperparameter.

In linear regression, the weights $\mathbf{w}$ are determined by solving a least-squares minimization problem. A key challenge in regression is over-fitting. In particular, when a large model order O in (10.3) is selected, a large number of weights should be fitted. This can lead to a regression model that describes the data too closely, even describing the random noise in the data. To avoid overfitting, regularized least-squares estimation is commonly used. Here,

the *least absolute shrinkage and selection operator* (LASSO) method is utilized. The LASSO regression problem for a scalar output is expressed as [235]

$$\min_{\mathbf{w}} ||\hat{y} - y||_2^2 + \alpha ||\mathbf{w}||_1, \tag{10.5}$$

with α being the regularization hyperparameter. In classic linear regression, α is set to 0, leaving only the first term in the least squares problem (10.5). The selection of α governs what is known as the *bias-variance tradeoff* [218]. An excessively large value of α gives rise to *under-fitting* of the data, therefore leading to predictions with a large bias and a small variance. On the other hand, excessively small values of α cause *over-fitting* of the data, yielding predictions with small bias but high variance, since the regression model also captures the noise of the data [233]. The appropriate value of α is selected during the validation step, as described in Section 10.4.1.

The RMSE metric (10.1) provides a measure of the average error between true values and predictions; however, this metric is not sufficiently sensitive to noise in the measurement. Therefore the metric R^2 *score* is also employed. R^2 indicates the capability of the regression model in capturing the variability in the output variables. The R^2 score is defined by

$$\text{R}^2 = 1 - \frac{\sum_{i=1}^{N}(y_i - \hat{y}_i)^2}{\sum_{i=1}^{N}(\overline{y} - \hat{y}_i)^2}, \tag{10.6}$$

where N is the total number of samples, $\hat{y}$ is computed from (10.3), y_i is the i$^{\text{th}}$ measured sample of the scalar output y, and $\overline{y}$ is the mean of the true values of the scalar output

$$\overline{y} = \frac{1}{N}\sum_{i=1}^{N} y_i. \tag{10.7}$$

10.2.2 k-Means Clustering

k-means clustering is an unsupervised ML method used to separate data into k distinct groups or clusters [207]. The clusters are characterized in terms of their center points or *centroids*. In k-means clustering, the centroids of the clusters are initialized at random points and the distance between each input in a cluster to the corresponding centroid is evaluated in terms of some distance metric such as the Euclidean norm. The clusters are then iteratively updated and input clustering is refined by minimizing the sum of distances between the centroids and the inputs in each cluster. k-means clustering relies on the minimization problem

$$\min_{\mathcal{S}} \sum_{i=1}^{k} \sum_{\mathbf{x} \in \mathcal{S}_i} ||\mathbf{x} - \boldsymbol{\mu}_i||_2^2, \tag{10.8}$$

where $\mathcal{S}_i$ is the set corresponding to the ith cluster, $\boldsymbol{S} \in \mathcal{R}^n$ is the set of sets $\mathcal{S}_i$, and $\boldsymbol{\mu}_i \in \mathcal{R}^n$ denotes the centroid of the cluster i. The user-defined hyperparameter in k-means clustering is the value of k. The choice of k can depend on some prior knowledge of data, or can rely on heuristics. In the case study presented in Section 10.4.2, prior knowledge of data is utilized for selection of k.

Note that since k-means clustering is an unsupervised learning method it does not predict clusters of new samples [233]. Nevertheless, new samples can be assigned to a cluster either by pre-computing the relevant groups and dividing the space into regions or by retraining the k-means clustering model when new data becomes available.

10.2.3   Gaussian Process Regression

Gaussian process (GP) regression is a non-parametric supervised ML method that relies on a probabilistic interpretation of the data [236]. In GP regression models, the outputs are assumed to have a joint Gaussian distribution [219]. Thus, the GP regression problem is formulated as estimation of the probability distribution of the predicted variables *conditional* on the training data. The joint *prior* probability distribution of the outputs is expressed as

$$\begin{pmatrix} Y \\ \hat{Y} \end{pmatrix} \sim \mathcal{N}\left(\mathbf{0}, \Sigma\right), \tag{10.9}$$

where $\mathcal{N}$ represents a Gaussian distribution with mean $\mathbf{0}$ and covariance matrix Σ. Without loss of generality, the mean of the joint distribution can be assumed to be zero. Even if the outputs are distributed around some non-zero mean, this value can be subtracted from the joint distribution to satisfy the zero-mean assumption. The covariance matrix Σ is defined by

$$\Sigma = \begin{pmatrix} K & K_* \\ K_*^\top & K_{**} \end{pmatrix}, \tag{10.10}$$

where K, K_*, and K_{**} denote the individual covariance matrices corresponding to combinations of training and test data sets: $K = K(X_{\text{train}}, X_{\text{train}})$, $K_* = K(X_{\text{train}}, X_{\text{test}})$, and $K_{**} = K(X_{\text{test}}, X_{\text{test}})$. The covariance matrices K can be defined in terms of a positive definite kernel function:

$$K(\mathbf{x}, \mathbf{x}') = -\lambda\exp\left(\frac{1}{2\sigma^2}||\mathbf{x} - \mathbf{x}'||_2^2\right), \tag{10.11}$$

where $\mathbf{x}$ and $\mathbf{x}'$ are inputs pairs belonging to appropriate data sets, and σ and λ are the model hyperparameters. The kernel function K describes a measure of distance or similarity between the input pairs. Given the prior Gaussian distribution (10.9), the goal in GP regression is to predict the *posterior* distribution of the test data *conditional* on the training data. Then, the expected value $\mathbb{E}$ and covariance $\hat{\Sigma}$ of this posterior distribution are extracted using standard formulas for conditioning of multivariate Gaussian distributions, based on Bayes' rule [236]:

$$\mathbb{E}(\hat{Y}|Y, X_{\text{train}}, X_{\text{test}}) = K_*K^{-1}Y, \tag{10.12}$$

and

$$\hat{\Sigma}(\hat{Y}|Y, X_{\text{train}}, X_{\text{test}}) = K_{**} - K_* K^{-1} K_*. \tag{10.13}$$

Expressions (10.12) and (10.13) fully define the distribution of outputs predicted by GP.

A key difference between GP and linear regression is that a GP model does not have a parametric functional form. Instead, GP explicitly uses the provided training data when making predictions. The hyperparameters of the kernel function (10.11) can be obtained a priori, for example, by maximizing the log marginal likelihood function with respect to the hyperparameters [236]. The non-parametric nature of GP is advantageous in predicting arbitrarily nonlinear behaviors. Another important feature of GP regression is that it predicts a variance associated with the expected value of the prediction, which provides confidence bounds on the model predictions.

10.3 Experimental Methods

Two different CAP sources are utilized to demonstrate the applicability of ML to different types of discharges; a kHz-range APPJ in helium described in Chapter 3 and the "Plasma Flashlight" [237], a hand-held corona-like discharge in air. The kHz-range APPJ has the advantage of being a very stable discharge with easily-obtainable OES spectra. On the other hand, the corona-like discharge produces clearly audible electro-acoustic emission.

Fitting accurate ML models generally require large amounts of data which are both labor and time intensive to collect manually. Therefore, automation of data acquisition and processing is a key requirement for effective implementation of ML strategies. To this end, both setups are equipped with automated data acquisition and actuation systems similar to that is described in Chapter 3 based on the open-source microcontroller Arduino UNO and the single board computer Raspberry Pi 3. Automated data collection and actuation is implemented in Python and the ML methods are implemented using scikit-learn package [230].

The details of the APPJ configuration is presented in detail in Chapter 3. The APPJ is ignited at a frequency of 20kHz with a borosilicate glass coverslip and aluminum ground plate used as substrates. The schematic representation of the corona-like discharge is shown in Figure 10.3). This device is identical to the Plasma Flashlight device reported in [237]. The device consists of a needle-type electrode situated in a plastic nozzle. The plasma is ignited by DC voltage amplified by booster circuit and exhibits self-pulsing behavior. The separation distance between the tip of the electrode in the Plasma Flashlight and the substrate is manipulated through a linear actuator based on a stepper motor controlled by the Arduino UNO. The electro-acoustic emission is collected in the range of 0.5-25 kHz with a resolution of 200 Hz using an adjustable gain microphone (MAX4466). The fast Fourier transform (FFT) of the signal is implemented via the Open Music library [238].
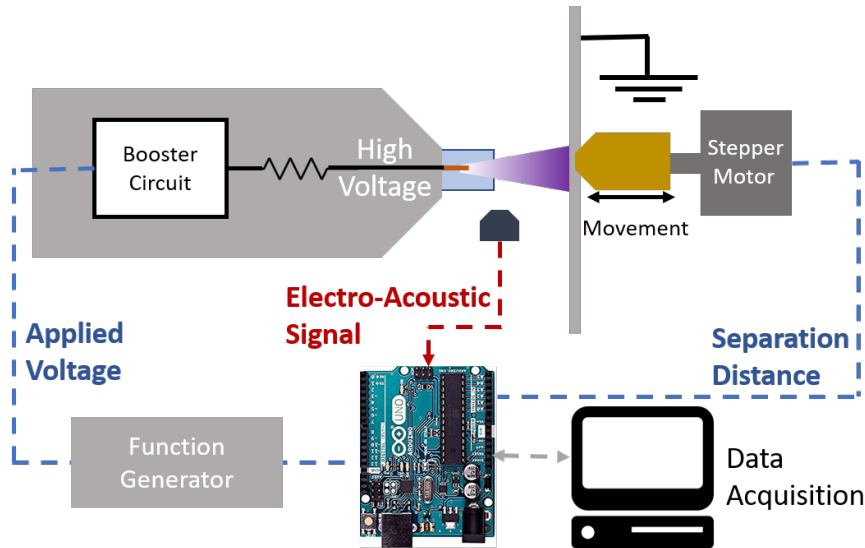
Figure 10.1: The experimental setup for the Plasma Flashlight. Dashed lines indicate the flow of information, where blue represents actuation and red represents measurements.

10.4 Results and Discussion

The application of the ML methods of Section 10.2 is discussed for real-time diagnostics of CAP operation using three case studies: (i) determination of rotational and vibrational temperatures of APPJ using OES, (ii) discrimination between a conductive and an insulating substrate using OES, and (iii) determination of the discharge gap distance using electro-acoustic emission.

10.4.1 Determination of Rotational and Vibrational Temperatures using OES

Rotational (T_{rot}) and vibrational (T_{vib}) temperatures contain vital information about gas temperature and energy transport processes within the discharge. Different OES peaks such as OH (A $^2\Sigma^+ \to$ X $^2\Pi$ at 306-328 nm) and N_2 ($C^3\Pi_u \to$ B $^3\Pi_g$ at 365-390 nm) transitions are commonly used to estimate rotational and vibrational temperatures [145]. The current practice is to estimate these temperatures offline using specialized software (such as SpecAir [145]) to achieve a fit between generated synthetic spectra and measured OES spectra. Due to the presence of a large number of fitting parameters, this approach can be computationally expensive for real-time diagnostics, taking several seconds to a few minutes. Here, a data-driven diagnostics tool based on linear regression (see Section 10.2.1) is proposed for real-time inference of the rotational and vibrational temperatures from the OES spectra.

The regression model is trained using 1500 samples of the normalized peaks of N_2 second positive system between 365-385 nm (input) and estimated rotational and vibrational
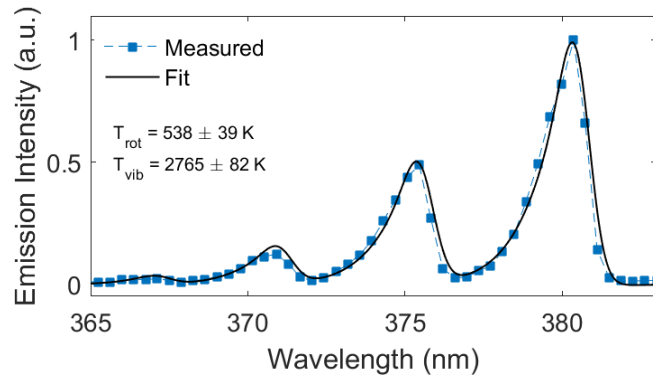
Figure 10.2: An example OES spectrum of N_2 ($C^3\Pi_u \to B\ ^3\Pi_g$) second positive transition and corresponding fit from Massive OES [213], used to estimate rotational and vibrational temperatures of the APPJ operated at $P = 3$ W and $q = 1.5$ slm over glass substrate.

temperatures (outputs). A typical OES spectrum over the wavelengths corresponding to N_2 ($C^3\Pi_u \to B\ ^3\Pi_g$) transition and the fit of the synthetic spectrum is shown in Figure 10.2. The training data for values T_{rot} and T_{vib} are determined via fitting synthetic spectra in Massive OES [213]. The data set is collected over a range of operating conditions: varying He flow, applied power, and substrate type (i.e., insulating and conductive). The data are split into 80% training and 20% testing segments. The training data are presented in Appendix E.

Two hyperparameters for linear regression are considered: the model order as defined by the choice of basis functions (10.4) and the choice of the regularization parameter α in (10.5). The model is validated using 10-fold cross-validation. Figures 10.3(a) and 10.3(b) show the

(a)

(b)
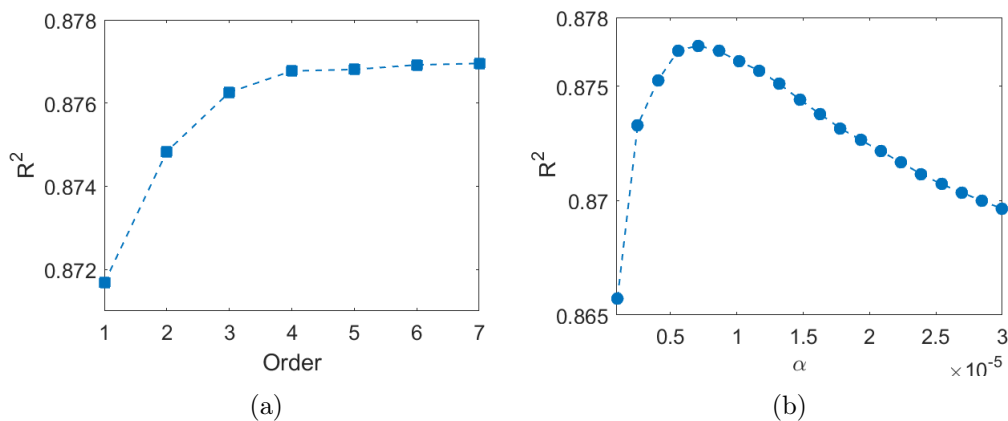
Figure 10.3: Determination of rotational and vibrational temperature using linear regression. Effect of (a) the order of the linear regression model and (b) the regularization parameter α on the predictive capability of the model as quantified by R^2 score.

average R^2 score of the model predictions over 10 folds as a function of the model order and as a function of the regularization parameter α, respectively. The R^2 score increases with model order and appears to plateau at an order of four (Figure 10.3(a)). Above this model order, increasing the complexity of the model does not provide further improvement in the predictive capability of the model. In contrast, R^2 score is low for low values of α, possibly causing the model to over-fit (Figure 10.3(b)). In this case the model is unnecessarily complex due to fitting the noise in the output data. When α is increased beyond $\alpha = 0.7{\times}10^{-5}$, the model tends to under-fit. Thus, the model order $O = 3$ in (10.3) and regularization parameter $\alpha = 0.7{\times}10^{-5}$ in (10.5) are chosen in order to strike a balance in the bias-variance trade-off.

Figure 10.4 depicts the predictions of the linear regression model against the test data. The operating conditions under which the test data are obtained are shown in Figure 10.4(b). The predictive capability of the linear regression model is quantified separately for the two outputs T_{rot} and T_{vib}. The RMSE values, calculated using (10.1), are 30.2 K and 141.0 K, respectively, and R^2 scores are computed as 0.79 for both outputs. Figure 10.4(a) suggests that the regression model can describe the fitted T_{rot} and T_{vib} fairly well. Notably, poor performance is observed between sampling instances 210 - 250, where the flow rate is decreased and power is increased on the metal substrate. Under these conditions, the fitted temperatures are subject to more noise. This can be attributed to the fact that the plasma jet under these conditions moves rapidly from point to point on the surface, disrupting the OES signal collection.

The results illustrated in Figure 10.4 indicate that the predictions of the linear regression model are comparable to the fitted values from Massive OES under a range of operating conditions. Further testing also revealed that the linear regression model retains its accuracy even under additional variations which may be expected to significantly impact the emission from the second positive transition of N_2 such as jet-tip-to-substrate separation distance and O_2 admixture in the working gas as shown in Figure 10.5. The robustness of the linear regression model can be attributed, in part, to the inherent repeatability of underlying physical phenomena in this type of discharges [101].

The real-time diagnostics for T_{rot} and T_{vib} can be directly incorporated into feedback control schemes. As an example, a PI controller is configured between T_{rot} manipulating the discharge power P. The PI control results for setpoint tracking and rejection of disturbances in separation distance are shown in Figure 10.6. The results demonstrate that the linear regression model opens up the ability to control T_{rot} in the discharge. Particularly, in the presence of disturbances in separation distance regulation of T_{rot} can provide a significant advantage.

Thus, the linear regression model can provide an effective tool for real-time inference of T_{rot} and T_{vib}. This type of regression model relating OES to physical quantities can be a powerful diagnostic tool even beyond the determination of temperatures. When additional quantitative measurements such as LIF and picosecond second harmonic generation are available for training, supervised regression models might be developed using OES data to provide real-time estimates of other process variables such as chemical species concentrations
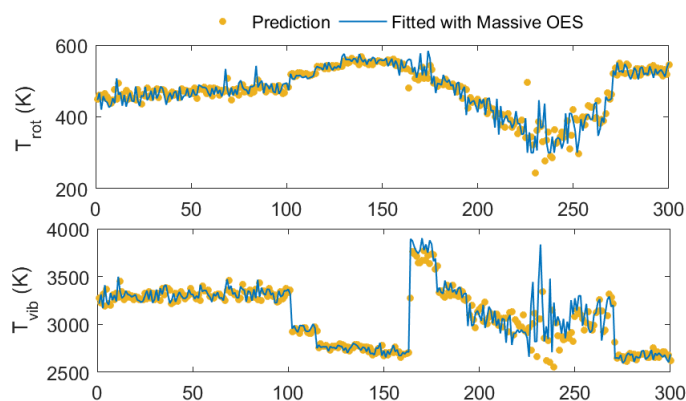
(a)
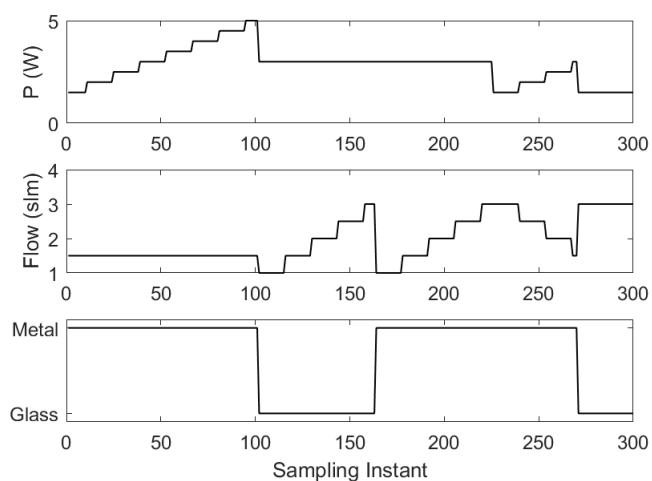
(b)

Figure 10.4: Determination of rotational and vibrational temperature using linear regression. (a) Predictions of the linear regression model for T_{rot} and T_{vib} compared against the fitted values from Massive OES using the test data and (b) operating conditions (applied power, He flow rate, and substrate type) under which the test data are obtained.

and electric field strength. These diagnostic tools, in turn, can allow real-time control of these difficult-to-measure discharge properties.

10.4.2 Substrate Discrimination using OES

APPJ characteristics can significantly change as a function of the substrate properties such as the conductive or insulating nature of the substrate [25]. However, it is often impractical
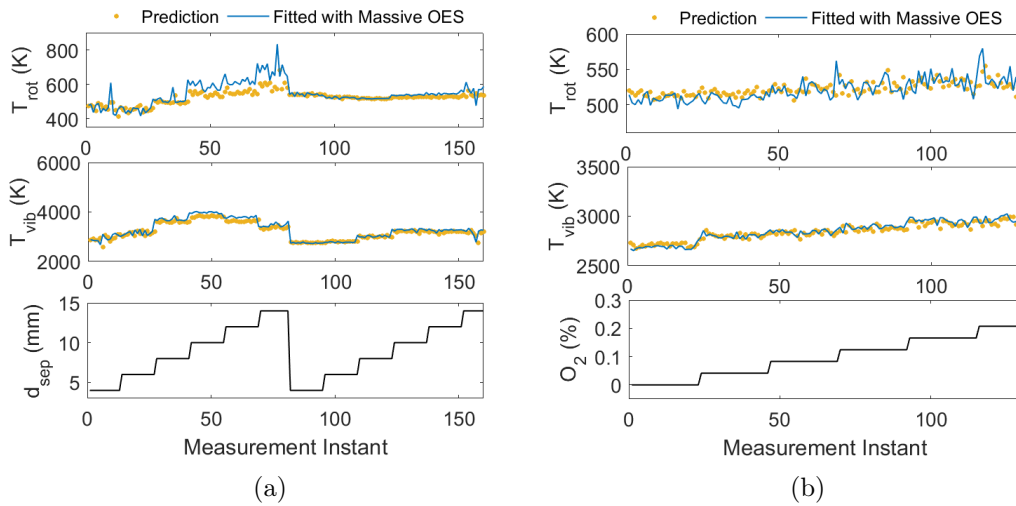
Figure 10.5: Determination of rotational and vibrational temperature using linear regression. Predictions of the linear regression model for T_{rot} and T_{vib} compared against the fitted values from Massive OES (a) under varying separation distance over glass (t < 180 s) and metal (t < 180 s) substrates, and (b) under increasing O_2 admixture to feed gas.
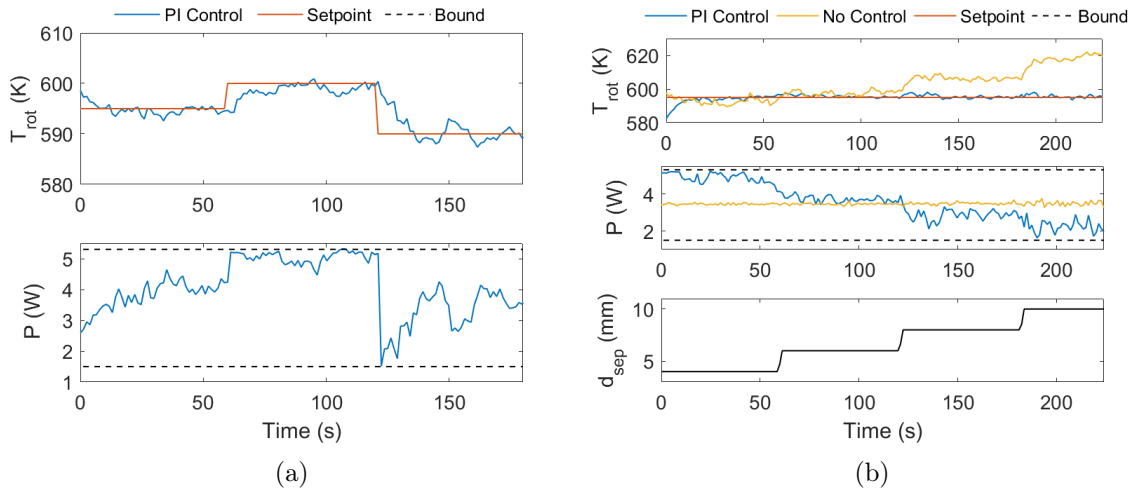
Figure 10.6: Control of rotational temperature based on estimates obtained from the linear regression mode. (a) Setpoint tracking in T_{rot} and (b) rejection of disturbance in separation distance compared against the no control case.

to directly measure the substrate properties in real time. Changes in the optical emission of the discharge can provide an indication of changing substrate properties and allow detection of distinct substrates such as tumorous tissues as compared to healthy tissue [239]. Here, real-time diagnostics tool is developed based on k-means clustering to detect the substrate
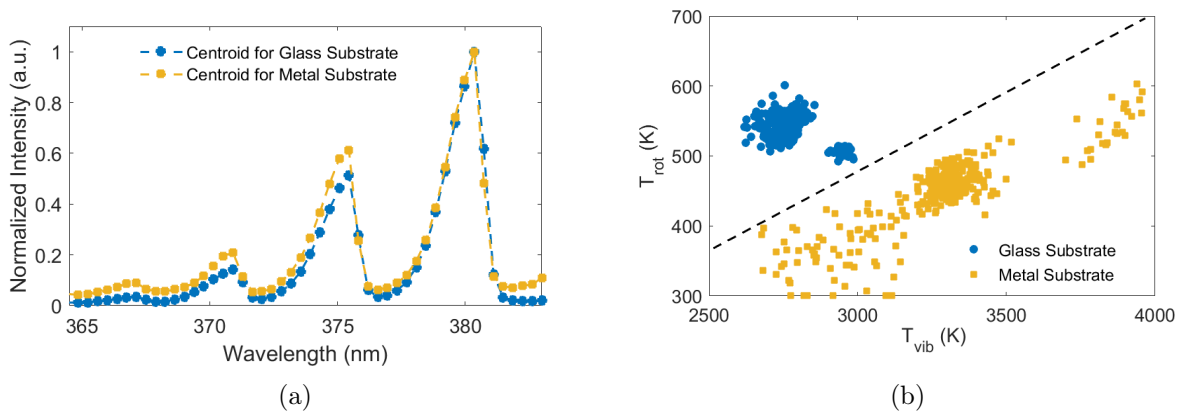
Figure 10.7: Substrate discrimination using k-means. (a) Centroids of the clusters that correspond to glass and metal substrates and (b) the rotational temperature T_{rot} and vibrational temperature T_{vib} in the training data, fitted using Massive OES.

type based on OES measurements. The same data set as in the previous section is used for training (see Appendix E). The data set consists of 1500 samples, 1000 of which are collected over a glass substrate and 500 are collected over a metal substrate. The inputs are the raw OES spectra of the second positive transition of N_2 as in the previous section. Labels of the substrate types are the outputs. However, as k-means is an unsupervised method, the output labels are not used for training. The OES spectra are intended to be clustered in two distinct groups ($k = 2$) using k-means clustering. 10-fold cross-validation is used to validate the ability of the k-means method to assign data to appropriate classes. k-means model is able to classify the glass and metal substrates with an error fraction (10.2) of 0.01. This means that the clustering model misclassifies the substrate only 1% of the time.

The centroids, or the average spectra, corresponding to the two clusters are shown in Figure 10.7(a). The k-means method clusters the OES spectra into two classes coinciding with glass and metal substrates. The clustering is further verified respect to the two substrate types by plotting the T_{rot} and T_{vib} values fitted from Massive OES. As shown in Figure 10.7(b), the temperatures over glass and metal are clearly separated by the dashed diagonal line. This clustering of temperatures is not particularly surprising given the sensitivity of the discharge to electrical properties of the substrate. However, to the authors' knowledge, this clustering behavior has not been previously reported.

This clustering model is further tested for substrate discrimination in real-time. In this scenario, the glass coverslip used as the insulating substrate is removed from under the jet after 30 seconds of operation and is re-inserted after another 30 seconds. The jet is operated with 3 W of applied power and He flow of 1.5 slm. Under these conditions, perfect identification of the substrate type is observed (an error fraction of 0), indicating the promising potential for the real-time use of k-means clustering. Note that the case examined here is fairly simple since the transition between a purely conductive and a purely insulating

substrate is fairly drastic. Nevertheless, this case study demonstrates the promise of unsupervised clustering for real-time diagnostics of discrete phenomena. Knowledge of discrete phenomena, such as substrate type or discharge modes can greatly increase the flexibility of operation, for example, for treatment of electrically heterogeneous substrates.

10.4.3 Determination of Separation Distance using Electro-acoustic Emission
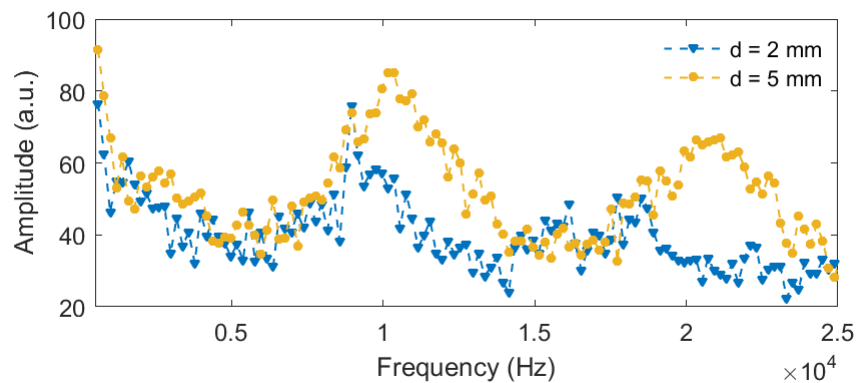
Figure 10.8: Fast Fourier Transform of the electro-acoustic emission of the Plasma Flashlight, recorded at two different inter-electrode separation distances of $d = 2$ mm and $d = 5$ mm.

Here, the hand-held battery-operated air discharge, the Plasma Flashlight [237] is used. This device exemplifies typical plasma medical devices, such as KINPen (neoplas tools GmbH [15]), in the sense that it is hand-held and relies on the expertise of the user for reliable operation. In these devices, changes in the electrode-to-substrate distance can generate significant variability in operation, caused by the sharp gradients and drastic changes in discharge properties [8]. Hence, real-time measurement of the separation distance can be useful. Conventional non-contact sensors based on infrared [240], ultrasound [241] or time-of-flight [242] may not be able to readily address this issue as the desired measurement range is particularly small, and the discharge interference with electronics limit their use. Here the information provided by the discharge is employed to extract information about separation distance.

The Plasma Flashlight has audible electro-acoustic emission, which noticeably changes with variations in the separation distance. Based on the literature [215], [216], fast Fourier Transform is employed to analyze the effect of the separation distance on the sound signal in the frequency domain. Figure 10.8 shows an example of fast Fourier Transforms of the electro-acoustic emission collected under two separation distances at 2 mm and 5 mm. GP regression is used to describe the complex relationship between the fast Fourier Transform of the electro-acoustic emission and the separation distance. The data set for training and

testing the GP regression model consists of 2500 samples collected over a range of labeled separation distances d_{sep}, which is also the output. 60% of the data are used for training and validation while the rest is reserved for testing. The GP regression model is trained as described in Section 10.2.3. The training data are given in Appendix E.
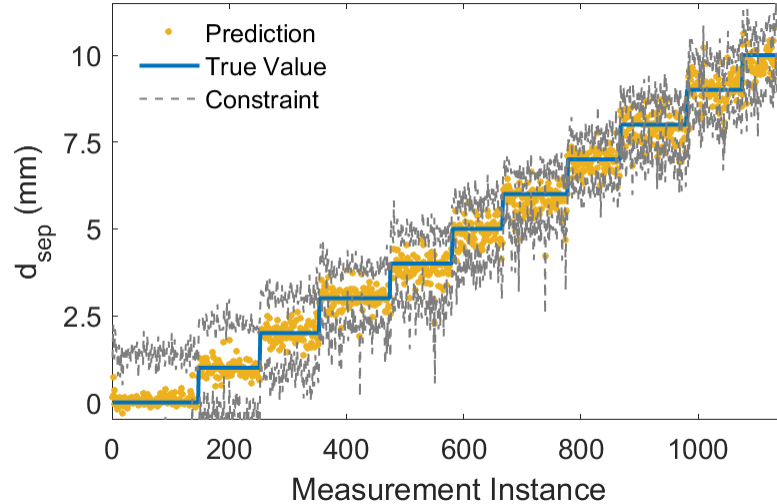
Figure 10.9: Determination of separation distance using GP regression. Comparison of predictions of the GP regression model against the test data. The confidence interval of in the GP predictions, quantified within one standard deviation shown with solid gray lines.

In the GP regression model, the hyperparameters in (10.11) are systematically chosen by maximizing the log marginal likelihood of predictions with respect to the hyperparameters [236]. This results in $\lambda = 1.73$ and $\sigma = 0.08$. After training and validation of the GP model, its performance is evaluated with respect to the test data, as shown in Figure 10.9. The performance of the GP model is quantified with an R^2 score of 0.98 and RMSE of 0.34 mm. Figure 10.9 suggests that the GP model reliably predicts the true value of the separation distance. The noisy nature of the prediction is attributed to the high noise level of the raw electro-acoustic emission data. Notably, the standard deviation predicted by the GP prediction is smaller for larger separation distances, as indicated by the dashed lines in Figure 10.9. Overall, the GP regression model is capable of predicting the separation distance based on electro-acoustic emission with reasonable accuracy. Thus, the GP regression model provides a real-time diagnostic for determination of the separation distance, for example, to monitor if the separation distance is outside a prescribed region that is safe for plasma treatment.

10.5   Conclusions

This chapter demonstrated three examples of data analytics applications to real-time diagnostics of atmospheric pressure plasma devices: (i) determination of T_{rot} and T_{vib} from OES using linear regression, (ii) discrimination of glass and metal substrates from OES using k-means clustering and (iii) determination of separation distance from electro-acoustic emission using GP. A common feature of all the investigated examples is that difficult-to-obtain information is extracted from data which are available in real time. The caveat is that large quantities of data have to be collected and processed off-line in order to be able to draw accurate inferences. Where possible, this off-line processing and external measurements is employed (as in determination of T_{rot}, T_{vib} and separation distance) in conjunction with supervisory methods. In addition, the use of unsupervised methods to obtain insight on physical characteristics is demonstrated (e.g., the clustering of T_{rot}, T_{vib} based on substrate types) from patterns in the data. The results indicate that, despite the simplicity of the utilized methods, the performance of the ML inferences is more than adequate in the context of the respective examples. A key feature of the diagnostics tools developed in this chapter is that they provide a significant advantage in terms of time required to obtain inferences. For example, generating and fitting synthetic spectra to a single spectrum to obtain T_{rot}, T_{vib} can take 40 - 50 s. In contrast, linear regression takes on the order of 1 millisecond for the same task. Moreover, it only takes about two hours to collect the data required to train the linear regression model. Classification of the substrate type is also achieved with the same data set in a few milliseconds. Similarly, two hours worth of electro-acoustic emission data allows training the GP regression to infer the separation distance in about 5 milliseconds. This serves to show the potential promise of ML methods in the context of CAPs. In particular, ML methods can create vast opportunities in plasma medicine for modeling the end effects (i.e., *dose*) of plasma treatment and enabling the development of personalized treatment protocols.

A key challenge in applying data analytics to real-time diagnostics is the choice of appropriate sources of spectral information and ML methods. For example, in the third case, the electro-acoustic signal is used due to its ease of collection. The GP method was chosen since simpler regression methods like linear regression did not produce adequate results. It may not be possible to readily extend the same approach in all circumstances; for example, in radio frequency discharges, the excitation frequency considerably exceeds the audible range. Discovering the appropriate combinations of methods and measurements, then, largely relies on heuristics. Employing data analytics tools for building accurate data-driven models of the plasma can provide significant advantages in addressing modeling challenges (see Chapter 4). Advanced ML methods based on neural networks such as reinforcement learning can be used for generating more complex models or directly training control agents with capabilities beyond conventional controllers. Such methods have the capacity to be combined with the real-time diagnostic tools presented in this work to achieve high-performance automation and process control on CAP devices.

Chapter 11

Conclusions

> This work investigated the advanced control of atmospheric pressure plasma jets. The presented results reveal that optimization-based control strategies are crucial for effective regulation of multiple plasma effects and the delivery of multi-variable and spatially distributed dose metrics in presence of disturbances. This chapter summarizes the main conclusions of this work and presents some key questions to be addressed going forward

This dissertation has investigated the advanced feedback control of atmospheric pressure plasma jets (APPJs). The key issues of control-oriented modeling and control problem formulation are undertaken for the development of effective model-based control strategies. Some key modeling and control approaches are presented which can greatly improve the reliability, repeatability and effectiveness of APPJ treatment. An experimental setup, modeling frameworks, and control structures are presented to systematically address some of the key issues in APPJ operation. The effectiveness of the presented approaches in the reduction of process variability and reliable dose delivery is demonstrated experimentally.

The first part of the dissertation focused on the fundamentals of atmospheric pressure plasmas, the design of an automated experimental setup for control, and control-oriented modeling approaches. APPJs are established as the setup of choice for this investigation due to their widespread use and their broad operating range owing multiple available manipulated variables. The sources of variability in APPJs are outlined motivating the need for feedback control for safe, reliable, and repeatable treatment. An experimental setup is developed for automated sensing and actuation to enable the application of control algorithms. The investigation of control-oriented modeling of the APPJ revealed the potential for both physics-based and data-driven techniques for describing control-relevant system dynamics. The key issue of modeling a "plasma dose" is identified, with metrics for thermal and non-thermal dose delivery adopted from the literature. Simple lumped-parameter models were developed to effectively represent the dynamics of discharge power, and gas and substrate temperatures. A more complicated, spatially resolved fluid model is used to inform the simplified model structure and the values of the lumped parameters. For variables that are difficult to model with a physics-based approach, data-driven linear models were shown to be a viable alternative, albeit for a limited operating range.

The effectiveness of control algorithms was evaluated for rejection of disturbances and dose delivery. Basic control strategies (i.e., proportional-integral (PI) controls) were shown to be effective in rejecting a variety of disturbances in a single-input-single-output context. However, results revealed that the PI control strategies have limitations for regulating multiple discharge effects simultaneously. For this task, model predictive control (MPC) strategies were shown to outperform PI controls, even when they are based on a linear data-driven model valid only for a narrow operating range. The operating range of the MPC is extended using a nonlinear physics-based lumped-parameter model. The effectiveness of the nonlinear MPC (NMPC) strategy is demonstrated for multi-component dose delivery in the presence of disturbances in jet-tip-to-substrate separation distance and substrate type. PI controls were found to have a limited capacity for dose delivery, even though soft-sensing methods were used to alleviate issues stemming from nonlinear and cumulative aspects of the dose delivery problem.

NMPC and PI control strategies were used synergistically in a hierarchical control structure to address the spatial aspects of the thermal dose delivery problem. In this case, the PI control strategy was employed to allow fast disturbance rejection, while MPC managed the more complicated task of planning spatial dose delivery. The issue of APPJ translation across treated substrates was undertaken systematically, demonstrating the trade-off between the translation rate and dose delivery performance. Calculation of an "optimal" translation trajectory is demonstrated, given the interdependence between the APPJ translation, the dynamics and spatial distribution of the substrate temperature, and the treatment objective. The hierarchical control strategy based on NMPC was found to drastically improve spatially uniform thermal dose delivery performance in presence of disturbances of large magnitudes.

The key conclusion of this work is that the advanced control strategies are crucial for APPJs in addressing the issues of variability in operation and reliable dose delivery. Particularly in the context of medical applications, where high-performance operation is necessary, the advanced control strategies can greatly improve the reliability of APPJs. The methods developed in this work can also be applied to other APPJ treatment problems such as materials processing. The variability issues in operation and the end-goal of delivery of cumulative APPJ effects are common to applications such as deposition, etching, and surface activation. The next sections present some suggestions for future work. The key areas of suggested future work include development improved optimization methods and problem formulations, and broader use of machine learning methods to address modeling and control challenges of APPJs.

11.1 Suggestions for Future Work

11.1.1 Optimization Algorithms

Improving the efficiency of the optimization algorithms remains one of the key open issues for advanced control of APPJs. In particular, the nonlinear lumped-parameter physics-based

model (see Chapter 4) comprising of differential-algebraic models can present numerical challenges for solving optimal control problems online. Note that this work focused primarily on the thermal effects of the APPJs and considerably simple models of the APPJ-substrate interactions. Improving the model accuracy and incorporating additional discharge phenomena to control-oriented models is a clear goal for future research efforts. However, with increasing model complexity, challenges pertaining to numerical issues and the solution time of the optimal control problems are liable to grow. Moreover, plasma medicine applications require regulation of multiple spatially distributed discharge effects (e.g., spatially distributed electric fields, species concentrations etc.). With an increasing number of controlled variables and spatial dimensions, MPC strategies can suffer from increased computational complexity. This can quickly make real-time solution of optimal control problems intractable. Thus, the development of efficient optimization algorithms is a key area of interest to further extend the effectiveness advanced control strategies developed in this work. One potential avenue is the use of so-called "explicit MPC" methods, which enable embedded control at the millisecond timescales. However, while there are well-established methods for linear explicit MPC [243], development of explicit NMPC strategies is an open area of research.

11.1.2   Real-time Trajectory Planning

As demonstrated in Chapters 8 and 9, the translation trajectory has a significant impact on dose delivery. Especially in the presence of disturbances the ability to re-calculate the translation trajectory online can provide a key advantage. However, introducing the translation trajectory as a decision variable to the optimal control problem can make the real-time implementation prohibitively expensive. Particularly, as the treated areas and the total treatment time increases, the real-time implementation of NMPC becomes increasingly challenging. One potential remedy for this problem is improving the efficiency of the optimization algorithms as discussed above. Other avenues involve introducing parametrizations of the translation trajectory and the dose distribution. For example, spectral de-composition of the delivered dose profiles can allow representation of the spatial dose distribution with fewer variables, decreasing computational burden. Similarly, the parametrization of the translation trajectory can reduce the number of decision variables to reduce the time required for optimization at the expense of some flexibility (e.g., parametrization may limit the accessible subset of translation trajectories). Given the sensitivity of the dose delivery to the translation trajectory, developing means for effective real-time trajectory planning for APPJ treatments is a clear need. This problem of real-time trajectory planning also bears similarities to problems arising in robotics [244] and autonomous navigation [245]. Thus methods developed in these fields may provide some insight on potential solutions to this problem.

11.1.3   Control of APPJ Chemistry

Considering that one of the major sources of the medicinal effects of the APPJs is the delivery of reactive oxygen and nitrogen species, the control of APPJ chemistry has clear significance.

The key issue hindering the control of chemical effects of the APPJ is the challenging diagnostics. Measurement of gas-phase chemistry and its effect on substrates are difficult to quantify. The conventional methods for the measurement of reactive species concentrations rely on complicated techniques (e.g, laser-induced fluorescence LIF spectroscopy [181]) which can be difficult to utilize in real time and cannot easily accommodate the flexibility required for medical treatment (e.g., the need to translate the APPJ). Moreover, the key area of interest for plasma medicine is the chemical effects of the APPJ on the substrates. Methods for quantifying the chemical response of substrates can even be more daunting.

One key area of active research is the development of tissue substitutes to test APPJ effects [246]–[248]. Similar to the idea of a "tissue phantom" in radiation and ultrasound therapies, a standardized platform which bears electrical and chemical resemblance to human tissue can greatly aid quantification of discharge effects. Use of fluorescent and color changing indicators in conjunction with such a platform can allow a semi-quantitative diagnostics of the chemical effects of discharges [246], [247]. Specialized chemical detector strips, in the same way, can be used to asses the chemical footprint of different species the APPJ delivers [121]. Quantifying and assimilating the available information about the chemical effects of the discharge to a tractable model remains a key open question for control of APPJ chemistry. This problem requires a repeatable and easy-to-use platform and methods for quantifying the dynamics of the "chemical dose" of the APPJ, as it varies with the manipulated inputs. Preferably, real-time measurements of the chemical dose would be available. The increasingly powerful methods for image processing [249] can provide one potential avenue to tackle this challenge. Another possibility may be to develop real-time diagnostics methods for discharge chemical effects using data analytics methods as pointed out in Chapter 10.

11.1.4 Machine Learning Methods for Modeling, Diagnostics, and Control

Chapter 10 hint at the potential for machine learning (ML) methods for APPJ applications. APPJ, and non-equilibrium plasma applications, in general, can particularly benefit from ML methods. As described in Chapter 4 developing high fidelity plasma models and in particular models of plasma effects on treated surfaces (i.e., dose models) can be a significant challenge. Moreover, the fast timescales of plasma dynamics require diagnostics and control strategies that can be deployed rapidly, while accounting for the complexities of the plasma dynamics. On the other hand, copious amounts of indirect information can be collected from plasmas with relative ease (such as optical emission spectra, voltage-current waveforms, and electro-acoustic emission) without practical means for relating them to operationally relevant plasma characteristics. Hence, non-equilibrium plasma sources are particularly suited for application of ML methods for modeling, monitoring and diagnostics, and process control [250].

The potential for data-driven modeling strategies is demonstrated in Section 4.6.2 with linear subspace identified models. However, linear models are only valid for a limited operating range. Advanced ML methods such as Gaussian processes and artificial neural networks

can capture multi-variable and nonlinear aspects of APPJ-substrate interactions. Difficult-to-model phenomena such as time-varying response of biological substrates to APPJ treatment (e.g., blood coagulation during treatment [251]–[253]) can be modeled using ML methods. Moreover, so-called on-line learning strategies can be used to update a system model in real-time, based on measured changes in the dynamics. Thus adaptive control strategies can be developed based on ML methods. ML methods can also allow personalized treatment models to accurately quantify the plasma dose and to account for patient-to-patient variations in plamsa medicine applications.

Example uses of ML methods for real-time diagnostics are demonstrated in Chapter 10. A key area of opportunity for the use of ML methods in diagnostics is the development of tools for real-time estimation of reactive species concentrations in the plasma. Correlation of independent measurements of concentrations of key chemical species (e.g., from LIF, IR spectroscopy or Mass spectrometry) with optical and electro-acoustic emission signals can provide a significant advantage for non-equilibrium plasma applications. Effective real-time diagnostics can create opportunities for probing the dynamic behavior of reactive species concentrations in real time as well as the feedback control of the discharge chemistry. Moreover, classification algorithms can be used to detect modes of failure and abnormal operation based on the various information-rich signals. For example, detection of transitions to undesired modes (e.g., arcing) can provide a key advantage in improving the safety of APPJ applications.

Lastly, ML methods can be directly employed as control agents. Artificial neural networks trained on offline-generated data can approximate the solution of a nonlinear MPC optimization. This method would enable the rapid computation of control actions, circumventing the computational burden of real-time optimization. Another approach may involve training an artificial neural network to directly compute the control actions. Data generated based on a dynamic system model can be used to implement so-called sim-to-real transfer reinforcement learning. This method involves training a neural network agent in a simulation environment, which is then capable of performing similarly *in-situ*. Domain or dynamics randomization methods are employed to expose the neural network control agent to a range of possible dynamics (e.g., varying thermal dynamics with substrate type) in simulations. Thus the mismatch between the simulation and real environments and the uncertainties in controlled dynamics can be accommodated [254], [255].

Appendix A

Diagrams of Experimental Setup Components

The chapter contains diagrams of the actuation and measurement circuitry as well the technical drawings of the custom-designed and 3D-printed parts used in the APPJ setup. The function generator circuitry consists of the digital-to-analog converter (Figure A.1), an operational amplifier (Figure A.2), the monolithic function generator (Figure A.3) and the switching circuit (Figure A.4). The digital-to-analog converter (Figure A.1) is also utilized to actuate gas flow rates. The custom-designed 3D printed parts include the substrate support (Figure A.6), the z-axis holder assembly (Figure A.7 and A.8) and the optical emission adaptor (Figure A.9). The designed parts are 3D printed in poly-lactic acid (PLA) filament using a Monoprice Mini v1 3D printer.

A.1   Circuit Diagrams
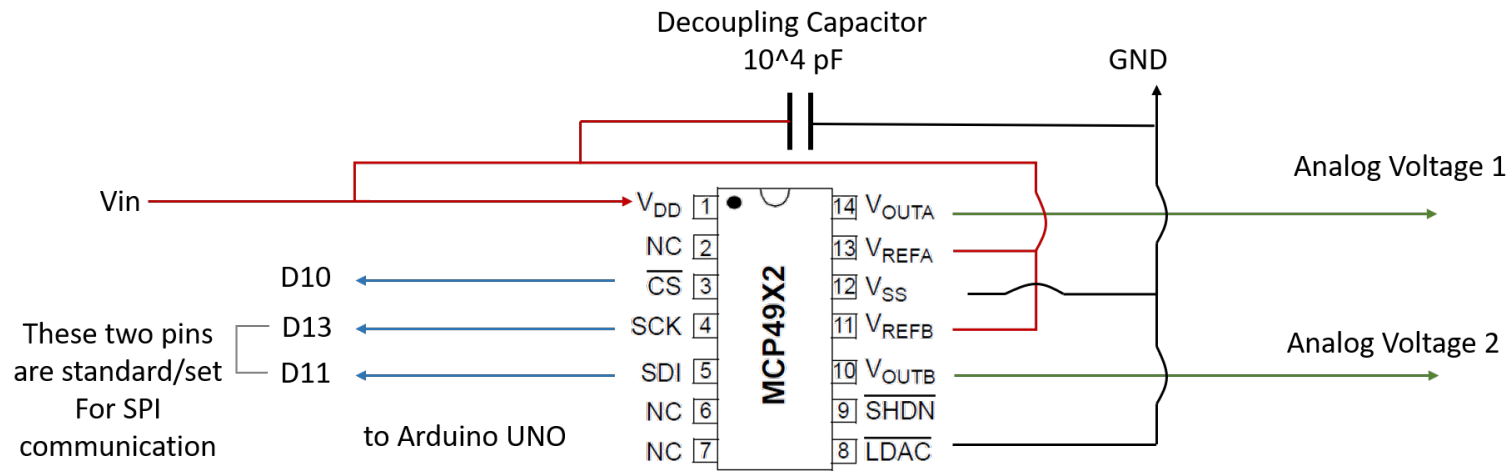
Figure A.1: Circuit diagram of the digital-to-analog converter MCP4922
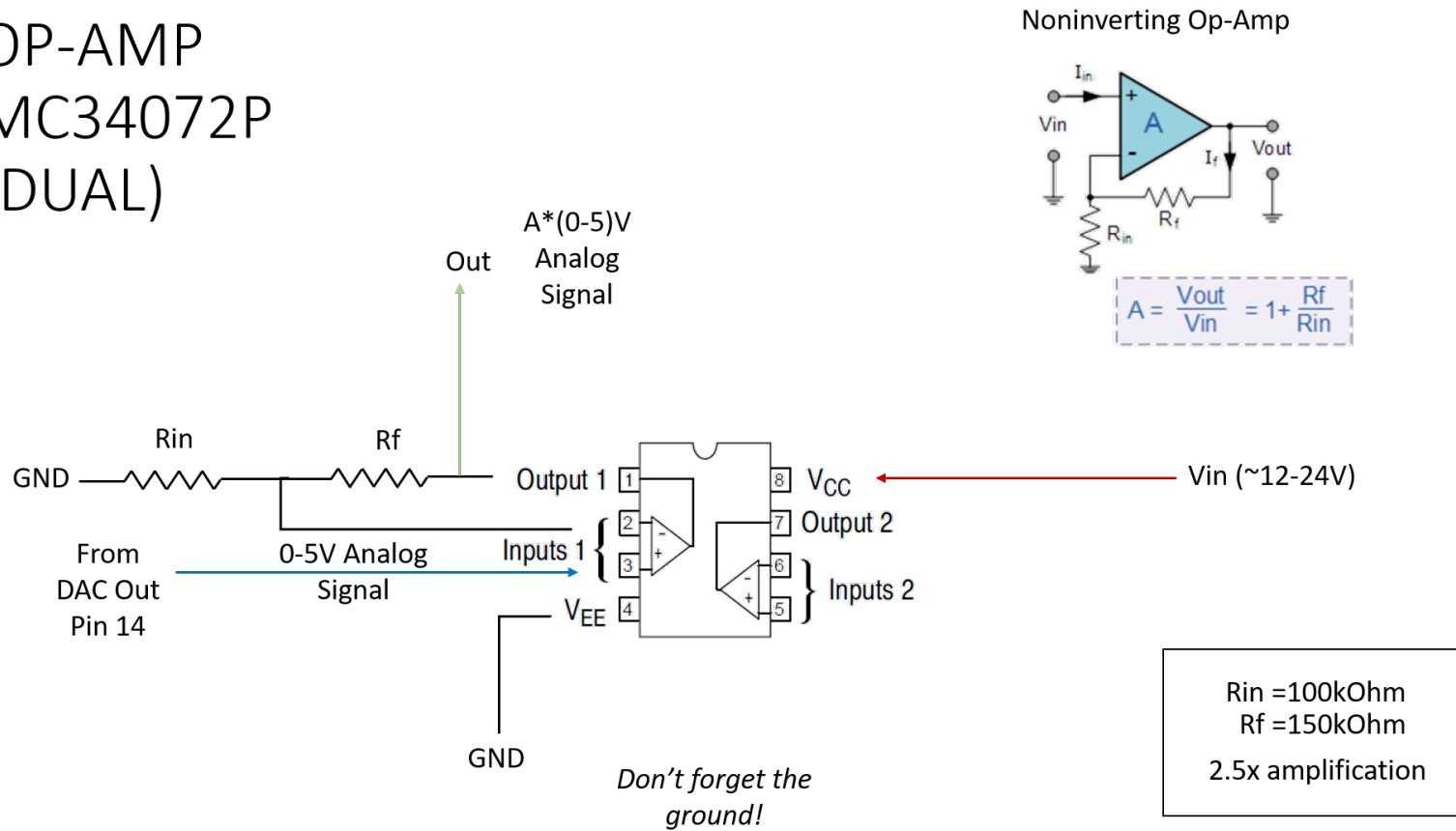
Figure A.2: Circuit diagram of the dual operational amplifier MC340727P.

Monolithic function generator XR-2206CP
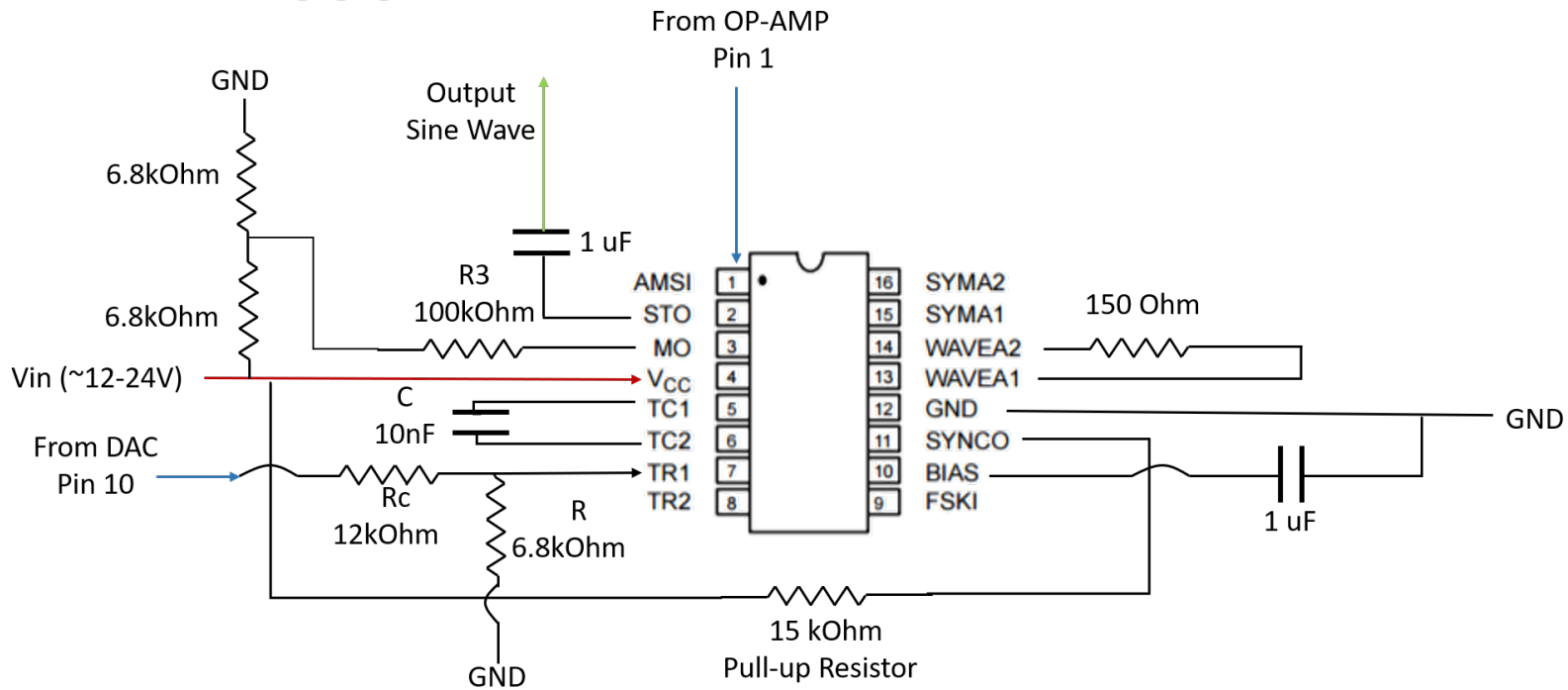
Figure A.3: Circuit diagram of the monolithic function generator XR-2206CP configured to a generate sinusoidal signal

Switching Circuit

OA1 – Produces +9V if PWM is ON
OA2 – Produces -9V if PW ON, +9V if PWM is OFF
PWM HIGH => Switch A closed
Switch B open
OUT=FGEN
PWM LOW => Switch A open
Switch B closed
OUT=GND

IN
PWM

+9V

-9V

+9
V
+
OA 1
-
-9V

+9
V
+
OA2
-
-9V

-9V 7

1

13

3

IN   OUT
CTR
L

IN   OUT
CTR
L

+9
1   V
2

4

CD4016BE
Or
CD4066B

OUT
To
AMP
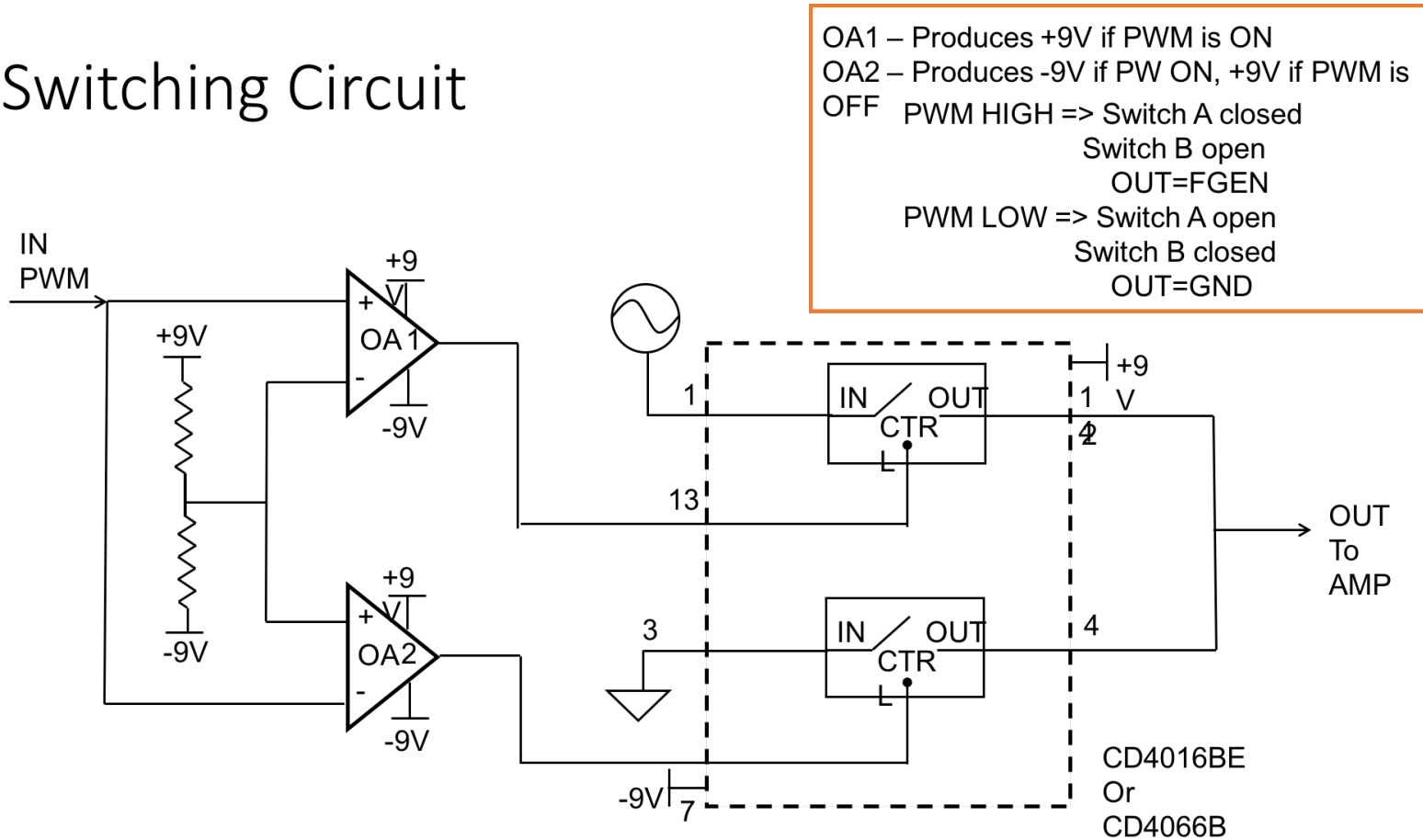
Figure A.4: Circuit diagram of the switching circuit used to modulate the duty cycle of the applied voltage.
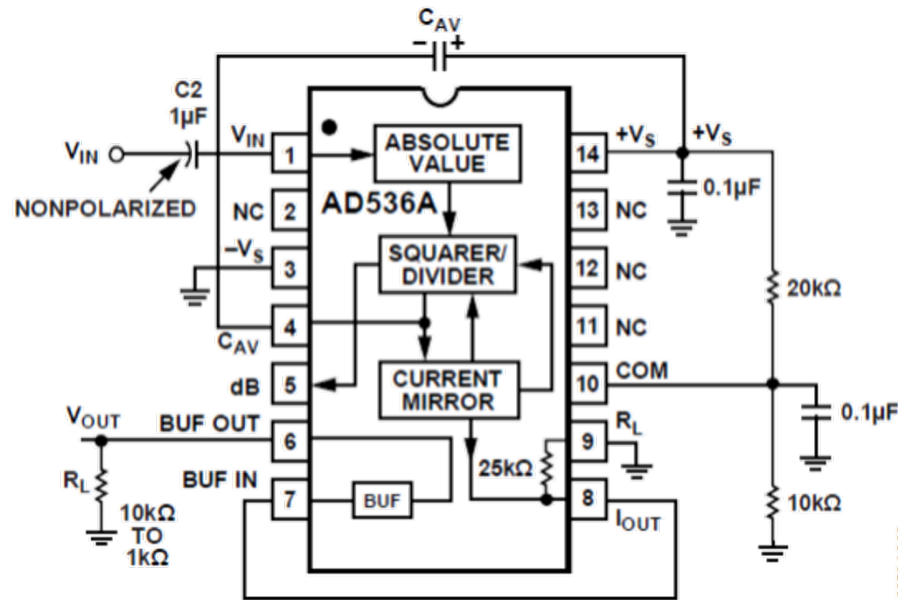
Figure A.5: Circuit diagram of the AC to RMS converter.

A.2 Technical Drawings
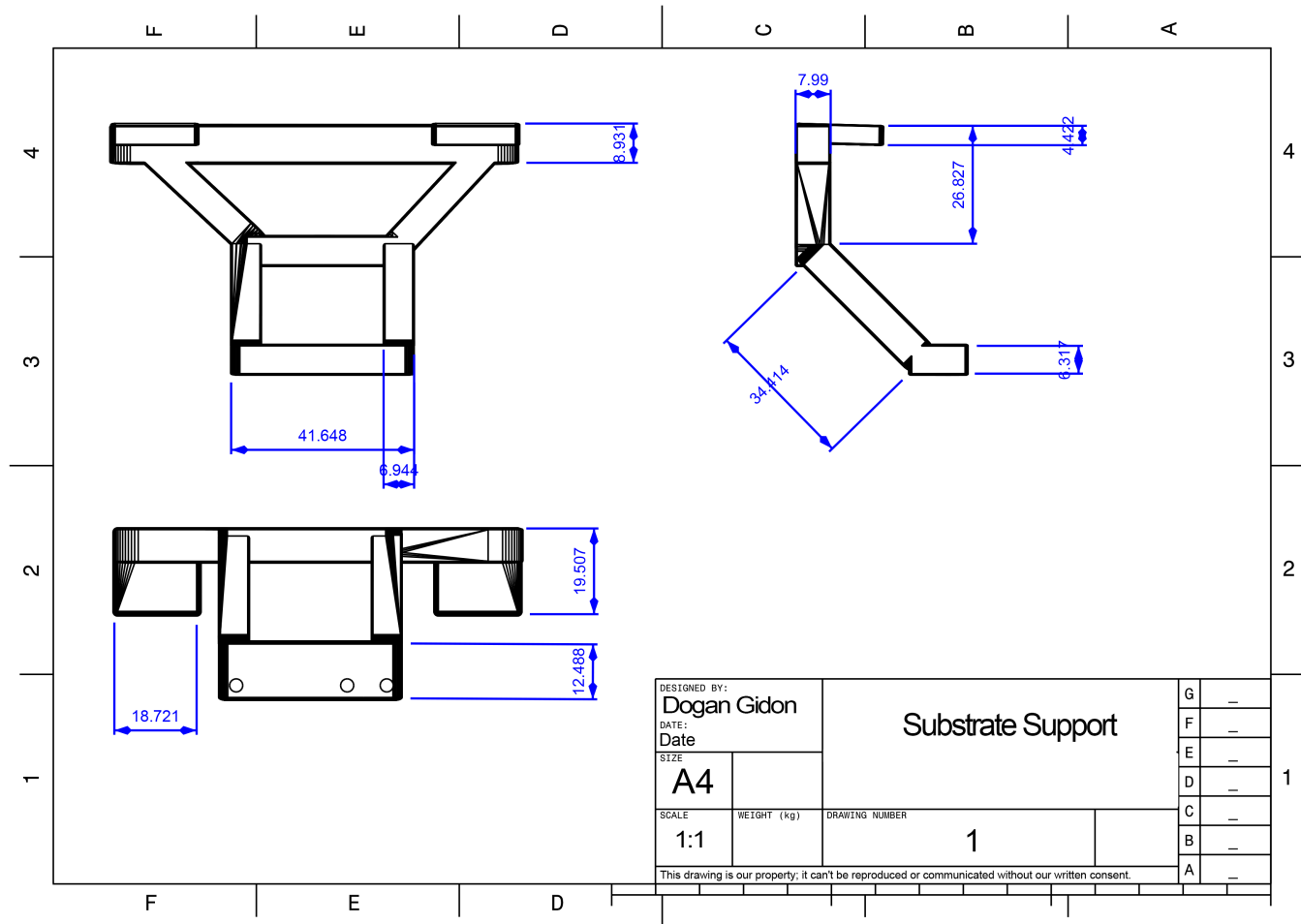
Figure A.6: Technical drawing depicting the substrate support.The bottom of the end of the part connects to the x-y axis gantry while the two extended ends of the surface supports the grounded metal plate.
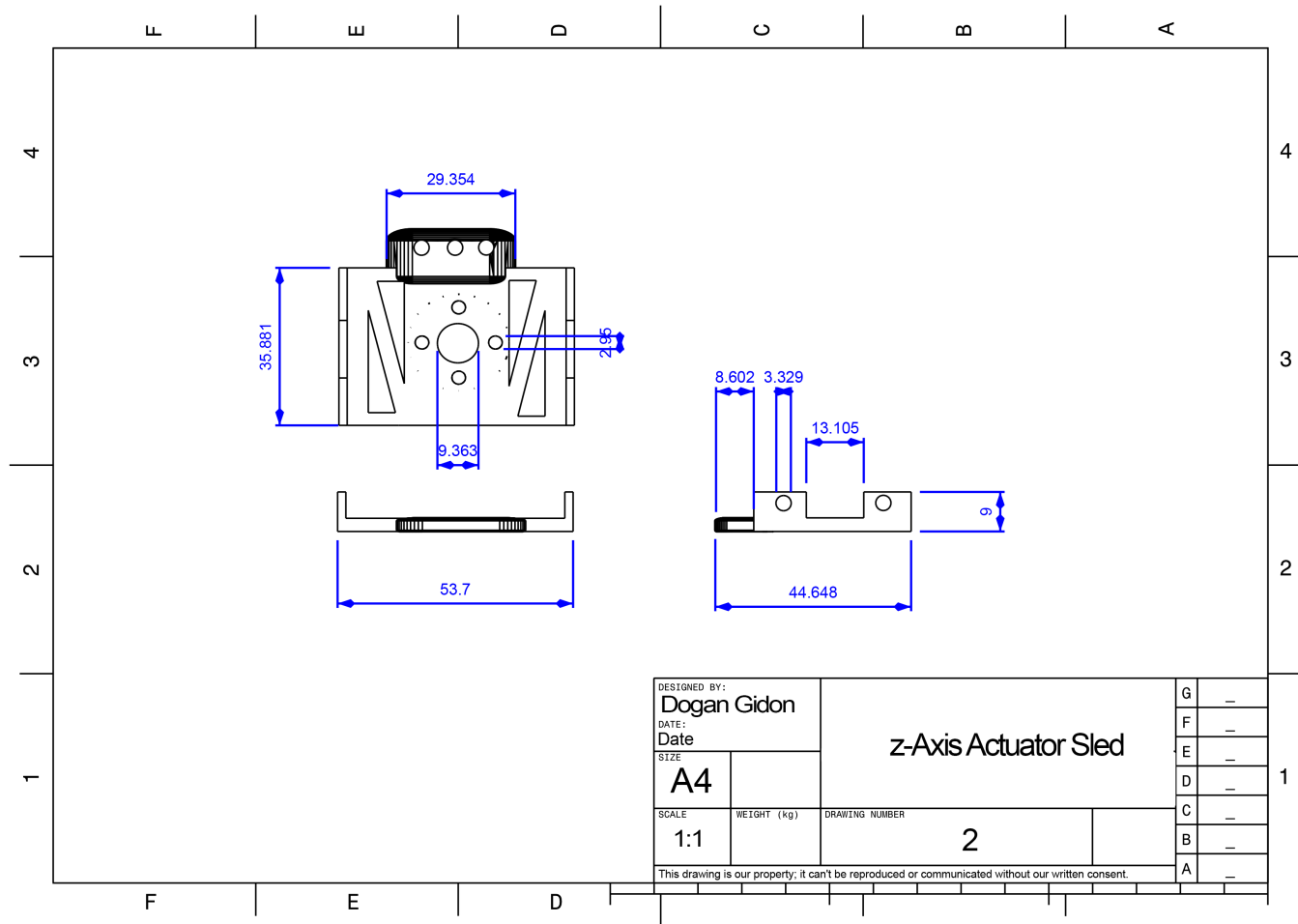
Figure A.7: Technical drawing depicting the first part of the z-axis holder assembly. The lead screw is situated in the center hole. The extension with three holes allows different parts to fixed to the z-axis gantry.
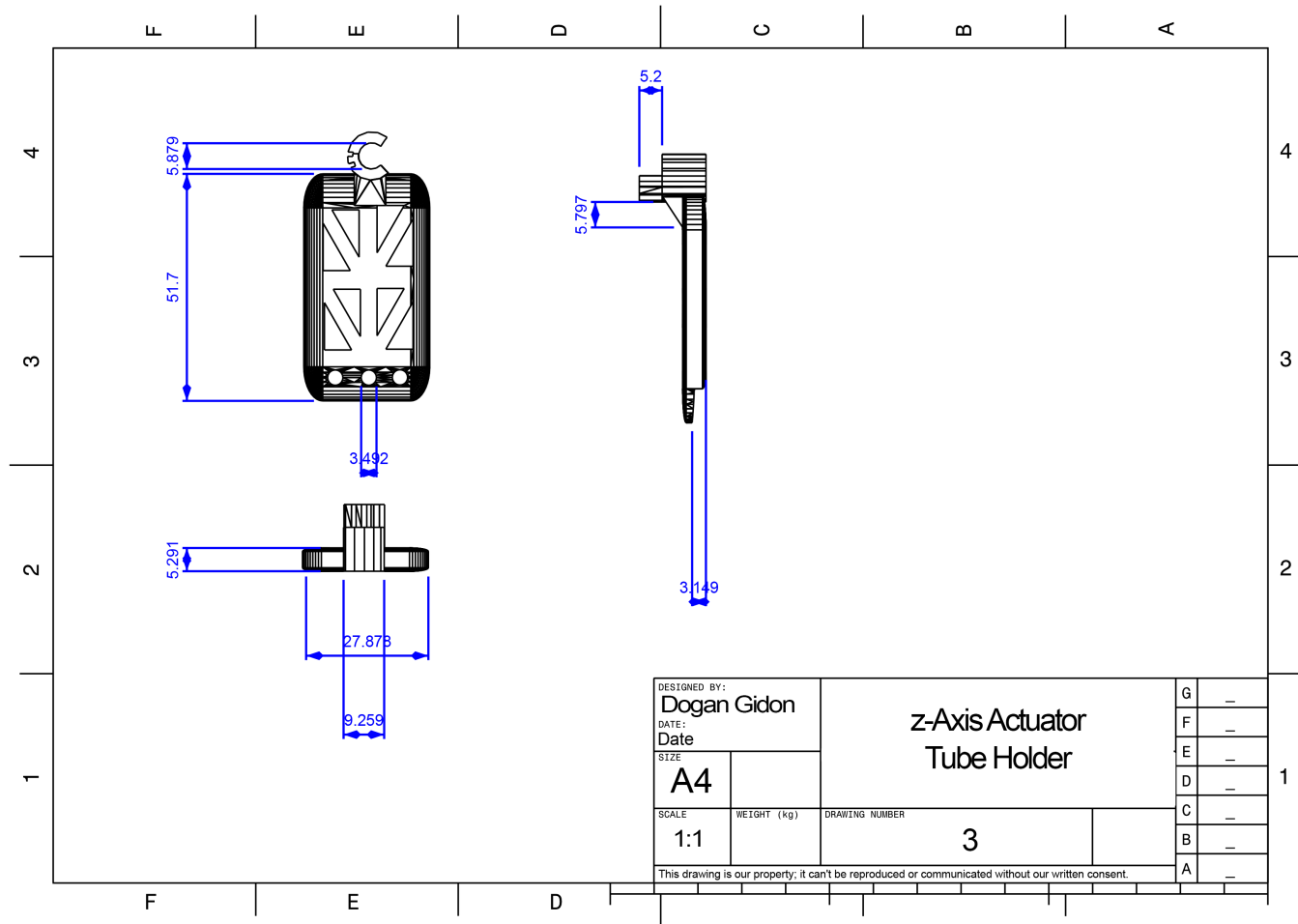
Figure A.8: Technical drawing depicting the second part of the z-axis holder assembly. The three holes and connect to the first part of the assembly while the circular end situates the APPJ tube.
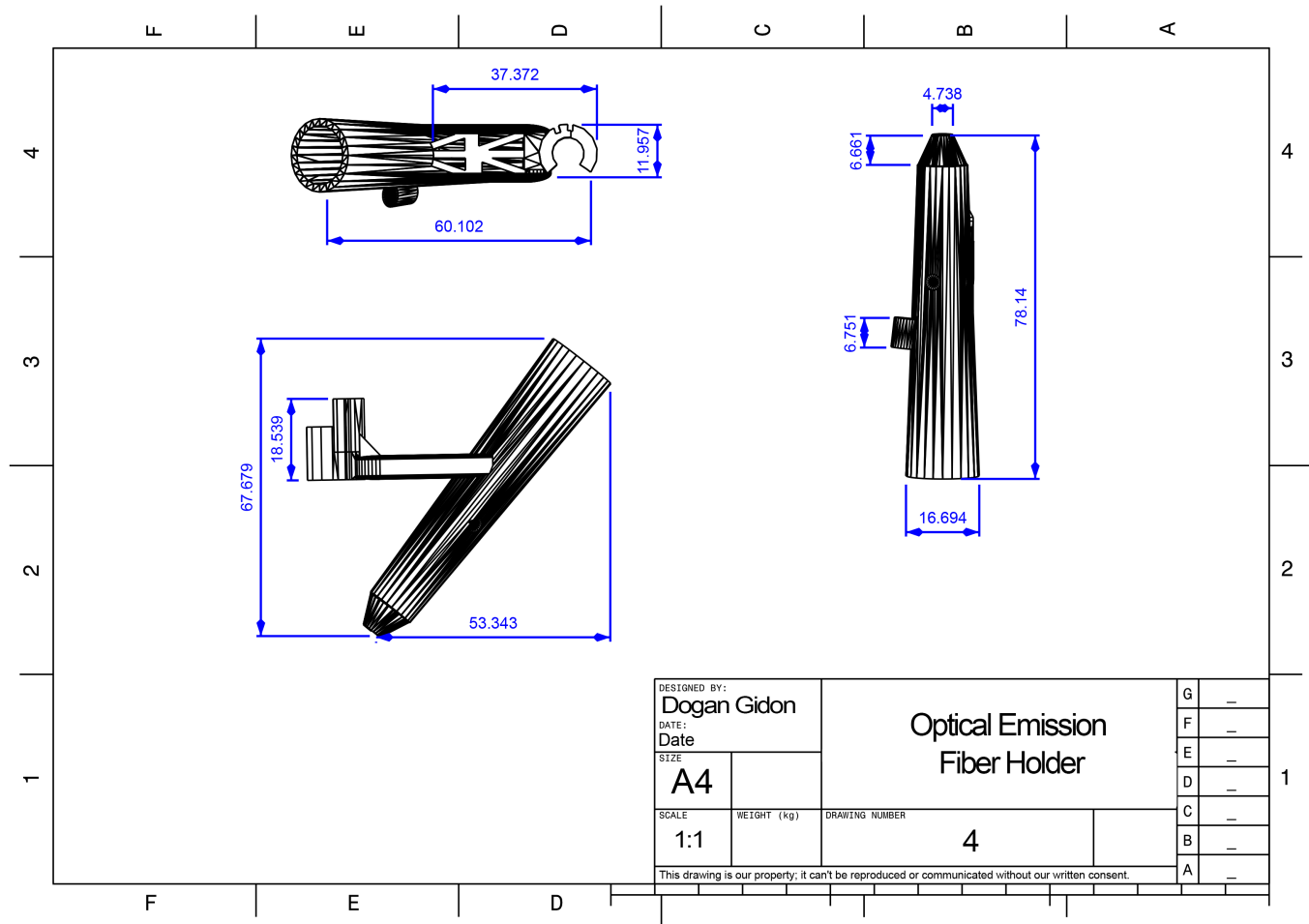
Figure A.9: Technical drawing depicting the OES adaptor. The APPJ tube is situated in the semi-circular end of the part and the OES probe is inserted to the hollow area. The ring-shaped overhang at the side of the part accommodates an additional fiber-optic cable (without any connectors) for total intensity measurement at the same location.

Appendix B

Code

This chapter presents the scripts used in conjunction with the experimental setup for coordinating actuating and synchronizing and recording measurements from different sources. The firmware coded in C++, running on the Arduino micro-controllers and the coordination software coded in Python is based on previous work [147]. The code is presented below.

B.1 Firmware

Listing B.1: Firmware running on the Arudino micro-controllers in the embedded layer. This version of the code includes embedded the embedded PI controller for maintaining the power by manipulating the applied voltage.

```cpp
char junk;
// running with 24V power supply for op amp and function generator

/* This minimal example shows how to get a single-shot range
measurements from the VL6180X.
The range readings are in units of mm. */

// DEFINES
#define DEBUG falsev

// IMPORTS
#include <Wire.h>
#include <MCP4922.h>
#include <VL6180X.h> // library: VL6180X proximity sensor
#include <avr/wdt.h> // library: watchdog timer
#include <MCP4922.h> // library: DAC
#include <SPI.h>
#include <Adafruit_MotorShield.h>
#include "utility/Adafruit_MS_PWMServoDriver.h"
#include <Adafruit_MLX90614.h> // library: MLX90614 thermopile
#include <SPI.h>
```

```cpp
#include <Wire.h>

// GLOBAL VARS
VL6180X proxsensor;
//MCP4922 DAC(51,52,53,5); // (MOSI,SCK,CS,LDAC) define Connections for MEGA_board
MCP4922 DAC_FXN(11,13,10,5); // (MOSI,SCK,CS,LDAC) define Connections for UNO_board
MCP4922 DAC_MFC(11,13,9,5); // (MOSI,SCK,CS,LDAC) define Connections for UNO_board
Adafruit_MLX90614 mlx_5deg = Adafruit_MLX90614(0x5A); // default address of MLX90614
    ↪ thermopile

// Create the motor shield object with the default I2C address
Adafruit_MotorShield AFMS(0x60); //top shield
Adafruit_MotorShield AFMS_bot(0x61); //bottom shield

// Connect a stepper motor with 200 steps per revolution (1.8 degree)
// to motor port #1 (M3 and M4)
Adafruit_StepperMotor *dMotor = AFMS.getStepper(150, 1);
// to motor port #1 (M1 and M2)
Adafruit_StepperMotor *xMotor = AFMS.getStepper(150, 2);
// to motor port #1 (M1 and M2) bottom shield
Adafruit_StepperMotor *yMotor = AFMS_bot.getStepper(150, 1);

String inputString = ""; // a string to hold incoming data

const int read_num = 100;
int read_data[read_num];
float read_average = 0;
int read_index = 0;
int read_total = 0;

// GLOBAL CONSTANTS
const double SERIAL_BAUD = 38400;
const int PROXIMITY_TIMEOUT = 25;
const int LOOPDELAY = 1; // milliseconds
const int DACSTEPS = 4096;
const int t_samp = 20; //milliseconds
double t_prev = 0;

// PINOUT
const int PIN_PHOTO_A = 0;
const int PIN_PHOTO_B = 1;
const int PIN_DAC_A = 2;
const int PIN_DAC_B = 3;
const int PIN_V_RMS = A3;
const int PIN_I_RMS = A2;
const int PIN_PWM = 5;

namespace data {
  int dac_a;
  int dac_b;
```

```cpp
  int dist;
  int x_pos;
  int photo_a;
  int photo_b;
  float v_rms;
  float i_rms;
  float t_emb;
  float p_rms;
}

namespace PI_V{
  float Kc = 3/(0.56*20);
  float Tau_i = 3;
  float I = 0;
  float err = 0 ;
}

namespace time_var{
  double ts=1.3;
  double t_prev=0;
  }

namespace setpoint {
  float voltage = 0.1;
  float power=0;
  float vapp = 0;
  float frequency = 20;
  float flowrate = 0;
  float flowrate2 = 0;
  float dist = 400;
  float x_pos = 0;
  float y_pos = 0;
  float duty = 0;
  float pow_mod=0;
}

float v_calc=0;

namespace location {
  float delta = 0;
  float cur_loc = 400;
  float delta_x = 0;
  float cur_x = 0;
  float delta_y = 0;
  float cur_y = 0;
}

/////////////////////// CYCLIC REDUNDANCY CHECK
///////////////////////
static const uint8_t PROGMEM dscrc_table[] = {
```

```
     0, 94,188,226, 97, 63,221,131,194,156,126, 32,163,253, 31, 65,
   157,195, 33,127,252,162, 64, 30, 95, 1,227,189, 62, 96,130,220,
    35,125,159,193, 66, 28,254,160,225,191, 93, 3,128,222, 60, 98,
   190,224, 2, 92,223,129, 99, 61,124, 34,192,158, 29, 67,161,255,
    70, 24,250,164, 39,121,155,197,132,218, 56,102,229,187, 89, 7,
   219,133,103, 57,186,228, 6, 88, 25, 71,165,251,120, 38,196,154,
   101, 59,217,135, 4, 90,184,230,167,249, 27, 69,198,152,122, 36,
   248,166, 68, 26,153,199, 37,123, 58,100,134,216, 91, 5,231,185,
   140,210, 48,110,237,179, 81, 15, 78, 16,242,172, 47,113,147,205,
    17, 79,173,243,112, 46,204,146,211,141,111, 49,178,236, 14, 80,
   175,241, 19, 77,206,144,114, 44,109, 51,209,143, 12, 82,176,238,
    50,108,142,208, 83, 13,239,177,240,174, 76, 18,145,207, 45,115,
   202,148,118, 40,171,245, 23, 73, 8, 86,180,234,105, 55,213,139,
    87, 9,235,181, 54,104,138,212,149,203, 41,119,244,170, 72, 22,
   233,183, 85, 11,136,214, 52,106, 43,117,151,201, 74, 20,246,168,
   116, 42,200,150, 21, 75,169,247,182,232, 10, 84,215,137,107, 53};

uint8_t crc8(const uint8_t *addr, uint8_t len)
{
  uint8_t crc = 0;
  while (len--) {
    crc = pgm_read_byte(dscrc_table + (crc ^ *addr++));
  }
  return crc;
}

void setup_serial() {
  // set up serial connection
  // initialize serial communication at specified baudrate
  Serial.begin(SERIAL_BAUD);
  #if DEBUG
    Serial.println();
    Serial.println();
    Serial.println("Serial connection established!");
  #endif
}

void setup_watchdog() {
  // enable the watchdog timer
  // if Arduino stops responding, auto-resets
  // Watchdog Timeouts: WDTO_{1,2,4,8}s
  // WDTO_{15,30,60,120,250,500}MS
  // http://www.megunolink.com/articles/how-to-detect-lockups-using-the-arduino-watchdog/
  #if DEBUG
    Serial.println("enabling watchdog timer...");
  #endif
  wdt_enable(WDTO_500MS);

  #if DEBUG
    Serial.println("watchdog timer enabled!");
```

```
  #endif
}

///////////////////////// READING FROM SERIAL ////////////////////////////

///////////////////////// GET STRING ////////////////////////////

void get_serial() {
  // gets manual input from the serial port
  #if DEBUG
    Serial.println("getting serial input...");
  #endif

  boolean stringComplete = false; // whether the string is complete
  while (Serial.available() > 0) {

    // get the new byte:
    char inChar = (char)Serial.read();

    #if DEBUG
      Serial.println(String(inChar));
    #endif

    // add it to the inputString:
    inputString += inChar;

    // if the incoming character is a newline, set a flag
    // so the main loop can do something about it:
    if (inChar == '\n') {
      stringComplete = true;
      break;
    }
  }

  if ( stringComplete == true && inputString.length() > 0 ) {
    // if you have a non-blank input string and it's complete...
    #if DEBUG
      Serial.print("got serial input: ");
      Serial.print(inputString);
      Serial.println();
    #endif
    // process it with your manual_input function!
    manual_input(inputString);
    inputString = "";
  }
}

///////////////////////// PARSE INPUTS ////////////////////////////

void manual_input(String input) {
```

```
// process the manual request received via serial
#if DEBUG
  Serial.println("processing serial input!");
#endif

switch( input.charAt(0) ) {
  case 'v' :
    // you sent v,###
    if (input.substring(2).toFloat() > 10) {setpoint::voltage=10;}
    else {
    setpoint::voltage = input.substring(2).toFloat();}
    #if DEBUG
      Serial.println("voltage set!");
    #endif
    actuate_inputs();
    break;

  case 'f' :
    // you sent f,###
    if (input.substring(2).toFloat() > 20) {setpoint::frequency=20;}
    else if (input.substring(2).toFloat() < 10) {setpoint::frequency=10;}
    else {
    setpoint::frequency = input.substring(2).toFloat();};
    #if DEBUG
      Serial.println("frequency set!");
    #endif
    actuate_inputs();
    break;

  case 'q' :
    // you sent q,###
    if (input.substring(2).toFloat() > 10) {setpoint::flowrate=10;}
    else if (input.substring(2).toFloat() < 0) {setpoint::flowrate=0;}
    else {
    setpoint::flowrate = input.substring(2).toFloat();};
    #if DEBUG
      Serial.println("flowrate set!");wa
    #endif
    actuate_inputs();
    break;


  case 'o' :
    // you sent q,###
    if (input.substring(2).toFloat() > 10) {setpoint::flowrate2=10;}
    else if (input.substring(2).toFloat() < 0) {setpoint::flowrate2=0;}
    else {
    setpoint::flowrate2 = input.substring(2).toFloat();};
    #if DEBUG
      Serial.println("Second flowrate set!");
```

```
 #endif
 actuate_inputs();
 break;

case 'w' :
// you sent w,###
 if (input.substring(2).toFloat() > 12) {setpoint::power=12;}
 else if (input.substring(2).toFloat() < 0) {setpoint::power=0;}
 else {
 setpoint::power = input.substring(2).toFloat();};
 #if DEBUG
   Serial.println("Second flowrate set!");
 #endif
 actuate_inputs();
 break;

case 'd' :
// you sent d,###
 if (input.substring(2).toFloat() > 15) {setpoint::dist=1500;}
 else if (input.substring(2).toFloat() < 0) {setpoint::dist=0;}
 else {
 setpoint::dist = input.substring(2).toFloat()*100;}
 location::delta = -location::cur_loc + setpoint::dist;
 //Serial.println(location::delta);
 #if DEBUG
   Serial.println("stepper distance set!");
 #endif
 actuate_inputs();
 break;

case 'x' :
// you sent x,###
 if (input.substring(2).toFloat() > 1000) {setpoint::x_pos=10000;}
 else if (input.substring(2).toFloat() < -1000) {setpoint::x_pos=-10000;}
 else {
 setpoint::x_pos = input.substring(2).toFloat()*10;}
 location::delta_x = -location::cur_x + setpoint::x_pos;
 //Serial.println(location::delta);
 #if DEBUG
   Serial.println("stepper distance set!");
 #endif
 actuate_inputs();
 break;

 case 'y' :
// you sent x,###
 if (input.substring(2).toFloat() > 1000) {setpoint::y_pos=10000;}
 else if (input.substring(2).toFloat() < -1000) {setpoint::y_pos=-10000;}
 else {
 setpoint::y_pos = input.substring(2).toFloat()*10;}
```

```
      location::delta_y = -location::cur_y + setpoint::y_pos;
      //Serial.println(location::delta);
      #if DEBUG
        Serial.println("stepper distance set!");
      #endif
      actuate_inputs();
      break;

      case 'p' :
      if (input.substring(2).toFloat() < 10) {setpoint::duty=10;}
      else if (input.substring(2).toFloat() > 100) {setpoint::duty=100;}
      else {
      setpoint::duty = input.substring(2).toFloat();};
      // you sent p,###
      #if DEBUG
        Serial.println("duty cycle set!");
      #endif
      actuate_inputs();
      break;
  }
}

//////////////////////////// STEPPER MOVEMENT ////////////////////////////////


int move_to_pos(float delt, Adafruit_StepperMotor *motor) {
  //Serial.print(aaReal.x);
  //Serial.print('\n');

  if (delt < 0) {
      motor->step(1, FORWARD, DOUBLE); //// STEP SIZE calibrated 12/08/2017
      motor->release();
      delt=delt + 4;
      delay(2);
    return delt;
  } else if (delt > 0) {
      motor->step(1, BACKWARD, DOUBLE);
      motor->release();
      delt=delt - 4;
      delay(2);
    return delt;
  } else if (delt == 0) {
    return delt;
  }
}

int move_to_pos_x(float delt, Adafruit_StepperMotor *motor) {
  //Serial.print(aaReal.x);
  //Serial.print('\n');
```

```
  if (delt < 0) {
      motor->step(1, FORWARD, SINGLE); //// STEP SIZE calibrated 02/07/2018
      //motor->release();
      delt=delt + 1;
      delay(2);
    return delt;
  } else if (delt > 0) {
      motor->step(1, BACKWARD,SINGLE); //// STEP SIZE calibrated 02/07/2018
      //motor->release();
      delt=delt - 1;
      delay(2);
    return delt;
  } else if (delt == 0) {
    return delt;
  }
}


int move_to_pos_y(float delt, Adafruit_StepperMotor *motor) {
  //Serial.print(aaReal.x);
  //Serial.print('\n');

  if (delt < 0) {
      motor->step(1, FORWARD, SINGLE); //// STEP SIZE calibrated 02/07/2018
      //motor->release();
      delt=delt + 1;
      delay(2);
    return delt;
  } else if (delt > 0) {
      motor->step(1, BACKWARD, SINGLE); //// STEP SIZE calibrated 02/07/2018
      //motor->release();
      delt=delt - 1;
      delay(2);
    return delt;
  } else if (delt == 0) {
    return delt;
  }
}

/////////////////////////////////// ACTUATION ///////////////////////////////////////

void actuate_inputs() {
  // actuates the system inputs via the DACs
  #if DEBUG
    Serial.println("actuating␣inputs...");
  #endif
  //DAC_FXN.Set(mapfloat(setpoint::voltage,0,10,0,DACSTEPS-1), mapfloat(setpoint::
      ↪ frequency,0,10,DACSTEPS-1,0));
  //DAC_FXN.Set(mapfloat(setpoint::voltage,0,10,((float) 6 / 10)*DACSTEPS,((float) 2 /
      ↪ 10)*DACSTEPS), mapfloat(setpoint::frequency,0,10,DACSTEPS-1,0));
```

```cpp
  // tuned for Brandon's development setup on 24V supply:
  //DAC_FXN.Set(mapfloat(setpoint::voltage,0,10,0.96*(DACSTEPS-1),0.55*(DACSTEPS-1)),
  // mapfloat(setpoint::frequency,10,20,0.92*(DACSTEPS-1),0.1*(DACSTEPS-1)));

  // tuned for the control jet setup on 24V supply:

  ////////////// EMBEDDED CONTROL ///////////////////////////////////////////////
  v_calc=setpoint::vapp + PI_V::Kc*(PI_V::err+PI_V::I/PI_V::Tau_i);

\\\ Anti-wind-up
  if(v_calc>=11 && PI_V::err>=0){
    PI_V::I=PI_V::I;
    setpoint::vapp=11;}
  else if (v_calc>=11 && PI_V::err<0){
     PI_V::I = PI_V::I + PI_V::err*(time_var::ts-time_var::t_prev)*1e-3;
    setpoint::vapp=11;}
  else if(v_calc<=0 && PI_V::err<=0){
    PI_V::I=PI_V::I;
    setpoint::vapp=0.;}
  else if (v_calc<=0. && PI_V::err>0){
     PI_V::I = PI_V::I + PI_V::err*(time_var::ts-time_var::t_prev)*1e-3;
     setpoint::vapp=0.;}
  else {
    PI_V::I = PI_V::I + PI_V::err*(time_var::ts-time_var::t_prev)*1e-3;
    setpoint::vapp=v_calc;
    };


  // tuned for the control jet setup on 24V supply:
  DAC_FXN.Set(mapfloat(setpoint::vapp,0,12,0.96*(DACSTEPS-1),0.46*(DACSTEPS-1)),
         mapfloat(setpoint::frequency,10,20,0.90*(DACSTEPS-1),0.085*(DACSTEPS-1)));

//voltage control off
// DAC_FXN.Set(mapfloat(setpoint::voltage,0,12,0.96*(DACSTEPS-1),0.46*(DACSTEPS-1)),
// mapfloat(setpoint::frequency,10,20,0.90*(DACSTEPS-1),0.085*(DACSTEPS-1)));

  // MFC DAC
 DAC_MFC.Set(mapfloat(setpoint::flowrate,0,10,0,4095),mapfloat(setpoint::flowrate2
    ↪ ,0,20,0,4095));

 location::delta=move_to_pos(location::delta, dMotor);
 location::cur_loc = -location::delta + setpoint::dist;

 location::delta_x=move_to_pos_x(location::delta_x, xMotor);
 location::cur_x = - location::delta_x + setpoint::x_pos;


 location::delta_y=move_to_pos_y(location::delta_y, yMotor);
 location::cur_y = - location::delta_y + setpoint::y_pos;
```

```
  // set duty cycle
  analogWrite(PIN_PWM, mapfloat(setpoint::duty,0,100,0,255));


}

float mapfloat(float x, long in_min, long in_max, long out_min, long out_max)
{
 return (x - in_min) * ((float)out_max - out_min) / ((float)in_max - in_min) + out_min;
}

void addRead(int value)
{
  read_total = read_total - read_data[read_index];
  read_data[read_index] = value;
  read_total = read_total + read_data[read_index];
  read_average = ((float)read_total) / read_num;
  read_index++;
  if (read_index >= read_num)
  {
    read_index = 0;
  }
}

/////////////////////////// SETUP ////////////////////////////////

void setup()
{
  setup_serial();
  setup_watchdog();
  SPI.begin();
  Wire.begin();

  AFMS.begin(); // create with the default frequency 1.6KHz
  AFMS_bot.begin(); // create with the default frequency 1.6KHz

  dMotor->setSpeed(40); // 10 rpm
  xMotor->setSpeed(40); // 10 rpm
  yMotor->setSpeed(40); // 10 rpm

  // set up VL6180X sensor
  proxsensor.init();
  proxsensor.configureDefault();
  proxsensor.setTimeout(PROXIMITY_TIMEOUT);

  actuate_inputs();
}

/////////////////////////// LOOP ////////////////////////////////
```

```cpp
void loop()
{
  // reset the watchdog timer
  // if this doesn't occur within WDTO_X, system resets
  wdt_reset();

  if (Serial.available() > 0) {
    #if DEBUG
      Serial.println("bytes available: " + String(Serial.available()));
    #endif
    get_serial();
  }

  // get the timestamp
   time_var::ts = millis();

  // read and save data from sensors
  data::dac_a = analogRead(PIN_DAC_A);
  data::dac_b = analogRead(PIN_DAC_B);
  data::photo_a = analogRead(PIN_PHOTO_A);
  data::photo_b = analogRead(PIN_PHOTO_B);
  data::v_rms = ((analogRead(PIN_V_RMS)*5.0/1024.0) -0.0029)/0.97;
  data::i_rms = (analogRead(PIN_I_RMS)*5.0/1024.0);
  data::dist = proxsensor.readRangeSingleMillimeters(); // read VL6180X distance
  data::t_emb = mlx_5deg.readObjectTempC();
  data::p_rms=0.85*((data::v_rms*data::i_rms)*1.3+0.29)+0.093; //calibrated

/// account for duty cycle in assigning power setpoint
   if(setpoint::power*setpoint::duty/100. > 10){setpoint::pow_mod==10;}
   else if (setpoint::power*setpoint::duty/100. < 0){setpoint::pow_mod==0;}
   else { setpoint::pow_mod=setpoint::power*setpoint::duty/100;};

/// calculate PI error
   PI_V::err = setpoint::pow_mod - data::p_rms;

  actuate_inputs();

  // build the string from the data
  String mystring = "";
  mystring += time_var::ts;
  mystring += ',';
  mystring += setpoint::vapp;
  mystring += ',';
  mystring += setpoint::frequency;
  mystring += ',';
  mystring += setpoint::flowrate;
  mystring += ',';
  mystring += location::cur_loc/100;
  mystring += ',';
  mystring += setpoint::duty;
```

```cpp
  mystring += data::photo_a;
  mystring += ',';
  mystring += data::photo_b;
  mystring += ',';
  mystring += data::v_rms;
  mystring += ',';
  mystring += data::t_emb;
  mystring += ',';
  mystring += data::i_rms;
  mystring += ',';
  mystring += location::cur_x/10;
  mystring += ',';
  mystring += location::cur_y/10;
  mystring += ',';
  mystring += setpoint::flowrate2;
  mystring += ',';
  mystring += setpoint::power;
  mystring += ',';
  mystring += data::p_rms;

  // calculate the CRC8 of the string
  // first, convert string to array of chars (signed ints)
  char mychars[mystring.length()+1];
  mystring.toCharArray(mychars,sizeof(mychars));
  // then, convert chars into unsigned ints
  uint8_t myuints[sizeof(mychars)];
  for (int i=0; i < sizeof(mychars); i++) {
    myuints[i] = (uint8_t) mychars[i];
  }
  // finally, calculate the crc of the unsigned ints
  int mycrc = crc8(myuints,sizeof(myuints));

  // printing the data string
  Serial.print(mystring);
  Serial.print(',');
  Serial.print(mycrc);
  Serial.println();
  delay(LOOPDELAY);
  time_var::t_prev = time_var::ts;

}
```

B.2 Coordination Software

Listing B.2: Python script running on the single board computer to coordinate measurements and actuation from the embedded layer and peripheral instruments.

```python
# Do not write bytecode to maintain clean directories
import sys
sys.dont_write_bytecode = True

# Import required packages.
from casadi import *
import numpy as NP
import matplotlib.pyplot as plt
import scipy.io
from matplotlib.ticker import MaxNLocator
from scipy import linalg
from scipy import signal
from numpy import random
from scipy import io as sio
import matplotlib.pyplot as plt
import os
import datetime
import time
import cv2
import argparse
from pylepton import Lepton
import RPi.GPIO as gpio
gpio.setwarnings(False)
import subprocess
import select
import scipy.io as scio
from scipy.optimize import curve_fit
import serial
import crcmod
import visa
sys.path.append('/python-seabreeze')
import seabreeze.spectrometers as sb
import asyncio
import usbtmc
import socket
import pickle
import sklearn
from scipy.interpolate import interp1d
from scipy.interpolate import interp2d

## load linear regressor for rotational and vibrational temperature
f_reg=open('linear_Trot.pkl','rb')
cl=pickle.load(f_reg, encoding="latin1")

## load substrate classifier
f_reg=open('knn_subs.pkl','rb')
knn=pickle.load(f_reg, encoding="latin1")

crc8 = crcmod.predefined.mkCrcFun('crc-8-maxim')
```

```python
## initialize oscilloscope
instr = usbtmc.Instrument(0x1ab1, 0x04ce)
instr.open()
while not (instr.timeout == 0.5 and instr.rigol_quirk == False):
    instr.timeout = 0.5
    instr.rigol_quirk = False
idg = ''
while not idg:
    try:
        idg = instr.ask("*IDN?")
    except Exception as e: # USBErrors
        print("{} in get_oscilloscope".format(e))
        time.sleep(0.4)
print("device info: {}".format(idg))
print("device timeout: {}".format(instr.timeout))
time.sleep(0.5)

## initialize spectrometer
devices = sb.list_devices()
t_int=12000*6
print("Available devices {}".format(devices))
spec = sb.Spectrometer(devices[0])
print("Using {}".format(devices[0]))
spec.integration_time_micros(t_int)
print("integratiopn time {} seconds.".format(t_int/1e6))
time.sleep(0.5)

class DummyFile(object):
    def write(self, x): pass

def nostdout(func):
    def wrapper(*args, **kwargs):
        save_stdout = sys.stdout
        sys.stdout = DummyFile()
        func(*args, **kwargs)
        sys.stdout = save_stdout
    return wrapper

## get arguments to run the script with
def get_runopts():
  """g
  Gets the arguments provided to the interpreter at runtime
  """
  parser = argparse.ArgumentParser(description="runs MPC",
            epilog="Example: python mpc_lin_test.py --quiet")
  parser.add_argument("--faket", help="use fake temperature data", action="store_true")
  parser.add_argument("--fakei", help="use fake intensity data", action="store_true")
  parser.add_argument("--timeout", type=float, help="timout (seconds) on oscilloscope
      ↪ operations",
```

```python
                          default=0.4)
  parser.add_argument("--save_therm", help="save␣thermography␣photos", action="store_true
      ↪ ")
  parser.add_argument("--save_spec", help="save␣OES␣spectra", action="store_true")
  parser.add_argument("--save_osc", help="save␣current␣waveform", action="store_true")
  parser.add_argument("--dir", type=str, default="data",help="relative␣path␣to␣save␣the␣
      ↪ data")
  parser.add_argument("--tag", type=str, default="",help="tag␣the␣saved␣files␣for␣easy␣
      ↪ recognition")
  parser.add_argument("--auto",help="run␣the␣code␣without␣connection␣to␣laptop", action="
      ↪ store_true")
  runopts = parser.parse_args()
  return runopts

runopts = get_runopts()

## record the time at which the script starts
curtime1 = datetime.datetime.now().strftime("%Y-%m-%d_%H%M%S.%f")

## generate directories to save peripheral measurements
SAVEDIR_therm = os.path.join(os.getcwd(),runopts.dir,"{}_thermography-{}".format(curtime1
    ↪ ,runopts.tag)) # path to the directory to save thermography files
SAVEDIR_spec = os.path.join(os.getcwd(),runopts.dir,"{}_spectroscopy-{}".format(curtime1,
    ↪ runopts.tag)) # path to the directory to save thermograph
SAVEDIR_osc = os.path.join(os.getcwd(),runopts.dir,"{}_oscilloscope-{}".format(curtime1,
    ↪ runopts.tag)) # path to the directory to save oscilloscope wavefomr current

if runopts.save_therm and not os.path.exists(SAVEDIR_therm):
  print("Creating␣directory:␣{}".format(SAVEDIR_therm))
  os.makedirs(SAVEDIR_therm)

if runopts.save_spec and not os.path.exists(SAVEDIR_spec):
  print("Creating␣directory:␣{}".format(SAVEDIR_spec))
  os.makedirs(SAVEDIR_spec)

if runopts.save_osc and not os.path.exists(SAVEDIR_osc):
  print("Creating␣directory:␣{}".format(SAVEDIR_osc))
  os.makedirs(SAVEDIR_osc)

############ Define Functions #############################
def save_data(SAVEDIR,data,fname):
  """
  Save data from measurment stored in an array
  """
  print("saving␣{}.csv".format(os.path.join(SAVEDIR,fname)))
  np.savetxt(os.path.join(SAVEDIR,"{}.csv".format(fname)),data,delimiter=',',fmt='%.4e')

def send_inputs_direct(device,U):

  Vn = U[0]
```

```python
  Fn = U[1]
  Qn = U[2]
  Dn = U[3]
  Xn = U[4]
  Yn = U[5]
  input_string='echo␣"v,{:.2f}"␣>␣/dev/arduino␣&&␣echo␣"f,{:.2f}"␣>␣/dev/arduino␣&&␣echo␣
      ↪ "q,{:.2f}"␣>␣/dev/arduino'.format(Vn, Fn, Qn)
  device.reset_input_buffer()
  device.write("v,{:.2f}\n".format(Vn).encode('ascii'))
  time.sleep(0.200)
  device.write("f,{:.2f}\n".format(Fn).encode('ascii'))
  time.sleep(0.200)
  device.write("q,{:.2f}\n".format(Qn).encode('ascii'))
  time.sleep(0.200)
  device.write("d,{:.2f}\n".format(Dn).encode('ascii'))
  time.sleep(0.400)
  device.write("x,{:.2f}\n".format(Xn).encode('ascii'))
  time.sleep(0.200)
  device.write("y,{:.2f}\n".format(Yn).encode('ascii'))
  time.sleep(0.200)

  print("input␣values:␣{:.2f},{:.2f},{:.2f},{:.2f},{:.2f},{:.2f}".format(Vn,Fn,Qn,Dn,Xn,
      ↪ Yn))

def send_inputs(device,U):
  """
  Sends input values to the microcontroller to actuate them using the subprocess package
      ↪ via the UNIX terminal
  """
  Vn = U[0]
  Fn = U[1]
  Qn = U[2]
  Dn = U[3]
  Xn = U[4]
  Yn = U[5]
  Pn = U[6]
  input_string='echo␣"v,{:.2f}"␣>␣/dev/arduino␣&&␣echo␣"f,{:.2f}"␣>␣/dev/arduino␣&&␣echo␣
      ↪ "q,{:.2f}"␣>␣/dev/arduino'.format(Vn, Fn, Qn)
  device.reset_input_buffer()

  subprocess.run('echo␣""␣>␣/dev/arduino', shell=True)
  time.sleep(0.0500)

  subprocess.run('echo␣"v,{:.2f}"␣>␣/dev/arduino'.format(Vn), shell=True)
  time.sleep(0.0500)

  subprocess.run('echo␣"f,{:.2f}"␣>␣/dev/arduino'.format(Fn), shell=True)
  time.sleep(0.0500)

  subprocess.run('echo␣"q,{:.2f}"␣>␣/dev/arduino'.format(Qn), shell=True)
```

```python
  time.sleep(0.0500)

  subprocess.run('echo "d,{:.2f}" > /dev/arduino'.format(Dn), shell=True)
  time.sleep(0.0500)

  subprocess.run('echo "x,{:.2f}" > /dev/arduino'.format(Xn), shell=True)
  time.sleep(0.0500)

  subprocess.run('echo "y,{:.2f}" > /dev/arduino'.format(Yn), shell=True)
  time.sleep(0.0500)

  subprocess.run('echo "p,{:.2f}" > /dev/arduino'.format(Pn), shell=True)
  time.sleep(0.0500)

  print("input values: {:.2f},{:.2f},{:.2f},{:.2f},{:.2f},{:.2f},{:.2f}".format(Vn,Fn,Qn,
      ↪ Dn,Xn,Yn,Pn))


def send_inputs_all(device,device2,Vn,Fn,Qn,Yn,Xn,Pn,Dn,On):
  """
  Sends input values to the microcontrollers to actuate them usig the serial pacakge
  """
  device.reset_input_buffer() #master arduino
  device2.reset_input_buffer() #complementary arduino

  subprocess.run('echo "" > /dev/arduino_m', shell=True)
  time.sleep(0.0100)
  #subprocess.run('echo "v,{:.2f}" > /dev/arduino_m'.format(Vn), shell=True) #for voltage
  subprocess.run('echo "w,{:.2f}" > /dev/arduino_m'.format(Vn), shell=True) #for power
  time.sleep(0.0100)
  subprocess.run('echo "y,{:.2f}" > /dev/arduino_c'.format(Yn), shell=True)
  time.sleep(0.0500)
  subprocess.run('echo "x,{:.2f}" > /dev/arduino_c'.format(Xn), shell=True)
  time.sleep(0.0500)
  subprocess.run('echo "d,{:.2f}" > /dev/arduino_c'.format(Dn), shell=True)
  time.sleep(0.100)
  subprocess.run('echo "p,{:.2f}" > /dev/arduino_m'.format(Pn), shell=True)
  time.sleep(0.0100)
  subprocess.run('echo "f,{:.2f}" > /dev/arduino_m'.format(Fn), shell=True)
  time.sleep(0.0100)
  subprocess.run('echo "q,{:.2f}" > /dev/arduino_m'.format(Qn), shell=True)
  time.sleep(0.0100)
  subprocess.run('echo "o,{:.2f}" > /dev/arduino_m'.format(On), shell=True)
  time.sleep(0.0100)
  print("input values: V:{:.2f},F:{:.2f},Q:{:.2f},Y:{:.2f}".format(Vn,Fn,Qn,Yn))

def is_valid(line):
  """
  Verify that the line is complete and correct
  """
```

```python
  l = line.split(',')
  crc = int(l[-1])
  data = ','.join(l[:-1])
  return crc_check(data,crc)

def crc_check(data,crc):
  """
  Cyclic redundancy check
  """
  crc_from_data = crc8("{}\x00".format(data).encode('ascii'))
  print("crc:{} calculated: {} data: {}".format(crc,crc_from_data,data))
  return crc == crc_from_data

def gaus(x,a,x0,sig):
    """
    Gaussian distribution
    """
    return a*NP.exp(-(x-x0)**2/(sig**2))

def get_temp_max(runopts):
  """
  Gets x and y position of the maximum temperature
  """
  if runopts.faket:
    return 24

  run = True
  for rr in range(8):
    try:
      with Lepton("/dev/spidev0.1") as l:
        data,_ = l.capture(retry_limit = 3)
      if l is not None:
        Ts = NP.amax(data[6:50,:,0]) / 100 - 273;
        mm= NP.where( data == NP.amax(data[6:50,:,0]) )
        print('max point at {},{}'.format(*mm))
        for line in data:
          l = len(line)
          if (l != 80):
              print("error: should be 80 columns, but we got {}".format(l))
          elif Ts > 150:
              print("Measured temperature is too high: {}".format(Ts))
        time.sleep(0.070)
        run = False
    except Exception as e:
      print(e)
      ## restart fail-check for hang-ups
      print("\nHardware error on the thermal camera. Lepton restarting...")
      gpio.output(35, gpio.HIGH)
      time.sleep(0.5)
      gpio.output(35, gpio.LOW)
```

```python
      print("Lepton restart completed!\n\n")

  return [int(mm[0]), int(mm[1])]

####### Asynchronous function definitions ############

async def get_temp_a(runopts,a):
  """
  Gets treatment temperatures with the Lepton thermal camera
  """
  if runopts.faket:
    return 24

  run = True
  while run:
    try:
      with Lepton("/dev/spidev0.1") as l:
        data,_ = l.capture(retry_limit = 3)
      if l is not None:
        mm=a ### This may need calibration #############
        Ts = NP.amax(data[int(mm[0]),int(mm[1]),0]) / 100 - 273;

        for line in data:
          l = len(line)
          if (l != 80):
            print("error: should be 80 columns, but we got {}".format(l))
          elif Ts > 150:
            print("Measured temperature is too high: {}".format(Ts))
        Tt = NP.amax(data[0:5,:,0]) / 100 - 273 #tube temeprature

        Ts_lin=data[int(mm[0]),:,0] /100 - 273 #crossection of substrate temperature
        yy=Ts_lin-Ts_lin[0]

        Ts2 = (Ts_lin[int(mm[1])+2]+Ts_lin[int(mm[1])-2])/2 #adjacent T1
        Ts3 = (Ts_lin[int(mm[1])+12]+Ts_lin[int(mm[1])-12])/2 #adjacent T2
        Ts_lin_out=Ts_lin[int(mm[1])-13:int(mm[1])+13] #1D temperature distribution in x

        Ts_2d_out=NP.array(data[int(mm[0])-13:int(mm[0])+13,int(mm[1])-13:int(mm[1])
            ↪ +13:,0])/100 - 273 #2D temperature distribution

        sig2=2.88/(NP.sqrt(-NP.log((Ts2-Ts3)/(Ts-Ts3)))) ## manual calculation for sigma

        Ts_fit=Ts_lin_out-Ts3 ## use curve fitting for sigma
        x_fit=NP.arange(-13*1.43,13*1.43,1.43)

        popt,pcov=curve_fit(gaus, x_fit, Ts_fit, p0=[10,0,3])
        sig=popt[2]

        #check options and save data
        if runopts.save_therm:
```

```python
            curtime = datetime.datetime.now().strftime("%Y-%m-%d_%H%M%S.%f")
            fname = "{}".format(curtime)
            save_data(SAVEDIR_therm,data[:,:,0]/100.0 - 273 ,fname)

        if runopts.save_spec:
            wv=spec.wavelengths()
            sp_int=spec.intensities()
            sp_data=[wv,sp_int]
            curtime = datetime.datetime.now().strftime("%Y-%m-%d_%H%M%S.%f")
            fname = "{}".format(curtime)
            save_data(SAVEDIR_spec,sp_data,fname)

        time.sleep(0.070)
        run = False
    except Exception as e:
      print(e)
      print("\nHardware error on the thermal camera. Lepton restarting...")
      gpio.output(35, gpio.HIGH)
      time.sleep(0.5)
      gpio.output(35, gpio.LOW)
      print("Lepton restart completed!\n\n")

  return [Ts, Ts2, Ts3, Ts_lin_out, Tt, sig, sig2, Ts_2d_out, data]

async def get_intensity_a(f,f2,runopts):
  """
  Get information from the two microcontollers
  """

  if runopts.fakei:
    Is = 5
  else:
    run1 = True #initialize measurements to prevent errors
    run2 = True
    v_rms=0
    Is=0
    U=[0,0,0]
    x_pos=0
    y_pos=0
    dsep=0
    P_emb=0
    I_emb=0
    T_emb=0
    Dc=0
    q_o=0
    while run1:
      try:
        f.reset_input_buffer()
        f.readline()
        line = f.readline().decode('ascii')
```

```python
        if is_valid(line):
          run1 = False
          Is = int(line.split(',')[6])
          V_emb = float(line.split(',')[7])
          V = float(line.split(',')[1])
          f = float(line.split(',')[2])
          q = float(line.split(',')[3])
          Dc = float(line.split(',')[5])
          T_emb=float(line.split(',')[8])
          I_emb=float(line.split(',')[9])
          P_emb=float(line.split(',')[-2])
          q_o=float(line.split(',')[12])
        else:
          print("CRC8 failed. Invalid line!")
        U=[V,f,q,dsep]
      except:
        pass
    while run2:
      try:
        f2.reset_input_buffer()
        f2.readline()
        line = f2.readline().decode('ascii')
        if is_valid(line):
          run2 = False
          dsep=float(line.split(',')[4])
          x_pos=float(line.split(',')[10])
          y_pos=float(line.split(',')[11])
        else:
          print("CRC8 failed. Invalid line!")
        U=[V,f,q,dsep]
      except:
        pass
  return [Is,v_rms,U,x_pos,y_pos,dsep,T_emb,P_emb,Dc,q_o]

def gpio_setup():
    """
    Hardware-restart for thermal camera hang-ups
    """
  gpio.setmode(gpio.BOARD)
  gpio.setup(35, gpio.OUT)
  gpio.output(35, gpio.HIGH)

async def get_oscilloscope_a(instr,runopts):
    '''
    Get measurements from the oscilloscope
    '''
    try:
        instr.write(":MEAS:SOUR CHAN2")
        Imax=float(instr.ask("MEAS:VMAX?"))*1000
        Ip2p=float(instr.ask("MEAS:VPP?"))*1000
```

```python
        rdel=float(instr.ask("MEAS:ITEM?␣RDEL"))
        y_raw=instr.ask(':WAV:DATA?')
        y_data=np.fromstring(y_raw[11:],dtype=float,sep=',')

        if runopts.save_osc:
            curtime = datetime.datetime.now().strftime("%Y-%m-%d_%H%M%S.%f")
            fname = "{}".format(curtime)
            save_data(SAVEDIR_osc,y_data,fname)

        instr.write(":MEAS:SOUR␣MATH")
        P=float(instr.ask("MEAS:VAVG?"))
        Prms=float(instr.ask("MEAS:ITEM?␣PVRMS"))

        if P>1e3:
            print('WARNING:␣Measured␣power␣is␣too␣large')
            time.sleep(0.8)
            instr.write(":MEAS:SOUR␣MATH")
            P=float(instr.ask("MEAS:VAVG?"))

        rdel=rdel*1.e6
        fdel=0
    except Exception as e:
        print('oscilloscope␣error!')
        print(e)
        P=0
        Ip2p=0
        Prms=0
        rdel=0
        Imax=0
        pass

    return [P,Ip2p,Prms,rdel,Imax]

async def get_spec_a(spec):
    '''
    Get measurements from the spectrometer
    '''
    wv=spec.wavelengths()
    sp_int=spec.intensities()

    int_N2CB=sp_int[63:114]-NP.mean(sp_int[-10:-1])
    int_full=sp_int[10:]-NP.mean(sp_int[-10:-1])
    int_n=int_N2CB/max(int_N2CB)

    int_full_n=int_full/max(int_full)

    r2=knn.predict(int_full_n.reshape(1,-1)) #classifier prediction
    Tspec=cl.predict(int_n.reshape(1,-1)) #regressor prediction
    print('Trot',Tspec[0][0]*550)
```

```python
    if r[0]==0:
        print('Capacitative Substrate!')
    elif r[0]==1:
        print('Conductive Substrate!')
    else:
        print('Classifier Error')
    sp_int=sp_int-NP.mean(sp_int[-20:-1])
    sum_int=NP.sum(sp_int[20:])

    O777=max(sp_int[1200:1250]) #varios important spectrum lines
    O844=max(sp_int[1405:1455])
    N391=max(sp_int[126:146])
    He706=max(sp_int[990:1100])

    return [O777,O844,N391,He706,sum_int,r,r2,Tspec[0]]

async def asynchronous_measure(f,instr,runopts,max_pt):
    '''
    Define series of asynchronous tasks for measurement from the different sources
    '''
        tasks=[asyncio.ensure_future(get_temp_a(runopts,max_pt)),
            asyncio.ensure_future(get_intensity_a(f,f_move,runopts)),
            asyncio.ensure_future(get_oscilloscope_a(instr,runopts)),
            asyncio.ensure_future(get_spec_a(spec))]

        await asyncio.wait(tasks)
        return tasks


################# SET AND TEST MEASUREMENTS #######################

## initialize measurements
Ts_old=37
Ts2_old=32
Ts3_old=25
Tslin_old=[37]*26
Pold=2

runopts = get_runopts()
gpio_setup()

## connect to the microcontollers
f = serial.Serial('/dev/arduino_m', baudrate=38400,timeout=1) #master
f_move = serial.Serial('/dev/arduino_c', baudrate=38400,timeout=1) #complementary
max_pt=get_temp_max(runopts) ##get maximum point

if os.name == 'nt':
    ioloop = asyncio.ProactorEventLoop() # for subprocess' pipes on Windows
    asyncio.set_event_loop(ioloop)
else:
```

```python
    ioloop = asyncio.get_event_loop()

print(instr)

# run the measurement tasks once and extract values
a=ioloop.run_until_complete(asynchronous_measure(f,instr,runopts,max_pt))

Temps=a[0].result()
Ts=Temps[0]
Ts2=Temps[1]
Ts3=Temps[2]
Ts_lin=Temps[3]
Tt=Temps[4]
sig=Temps[5]
sig2=Temps[6]
Ts_2d_out=Temps[7]
sig0=sig
Zm0=8.3

Ard_out=a[1].result()
Is=Ard_out[0]
v_rms=Ard_out[1]
x_pos=Ard_out[3]
y_pos=Ard_out[4]
d_sep=Ard_out[5]
T_emb=Ard_out[6]

Osc_out=a[2].result()
Vrms=Osc_out[0]
P=Osc_out[0]

delta=3.0
Ts_lin_old=Ts_lin

# print measured temperature and power confirm measurement working
msg="Temperature:␣{:.2f}␣Power:␣{:.2f}".format(Ts,P)
print('Measurment␣working...')
CEM=np.zeros(np.shape(Ts_lin)) #initialize CEM measurement
CEM2D=np.zeros([9,9]) #initialize 2D CEM measurement
print(msg)

## check if the script requires connection from external client, if so start a websocket
    ↪ client
if not runopts.auto:
    s=socket.socket(socket.SO_REUSEADDR,1)
    host='pi3.dyn.berkeley.edu'
    port=2223
    s.bind((host,port))
    s.listen(5)
    print('\n')
```

```python
    print('Server is listening on port' ,port)
    print('Waiting for connection...')

    c, addr = s.accept()
    c.settimeout(0.2)

    print('Got connection from', addr)

## set upper and lower bounds for inputs
# for voltage
#u_ub=[10.,20,4.,100.]
#u_lb=[6.,10.,1.2,100.]

#for power
u_ub=[5.3,20,4.,100.]
u_lb=[1.5,10.,1.2,10.]


########### INITIAL INPUT PARAMETERS ####################
V=4. #initial applied power/voltage
O=0 # initial oxygen admixture flowrate
Dc=100. #initial duty cycle
F=20. #initial frequency
Q=1.5 #initial flow
q=1.5

x0_ff=NP.array([[0],[0],[0]]) #feedforward states
u0_fb=V


############################## setpoints ####################
Tset=41. #initial setpoint
sigset=8.5 #initial setpoint
Pset=3. #initial setpoint



ind_i=1
################## set timers ####################

t_el=0 #seconds sup. control timer
tm_el=0
move=0
e1=0.
e10=0.

Delta_y=11. #mm movement disturbance

t_mel=0 #PI control timer
I1=0
I2=0
Dsep=4.0
```

```python
Y_dir=-1 #movement direction

t_dis=100.0 #period of disturbances, step tests and movement
t_step=60.
t_move=60.*2.

int_flag=0 #flags
calib_flag=0
r_old=0

############ initialize jet position #######################
Y_pos=0.
X_pos=0.

if runopts.auto:
    send_inputs_all(f,f_move,V,F,Q,Y_pos,X_pos,Dc,Dsep,O)
    print('initializing jet position...')
    time.sleep(5.)

############ initialize save document ###############################


sv_fname = os.path.join(runopts.dir,"PI_Server_Out_{}-{}".format(curtime1,runopts.tag))
save_fl=open(sv_fname,'a+')
save_fl.write('time,Tset,Ts,Ts2,Ts3,P,Imax,Ip2p,O777,O845,N391,He706,sum_int,*U_m,q_o,D_c
    ↪ ,x_pos,y_pos,T_emb,V,P_emb,Prms,Rdel,Is,sig,subs_type,Rot,tm_el\n')


################## MAIN LOOP ####################

t_move_now=time.time() ##movement_start
t_move_dis=time.time() ##disturbance_start
t_move_step=time.time() #step_start

while True:
    try:
        t0=time.time()

        ######### Disturbance MOVE BACK AND FORTH ##########

        print('time remaining {:6.2f}'.format(t_move-time.time()+t_move_now))

# if X_pos==0: #for case I and II
# X_dir=-1
# if X_pos==-11: #for case I and II
# X_dir=1
# if X_dir==1 and (time.time()-t_move_now)>=t_move: #for case I and II
# print('Moving')
# X_pos=X_pos+Delta_y
# t_move_now=time.time()
```

```python
# elif X_dir==-1 and (time.time()-t_move_now)>=t_move: #for case I and II
# print('Moving')
# X_pos=X_pos-Delta_y


        ############# MOVE TO AND STAY #################

# if (time.time()-t_move_now)>=t_move:
# move=1

# if Y_dir==1 and Y_pos<=44 and move==1: #for case I and II
# print('Moving')
# Y_pos=Y_pos+Delta_y

# elif Y_dir==-1 and Y_pos>=8 and move==1: #for case I and II
# print('Moving')
# Y_pos=Y_pos-Delta_y

# if round(Y_pos)<=8 and move==1:
# Y_dir=1
# move=0
# t_move_now=time.time()
# if round(Y_pos)==28 and move==1:
# move=0
# t_move_now=time.time()
# if round(Y_pos)>=44 and move==1: #for case I and II
# Y_dir=-1
# move=0
# t_move_now=time.time()


##### STEP AND DISTURBANCE TESTS ###########
        print('time remaining {:6.2f}'.format(t_step-time.time()+t_move_step))

    # if (time.time()-t_move_step)>=t_step:
        #Tset=Tset+1.5
    # Tset=Tset_list[ind_i]
    # Q=Q_list[ind_i]
    # ind_i=ind_i+1

    # t_move_step=time.time()


        ########## RECEIVE FROM CLIENT ############
        try:

            data=c.recv(512).decode()
            data_str=data.split(',')
            data_flt=[float(i) for i in data_str]
            Tset=data_flt[0]
            #Vover=data_flt[0]
```

```python
        X_pos=data_flt[1]
        Y_pos=data_flt[2]
        int_flag=data_flt[3]
        t_el=data_flt[4]

        print('Optimal Reference Recieved!')
        print('Tref: {:6.2f}, t_el:{:6.2f}'.format(Tset,t_el))
    except:
        print('no #####data yet')

    ############### SEND INPUTS ###############
    print("Sending inputs...")

    send_inputs_all(f,f_move,V,F,Q,Y_pos,X_pos,Dc,Dsep,O)

    print("Inputs sent!")


    if int_flag==1 and calib_flag==0:
        max_pt=get_temp_max(runopts) ##get maximum point
        calib_flag=1

    ## run measurement tasks and extract measurments
    a=ioloop.run_until_complete(asynchronous_measure(f,instr,runopts,max_pt))


    Temps=a[0].result()
    Ts_k=Temps[0]
    Ts2=Temps[1]
    Ts3=Temps[2]
    Ts_lin_k=Temps[3]
    Tt=Temps[4]
    sig_k=Temps[5]
    sig2=Temps[6]
    Ts_2d_out_k=Temps[7]



    sig=sig_k #no filter

    Ard_out=a[1].result()
    Is=Ard_out[0]
    v_rms=Ard_out[1]
    U_m=Ard_out[2]
    x_pos=Ard_out[3]
    y_pos=Ard_out[4]
    d_sep=Ard_out[5]
    T_emb=Ard_out[6]
    P_emb=Ard_out[7]
    D_c=Ard_out[8]
```

```python
        q_o=Ard_out[9]

        Osc_out=a[2].result()
        P=Osc_out[0]
        Ip2p=Osc_out[1]
        Prms=Osc_out[2]
        Rdel=Osc_out[3]
        Imax=Osc_out[4]

        Spec_out=a[3].result()
        O777=Spec_out[0]
        O845=Spec_out[1]
        N391=Spec_out[2]
        He706=Spec_out[3]
        sum_int=Spec_out[4]
        r=Spec_out[5]
        r2=Spec_out[6]
        if r2[0]>1.:
            r2[0]=1.
        Tspec=Spec_out[7]

        if Ip2p==0:
            P=P_old
            Ip2p=Ip2p_old
            Prms=Prms_old
            Rdel=Rdel_old
            Imax=Imax_old
        else:
            P_old=P
            Ip2p_old=Ip2p
            Prms_old=Prms
            Rdel_old=Rdel
            Imax_old=Imax

        Zmeas=float(U_m[0]/Ip2p/4)

        print("Temperature:_{:.2f},_Sigma:_{:.2f},_Power:_{:.2f}".format(Ts,sig,P))
        print("Inputs:{:.2f},{:.2f},{:.2f},{:.2f}".format(*U_m))
        if abs(Ts)>60:
            Ts_k=Ts_old
            Ts2=Ts2_old
            Ts3=Ts3_old
            Ts_lin_k=Ts_lin_old
            Ts_2d_out_k=Ts_2d_old
            print('WARNING:_Old_value_of_Ts_is_used')
        else:
            Ts_old=Ts_k
            Ts2_old=Ts2
            Ts3_old=Ts3
            Ts_lin_old=Ts_lin_k
```

```python
        Ts_2d_old=Ts_2d_out
    if abs(P)>10:
        P=Pold
        print('WARNING: Old value of Ts is used')
    else:
        Pold=P


    ## filter for temperature
    Ts=Ts*0.7+Ts_k*0.3
    Ts_lin=Ts_lin*0.7+Ts_lin_k*0.3
    Ts_2d_out=0.7*Ts_2d_out+Ts_2d_out_k*0.3

    ## shift 2D temperature measurements based on position of the jet
    x_gen=NP.linspace(0,16,9) #range of points controlled [0-11mm]
    y_gen=NP.linspace(0,16,9) #range of points controlled [0-11mm]

    x_now=NP.linspace(-13*1.44,13*1.44,26)+y_pos-0.5 #positions corresponding to
        ↪ current measurement
    y_now=NP.linspace(13*2,-13*2,26)+x_pos+0.0 #positions corresponding to current
        ↪ measurement

    Tshift=interp1d(x_now,Ts_lin,bounds_error=False,fill_value=min(Ts_lin))(x_gen)
    Tshift2D=interp2d(x_now,y_now,Ts_2d_out,bounds_error=False,fill_value=18,kind='
        ↪ cubic')(x_gen,y_gen)

    # integrate the dose metric
    if int_flag==1:
        CEM2D=CEM2D+1.3*(9.74e-14/60.0)*np.exp(np.multiply(0.6964,Tshift2D))

    ############### FEED FORWARD ####################################


    ff_a=NP.array([[2.471,-1.009, 0.5438],[2, 0.0, 0.0],[0.0, 0.5, 0.0]])
    ff_b=NP.array([[2.0],[0.0],[0.0]])
    ff_c=NP.array([[0.7591,-0.6911,0.629]])
    ff_d=NP.array([-2.899])

    xk_ff=ff_a.dot(x0_ff)+ff_b.dot(r2[0])

    yk_ff=ff_c.dot(xk_ff)+ff_d.dot(r2[0])

    uk_ff=0*float(yk_ff[0])
    x0_ff=xk_ff


    ########### PI CONTROLS P=>T ##################
    ## tuning
    Kp=3.2##glass lambda 1.5
    Ki=0.12
```

```python
#### Un-comment for power control ###############
        uk_fb=u0_fb+Kp*e1+(-Kp+Ki*1.3)*e10

        u1=uk_fb-uk_ff #add feedforward

        if round(u1,2)>=u_ub[0] and Tset>=Ts:
            I1 = I1
            V=u_ub[0]
            u0_fb=u0_fb+Kp*e1+(-Kp+0*Ki*1.3)*e10
            print('*')
        elif round(u1,2)>=u_ub[0] and Tset<Ts:
            I1 = I1 + e1*t_mel
            V=u_ub[0]
            u0_fb=uk_fb
            print('*')
        elif round(u1,2)<=u_lb[0] and Tset<=Ts:
            I1 = I1
            V=u_lb[0]
            u0_fb=u0_fb+Kp*e1+(-Kp+0*Ki*1.3)*e10
            print('*')
        elif round(u1,2)<=u_lb[0] and Tset>Ts:
            I1 = I1 + e1*t_mel
            V=u_lb[0]
            u0_fb=uk_fb
            print('*')
        else:
            I1=I1+e1*t_mel
            u0_fb=uk_fb
            V=round(u1,2)

        e10=e1
###########################################################

        ############### Send measurement to client ###############

        ## for 2D temperature measurement
        #print(*CEM2D.flatten().shape)
        #CEM=CEM+tm_el*(9.74e-14/60.0)*np.exp(np.multiply(0.6964,Tshift))


        #msg='{:6.2f},{:6.2f},{:6.2f},{:6.2f},{:6.2f},{:6.2f},{:6.2f},{:6.2f},{:6.2f
            ↪ },{:6.2f},{:6.2f},{:6.2f},{:6.2f},{:6.2f},{:6.2f},{:6.2f},{:6.2f},{:6.2f
            ↪ },{:6.2f},{:6.2f},{:6.2f},{:6.2f},{:6.2f},{:6.2f},{:6.2f},{:6.2f} \n'.
            ↪ format(*CEM)

        msg_form='{:6.2f},'
        msg_str=msg_form*(1+len(Tshift2D.flatten()))
        msg_str=msg_str[:-1]+'\n'
        msg=msg_str.format(*CEM2D .flatten(),Ts)
```

```python
        msg2='{:6.2f}\n'.format(Ts)
        #print(msg2)

        if not runopts.auto:
            c.send(msg.encode())
            time.sleep(0.05)
            print('Measured outputs sent')


        tm_el=time.time()-t0

        if tm_el<1.3:
            time.sleep(1.3-tm_el)
            tm_el=1.3

        save_fl.write('{:6.2f},{:6.2f},{:6.2f},{:6.2f},{:6.2f},{:6.2f},{:6.2f},{:6.2f
            },{:6.2f},{:6.2f},{:6.2f},{:6.2f},{:6.2f},{:6.2f},{:6.2f},{:6.2f},{:6.2f
            },{:6.2f},{:6.2f},{:6.2f},{:6.2f},{:6.2f},{:6.2f},{:6.2f},{:6.2f},{:6.2f
            },{:6.2f},{:6.2f},{:6.2f},{:6.2f},{:6.2f},{:6.2f},{:6.2f},{:6.2f}\n'.format
            (time.time(),Tset,Ts,Ts2,Ts3,P,Imax,Ip2p,O777,O845,N391,He706,sum_int,*U_m,
            q_o,D_c,x_pos,y_pos,T_emb,V,P_emb,Prms,Rdel,Is,sig,sig2,r[0],r2[0],Tspec
            [0]*550,uk_ff,tm_el))
        save_fl.flush()

        if KeyboardInterrupt==1:
            sys.exit(1)

    except Exception as e:
        if not runopts.auto:
            c.close()
        print('There was an error !')
        print(e)
        sys.exit(1)
```

Appendix C

Modeling

C.1   Material Properties

Table C.1: Material properties for helium and air used for physics-based modeling of kHz-excited APPJ in He

Parameter	Value
Helium	
ρ_{He}	0.156 kgm^{-3}
$C_{p,He}$	5.191×10^3 Jkg^{-1}K^{-1}
k	0.153 Wm^{-1}K^{-1}
$D_{He,Air}$	71×10^{-6} m^{2}s^{-1}
Air	
ρ_{Air}	1.165 kgm^{-3}
$C_{p,Air}$	1×10^3 Jkg^{-1}K^{-1}
k	0.026 Wm^{-1}K^{-1}

Table C.2: Material properties of experimental setup components used for physics-based modeling of kHz-excited APPJ in He

Parameter	Value
Borosilicate Substrate	
ρ	2800 kgm^{-3}
k	1.2 Wm^{-1}K^{-1}
C_p	795 Jkg^{-1}K^{-1}
t_s	0.2 mm
Quartz Tube	
ρ	2200 kgm^{-3}
k	1.1 Wm^{-1}K^{-1}
C_p	480 Jkg^{-1}K^{-1}
Aluminum Ground Plate	
ρ	2700 kgm^{-3}
k	238 Wm^{-1}K^{-1}
C_p	900 Jkg^{-1}K^{-1}

C.2 Lumped Parameter Model of an RF-APPJ in Ar

This section presents the lumped-parameter control-oriented model of an RF-APPJ [1]. This APPJ configuration is used commonly in plasma medical applications popularized by the commercially available kINPen device [79]. The modeling strategy utilized for this device is similar to that presented in Chapter 4.

A schematic representation of the APPJ under study is shown in Figure C.1. The APPJ is RF-excited pure argon (Ar) plasma, with no additional gas admixing in the inlet. The RF-APPJ is used for direct treatment — there is no separate ground electrode on the dielectric tube. Thus, the plasma extends as a free jet, electrically coupled to surroundings and the target substrate (i.e., plasma current reaches the target substrate). The characteristics of the model jet are consistent with devices used in clinical applications of APPJs (e.g., kINPen, INP Greifswald [79]). The considered APPJ configuration has been extensively investigated for biomedical applications [106], [110], and has been the subject of several modeling studies [126], [157]. A key challenge in using APPJs for direct treatment applications (as in Figure C.1) arises from the strong dependence of the electrical and thermal characteristics of the plasma jet on variations in the separation distance between the substrate and device [256] as well as variations in the electrical properties of the substrate [25], [106].

---

[1]This section is previously published in [197]
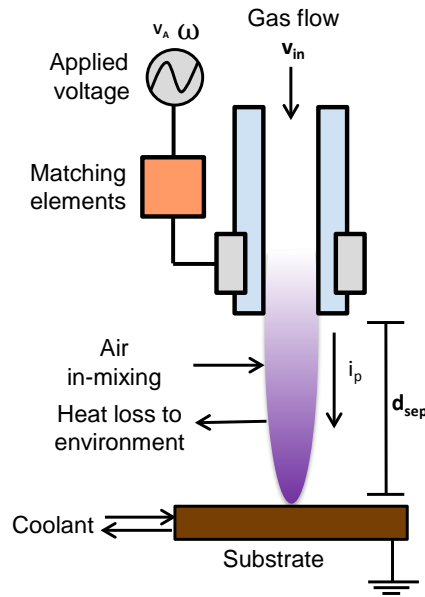
Figure C.1: Schematic of the RF-APPJ in pure argon. Ar flows through a dielectric tube, entering the tube at velocity v_{in} and is excited to form a plasma by an RF voltage VA applied via a matching network to an external electrode ring at frequency ω. Current i_p passes through the plasma plume to the substrate. The substrate, in general, has a complex electrical impedance Z_s, coupling the plasma current in the jet to ground. The tube tip is within a distance d_{sep} from the grounded, cooled substrate. Air components and heat are exchanged radially between the Ar jet and the surrounding air.

C.2.1 Power Deposition and Gas Heating in the Dielectric Tube
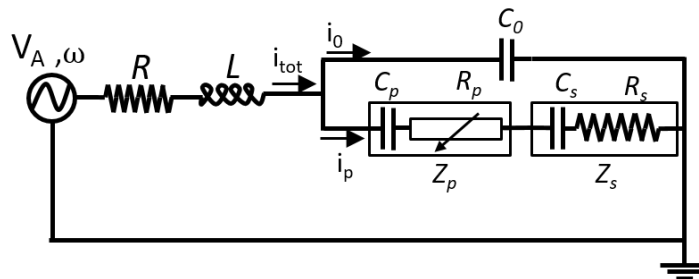
Figure C.2: Equivalent circuit for the RF-APPJ [106]. See text for details.

Figure C.2 shows an equivalent circuit for the RF-APPJ, where R is the external circuit resistance, L is the matching inductance, C_0 is the parasitic capacitance, Z_p is the plasma

complex impedance consisting of the bulk plasma resistance R_p and plasma capacitance C_p, and Z_s is the surface impedance with the resistive and capacitative components C_s and R_s, respectively. At steady state, the equivalent circuit can be modeled by Kirchhoff's second law

$$V_A - |Z_{ip}|i_p = 0, \tag{C.1}$$

where the overall impedance Z_{ip} relates the plasma current i_p to the applied voltage V_A. The expression for Z_{ip} can be derived from the circuit structure

Complex plasma impedance in terms of plasma current, developed through analogy with a 1D RF parallel-plate discharge model, associated with the α-γ mode transition [112]. The plasma impedance Z_p can be a function of the plasma current i_p, gas temperature T_{g0}, and separation distance d_{sep}. For an RF APPJ the following plasma resistance-current parameterization is adopted:

$$R_p(i_p) = (-\alpha i_p + \beta)\frac{d_{sep}}{T_{g0}}, \tag{C.2}$$

where the parameters α and β are estimated using predictions of a 1D model of a parallel-plate RF discharge in argon [112]. The characteristic V-I behavior of the parameterization (C.2) is shown in Figure C.3. The peak in the V-I characteristic curve can be related to plasma stability. The differential plasma conductivity ($d\mathrm{I}/d\mathrm{V}$) becomes negative when plasma current surpasses the peak value. This can result in a mode transition in the plasma [257]. Needle and ring-electrode APPJs can also exhibit similar characteristic V-I behavior as shown in [47], [110].

Figure C.3 shows the resulting voltage-current (V-I) characteristic curve, which adequately describes the V-I behavior obtained from a 1D fluid model of an RF parallel-plate discharge in argon [112].

To determine the gas temperature T_{g0} in (C.2), a volume-averaged, steady-state energy balance is formulated for the gas in the dielectric tube region

$$\rho_{in}v_{in}c_{p\mathrm{Ar}}A_c(T_{in} - T_{g0}) + \eta P = 0, \tag{C.3}$$

where T_{in}, ρ_{in}, and v_{in} are the inlet gas temperature, density, and velocity, respectively, $c_{p\mathrm{Ar}}$ is the specific heat capacity of argon, A_c is the cross-sectional area of the tube, η is an efficiency factor for the gas heating through power deposition into the neutral gas, and P is the total electrical power deposited in the plasma. The total power P is given by

$$P = \frac{1}{2}|i_p|^2|Z_p|cos(\phi), \tag{C.4}$$

where ϕ is the angle between the sinusoidal plasma current and applied potential. In the energy balance (C.3), the heat loss to the dielectric tube is neglected. Note that the total mass flow through the tube is equal to the product of gas density and velocity. Even though ρ and v vary with the gas temperature, the mass flow is constant and is equal to $\rho_{in}v_{in}$. Equations (C.1)-(C.4) constitute the equivalent circuit model in the dielectric tube.
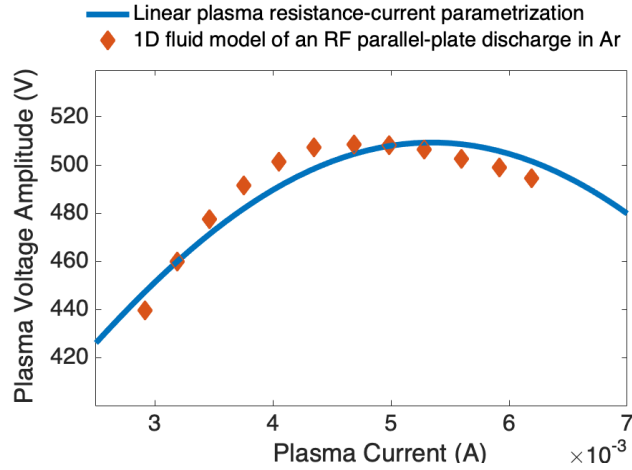
Figure C.3: The voltage-current behavior predicted by the adopted linear plasma resistance-current parameterization (C.2) and a 1D fluid model of an RF parallel-plate discharge in argon reported in [112].

C.2.2 Heat and mass transfer in the separation distance

The transport processes between the tip of the tube and substrate are described by a set of steady-state 1D mass and energy balances for a two-species system consisting of Ar and air. The steady-state energy balance along the gas flow axis is given by

$$\frac{dT_g}{dz} = -\frac{1}{\rho v c_p}\Big(\frac{U}{r}(T_g - T_{inf})\Big), \qquad T_g(0) = T_{g0}, \tag{C.5}$$

where $T_g(z)$ is the gas temperature along the flow axis z, U is the lumped (radial) heat transfer coefficient across the plume radius r, T_{inf} is the ambient air temperature, and ρ, v, and c_p are the density, velocity, and heat capacity of the gas plume, respectively. Since it is assumed that no mass transfer occurs along the flow axis, the continuity equation yields $\rho v = \rho_{in} v_{in}$. The gas temperature in the dielectric tube is used as the boundary condition at $z = 0$ for (C.5).

The gas density ρ is a function of gas composition, which in turn depends on the average molecular weight of the gas as it flows between the tip of the tube and the substrate. This is obtained from a steady-state mass balance for Ar

$$\frac{dm_{\text{Ar}}}{dz} = -\frac{P_{atm}}{R\rho_{in}v_{in}}\frac{1}{T_g}\Big(\text{Mw}_{\text{Ar}}m_{\text{Ar}} + \text{Mw}_{\text{Air}}(1 - m_{\text{Ar}})\Big)\frac{k}{r}(m_{\text{Ar}} - m_{inf}), \qquad m_{\text{Ar}}(0) = 1, \tag{C.6}$$

where $m_{\text{Ar}}(z)$ is the Ar mass fraction along the flow axis z, P_{atm} is atmospheric pressure, R is the ideal gas constant, Mw_{Ar} and Mw_{Air} are the molecular weights of Ar and air, respectively, k is the lumped (radial) mass transfer coefficient, and $m_{inf} = 0$ is the argon mass fraction

in ambient air. For the separation distance between the tip of the dielectric tube and the substrate, the continuity equation can be written as

$$\frac{d(\rho v)}{dz} = 0, \qquad \rho v|_{z=0} = \rho_{in} v_{in}, \tag{C.7}$$

which implies that ρv is constant in the gas plume. The ideal gas law is used to obtain the average gas density ρ as a function of the gas temperature along the flow axis

$$\rho(z) = \frac{P_{atm}}{R} \frac{1}{T_g(z)} \left(\mathrm{Mw}_{\mathrm{Ar}} m_{\mathrm{Ar}} + \mathrm{Mw}_{\mathrm{Air}} (1 - m_{\mathrm{Ar}}) \right). \tag{C.8}$$

From (C.7) and (C.8), the velocity of the plume gas is given by

$$v(z) = \rho_{in} v_{in} \frac{R}{P_{atm}} \frac{T_g(z)}{\left(\mathrm{Mw}_{\mathrm{Ar}} m_{\mathrm{Ar}} + \mathrm{Mw}_{\mathrm{Air}} (1 - m_{\mathrm{Ar}}) \right)}. \tag{C.9}$$

Expression (C.6) is obtained by inserting (C.9) into the 1D continuity equation for Ar. The lumped transport coefficients U and k in (C.5)-(C.6) are assumed to scale with the square root of the inlet argon velocity $\sqrt{v_{in}}$ since the gas flow is in laminar or near-laminar regime. The spatial integration bounds for (C.5)-(C.6) are set to $z = 0$ and $z = d_{sep}$. Thus, the heat and mass transfer in the gas plume is dependent on the separation distance between the tip of the dielectric tube and substrate. When the in-mixing of air along the gas plume is neglected, (C.5) can be solved analytically [258].

C.2.3   Substrate Temperature

The thermal dose metric is defined in terms of the substrate temperature. The substrate is considered to be continuously cooled from below. In a biomedical context, this cooling would be provided by blood flow. Assuming that there exists no temperature gradients within the substrate, the dynamics of the maximum substrate temperature $T_{s,max}(t)$ can be described by the Pennes' bioheat equation [259]

$$\frac{dT_s, max}{dt} = -\frac{\lambda_b c_b}{\rho_s c_{ps}} \left(T_{s,max} - T_b \right) + \frac{h}{\rho_s c_{ps} d_s} \left(T_g(d_{sep}) - T_{s,max} \right) + \frac{0.5 i_p^2 R_s}{A_c \rho_s c_{ps} d_s}, \quad T_{s,max}(0) = 311\,\mathrm{K}, \tag{C.10}$$

where d_s is the thickness of the substrate, λ_b, T_b, and c_b are the perfusion rate, temperature, and specific heat capacity of the coolant, respectively, ρ_s and c_{ps} are the density and specific heat capacity of the substrate, respectively, h is the heat transfer coefficient between the gas plume and the substrate, and $T_g(d_{sep})$ is the gas plume temperature adjacent to the substrate. The last term in the right-hand side of (C.10) accounts for ohmic heating of the substrate due to the plasma current i_p.

C.2.4   Model Parameters

Table C.3: Parameter values of the equivalent circuit model for the RF-APPJ in Ar.

Parameter	Value
ω	13.56 MHz
R	50 Ω
L	1.04×10^5 H
C_0	0.1 μF
C_p	0.14 nF
α	-6×10^9 Ω K A^{-1} mm^{-1}
β	6.42×10^7 Ω K mm^{-1}
C_s	11.7 nF
R_s	100 Ω
η	0.5
$c_{p\text{Ar}}$	521.5 J/kg K
ρ_{in}	1.63 kg m^{-3}

Table C.4: Parameter values of the heat and mass transfer model for the RF-APPJ in Ar.

Parameter	Value
U	$100\sqrt{v_{in}}$ W m^{-2} K^{-1}
k	$0.1\sqrt{v_{in}}$ m^2 s^{-1}
T_{inf}	298 K
r	1 mm
Mw$_{\text{Ar}}$	40 gmol^{-1}
Mw$_{\text{Air}}$	29 gmol^{-1}

Table C.5: Parameter values of the substrate temperature model for the RF-APPJ in Ar.

Parameter	Value
d_s	5 mm
λ_b	1 kg m^{-3} s^{-1}
T_b	310 K
c_b	3650 J kg^{-1} K^{-1}
c_{ps}	3680 J kg^{-1} K^{-1}
ρ_s	1020 kg m^{-3}
h	$36\sqrt{v_{in}}$ W m^{-2} K^{-1}

C.3 Parameters for the kHz-APPJ model in He

Table C.6: Parameters for the circuit model of kHz-APPJ in He.

Parameter	Value
R	50 Ω
C_0	8.07 pF
C_s	28.67 nF
C_p	9.40 pF
$R_{p,0}$	1.87 MΩ
d_{sep}	4 mm

Table C.7: Parameters for transport model of kHz-APPJ in He.

Parameter	Value
η	0.47
U_I	1.6 Wm^{-2}K^{-1}
U_{II}	$1.8\sqrt{v}$ Wm^{-2}K^{-1}
U_{III}	$50v^{0.8}$ Wm^{-2}K^{-1}
U_{IV}	$10\sqrt{v}$ Wm^{-2}K^{-1}
K	$0.017\sqrt{v}$m^{2}s^{-1}
r_r	5 mm
r	1.5 mm

C.4 Transfer function models

Fitted transfer functions between the Laplace transform of the maximum substrate temperature $T(s)$ and and applied voltage $V(s)$,

$$\frac{T(s)}{V(s)} = \frac{0.09274}{s + 0.03442}, \tag{C.11}$$

and between the Laplace transform of the maximum substrate temperature $T(s)$ and substrate type $M(s)$,

$$\frac{T(s)}{M(s)} = \frac{1.374s^2 - 1.586s + 0.09325}{s^3 + 1.278s^2 + 0.4847s + 0.0194}. \tag{C.12}$$

The mathematical function describing the change in substrate type in (C.12) between glass and metal is represented by a unit step function,

$$m(t) = \begin{cases} 0 & \text{APPJ is on glass} \\ 1 & \text{APPJ is on metal.} \end{cases} \tag{C.13}$$

C.5 Subspace identification model matrices

The A, B and C matrices in (4.27) determined as a result of subspace identification are as follows,

$$A = \begin{bmatrix} 2.59 & -7.40 & 5.85 & 0.15 & -4.46 & -2.92 & 7.25 \\ 2.68 & -7.68 & 6.04 & 0.16 & -4.63 & -2.99 & 7.49 \\ 2.76 & -7.90 & 6.18 & 0.17 & -4.77 & -3.11 & 7.75 \\ -0.47 & 1.10 & -0.65 & -0.03 & 0.78 & 0.97 & -0.73 \\ -0.37 & 0.85 & -0.50 & -0.02 & 0.63 & 0.72 & -0.34 \\ -0.48 & 1.13 & -0.68 & -0.03 & 0.81 & 0.89 & -0.68 \\ -0.45 & 1.05 & -0.64 & -0.03 & 0.76 & 0.86 & -0.60 \end{bmatrix} \tag{C.14}$$

$$B = \begin{bmatrix} 4.46 & 2.25 & -13.68 \\ 3.71 & 2.18 & -9.47 \\ 2.63 & 1.41 & -5.20 \\ 6.83 & 3.34 & 35.4 \\ 0.91 & -0.01 & 2.55 \\ -0.56 & -0.23 & -0.41 \\ 0.30 & 0.14 & -0.001 \end{bmatrix} \tag{C.15}$$

$$C = \begin{bmatrix} 1 & 0 & 0 & 0 & 0 & 0 & 0 \\ 0 & 0 & 0 & 1 & 0 & 0 & 0 \end{bmatrix} \tag{C.16}$$

$$D = 0 \tag{C.17}$$

C.6 Subspace-identified closed-loop model

The closed-loop system (9.3), determined as a result of subspace identification is presented in Figure C.4. The A, B and C matrices are as follows,

$$A = \begin{bmatrix} 0.6553 & 0.1823 \\ -0.09884 & 0.6771 \end{bmatrix} \tag{C.18}$$

$$B = \begin{bmatrix} 0.02282 & -0.03575 \\ 0.01151 & 0.0669 \end{bmatrix} \tag{C.19}$$

$$C = \begin{bmatrix} 13.69 & -0.6244 \\ -1.225 & 6.085 \end{bmatrix} \tag{C.20}$$
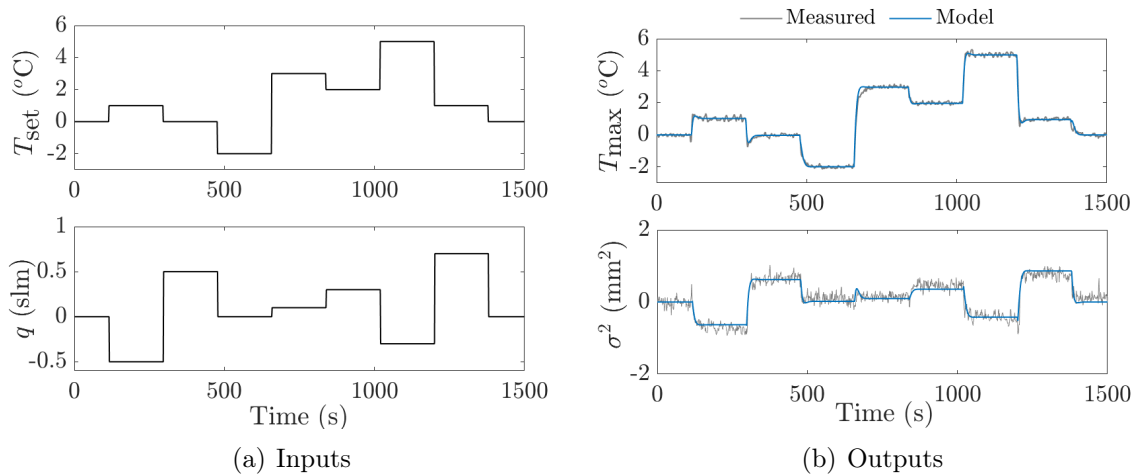
(a) Inputs

(b) Outputs

Figure C.4: Multi-step excitation of the closed-loop with cascaded control strategy in Section 9.3.2. (a) Inputs and (b) outputs compared against the second-order subspace identification model.

Appendix D

Controller Tunings

D.1   Single Loop PI Controllers

Table D.1: Tuning parameters of the single loop maximum substrate temperature PI controllers.

V_{p2p} **paired with** $T_{s,max}$	
k_p	τ_I
0.133 °C/kV	28.8 s
q **paired with** $T_{s,max}$	
k_p	τ_I
-0.025 °C/slm	12.0 s

Table D.2: Tuning parameters of the embedded PI controllers for electrical characteristics of the APPJ.

Embedded Voltage Controller	
k_p	τ_I
0.47 kV/kV	20 ms
Embedded Power Controller	
k_p	τ_I
0.268 W/kV	30 ms

Table D.4: Tuning parameters of the PI controllers in the multi-loop control strategy compared against the linear MPC.

	k_p	τ
PI$_1$	1.36×10^{-4} slm/a.u.	4 s
PI$_2$	2.96×10^{-2} °C/kV	0.1 s

D.2 Cascade PI Controllers

Table D.3: Tuning parameters of the cascade maximum substrate temperature PI controllers.

Cascade $T_{s,max}$ controller	
k_p	τ_I
3.2 °C/W	0.12 s
Cascade $T_{s,max}$ controller for O_2 addition	
k_p	τ_I
0.346 °C/W	0.02 s

D.3 Multi Loop PI Controllers

Table D.5: Tuning parameters of the PI controllers in the multi-loop control strategy used in the simulation studies on the RF APPJ.

Proportional controller (P paired with V_A)	
Parameter	Value
k_P	-20 V W^{-1}
Proportional integral controller (T_s paired with v_{in})	
Parameter	Value
k_p	158 m s^{-1} K^{-1}
τ_i	96 s

Table D.6: Tuning parameters of the PI controllers in the multi-loop control strategy compared against the NMPC in experimental investigation.

	k_p	τ
PI$_1$	0.27 W/kV	1 s
PI$_2$	-0.025 °C/slm	12.0 s

D.4 Linear MPC

Table D.7: Parameters of the Linear MPC controller used in experimental investigation.

N	10
Q	diag(1,0.5)
R	diag(1,1)
B_d	0
C_d	I

D.5 Nonlinear MPC

Table D.8: Parameters of NMPC controller used in experimental investigation.

N	7
w_p	3.3×10^{-4}
Q_k	diag(8.3×10^{-3}, 0, 8.8×10^{-3}, 8.4×10^{-3}, 8.0×10^{-3}, 8.0×10^{-3})
R_k	diag(0.044, 0.021, 0.0129)
P_0	diag(0.01, 0, 0.011, 0.011, 0.01, 0.01, 0.0255, 0.0129, 0.169, 0.01)

Appendix E

Training Data Sets
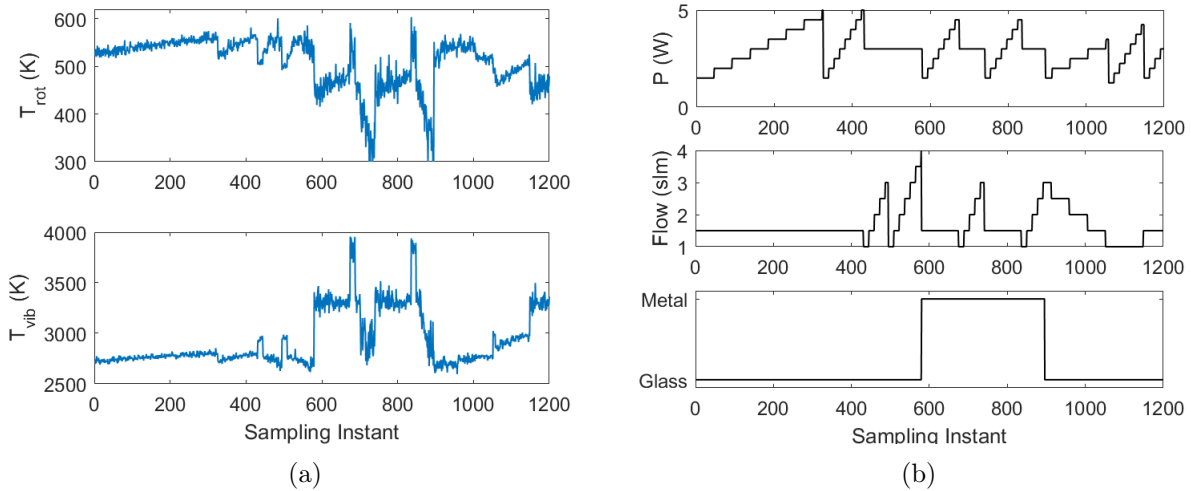
Figure E.1: Training data set collected from the APPJ set-up, used in linear regression and k-means classification. (a) T_{rot} and T_{vib} estimates from Massive OES and (b) corresponding operating conditions.

The OES signal is collected over varying power, flow rate and over two substrate types (dielectric and metal). Synthetic spectra is fitted using Massive OES [213] to obtain corresponding values of the outputs T_{rot} and T_{vib} for each condition. The operating conditions as well as the output variables used for training are shown in Figure E.1. This training data is used for both determination of temperature T_{rot} and T_{vib} and substrate discrimination.

For the separation distance estimation, electro-acoustic emission from the Plasma Flashlight is collected over a range of separation distances for which the discharge remains coupled to the ground plate. The conditions over which the training data are collected is presented in Figure E.2.
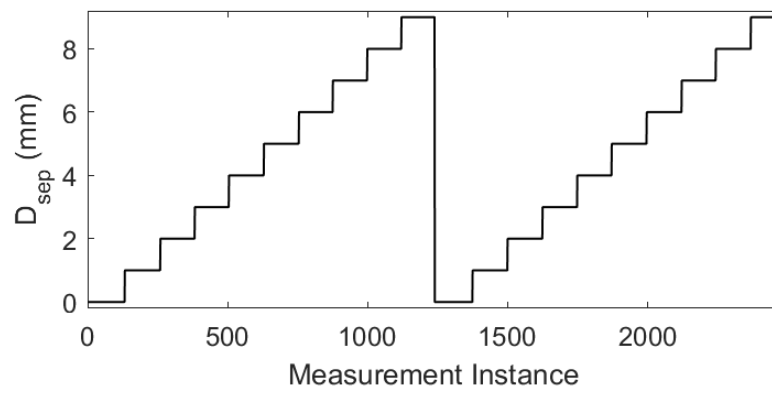
Figure E.2: Training data set collected from the Plasma Flashlight set-up used in GP regression.

Bibliography

[1] A. Schutze, J. Y. Jeong, S. E. Babayan, J. Park, G. S. Selwyn, and R. F. Hicks, "The atmospheric-pressure plasma jet: a review and comparison to other plasma sources," *Plasma Science, IEEE Transactions on*, vol. 26, no. 6, pp. 1685–1694, 1998.

[2] J. Y. Jeong, S. E. Babayan, V. J. Tu, J. Park, I. Henins, R. F. Hicks, and G. S. Selwyn, "Etching materials with an atmospheric-pressure plasma jet," *Plasma Sources Science and Technology*, vol. 7, pp. 282–285, 1998.

[3] W. Stolz, G. Morfill, M. G. Kong, and M. Laroussi, *Plasma Medicine: Applications of Low-temperature Gas Plasmas in Medicine and Biology*. Cambridge University Press, 2012.

[4] P. Bruggeman and R. Brandenburg, "Atmospheric pressure discharge filaments and microplasmas: physics, chemistry and diagnostics," *Journal of Physics D: Applied Physics*, vol. 46, no. 46, p. 464 001, 2013.

[5] J. Winter, K. Wende, K. Masur, S. Iseni, M. Dünnbier, M. U. Hammer, H. T. And, K.-D. Weltmann, and S. Reuter, "Feed gas humidity: a vital parameter affecting a cold atmospheric-pressure plasma jet and plasma-treated human skin cells," *Journal of Physics D: Applied Physics*, vol. 46, no. 29, p. 295 401, 2013.

[6] B. L. Klarenaar, O. Guaitella, R. Engeln, and A. Sobota, "How dielectric, metallic and liquid targets influence the evolution of electron properties in a pulsed He jet measured by Thomson and Raman scattering," *Plasma Sources Science and Technology*, vol. 27, no. 8, 2018.

[7] D. Breden and L. L. Raja, "Computational study of the interaction of cold atmospheric helium plasma jets with surfaces," *Plasma Sources Science and Technology*, vol. 23, no. 6, p. 065 020, 2014.

[8] M. Dünnbier, A. Schmidt-Bleker, J. Winter, M. Wolfram, R. Hippler, K.-D. Weltmann, and S. Reuter, "Ambient air particle transport into the effluent of a cold atmospheric-pressure argon plasma jet investigated by molecular beam mass spectrometry," *Journal of Physics D: Applied Physics*, vol. 46, no. 43, p. 435 203, 2013.

[9] J. Shin and L. L. Raja, "Run-to-run variations, asymmetric pulses, and long time-scale transient phenomena in dielectric-barrier atmospheric pressure glow discharges," *Journal of Physics D: Applied Physics*, vol. 40, no. 10, pp. 3145–3154, 2007.

[10] M. G. Kong, G. Kroesen, G. Morfill, T. Nosenko, and T. Shimizu, "Plasma medicine: An introductory review," *New Journal of Physics*, vol. 11, 2009.

[11] I. Gerber, I. Mihaila, D. Hein, A. Nastuta, R. Jijie, V. Pohoata, and I. Topala, "Time behavior of helium atmospheric pressure plasma jet electrical and optical parameters," *Applied Sciences*, vol. 7, no. 8, p. 812, 2017.

[12] H.-R. Metelmann, T. von Woedtke, and K.-D. Weltmann, Eds., *Comprehensive Clinical Plasma Medicine: Cold Physical Plasma for Medical Application*. Springer, 2018.

[13] H. R. Metelmann, C. Seebauer, R. Rutkowski, M. Schuster, S. Bekeschus, and P. Metelmann, "Treating cancer with cold physical plasma: On the way to evidence-based medicine," *Contributions to Plasma Physics*, no. August 2017, pp. 1–5, 2018.

[14] G. Isbary, J. L. Zimmermann, T. Shimizu, Y. F. Li, G. E. Morfill, H. M. Thomas, B. Steffes, J. Heinlin, S. Karrer, and W. Stolz, "Non-thermal plasma-More than five years of clinical experience," *Clinical Plasma Medicine*, vol. 1, no. 1, pp. 19–23, 2013.

[15] K.-D. Weltmann, E. Kindel, R. Brandenburg, C. Meyer, R. Bussiahn, C. Wilke, and T. von Woedtke, "Atmospheric Pressure Plasma Jet for Medical Therapy: Plasma Parameters and Risk Estimation," *Contributions to Plasma Physics*, vol. 49, no. 9, pp. 631–640, 2009.

[16] S. Arndt, A. Schmidt, S. Karrer, and T. von Woedtke, "Comparing two different plasma devices kINPen and Adtec SteriPlas regarding their molecular and cellular effects on wound healing," *Clinical Plasma Medicine*, no. January, 24–33, 2018.

[17] T. Bortfeld, "IMRT: A review and preview," *Physics in Medicine and Biology*, vol. 51, no. 13, 2006.

[18] J. L. Roti, "Cellular responses to hyperthermia (40-46 degrees C): cell killing and molecular events," *International Journal of Hyperthermia*, vol. 24, no. 1, pp. 3–15, 2008.

[19] J. W. Lackmann, S. Schneider, E. Edengeiser, F. Jarzina, S. Brinckmann, E. Steinborn, M. Havenith, J. Benedikt, and J. E. Bandow, "Photons and particles emitted from cold atmospheric-pressure plasma inactivate bacteria and biomolecules independently and synergistically," *Journal of the Royal Society Interface*, vol. 10, no. 89, 2013.

[20] Y. Ogawa, N. Morikawa, A. Ohkubo-Suzuki, S. Miyoshi, H. Arakawa, Y. Kita, and S. Nishimura, "An epoch-making application of discharge plasma phenomenon to gene-transfer," *Biotechnology and Bioengineering*, vol. 92, no. 7, pp. 865–870, 2005.

[21] S. A. Norberg, E. Johnsen, and M. J. Kushner, "Helium atmospheric pressure plasma jets interacting with wet cells: Delivery of electric fields," *Journal of Physics D: Applied Physics*, vol. 49, no. 18, 2016.

[22] R. Albanese and G. Ambrosino, "Current, position and shape control of tokamak plasmas: A literature review," *IEEE International Conference on Control Applications*, pp. 385–394, 2000.

[23] T. F. Edgar, S. W. Butler, W. J. Campbell, C. Pfeiffer, C. Bode, S. Hwang, K. Balakrishnan, and J. Hahn, "Automatic control in microelectronics manufacturing: Practices, challenges, and possibilities," *Automatica*, vol. 36, no. 11, pp. 1567–1603, 2000.

[24] Y. Sakiyama and D. B. Graves, "Finite element analysis of an atmospheric pressure RF-excited plasma needle," *Journal of Physics D: Applied Physics*, vol. 39, no. 16, pp. 3451–3456, 2006.

[25] S. A. Norberg, E. Johnsen, and M. J. Kushner, "Helium atmospheric pressure plasma jets touching dielectric and metal surfaces," *Journal of Applied Physics*, vol. 118, no. 1, pp. 1–13, 2015.

[26] P. Van Overschee and B. De Moor, *Subspace identification for linear systems: Theory—Implementation—Applications*. Springer Science & Business Media, 2012.

[27] S. A. Sapareto and W. C. Dewey, "Thermal dose determination in cancer therapy," *International Journal of Radiation Oncology, Biology, Physics*, vol. 10, no. 6, pp. 787–800, 1984.

[28] D. Arora, M. Skliar, and R. B. Roemer, "Minimum-time thermal dose control of thermal therapies," *IEEE Transactions on Biomedical Engineering*, vol. 52, no. 2, pp. 191–200, 2005.

[29] D. E. Seaborg, T. F. Edgar, D. A. Mellichamp, and F. J. Doyle III, *Process Dynamics and Control*. Hoboken, NJ: John Wiley and Sons Inc., 2011.

[30] B. W. Bequette, *Process Control: Modeling, Design, and Simulation*. Upper Saddle River, NJ: Prentice Hall, 2002.

[31] H. J. Kim, D. H. Shim, and S. Sastry, "Nonlinear model predictive tracking control for rotorcraft-based unmanned aerial vehicles," in *Proceedings of the American Control Conference*, Anchorage, AK, 2002, pp. 3576–3581.

[32] G. Klancar and I. Skrjanc, "Tracking-error model-based predictive control for mobile robots in real time," *Robotics and Autonomous Systems*, vol. 55, no. 6, pp. 460–469, 2007.

[33] Y. Ma, F. Borrelli, B. Hencey, B. Coffey, S. Bengea, and P. Haves, "Model Predictive Control for the Operation of Building Cooling Systems," *IEEE Transactions on Control Systems Technology*, vol. 20, no. 3, pp. 796–803, 2012.

[34] M. Morari and J. H. Lee, "Model predictive control: past, present and future," *Computers & Chemical Engineering*, vol. 23, pp. 667–682, 1999.

[35] J. B. Rawlings and D. Q. Mayne, *Model Predictive Control: Theory and Design*. Nob Hill Publishing, Madison, WI, 2015.

[36] K. J. Åström and T. Hägglund, "The future of PID control," *Control Engineering Practice*, vol. 9, no. 11, pp. 1163–1175, 2001.

[37] F. F. Chen, *Introduction to Plasma Physics and Controlled Fusion*, 2nd. New York, USA: Plenum Press, 1983, vol. 1.

[38] Y. P. Razier, *Gas Discharge Physics*. Berlin, Heidelberg: Springer-Verlag, 1991.

[39] M. Lieberman and A. J. Lichtenberg, *Principles of Plasma Discharges and Materials Processing*. Hoboken, NJ, USA: Wiley-Interscience, 2005.

[40] P. Fauchais and A. Vardelle, "Thermal plasmas," *IEEE Transactions on Plasma Science*, vol. 25, no. 6, pp. 1258–1280, 1997.

[41] R. G. Badger, *Devoted to the Diagnostic and Therapeutic Uses of Electricity*. Boston, USA: Gorham Press, 1906.

[42] N. Tesla, "High Frequency Oscillators for Electro-Therapeutic and Other Purposes," *Proceedings of the IEEE*, vol. 87, no. 7, p. 1282, 1999.

[43] N. M. Eberhart, *A working manual of high frequency currents*. New medicine Publishing Company, 1919.

[44] D. B. Graves, "Lessons from tesla for plasma medicine," *IEEE Transactions on Radiation and Plasma Medical Sciences*, vol. 2, no. 6, pp. 594–607, 2018.

[45] "Misbranding of violet ray device. u. s, v. 13 cases, etc.," no. F. D. C. No. 26005. Sample Noe. 25833-K, 25834-K. 1494.

[46] J. Winter, R. Brandenburg, and K.-D. Weltmann, "Atmospheric pressure plasma jets: an overview of devices and new directions," *Plasma Sources Science and Technology*, vol. 24, no. 6, p. 064 001, 2015.

[47] E. Stoffels, a. J. Flikweert, W. W. Stoffels, and G. M. W. Kroesen, "Plasma needle: a non-destructive atmospheric plasma source for fine surface treatment of (bio)materials," *Plasma Sources Science and Technology*, vol. 11, pp. 383–388, 2002.

[48] M. Laroussi, C. Tendero, X. Lu, S. Alla, and W. L. Hynes, "Inactivation of bacteria by the plasma pencil," *Plasma Processes and Polymers*, vol. 3, pp. 470–473, 2006.

[49] K.-D. Weltmann, R. Brandenburg, T. von Woedtke, J. Ehlbeck, R. Foest, M. Stieber, and E. Kindel, "Antimicrobial treatment of heat sensitive products by miniaturized atmospheric pressure plasma jets (APPJs)," *Journal of Physics D: Applied Physics*, vol. 41, no. 19, p. 194 008, 2008.

[50] M. G. Kong, G. Kroesen, G. Morfill, T. Nosenko, T. Shimizu, J. van Dijk, and J. L. Zimmermann, "Plasma medicine: an introductory review," *New Journal of Physics*, vol. 11, no. 11, p. 115 012, 2009.

[51] G. Fridman, G. Friedman, A. Gutsol, A. B. Shekhter, V. N. Vasilets, and A. Fridman, "Applied plasma medicine," *Plasma Processes and Polymers*, vol. 5, pp. 503–533, 2008.

[52] J. Ehlbeck, U. Schnabel, M. Polak, J. Winter, T. von Woedtke, R. Brandenburg, T. von dem Hagen, and K.-D. Weltmann, "Low temperature atmospheric pressure plasma sources for microbial decontamination," *Journal of Physics D: Applied Physics*, vol. 44, no. 1, p. 13 002, 2011.

[53] M. Naïtali, J.-M. Herry, E. Hnatiuc, G. Kamgang, and J.-L. Brisset, "Kinetics and Bacterial Inactivation Induced by Peroxynitrite in Electric Discharges in Air," *Plasma Chemistry and Plasma Processing*, vol. 32, no. 4, pp. 675–692, 2012.

[54] R. E. J. Sladek and E. Stoffels, "Deactivation of Escheria coli by the Plasma Needle," *Journal of Physics D: Applied Physics*, vol. 38, pp. 1716–1721, 2005.

[55] R. Brandenburg, J. Ehlbeck, M. Stieber, T. V. Woedtke, J. Zeymer, O. Schlüter, and K. D. Weltmann, "Antimicrobial treatment of heat sensitive materials by means of atmospheric pressure Rf-driven plasma jet," *Contributions to Plasma Physics*, vol. 47, no. 1-2, pp. 72–79, 2007.

[56] B. Liu, "Killing of S . mutans Bacteria Using a Plasma Needle at Atmospheric Pressure," *Image (Rochester, N.Y.)*, vol. 34, no. 4, pp. 2010–2011, 2011.

[57] X. Pei, X. Lu, J. Liu, D. Liu, Y. Yang, K. Ostrikov, P. K. Chu, and Y. Pan, "Inactivation of a 25.5 um *Enterococcus faecalis* Biofilm By a Room-Temperature, Battery-Operated, Handheld Air Plasma Jet," vol. 45, p. 165 205, 2012.

[58] I. Koban, R. Matthes, N.-O. Hübner, A. Welk, P. Meisel, B. Holtfreter, R. Sietmann, E. Kindel, K.-D. Weltmann, A. Kramer, and T. Kocher, "Treatment of Candida albicans biofilms with low-temperature plasma induced by dielectric barrier discharge and atmospheric pressure plasma jet," *New Journal of Physics*, vol. 12, no. 7, p. 73 039, 2010.

[59] R. E. J. Sladek, S. K. Filoche, C. H. Sissons, and E. Stoffels, "Treatment of Streptococcus mutans biofilms with a nonthermal atmospheric plasma," *Letters in Applied Microbiology*, vol. 45, no. 3, pp. 318–323, 2007.

[60] H. A. Aboubakr, P. Williams, U. Gangal, M. M. Youssef, S. A. A. El-Sohaimy, P. J. Bruggeman, and S. M. Goyal, "Virucidal effect of cold atmospheric gaseous plasma on feline calicivirus, a surrogate for human norovirus," *Applied and Environmental Microbiology*, vol. 81, no. 11, pp. 3612–3622, 2015.

[61] Z. Xiong, J. Roe, T. C. Grammer, and D. B. Graves, "Plasma Treatment of Onychomycosis," *Plasma Processes and Polymers*, vol. 13, no. 6, pp. 588–597, 2016.

[62] G. Daeschlein, S. Scholz, T. Von Woedtke, M. Niggemeier, E. Kindel, R. Brandenburg, K. D. Weltmann, and M. Junger, "In vitro killing of clinical fungal strains by low-temperature atmospheric-pressure plasma jet," *IEEE Transactions on Plasma Science*, vol. 39, no. 2, pp. 815–821, 2011.

[63] R. Sladek, E. Stoffels, R. Walraven, P. Tielbeek, and R. Koolhoven, "Plasma Treatment of Dental Cavities: A Feasibility Study," *IEEE Transactions on Plasma Science*, vol. 32, no. 4, pp. 1540–1543, 2004.

[64] B. Yang, J. Chen, Q. Yu, H. Li, M. Lin, A. Mustapha, L. Hong, and Y. Wang, "Oral bacterial deactivation using a low-temperature atmospheric argon plasma brush.," *Journal of dentistry*, vol. 39, no. 1, pp. 48–56, 2011.

[65] K. R. Stalder, D. F. McMillen, and J. Woloszko, "Electrosurgical plasmas," *Journal of Physics D: Applied Physics*, vol. 38, no. 11, pp. 1728–1738, 2005.

[66] J. Raiser and M. Zenker, "Argon plasma coagulation for open surgical and endoscopic applications: state of the art," *Journal of Physics D: Applied Physics*, vol. 39, no. 16, pp. 3520–3523, 2006.

[67] H.-R. Metelmann, D. S. Nedrelow, C. Seebauer, M. Schuster, T. V. Woedtke, K.-D. Weltmann, S. Kindler, P. H. Metelmann, S. E. Finkelstein, D. D. Von Hoff, and F. Podmelle, "Head and neck Cancer treatment and physical plasma," *Clinical Plasma Medicine*, vol. 3, no. 1, 2015.

[68] S. Arndt, E. Wacker, Y.-F. Li, T. Shimizu, H. M. Thomas, G. E. Morfill, S. Karrer, J. L. Zimmermann, and A.-K. Bosserhoff, "Cold atmospheric plasma, a new strategy to induce senescence in melanoma cells.," *Experimental dermatology*, vol. 22, no. 4, pp. 284–289, 2013.

[69] J. Schlegel, J. Köritzer, and V. Boxhammer, "Plasma in cancer treatment," *Clinical Plasma Medicine*, vol. 1, no. 2, pp. 2–7, 2013.

[70] X. Cheng, J. Sherman, W. Murphy, E. Ratovitski, J. Canady, and M. Keidar, "The effect of tuning cold plasma composition on glioblastoma cell viability," *PLoS ONE*, vol. 9, no. 5, pp. 1–9, 2014.

[71] A. M. Hirst, F. M. Frame, N. J. Maitland, and D. O'Connell, "Low Temperature Plasma: A Novel Focal Therapy for Localized Prostate Cancer?" *BioMed research international*, vol. 2014, p. 878 319, 2014.

[72] A. Kramer, U. Lindequist, K.-D. Weltmann, C. Wilke, and T. von Woedtke, "Plasma Medicine - its perspective for wound therapy.," *GMS Krankenhaushygiene interdisziplinär*, vol. 3, no. 1, 2008.

[73] A. V. Nastuta, I. Topala, C. Grigoras, V. Pohoata, and G. Popa, "Stimulation of wound healing by helium atmospheric pressure plasma treatment," *Journal of Physics D: Applied Physics*, vol. 44, no. 10, 2011.

[74] S. Arndt, A. Schmidt, S. Karrer, and T. von Woedtke, "Comparing two different plasma devices kINPen and Adtec SteriPlas regarding their molecular and cellular effects on wound healing," *Clinical Plasma Medicine*, 2018.

[75] G. C. Kim, G. J. Kim, S. R. Park, S. M. Jeon, H. J. Seo, F. Iza, and J. K. Lee, "Air plasma coupled with antibody-conjugated nanoparticles: A new weapon against cancer," vol. 42, no. 3, 2009.

[76] V. Vijayarangan, A. Delalande, S. Dozias, J.-M. Pouvesle, C. Pichon, and E. Robert, "Cold Atmospheric Plasma Parameters Investigation for Efficient Drug Delivery in HeLa Cells," *IEEE Transactions on Radiation and Plasma Medical Sciences*, vol. 7311, pp. 1–1, 2017.

[77] F. Mwale, H. T. Wang, V. Nelea, L. Luo, J. Antoniou, and M. R. Wertheimer, "The effect of glow discharge plasma surface modification of polymers on the osteogenic differentiation of committed human mesenchymal stem cells," *Biomaterials*, vol. 27, no. 10, pp. 2258–2264, 2006.

[78] Z. Xiong, S. Zhao, X. Mao, X. Lu, G. He, G. Yang, M. Chen, M. Ishaq, and K. Ostrikov, "Selective neuronal differentiation of neural stem cells induced by nanosecond microplasma agitation," *Stem Cell Research*, vol. 12, no. 2, pp. 387–399, 2014.

[79] T. von Woedtke, H.-R. Metelmann, and K.-D. Weltmann, "Clinical Plasma Medicine: State and Perspectives of in Vivo Application of Cold Atmospheric Plasma," *Contributions to Plasma Physics*, vol. 54, no. 2, pp. 104–117, 2014.

[80] M. Laroussi and F. Leipold, "Evaluation of the roles of reactive species, heat, and UV radiation in the inactivation of bacterial cells by air plasmas at atmospheric pressure," *International Journal of Mass Spectrometry*, vol. 233, no. 1-3, pp. 81–86, 2004.

[81] D. B. Graves, "The emerging role of reactive oxygen and nitrogen species in redox biology and some implications for plasma applications to medicine and biology," *Journal of Physics D: Applied Physics*, vol. 45, no. 26, p. 263 001, 2012.

[82] Graves, David B, "Oxy-nitroso shielding burst model of cold atmospheric plasma therapeutics," *Clinical Plasma Medicine*, vol. 2, no. 2, pp. 38–49, 2014.

[83] T. Kaneko, S. Sasaki, Y. Hokari, S. Horiuchi, R. Honda, and M. Kanzaki, "Improvement of cell membrane permeability using a cell-solution electrode for generating atmospheric-pressure plasma," *Biointerphases*, vol. 10, no. 2, p. 029 521, 2015.

[84] J. Robotis, P. Sechopoulos, and T. Rokkas, "Argon plasma coagulation : Clinical applications in Gastroenterology," *Annals of Gastroenterology*, vol. 16, no. 2, pp. 131–137, 2003.

[85] G. Collet, E. Robert, a. Lenoir, M. Vandamme, T. Darny, S. Dozias, C. Kieda, and J. M. Pouvesle, "Plasma jet-induced tissue oxygenation: potentialities for new therapeutic strategies," *Plasma Sources Science and Technology*, vol. 23, p. 012 005, 2014.

[86] V. Miller, A. Lin, and A. Fridman, "Why Target Immune Cells for Plasma Treatment of Cancer," *Plasma Chemistry and Plasma Processing*, vol. 36, no. 1, pp. 259–268, 2016.

[87] C. Tendero, C. Tixier, P. Tristant, J. Desmaison, and P. Leprince, "Atmospheric pressure plasmas: A review," *Spectrochimica Acta Part B: Atomic Spectroscopy*, vol. 61, no. 1, pp. 2–30, 2006.

[88] S. Hofmann, a. F. H. van Gessel, T. Verreycken, and P. Bruggeman, "Power dissipation, gas temperatures and electron densities of cold atmospheric pressure helium and argon RF plasma jets," *Plasma Sources Science and Technology*, vol. 20, no. 6, p. 065 010, 2011.

[89] M. R. Wertheimer, M. Ahlawat, B. Saoudi, and R. Kashyap, "Accurate in-situ gas temperature measurements in dielectric barrier discharges at atmospheric pressure," *Applied Physics Letters*, vol. 100, no. 20, 2012.

[90] M. Laroussi and T. Akan, "Ueber die zum Funkenübergang in Luft, Wasserstoff und Kohlensäure bei verschiedenen Drucken erforderliche Potentialdifferenz (On the potential difference required for spark initiation in air, hydrogen, and carbon dioxide at different pressures)," *Annalen der Physik*, vol. 5, no. 273, pp. 69–75, 1889.

[91] K. Niemi, J. Waskoenig, N. Sadeghi, T. Gans, and D. O'Connell, "The role of helium metastable states in radio-frequency driven helium–oxygen atmospheric pressure plasma jets: measurement and numerical simulation," *Plasma Sources Science and Technology*, vol. 20, no. 5, p. 055 005, 2011.

[92] K. H. Becker, U. Kogelschatz, K. H. Schoenbach, and R. J. Barker, *Non-Equilibrium Air Plasmas at Atmospheric Pressure*. Bristol, UK: IOP Publishing, 2005.

[93] M. Janda, Z. MacHala, A. Niklová, and V. Martišovitš, "The streamer-to-spark transition in a transient spark: A dc-driven nanosecond-pulsed discharge in atmospheric air," *Plasma Sources Science and Technology*, vol. 21, no. 4, p. 045 006, 2012.

[94] D. Staack, B. Farouk, A. Gutsol, and A. Fridman, "Stabilization of the ionization overheating thermal instability in atmospheric pressure microplasmas," *Journal of Applied Physics*, vol. 106, no. 1, 2009.

[95] T. Yokoyama, M. Kogoma, T. Moriwaki, and S. Okazaki, "The mechanism of the stabilisation of glow plasma at atmospheric pressure," *Journal of Physics D: Applied Physics*, vol. 23, no. 8, pp. 1125–1128, 2000.

[96] Y. Wang and P. Zhao, "Noncontact acoustic analysis monitoring of plasma arc welding," *International Journal of Pressure Vessels and Piping*, vol. 78, no. 1, pp. 43–47, 2001.

[97] B. L. Sands, B. N. Ganguly, and K. Tachibana, "A streamer-like atmospheric pressure plasma jet," *Applied Physics Letters*, vol. 92, no. 2008, pp. 1–4, 2008.

[98] M. Laroussi and T. Akan, "Arc-free atmospheric pressure cold plasma jets: A review," *Plasma Processes and Polymers*, vol. 4, no. 9, pp. 777–788, 2007.

[99] Y. B. Golubovskii, V. a. Maiorov, J. Behnke, and J. F. Behnke, "Modelling of the homogeneous barrier discharge in helium at atmospheric pressure," *Journal of Physics D: Applied Physics*, vol. 36, no. 1, pp. 39–49, 2002.

[100] F. Massines, N. Gherardi, N. Naudé, and P. Ségur, "Recent advances in the understanding of homogeneous dielectric barrier discharges," *The European Physical Journal-Applied Physics*, vol. 47, no. 2, 2009.

[101] X. Lu and K. (Ostrikov, "Guided ionization waves: The physics of repeatability," *Applied Physics Reviews*, vol. 5, no. 3, p. 031 102, 2018.

[102] F. Leroux, C. Campagne, A. Perwuelz, and L. Gengembre, "Atmospheric air plasma treatment of polyester textile materials. Textile structure influence on surface oxidation and silicon resin adhesion," *Surface and Coatings Technology*, vol. 203, no. 20-21, pp. 3178–3183, 2009.

[103] X. Lu, M. Laroussi, and V. Puech, "On atmospheric-pressure non-equilibrium plasma jets and plasma bullets," *Plasma Sources Science and Technology*, vol. 21, no. 3, p. 034 005, 2012.

[104] J. L. Walsh, J. J. Shi, and M. G. Kong, "Contrasting characteristics of pulsed and sinusoidal cold atmospheric plasma jets," *Applied Physics Letters*, vol. 88, no. 17, 2006.

[105] A. Sobota, O. Guaitella, and A. Rousseau, "The influence of the geometry and electrical characteristics on the formation of the atmospheric pressure plasma jet," *Plasma Sources Science and Technology*, vol. 23, no. 2, 2014.

[106] S. Hofmann, K. van Gils, S. van der Linden, S. Iseni, and P. Bruggeman, "Time and spatial resolved optical and electrical characteristics of continuous and time modulated RF plasmas in contact with conductive and dielectric substrates," *The European Physical Journal D*, vol. 68, no. 3, p. 56, 2014.

[107] G. Fridman, A. D. Brooks, M. Balasubramanian, A. Fridman, A. Gutsol, V. N. Vasilets, H. Ayan, and G. Friedman, "Comparison of Direct and Indirect Effects of Non-Thermal Atmospheric-Pressure Plasma on Bacteria," *Plasma Processes and Polymers*, vol. 4, no. 4, pp. 370–375, 2007.

[108] J.-P. Boeuf, L. L. Yang, and L. C. Pitchford, "Dynamics of a guided streamer ("plasma bullet") in a helium jet in air at atmospheric pressure," *Journal of Physics D: Applied Physics*, vol. 46, p. 13, 2013.

[109] X. Lu, G. V. Naidis, M. Laroussi, and K. Ostrikov, "Guided ionization waves: Theory and experiments," *Physics Reports*, vol. 540, no. 3, pp. 123–166, 2014.

[110] J. L. Walsh, F. Iza, N. B. Janson, V. J. Law, and M. G. Kong, "Three distinct modes in a cold atmospheric pressure plasma jet," *Journal of Physics D: Applied Physics*, vol. 43, no. 7, p. 075 201, 2010.

[111] J. J. Liu and M. G. Kong, "Sub-60ºC atmospheric helium-water plasma jets: modes, electron heating and downstream reaction chemistry," *Journal of Physics D: Applied Physics*, vol. 44, no. 34, p. 345 203, 2011.

[112] N. Balcon, G. J. M. Hagelaar, and J. P. Boeuf, "Numerical model of an argon atmospheric pressure RF discharge," *IEEE Transactions on Plasma Science*, vol. 36, no. 5, pp. 2782–2787, 2008.

[113] J. J. Shi, J. Zhang, G. Qiu, J. L. Walsh, and M. G. Kong, "Modes in a pulse-modulated radio-frequency dielectric-barrier glow discharge," *Applied Physics Letters*, vol. 93, no. 4, pp. 2006–2009, 2008.

[114] S. Wang, V. Schulz-Von der Gathen, and H. F. Döbele, "Discharge comparison of nonequilibrium atmospheric pressure Ar/O 2 and He/O2 plasma jets," *Applied Physics Letters*, vol. 83, no. 2003, pp. 3272–3274, 2003.

[115] S. Z. Li, J. P. Lim, J. G. Kang, and H. S. Uhm, "Comparison of atmospheric-pressure helium and argon plasmas generated by capacitively coupled radio-frequency discharge," *Physics of Plasmas*, vol. 13, no. 9, p. 093 503, 2006.

[116] X. Lu, Z. Jiang, Q. Xiong, Z. Tang, X. Hu, and Y. Pan, "An 11 cm long atmospheric pressure cold plasma plume for applications of plasma medicine," *Applied Physics Letters*, vol. 92, pp. 2–3, 2008.

[117] E. Robert, V. Sarron, T. Darny, D. Riès, S. Dozias, J. Fontane, L. Joly, and J. M. Pouvesle, "Rare gas flow structuration in plasma jet experiments," *Plasma Sources Science and Technology*, vol. 23, no. 1, 2014.

[118] E. Karakas, M. Koklu, and M. Laroussi, "Correlation between helium mole fraction and plasma bullet propagation in low temperature plasma jets," *Journal of Physics D: Applied Physics*, vol. 43, no. 15, p. 155 202, 2010.

[119] O. Guaitella and A. Sobota, "The impingement of a kHz helium atmospheric pressure plasma jet on a dielectric surface," *Journal of Physics D: Applied Physics*, vol. 48, no. 25, p. 255 202, 2015.

[120] Y. Sakiyama and D. B. Graves, "Neutral gas flow and ring-shaped emission profile in non-thermal RF-excited plasma needle discharge at atmospheric pressure," *Plasma Sources Science and Technology*, vol. 18, no. 2, p. 025 022, 2009.

[121] K. P. Arjunan, A. Obrusník, B. T. Jones, L. Zajíčková, and S. Ptasinska, "Effect of Additive Oxygen on the Reactive Species Profile and Microbicidal Property of a Helium Atmospheric Pressure Plasma Jet," *Plasma Processes and Polymers*, vol. 13, no. 11, pp. 1087–1103, 2016.

[122] H. M. Joha, J. Y. Choi, S. J. Kim, T. H. Chung, and T.-H. Kang, "Effect of additive oxygen gas on cellular response of lung cancer cells induced by atmospheric pressure helium plasma jet.," *Scientific reports*, vol. 4, p. 6638, 2014.

[123] T. Gerling, A. V. Nastuta, R. Bussiahn, E. Kindel, and K.-D. K.-D. Weltmann, "Back and forth directed plasma bullets in a helium atmospheric pressure needle-to-plane discharge with oxygen admixtures," *Plasma Sources Science and Technology*, vol. 21, no. 3, p. 034 012, 2012.

[124] M. Moravej, X. Yang, M. Barankin, J. Penelon, S. E. Babayan, and R. F. Hicks, "Properties of an atmospheric pressure radio-frequency argon and nitrogen plasma," *Plasma Sources Science and Technology*, vol. 15, no. 2, pp. 204–210, 2006.

[125] S. Reuter, J. Winter, S. Iseni, A. Schmidt-Bleker, M. Dunnbier, K. Masur, K. Wende, and K. D. Weltmann, "The Influence of Feed Gas Humidity Versus Ambient Humidity on Atmospheric Pressure Plasma Jet-Effluent Chemistry and Skin Cell Viability," *IEEE Transactions on Plasma Science*, vol. 43, no. 9, pp. 3185–3192, 2014.

[126] A. Schmidt-Bleker, J. Winter, A. Bösel, S. Reuter, and K.-D. Weltmann, "On the plasma chemistry of a cold atmospheric argon plasma jet with shielding gas device," *Plasma Sources Science and Technology*, vol. 25, no. 1, p. 015 005, 2016.

[127] Z. Hao, S. Ji, H. Liu, and Y. Song, "Effect of the grounded electrode on cold ar atmospheric pressure plasma jet generated with a simple dbd configuration," *IEEE Transactions on Plasma Science*, vol. 42, no. 3, pp. 824–832, 2014.

[128] W.-C. Zhu, Q. Li, X.-M. Zhu, and Y.-K. Pu, "Characteristics of atmospheric pressure plasma jets emerging into ambient air and helium," *Journal of Physics D: Applied Physics*, vol. 42, no. 20, p. 202 002, 2009.

[129] Q. Li, J. T. Li, W. C. Zhu, X. M. Zhu, and Y. K. Pu, "Effects of gas flow rate on the length of atmospheric pressure nonequilibrium plasma jets," *Applied Physics Letters*, vol. 95, no. 14, p. 141 502, 2009.

[130] N. Jiang, A. Ji, and Z. Cao, "Atmospheric pressure plasma jet: Effect of electrode configuration, discharge behavior, and its formation mechanism," *Journal of Applied Physics*, vol. 106, no. 1, pp. 1–7, 2009.

[131] G. B. Sretenović, I. B. Krstić, V. V. Kovačević, B. M. Obradović, and M. M. Kuraica, "Spatio-temporally resolved electric field measurements in helium plasma jet," *Journal of Physics D: Applied Physics*, vol. 47, no. 10, p. 102 001, 2014.

[132] L. Cordesses, "Direct Digital Synthesis: A Tool for Periodic Wave Generation (Part 1)," *IEEE Signal Processing Magazine*, no. July 2004, pp. 50–54, 2004.

[133] G. V. Naidis, "Modeling of helium plasma jets emerged into ambient air: Influence of applied voltage, jet radius, and helium flow velocity on plasma jet characteristics," *Journal of Applied Physics*, vol. 112, no. 10, 0–5, 2012.

[134] R. A. Beasley, "Medical Robots: Current Systems and Research Directions," *Journal of Robotics*, vol. 2012, p. 14, 2012.

[135] P. I. Corke, "Visual control of robot manipulators–a review," in *Visual Servoing: Real-Time Control of Robot Manipulators Based on Visual Sensory Feedback*, World Scientific, 1993, pp. 1–31.

[136] L. Sciavicco and B. Siciliano, *Modelling and Control of Robot Manipulators*, 2nd ed. London: Springer-Verlag, 2000.

[137] Z. A. Freek Bos Rob Wolfs and T. Salet, "Additive manufacturing of concrete in construction: Potentials and challenges of 3d concrete printing, virtual and physical prototyping," vol. 11, pp. 209–225, 3 2016.

[138] F. Kong, L. Yuan, Y. F. Zheng, and W. Chen, "Automatic liquid handling for life science: A critical review of the current state of the art," *Journal of laboratory automation*, vol. 17, no. 3, pp. 169–185, 2012.

[139] Adafruit. (2014). Adafruit Motor/Stepper/Servo Shield, [Online]. Available: `https://www.adafruit.com/product/1438` (visited on 02/13/2019).

[140] B. Davies, "A review of robotics in surgery," *Proceedings of the Institution of Mechanical Engineers, Part H: Journal of Engineering in Medicine*, vol. 214, no. 1, pp. 129–140, 2000.

[141] J. Iqbal, R. U. Islam, S. Z. Abbas, A. A. Khan, and S. A. Ajwad, "Automating industrial tasks through mechatronic systems–a review of robotics in industrial perspective," *Tehnički vjesnik*, vol. 23, no. 3, pp. 917–924, 2016.

[142] J. Pandremenos, C. Doukas, P. Stavropoulos, and G. Chryssolouris, "Machining with robots: A critical review," *Proceedings of DET2011*, pp. 1–9, 2011.

[143] Thingverse. (2016). Robotic Arms, [Online]. Available: `https://www.thingiverse.com/Kamanji/collections/robotic-arms` (visited on 02/01/2019).

[144] FLIR. (2019). Lepton LWIR Micro Thermal Camera, [Online]. Available: `https://www.flir.com/products/lepton` (visited on 02/03/2019).

[145] C. O. Laux, T. G. Spence, C. H. Kruger, and R. N. Zare, "Optical diagnostics of atmospheric pressure air plasmas," *Plasma Sources Science and Technology*, vol. 12, no. 2, pp. 125–138, 2003.

[146] N. O. Connor, H. H. Humphreys, and S. Daniels, "Oxygen line ratio method for the determination of plasma parameters in atmospheric pressure discharges using air as the working gas," pp. 2–5, 2013.

[147] Brandon S. Curtis, *Plasma Analysis and Process Control*, Online; accessed 4-April-2019, https://github.com/brandoncurtis/plasma-control, 2017.

[148] C. Liechti. (2017). Python serial port access library, [Online]. Available: `https://github.com/pyserial/pyserial` (visited on 02/07/2019).

[149] K. Kiefer. (2015). python library for interfacing with FLIR lepton, [Online]. Available: `https://github.com/groupgets/pylepton` (visited on 02/07/2019).

[150] A. Forencich. (2017). USBTMC driver for controlling instruments over USB, [Online]. Available: `https://github.com/python-ivi/python-usbtmc` (visited on 02/07/2019).

[151] A. Poehlmann. (2016). Python module for oceanoptics spectrometers, [Online]. Available: `https://github.com/ap--/python-seabreeze` (visited on 02/07/2019).

[152] J. B. Rawlings, "Tutorial: model predictive control technology," *American Control Conference, 1999. Proceedings of the 1999*, vol. 1, pp. 662–676, 1999.

[153] G. V. Naidis, "Modelling of plasma bullet propagation along a helium jet in ambient air," *Journal of Physics D: Applied Physics*, vol. 44, no. 21, p. 215 203, 2011.

[154] D. Breden, K. Miki, and L. L. Raja, "Computational study of cold atmospheric nanosecond pulsed helium plasma jet in air," *Applied Physics Letters*, vol. 99, no. 11, pp. 2009–2012, 2011.

[155] D. Breden and L. L. Raja, "Computational study of the interaction of cold atmospheric helium plasma jets with surfaces," *Plasma Sources Science and Technology*, vol. 23, no. 6, p. 065 020, 2014.

[156] S. A. Norberg, E. Johnsen, and M. J. Kushner, "Helium atmospheric pressure plasma jets interacting with wet cells: Delivery of electric fields," *Journal of Physics D: Applied Physics*, vol. 49, no. 18, 2016.

[157] M. Schröder, A. Ochoa, and C. Breitkopf, "Numerical simulation of an atmospheric pressure RF-driven plasma needle and heat transfer to adjacent human skin using COMSOL," *Biointerphases*, vol. 10, no. 2, p. 029 508, 2015.

[158] L. Mangolini, C. Anderson, J. Heberlein, and U. Kortshagen, "Effects of current limitation through the dielectric in atmospheric pressure glows in helium," *Journal of Physics D: Applied Physics*, vol. 37, no. 7, pp. 1021–1030, 2004.

[159] J. Waskoenig, K. Niemi, N. Knake, L. M. Graham, S. Reuter, V. Schulz-von der Gathen, and T. Gans, "Atomic oxygen formation in a radio-frequency driven micro-atmospheric pressure plasma jet," vol. 045018, 2010.

[160] C. Lazzaroni, P. Chabert, M. a. Lieberman, a. J. Lichtenberg, and a. Leblanc, "Analytical-numerical global model of atmospheric-pressure radio-frequency capacitive discharges," *Plasma Sources Science and Technology*, vol. 21, p. 035 013, 2012.

[161] C. Lazzaroni, M. a. Lieberman, a. J. Lichtenberg, and P. Chabert, "Comparison of a hybrid model to a global model of atmospheric pressure radio-frequency capacitive discharges," *Journal of Physics D: Applied Physics*, vol. 45, no. 49, p. 495 204, 2012.

[162] W. Van Gaens and A. Bogaerts, "Corrigendum: Kinetic modelling for an atmospheric pressure argon plasma jet in humid air," *Journal of Physics D: Applied Physics*, vol. 47, no. 7, p. 079 502, 2014.

[163] I. E. Kieft, E. P. V. D. Laan, and E. Stoffels, "Electrical and optical characterization of the plasma needle," *New Journal of Physics*, vol. 6, pp. 1–14, 149 2004.

[164] N. Naudé, J.-P. Cambronne, N. Gherardi, and F. Massines, "Electrical model and analysis of the transition from an atmospheric pressure Townsend discharge to a filamentary discharge," *Journal of Physics D: Applied Physics*, vol. 38, no. 4, pp. 530–538, 2005.

[165]   E. Podgorsak, *Radiation Oncology Physics: A Handbook for Teachers and Students*. International Atomic Energy Agency, 2006.

[166]   B. Hildebrandt, P. Wust, O. Ahlers, A. Dieing, G. Sreenivasa, T. Kerner, R. Felix, and H. Riess, "The cellular and molecular basis of hyperthermia," *Critical Reviews in Oncology / Hematology*, vol. 43, no. 1, pp. 33–56, 2002.

[167]   D. Dobrynin, A. Wu, S. Kalghatgi, S. Park, N. Shainsky, K. Wasko, E. Dumani, R. Ownbey, S. Joshi, R. Sensenig, and A. D. Brooks, "Live Pig Skin Tissue and Wound Toxicity of Cold Plasma Treatment," *Plasma Medicine*, vol. 1, pp. 93–108, 2011.

[168]   M. W. Dewhirst, B. L. Viglianti, M. Lora-Michiels, M. Hanson, and P. J. Hoopes, "Basic principles of thermal dosimetry and thermal thresholds for tissue damage from hyperthermia," *International Journal of Hyperthermia*, vol. 19, no. 3, pp. 267–294, 2003.

[169]   K. Jambunathan, E. Lai, M. Moss, and B. Button, "A review of heat transfer data for single circular jet impingement," *International Journal of Heat and Fluid Flow*, vol. 13, no. 2, pp. 106–115, 1992.

[170]   N. Zuckerman and N. Lior, "Impingement Heat Transfer: Correlations and Numerical Modeling," *Journal of Heat Transfer*, vol. 127, no. 5, p. 544, 2005.

[171]   R. P. Satti and A. K. Agrawal, "Flow structure in the near-field of buoyant low-density gas jets," *International Journal of Heat and Fluid Flow*, vol. 27, no. 2, pp. 336–347, 2006.

[172]   T. S. O'Donovan and D. B. Murray, "Jet impingement heat transfer - Part I: Mean and root-mean-square heat transfer and velocity distributions," *International Journal of Heat and Mass Transfer*, vol. 50, no. 17-18, pp. 3291–3301, 2007.

[173]   A. Lindsay, C. Anderson, E. Slikboer, S. Shannon, and D. Graves, "Momentum , Heat , and Neutral Mass Transport in Convective Atmospheric Pressure Plasma-Liquid Systems and Implications for Aqueous Targets," *Journal of Physics D: Applied Physics*, vol. 48, no. 42, pp. 1–27, 2015.

[174]   M. Laroussi and X. Lu, "Room-temperature atmospheric pressure plasma plume for biomedical applications," *Applied Physics Letters*, vol. 87, no. 2005, pp. 92–95, 2005.

[175]   Z.-s. Chang, G.-j. Zhang, X.-j. Shao, and Z.-h. Zhang, "Diagnosis of gas temperature , electron temperature , and electron density in helium atmospheric pressure plasma jet Diagnosis of gas temperature , electron temperature , and electron density in helium atmospheric pressure plasma jet," vol. 073513, 2012.

[176]   B. Huang and R. Kadali, *Dynamic modeling, predictive control and performance monitoring*. London: Springer-Verlag, 2012.

[177]   L. Ji, W. Yan, Y. Xia, and D. Liu, "The effect of target materials on the propagation of atmospheric-pressure plasma jets," *Journal of Applied Physics*, vol. 123, no. 18, 2018.

[178] Y. Yue, X. Pei, D. Gidon, F. Wu, S. Wu, and X. Lu, "Investigation of plasma dynamics and spatially varying O and OH concentrations in atmospheric pressure plasma jets impinging on glass, water and metal substrates," *Plasma Sources Science and Technology*, vol. 27, no. 6, 2018.

[179] D. Gidon, B. Curtis, J. A. Paulson, D. B. Graves, and A. Mesbah, "Model-based feedback control of a khz-excited atmospheric pressure plasma jet," *IEEE Transactions on Radiation and Plasma Medical Sciences*, vol. 2, no. 2, pp. 129–137, 2018.

[180] A. A. Fridman, A. Lin, V. Miller, S. Bekeschus, K. Wende, and K.-D. Weltmann, "The plasma treatment unit: An attempt to standardize cold plasma treatment for defined biological effects," *Plasma Medicine*, vol. 8, no. 2, 2018.

[181] H. F. Döbele, T. Mosbach, K. Niemi, and V. Schulz-Von Der Gathen, "Laser-induced fluorescence measurements of absolute atomic densities: Concepts and limitations," *Plasma Sources Science and Technology*, vol. 14, no. 2, 2005.

[182] S. Große-Kreul, S. Hübner, S. Schneider, D. Ellerweg, A. Von Keudell, S. Matejčík, and J. Benedikt, "Mass spectrometry of atmospheric pressure plasmas," *Plasma Sources Science and Technology*, vol. 24, no. 4, 2015.

[183] K. J. Åström and T. Hägglund, *PID Controllers: Theory, Design, and Tuning.* Instrument Society of America, NC, 1995.

[184] S. Qin and T. a. Badgwell, "A survey of industrial model predictive control technology," *Control Engineering Practice*, vol. 11, no. 7, pp. 733–764, 2003.

[185] D. E. Rivera, M. Morari, and S. Skogestad, "Internal model control: PID controller design," *Industrial & Engineering Chemistry Process Design and Development*, vol. 25, no. 1, pp. 252–265, 1986.

[186] K. J. Astrom and L. Rundqwist, "Integrator Windup and How to Avoid It," *1989 American Control Conference*, pp. 1693–1698, 1989.

[187] S. Wu, Z. Wand, Q. Huang, X. Lu, and Y. Pan, "Study on a room-temperature air plasma for biomedical application," *IEEE Transactions on Plasma Science*, vol. 39, no. 6, pp. 1489–1495, 2011.

[188] E. R. Adhikari and S. Ptasinska, "Correlation between helium atmospheric pressure plasma jet (APPJ) variables and plasma induced DNA damage," *The European Physical Journal D*, vol. 70, no. 9, p. 180, 2016.

[189] Trek. (). Trek model 10/10B-HS high-speed high-voltage amplifier, [Online]. Available: `http://www.trekinc.com/products/10-10BHS.asp` (visited on 02/24/2019).

[190] F. Systems. (2018). High voltage amplifiers - Falco Systems, [Online]. Available: `http://www.falco-systems.com/High_voltage_amplifier_WMA-100.html` (visited on 02/24/2019).

[191] S. Skogestad and I. Postlethwaite, *Multivariate Feedback Control, Analysis and Design.* John Wiley & Sons, New York, 2001.

[192] J. H. Lee, "Model predictive control: Review of the three decades of development," *International Journal of Control, Automation and Systems*, vol. 9, pp. 415–424, 2011.

[193] G. Pannocchia and J. B. Rawlings, "Disturbance models for offset-free model predictive control," *AIChE journal*, vol. 49, pp. 426–437, 2003.

[194] R. E. Kalman, "A new approach to linear filtering and prediction problems," *Journal of Basic Engineering*, vol. 82, pp. 35–45, 1960.

[195] J. Andersson, "A General-Purpose Software Framework for Dynamic Optimization," PhD Thesis, KU Leuven, 2013.

[196] H. Ferreau, C. Kirches, A. Potschka, H. Bock, and M. Diehl, "qpOASES: A parametric active-set algorithm for quadratic programming," *Mathematical Programming Computation*, vol. 6, pp. 327–363, 2014.

[197] D. Gidon, D. B. Graves, and A. Mesbah, "Effective dose delivery in atmospheric pressure plasma jets for plasma medicine: A model predictive control approach," *Plasma Sources Science and Technology*, vol. 26, no. 8, pp. 85 005–85 019, 2017.

[198] A. Wächter and L. T. Biegler, "On the implementation of an interior-point filter line-search algorithm for large-scale nonlinear programming," *Mathematical Programming*, vol. 106, no. 1, pp. 25–57, 2006.

[199] K. Wende, P. Williams, J. Dalluge, W. V. Gaens, H. Aboubakr, J. Bischof, T. von Woedtke, S. M. Goyal, K.-D. Weltmann, A. Bogaerts, K. Masur, and P. J. Bruggeman, "Identification of the biologically active liquid chemistry induced by a nonthermal atmospheric pressure plasma jet.," *Biointerphases*, vol. 10, no. 2, p. 029 518, 2015.

[200] R. Kumar Mandela, R. Rengaswamy, S. Narasimhan, and L. N. Sridhar, "Recursive state estimation techniques for nonlinear differential algebraic systems," *Chemical Engineering Science*, vol. 65, no. 16, pp. 4548–4556, 2010.

[201] Y. G. Kulikov and M. Kulikova, "Recursive state estimation techniques for nonlinear differential algebraic systems," *IEEE Transactions on Automatic Control*, vol. 59, no. 1, pp. 273–279, 2014.

[202] D. Gidon, D. B. Graves, and A. Mesbah, "Spatial thermal dose delivery in atmospheric pressure plasma jets," *Plasma Sources Science and Technology*, vol. 28, no. 2, 2019.

[203] P. Alaei, P. D. Higgins, R. Weaver, and N. Nguyen, "Comparison of dynamic and step-and-shoot intensity-modulated radiation therapy planning and delivery," *Medical Dosimetry*, vol. 29, no. 1, pp. 1–6, 2004.

[204] G. A. Ezzell and S. Chungbin, "The overshoot phenomenon in step-and-shoot imrt delivery.," *Journal of Applied Clinical Medical Physics*, vol. 2, no. 3, pp. 138–148, 2001.

[205] D. Gidon, D. B. Graves, and A. Mesbah, "Predictive control of 2D spatial thermal dose delivery in atmospheric pressure plasma jets," *Plasma Sources Science and Technology*, 2019, Submitted.

[206] D. Luenberger, "Observers for multivariable systems," *IEEE Transactions on Automatic Control*, vol. 11, no. 2, pp. 190–197, 1966.

[207] D. Arthur and S. Vassilvitskii, "K-Means++: the Advantages of Careful Seeding," *Proceedings of the eighteenth annual ACM-SIAM symposium on Discrete algorithms*, vol. 8, 2007.

[208] D. Gidon, X. Pei, A. Bonzanini, D. B. Graves, and A. Mesbah, "Machine learning for real-time diagnostics of cold atmospheric plasma sources," *IEEE Transactions on Radiation and Plasma Medical Sciences*, 2019, Accepted.

[209] A. Lo, G. Cleon, P. Vervisch, and A. Cessou, "Spontaneous Raman scattering: A useful tool for investigating the afterglow of nanosecond scale discharges in air," *Applied Physics B: Lasers and Optics*, vol. 107, no. 1, pp. 229–242, 2012.

[210] A. Lo, G. Cléon, P. Vervisch, and A. Cessou, "Spontaneous Raman scattering: A useful tool for investigating the afterglow of nanosecond scale discharges in air," *Applied Physics B: Lasers and Optics*, vol. 107, no. 1, pp. 229–242, 2012.

[211] P. J. Bruggeman, N. Sadeghi, D. C. Schram, and V. Linss, "Gas temperature determination from rotational lines in non-equilibrium plasmas: a review," *Plasma Sources Science and Technology*, vol. 23, no. 2, p. 023 001, 2014.

[212] N. O'Connor, V. Milosavljevi, and S. Daniels, "Development of a real time monitor and multivariate method for long term diagnostics of atmospheric pressure dielectric barrier discharges: Application to He, He/N_2, and He/O_2 discharges," *Review of Scientific Instruments*, vol. 82, no. 8, 2011.

[213] J. Vorac, P. Synek, L. Potocnakova, J. Hnilica, and V. Kudrle, "Batch processing of overlapping molecular spectra as a tool for spatio-temporal diagnostics of power modulated microwave plasma jet," *Plasma Sources Science and Technology*, vol. 26, no. 2, 2017.

[214] M. Boinet, S. Verdier, S. Maximovitch, and F. Dalard, "Application of acoustic emission technique for in situ study of plasma anodising," *NDT and E International*, vol. 37, no. 3, pp. 213–219, 2004.

[215] V. J. Law, F. T. O'Neill, and D. P. Dowling, "Evaluation of the sensitivity of electro-acoustic measurements for process monitoring and control of an atmospheric pressure plasma jet system," *Plasma Sources Science and Technology*, vol. 20, no. 3, p. 035 024, 2011.

[216] N. O'Connor and S. Daniels, "Passive acoustic diagnostics of an atmospheric pressure linear field jet including analysis in the time-frequency domain," *Journal of Applied Physics*, vol. 110, no. 1, 2011.

[217] V. J. Law, F. T. O. Neill, D. P. Dowling, J. L. Walsh, F. Iza, and N. B. Janson, "Decoding of Atmospheric Pressure Plasma Emission Signals for Process Control," *Chaotic Modeling and Simulation*, vol. 1, no. June, pp. 69–76, 2011.

[218] C. M. Bishop, *Pattern Recognition and Machine Learning (Information Science and Statistics)*. Berlin, Heidelberg: Springer-Verlag, 2006.

[219] K. P. Murphy, *Machine Learning*. Berlin/Heidelberg: Springer-Verlag, 1991.

[220] M. A. DePristo, E. Banks, R. E. Poplin, K. V. Garimella, J. R. Maguire, C. Hartl, A. A. Philippakis, G. del Angel, M. A. Rivas, M. Hanna, A. McKenna, T. J. Fennell, A. M. Kernytsky, A. Y. Sivachenko, K. Cibulskis, S. B. Gabriel, D. Altshuler, and M. J. Daly, "A framework for variation discovery and genotyping using next-generation DNA sequencing data," *Nat Genet*, vol. 43, no. 5, pp. 491–498, 2011.

[221] M. Pal and P. M. Mather, "Support vector machines for classification in remote sensing," *International Journal of Remote Sensing*, vol. 26, no. 5, pp. 1007–1011, 2005.

[222] F. Sebastiani, "Machine Learning in Automated Text Categorization," *ACM computing surveys (CSUR)*, vol. 34, no. 1, pp. 1–47, 2002.

[223] B. Pang, L. Lee, and S. Vaithyanathan, "Thumbs up? Sentiment Classification using Machine Learning Techniques," *Proceedings of the 2002 Conference on Empirical Methods in Natural Language Processing (EMNLP2002)*, 2002. arXiv: `0205070 [cs]`.

[224] P. Duygulu, K. Barnard, J. F. G. de Freitas, and D. A. Forsyth, "Object Recognition as Machine Translation: Learning a Lexicon for a Fixed Image Vocabulary," *European Conference on Computer Vision*, pp. 97–112, 2002. arXiv: `arXiv:1011.1669v3`.

[225] K. Irani, J. Cheng, U. Fayyad, and Z. Qian, "Applying machine learning to semiconductor manufacturing," *IEEE Expert*, vol. 8, no. 1, pp. 41–47, 1993. eprint: `0604015`.

[226] B. Kim and S. Park, "An optimal neural network plasma model: A case study," *Chemometrics and Intelligent Laboratory Systems*, vol. 56, no. 1, pp. 39–50, 2001.

[227] P. H. Chou, M. J. Wu, and K. K. Chen, "Integrating support vector machine and genetic algorithm to implement dynamic wafer quality prediction system," *Expert Systems with Applications*, vol. 37, no. 6, pp. 4413–4424, 2010.

[228] G. Erten, A. Gharbi, F. Salam, T. Grotjohn, and J. Asmussen, "Using neural networks to control the process of plasma etching and deposition," *IEEE International Conference on Neural Networks - Conference Proceedings*, vol. 2, pp. 1091–1096, 1996.

[229] R. Yang and R. Chen, "Real-time plasma process condition sensing and abnormal process detection," *Sensors*, vol. 10, no. 6, pp. 5703–5723, 2010.

[230] F. Pedregosa, G. Varoquaux, A. Gramfort, V. Michel, B. Thirion, O. Grisel, M. Blondel, P. Prettenhofer, R. Weiss, V. Dubourg, J. Vanderplas, A. Passos, D. Cournapeau, M. Brucher, M. Perrot, and E. Duchesnay, "Scikit-learn: Machine learning in Python," *Journal of Machine Learning Research*, vol. 12, pp. 2825–2830, 2011.

[231] M. Abadi, P. Barham, J. Chen, Z. Chen, A. Davis, J. Dean, M. Devin, S. Ghemawat, G. Irving, M. Isard, M. Kudlur, J. Levenberg, R. Monga, S. Moore, D. G. Murray, B. Steiner, P. Tucker, V. Vasudevan, P. Warden, M. Wicke, Y. Yu, X. Zheng, and G. Brain, "TensorFlow: A System for Large-Scale Machine Learning TensorFlow: A system for large-scale machine learning," *12th USENIX Symposium on Operating Systems Design and Implementation (OSDI '16)*, pp. 265–284, 2016.

[232] A. C. Mueller and S. Guido, *Introuction to Machine Learning with Python*, 1st. Sebastopol, CA: O'Reilly Media Inc, 2016.

[233] Y. Tsai, Q. Lu, L. Rippon, S. Lim, A. Tulsyan, and B. Gopaluni, "Pattern and knowledge extraction using process data analytics: A tutorial," *Preprints of the 10th IFAC International Symposium on Advanced Control of Chemical Processes*, 2018.

[234] J. T. McClave and T. Sincich, *Statistics*. Pearson Prentice Hal, 2009.

[235] J. Friedman, T. Hastie, and R. Tibshirani, "Regularization Paths for Generalized Linear Models via Coordinate Descent," *Journal of Statistical Software*, vol. 33, pp. 7–10, 2010.

[236] C. E. Rasmussen and C. K. I. Williams, *Gaussian processes for machine learning*. Cambridge, Massachusetts: The MIT Press, 2006.

[237] X. Pei, X. Lu, J. Liu, D. Liu, Y. Yang, K. Ostrikov, P. K. Chu, and Y. Pan, "Inactivation of a 25.5 μm Enterococcus faecalis biofilm by a room-temperature, battery-operated, handheld air plasma jet," *Journal of Physics D: Applied Physics*, vol. 45, no. 16, p. 165 205, 2012.

[238] Open Music Labs, *ArduinoFFT - Fast Fourier Transform Library*, Online; accessed 23-August-2018, http://wiki.openmusiclabs.com/wiki/ArduinoFFT, 2015.

[239] D. Spether, M. Scharpf, J. Hennenlotter, C. Schwentner, A. Neugebauer, D. Nüßle, K. Fischer, H. Zappe, A. Stenzl, F. Fend, A. Seifert, and M. Enderle, "Real-time tissue differentiation based on optical emission spectroscopy for guided electrosurgical tumor resection," *Biomedical Optics Express*, vol. 6, no. 4, p. 1419, 2015.

[240] G. Bennet and F. Blanes and J.E. Simo and P. Perez, "Using infrared sensors for distance measurement in mobile robots," *Robotics and Autonomous Systems*, vol. 40, pp. 255–266, 2002.

[241] M. Kelemen, I. Virgala, T. Kelemenová, Ľ. Miková, T. Frankovský Peter adnd Lipták, and M. Lörinc, "Distance Measurement via Using of Ultrasonic Sensor," *Journal of Automation and Control*, vol. 3, no. 3, pp. 71–74, 2015.

[242] M. Lindner, I. Schiller, A. Kolb, and R. Koch, "Time-of-Flight sensor calibration for accurate range sensing," *Computer Vision and Image Understanding*, vol. 114, no. 12, pp. 1318–1328, 2010.

[243] A. Bemporad, F. Borrelli, M. Morari, *et al.*, "Model predictive control based on linear programming̃the explicit solution," *IEEE transactions on automatic control*, vol. 47, no. 12, pp. 1974–1985, 2002.

[244] A. A. Ata, "Optimal trajectory planning of manipulators: A review," *Journal of Engineering Science and Technology*, vol. 2, no. 1, pp. 32–54, 2007.

[245] D. González, J. Pérez, V. Milanés, and F. Nashashibi, "A review of motion planning techniques for automated vehicles," *IEEE Transactions on Intelligent Transportation Systems*, vol. 17, no. 4, pp. 1135–1145, 2016.

[246] E. J. Szili, J. W. Bradley, and R. D. Short, "A 'tissue model' to study the plasma delivery of reactive oxygen species," *Journal of Physics D: Applied Physics*, vol. 47, no. 15, p. 152 002, 2014.

[247] T. Kawasaki, W. Eto, M. Hamada, Y. Wakabayashi, Y. Abe, and K. Kihara, "Detection of reactive oxygen species supplied into the water bottom by atmospheric non- thermal plasma jet using iodine-starch reaction," *Japanese Journal of Applied Physics*, vol. 54, p. 086 201, 2015.

[248] D. Liu, T. He, Z. Liu, S. Wang, Z. Liu, M. Rong, and M. G. Kong, "Spatial-temporal distributions of ROS in model tissues treated by a He+O$_2$ plasma jet," *Plasma Processes and Polymers*, no. June, p. 1 800 057, 2018.

[249] M. Egmont-Petersen, D. de Ridder, and H. Handels, "Image processing with neural networks—a review," *Pattern recognition*, vol. 35, no. 10, pp. 2279–2301, 2002.

[250] A. Mesbah and D. B. Graves, "Machine learning for modeling, diagnostics, and control of non-equilibrium plasmas," *Journal of Applied Physics*, 2019, Accepted/In Press.

[251] S. U. Kalghatgi, G. Fridman, M. Cooper, G. Nagaraj, M. Peddinghaus, M. Balasubramanian, V. N. Vasilets, A. F. Gutsol, A. Fridman, and G. Friedman, "Mechanism of blood coagulation by nonthermal atmospheric pressure dielectric barrier discharge plasma," *IEEE Transactions on plasma science*, vol. 35, no. 5, pp. 1559–1566, 2007.

[252] G. Fridman, M. Peddinghaus, M. Balasubramanian, H. Ayan, A. Fridman, A. Gutsol, and A. Brooks, "Blood coagulation and living tissue sterilization by floating-electrode dielectric barrier discharge in air," *Plasma Chemistry and plasma processing*, vol. 26, no. 4, pp. 425–442, 2006.

[253] S. Kuo, O. Tarasenko, J. Chang, S. Popovic, C. Chen, H. Fan, A. Scott, M. Lahiani, P. Alusta, J. Drake, *et al.*, "Contribution of a portable air plasma torch to rapid blood coagulation as a method of preventing bleeding," *New Journal of Physics*, vol. 11, no. 11, p. 115 016, 2009.

[254] X. B. Peng, M. Andrychowicz, W. Zaremba, and P. Abbeel, "Sim-to-Real Transfer of Robotic Control with Dynamics Randomization," in *2018 IEEE Int. Conf. Robot. Autom.*, IEEE, 2018, pp. 1–8.

[255] J. Tobin, R. Fong, A. Ray, J. Schneider, W. Zaremba, and P. Abbeel, "Domain randomization for transferring deep neural networks from simulation to the real world," in *2017 IEEE/RSJ Int. Conf. Intell. Robot. Syst.*, 2017, pp. 23–30.

[256] E. Stoffels, I. E. Kieft, R. E. J. Sladek, L. J. M. V. D. Bedem, E. P. V. D. Laan, and M. Steinbuch, "Plasma needle for in vivo medical treatment: Recent developments and perspectives," *Plasma Sources Science and Technology*, vol. 15, no. 4, S169–S180, 2006.

[257] D. D. Hsu and D. B. Graves, "Microhollow cathode discharge stability with flow and reaction," *Journal of Physics D: Applied Physics*, vol. 36, no. 23, pp. 2898–2907, 2003.

[258] D. Gidon, D. B. Graves, and A. Mesbah, "Model predictive control of thermal effects of an atmospheric pressure plasma jet for biomedical applications," *In Proceedings of the American Control Conference, Boston*, pp. 4889–4894, 2016.

[259] H. Pennes, "Analysis of tissue and arterial blood temperatures in the resting human forearm," *Journal of Applied Physiology*, vol. 1, pp. 5–34, 1948.